DEVELOPMENT OF EFFICIENTLY COUPLED FLUID FLOW AND GEOMECHANICS MODEL FOR HIGHLY FRACTURED RESERVOIRS

A Dissertation

by

ANUSARN SANGNIMNUAN

Submitted to the Office of Graduate and Professional Studies of
Texas A&M University
in partial fulfillment of the requirements for the degree of

DOCTOR OF PHILOSOPHY

Chair of Committee,	Kan Wu
Committee Members,	Nobuo Morita
	Jihoon Kim
	Benchun Duan
Head of Department,	Jeff Spath

December 2019

Major Subject: Petroleum Engineering

Copyright 2019 Anusarn Sangnimnuan

ABSTRACT

Number of unconventional developments have increased greatly in the recent years to meet the global demand on hydrocarbon usages. Completion work can be very challenging due to complex characteristic of unconventional reservoir, which directly affects production performance. A rapid decline in parent well production has recently been observed in many unconventional developments, which subsequently increases the number of infill wells. Hydraulic fractures created from infill wells tend to propagate towards the parent well as a result of reservoir depletion. The interference between parent and infill well fractures due to a tight spacing is the main cause of poor production performance in both parent and infill wells. Stress change can be observed as the reservoir depletes due to the poroelastic effect. This leads to complex fracture geometry created during infill well completion, which is difficult to predict and ususally causes negative imacpt on well production. Therefore, it is important to be able to predict depletion-induced stress change in the reservoirs with complex fracture geometries. The prediction of fracture interference is sometimes not accurate compared to the field observation as most studies mainly focus on stress evolution in planar fracture geometries since it is difficult to model complex fracture geometries. Unstructured grids have been implemented to handle such problem but it usually comes with high computational cost and less computational efficiency, which is not a good option when simulating a field-scaled reservoir. This has become the main motivation of this work, which is to develop a coupled geomechanics and fluid flow model to characterize stress evolution due to reservoir depletion in highly fractured reservoirs with high computational efficiency.

In this dissertation, I have developed a coupled geomechanics and fluid flow using a well-known sequentially coupled method called fixed stress-split to capture stress change in both

magnitude and orientation during reservoir depletion. The coupling method was selected to ensure stability of the simulation while maining low computational cost. Embedded Discrete Fracture Model (EDFM) was coupled with the model to gain capability in simulating complex fracture geometries using structured gridding system. This significantly improves computational efficiency as well as opens the possibility of exploring cases with complex fracture network. The simulator was developed based on an open-source code called Open source Field Operation And Maniputation (OpenFOAM), allowing the simulation to be conducted in full 3D without significantly impacting computational cost. The developed model was used to predict refracturing performance in a highly fractured reservoir as well as infill well completion in a multi-payzone reservoir. In addition, the model was coupled with complex fracture propagation model to study how heterogeneous stress state affects fracture geometry created during infill well treatment, which can greatly help predict fracture interaction and maintain production performance. Two-phase flow was also implemented to the model for some field case studies such as water injection.

The results observed in this study suggest that fracture geometry is a main factor that affects stress change in magnitude and orientation. The presence of natural fractures and fracture spacing plays an important role in refracturing performance in highly fractured reservoirs. Critical time can be used to determine when the refracturing should be performed to ensure the successful results and obtain optimum refracturing locations. For the infill well completion in a reservoir with multiple pay zones, it is suggested that both parent wells should be placed in different layers to mitigate stress change in the infill zone. Fracture penetration effect should also be considered as it accelerates stress reorientation in the infill zone. Severe asymmetrical fracture geometries with the longer side being closer to the depleted zone can be observed in the infill well with short spacing

when coupling fracture propagation model with the reservoir-geomechanics model. These results are crucial and can be a guideline for field operation in reservoirs with complex fracture network.

DEDICATION

I dedicate this work to my parents and my fiancé.

ACKNOWLEDGMENTS

First of all, I would like to express deep gratitude to my advisor, Professor Kan Wu, for her patient guidance, advice, continuous support, and sharing her experiences throughout my PhD study. I would have never completed this work without her support.

I would also like to thank my committee members, Professor Nobuo Morita, Professor Jihoon Kim, and Professor Benchun Duan for the advice and suggestions to improve this work and the knowledge I have learned from all the geomechanics courses I have learned from both Dr. Morita and Dr. Kim, which allowed me to build the foundation for this work.

Then I would like to thank Chevron Corporation for the internship opportunity, which allowed me to expand my knowledge from academia to industry. I also received many helps from my co-workers including Yunhui Tan and mentor, Shugang Wang.

Thanks also go to my lab members: Jizhou Tang, Xuyang Guo, Shaowen Ma, Jiawei Li, Seunghwan Chun, and Ross Patterson and the department faculty and staff for making my time at Texas A&M University a great experience.

Finally, thanks to my brother, mother and father for their encouragement and selfless love and my fiance, Camilla Hellen Peixoto de Lima for her patience and love.

CONTRIBUTORS AND FUNDING SOURCES

Contributors

This work was supervised by a dissertation committee consisting of Professor Kan Wu [advisor], Professor Nobuo Morita, Professor Jihoon Kim of the Department of Petroleum Engineering and Professor Benchun Duan of the Department of Geology and Geophysics.

All work for the dissertation was completed independently by the student.

Funding Sources

Graduate study was supported financially by the Crisman Institute for Petroleum Research at Texas A&M University and Texas A&M Engineering Experiment Station (TEES).

NOMENCLATURE

u = Displacement vector, ft

u_x = Displacement in x-direction, ft

u_y = Displacement in y-direction, ft

u_z = Displacement in z-direction, ft

x = Location in x-direction, ft

y = Location in y-direction, ft

z = Location in z-direction, ft

σ = Total stress tensor, psi

σ_v = Volumetric mean total stress, psi

p = Fluid pressure, psi

ρ_b = Single-phase fluid bulk density, lb·ft^{-3}

g = Gravitational acceleration, ft·s^{-2}

σ_0 = Total stress tensor at initial state, psi

$\sigma_{v,0}$ = Volumetric mean total stress at initial state, psi

p_0 = Fluid pressure at initial state, psi

C_{dr} = Rank-4 elastic tensor, psi

ε = Strain tensor, psi

ε_v = Volumetric strain tensor, psi

V = Fluid flow rate, lb·ft^{-3}

q = Source or sink term, s^{-1}

M = Biot's modulus, psi

b = Biot's coefficient, dimensionless

c_f = Fluid compressibility, psi^{-1}

K_s = Bulk modulus of solid grain, psi

ϕ = Porosity, dimensionless

K_{dr} = Drain bulk modulus, psi

w = External load, psi

T = Traction force at the boundary, psi

p_b = Boundary pressure, psi

r_w = Well radius, ft

E = Young's Modulus, psi

ν = Poisson's ratio, dimensionless

μ_f = Fluid viscosity, cp

k = Matrix permeability, md

τ = Coupling strength, dimensionless

λ = 1st Lame constant, psi

μ = 2nd Lame constant, psi

S_w = Saturation of water phase, dimensionless

S_o = Saturation of oil phase, dimensionless

V_w = Velocity of water phase, $ft \cdot s^{-1}$

V_o = Velocity of oil phase, $ft \cdot s^{-1}$

ρ_w = Density of water phase, $lb \cdot ft^{-3}$

ρ_o = Density of oil phase, $lb \cdot ft^{-3}$

ρ_g = Density of gas phase, $lb \cdot ft^{-3}$

μ_w = Viscosity of water phase, cp

μ_o = Viscosity of oil phase, cp

μ_g = Viscosity of gas phase, cp

p_w = Pressure of water phase, psi

p_o = Pressure of oil phase, psi

k_{rw} = Relative permeability of water phase, dimensionless

k_{ro} = Relative permeability of oil phase, dimensionless

K = Matrix permeability, md

k_w = Permeability of water phase, md

k_o = Permeability of oil phase, md

c_w = Compressibility of water phase, psi^{-1}

c_o = Compressibility of oil phase, psi^{-1}

p_c = Capillary pressure, psi

q_w = Water injection rate, $ft^3 \cdot s^{-1}$

q_o = Oil production rate, $ft^3 \cdot s^{-1}$

M_w = Water phase mobility, $md \cdot cp^{-1}$

M_o = Oil phase mobility, md·cp^{-1}

L_w = Gravitational contribution of water phase, s

L_o = Gravitational contribution of oil phase, s

p_{wf} = Pressure of water phase in fracture domain, psi

p_{of} = Pressure of oil phase in fracture domain, psi

$p_{o,0}$ = Pressure of oil phase at initial state, psi

$\bar{p}$ = Averaged pressure between wet and dry phase, psi

$\bar{p}_0$ = Averaged pressure between wet and dry phase at the initial state, psi

S_{wf} = Saturation of water phase in fracture domain, dimensionless

S_{of} = Saturation of oil phase in fracture domain, dimensionless

M_{wf} = Water phase mobility in fracture domain, md·cp^{-1}

M_{of} = Oil phase mobility in fracture domain, md·cp^{-1}

ΔS_w = Variation of water saturation over a time step, dimensionless

Δt_n = Global time step, s

V_f = Volume of fracture segment, ft^3

S_{seg} = Area of fracture segment perpendicular to the fracture aperture, ft^2

w_f = Fracture width, ft

ϕ_f = Pore volume in fracture cell, dimensionless

V_b = Bulk volume of the cell assigned to the fracture segment, ft^3

λ_t = Relative mobility, cp^{-1}

T_{NNC} = NNC transmissibility, md·ft

Δp = Pressure difference between matrix and fracture cell, psi

$\bar{\bar{K}}$ = Matrix permeability tensor, md

$\vec{n}$ = Normal vector of fracture plane, dimensionless

d_{f-m} = Average normal distance from matrix to fracture, ft

p_f = Pressure of fluid inside fracture domain, psi

q_{f-m} = Flow from fracture domain to matrix domain and vise-Versa, $ft^3 \cdot s^{-1}$

q_{f-f} = Flow from fracture domain to another fracture domain and vise-versa, $ft^3 \cdot s^{-1}$

T_{f-m} = Transmissibility between fracture and matrix cell, md·ft

T_{f-f} = Transmissibility between two fracture cells, md·ft

T_{nfi-m} = Transmissibility between natural fracture set i and matrix, md·ft

T_{f-nfi} = Transmissibility between hydraulic fracture and natural fracture set i, md·ft

$T_{nfi-nfj}$ = Transmissibility between natural fracture set i and set j, md·ft

T_1 = Transmissibility inside fracture cell 1, md·ft

T_2 = Transmissibility inside fracture cell 2, md·ft

k_{f1} = Permeability inside fracture cell 1, md

k_{f2} = Permeability inside fracture cell 2, md

d_{f1} = Weighted average of the normal distances from centroids of subsection

to the intersection line in cell 1, ft

d_{f2} = Weighted average of the normal distances from centroids of subsection to the intersection line in cell 2, ft

w_{f1} = Fracture width in cell 1, ft

w_{f2} = Fracture width in cell 2, ft

A_f = Area of fracture segment, ft^2

L_{int} = Length of the intersection line, ft

M_f = Biot's modulus inside fracture domain, psi

k_f = Permeability inside fracture domain, md

x_n = Distance from fracture cell to matrix cell, ft

V_c = Cell volume, ft^3

t_d = Characteristic time, dimensionless

L = Domain length, ft

H = Domain height, ft

L_x = Domain length in x-direction, ft

L_y = Domain length in y-direction, ft

L_z = Domain length in z-direction, ft

N_x = Number of cells in x-direction, dimensionless

N_y = Number of cells in y-direction, dimensionless

N_z = Number of cells in z-direction, dimensionless

σ_{xx} = Total stress in x-direction, psi

σ_{yy} = Total stress in y-direction, psi

σ_{zz} = Total stress in z-direction, psi

$\Delta\sigma_{xx}$ = Induced stress in x-direction, psi

$\Delta\sigma_{yy}$ = Induced stress in y-direction, psi

$\Delta\sigma_{zz}$ = Induced stress in y-direction, psi

σ_{eff} = Effective stress, psi

$\sigma_{xx,0}$ = Initial total stress in x-direction, psi

$\sigma_{yy,0}$ = Initial total stress in y-direction, psi

$\sigma_{zz,0}$ = Initial total stress in z-direction, psi

σ_{Hmax} = Maximum horizontal stress, psi

σ_{hmin} = Minimum horizontal stress, psi

TABLE OF CONTENTS

Page

LIST OF FIGURES

Page

LIST OF TABLES

Page

CHAPTER 1: INTRODUCTION

1.1 Background and motivation

Developments in unconventional reservoirs have been of major interest to operators for hydrocarbon production in the past years. A recent drastic increase in production has been observed in many unconventional reservoirs to balance the worldwide demand (Holditch 2003, Bowman 2006, Jia et al. 2012). Unconventional reservoirs are very complex and often difficult to determine if the reservoir performance is worth the development. New and advanced technologies have arised to deal with unconventional reservoirs with low permeability including changing well orientation from vertical to horizonal with multi-stage fractures (McDaniel and Ripler 2009, Rahim et al. 2012). Unconventional reservoirs include tight-gas, tight-oil sands and gas and oil shales, which cannot be economically depleted without hydraulic fracturing. Fractures created during horizontal well completion can be very complex as a result of reservoir heterogeneity (Sierra 2016) and thus, resulting in lower-than-expected production performance.

Due to the recent decrease in oil price, one way to effectively gain more production while maining low operating cost is to perform a parent well refracturing since it is sometimes difficult to completely drain the reservoir from just the initial fracturing (Butula et al. 2015). The goal of refracturing is to access the un-depleted zones in the reservoir with the new fractures created during refracturing to gain more production, while minimizing operating cost. Difficulty in unconventional developments especially for refracturing include complex reservoir formation and heterogeneous stress states. Refracturing is a well-known process and has been performed since the 1950's in vertical wells. Mixed results have been observed as studied by Grieser et al. (2016). However, when it comes to developments in unconventional reservoirs, horizontal wells with

multistage hydraulic fracture treatments are preferable due to the complexity of reservoirs (Du et al., 2016). Prior to refracturing, it is important to justify if it is worth the investment as the goal of refracturing is to gain more production while avoiding the cost associated with completing a new well. The success is mostly subject to how candidates are selected for refracturing. Mcfall et al. (2017) studied refracturing operation in Eagle Ford Shale and provided guidelines for candidate selection for refracturing. Lindsay et al. (2016) investigated the characteristics of six different unconventional plays across the US for refracturing with chemical diverters. It was concluded that even at low oil prices, many basins have realized economically successful refracturing treatments, meaning that refracturing is a good alternative if candidates have been carefully selected. It is also crucial to understand if a well is underperforming due to an inefficient completion or due to reservoir conditions to determine if refracturing should be performed or not (Barree et al., 2017).

However, refracturing is not always successful due to many factors including complexity of the reservoir formation and the method to completely isolate the existing fractures in order to direct all the fluid to the newly created fractures. This is when another major development, which is infill well completion, comes into play. Infill well completion involves the creation of a new well in the neighbouring area of the existing well (parent well). Although drilling a new well can be costly, the production gain from this new well can be more substantial than refracturing the parent well. Some of the main factors to be considered when performing infill well completion includes well spacing and location of peforation clusters.

Unconventional reservoirs in the US have reached the point where the number of newly drilled wells or infill wells are surpassing existing wells or parent wells (Miller et al., 2016). Cao et al., (2017) shows that 60% of infill wells drilled from 2010 to 2016 are from the past 3 years. Lindsay et al., (2018) suggests that 70% of newly drilled Eagle Ford wells were from 2017, which

is still very recent. The rapid increase in the number of newly drilled wells leads to smaller spacings between parent and infill wells or sometimes between two infill wells, which directly impacts the production of both parent and infill wells (Malpani et al., 2015). Microseismic data also suggests that severe asymmetry of fractures with the longer side being the one closer to the depletion zone can be observed if the well spacing is too small (Cipolla et al., 2018). Poorer production performance in parent well can also be observed in Eagle Ford, Haynesville, and Marcellus shale plays (Malpani et al. 2015). Generally, production of infill wells is underperformance because of depletion from parent well and/or inter-well production competition among parent wells and adjacent infill wells, which alters reservoir characteristic and causes a detrimental effect on both parent and infill wells (Lindsay et al., 2018). King et al., (2017) showed a sudden decrease in the production of the parent well after the completion of infill well due to an interaction between parent and infill wells.

The interference of two wells sometimes is called “fracture hits” and can widely be observed in shale reservoir development and directly determines the efficiency of hydrocarbon recovery (Ajani et al., 2012). Lindsay et al. (2018) also shows that child well usually has poorer performance than parent well despite being completed under the same conditions. This helps confirm the occurrence of fracture hits, which has brought up the necessity of well spacing optimization that should be based on a good indicator like frac hits (Ajisafe et al., 2017 and Rafiee et al., 2017). Fracture hits are mainly a result of pressure depletion in the parent well, which induces unsysmetical propagation of fractures from adjacent wells. This results in a decrease in completion effectiveness. The propagation direction of fractures is determined based on the direction of the maximum horizontal stress. This direction changes as the stress state changes in magnitude and orientation induced by reservoir depletion.

Stress changes associated with reservoir depletion is often observed in the field and can greatly affect not only reservoir permeability and porosity but also orientation of principal stresses due to poroelastic effect. Stress reorientation determines the propagation direction of new fractures, which is important for unconventional reservoir developments, such as infill well completion and refracturing in parent well. Fractures can also turn 90^o as a result of stress reversal, which occurs when maximum horizontal stress becomes smaller than minimum horizontal stress (Safari et al., 2016). Most of the stress reversals can be observed along the longitudinal direction of the fractures as maximum horizontal stress becomes smaller than minimum horizontal stress (Roussel et al., 2013, Gupta et al., 2012) as the depletion mainly occurs along the longitudinal direction. This, in turn, can cause interaction between infill and parent well fractures and deteriorate production of both wells.

Depletion-induced stress changes can be predicted using coupled geomechanics and fluid flow models. Many coupled geomechanics and fluid flow models have been developed to investigate mechanism of depletion-induced stress state changes and provide the updated heterogeneous stress field, which can be used to predict fracture propagation in infill wells (Dean et al. 2006, Kim et al. 2009, Zoback 2010, Roussel et al. 2013, Safari et al. 2015, and Kumar et al. 2018). Some of the models also consider various physical effects such as hydraulic fracture propagation (Dean et al., 2009), stress reorientation in waterflood (Hwang et al., 2015), and thermodynamics effect (Blanco-Martin, 2016). The updated stress states are used as an input for fracture propagation model to predict fracture geometries (Wu and Olson, 2015a) created during refracturing or infill well completion, which can help determine the cause of frac hits and subsequently production loss in both parent and infill wells. Extended studies were also carried out to understand behaviors of fracture growth in infill wells (Rezaei et al. 2017, Guo et al. 2018,

and Huang et al. 2019) with the main goal to prevent or reduce fracture hits. Huang et al., 2015 incorporated geomechanics workflow for fracturing optimization in infill well completion to minimize production loss.

Although much work has been done to investigate stress evolution due to reservoir depletion (Roussel et al., 2013, Gupta et al., 2012, Safari et al., 2016), one main feature that is still missing is modeling reservoir geomechanics in reservoirs with complexfracture geometry. Previous studies are only based on planar fracture geometry in one payzone without effect of natural fractures as it does not require complex gridding system or a fully 3D simulator, which are not always the case in the field especially for unconventional reservoirs. This limits the possibility of investigating stress evolution in multi-payzone reservoirs due to non-planar or complex fracture geometries from parent and infill, which are key parameters when studying refracturing or infill well completion in unconventional reservoirs. Therefore, incorporating complex fracture geometries in the model can yield a more accurate result in terms of stress analysis and production forecast as actual fracture geometries in the field are used in the analysis.

Fractures can also propagate to a different layer due to weak bedding interface as suggested by Tang et al., 2018, which requires a 3D fracture propagation model to incorporate the effect of fracture height growth (Wu and Olson, 2015b). A 3D coupled geomechanics and fluid flow model is required in order to predict depletion-induced stress in a different layer, which is essential for determining the sequence of completion (vertical or lateral) in a multi-payzone reservoir. In addition, the presence of natural fracture fractures directly affects fracture propagation paths and tends to create much more complex fracture geometries (Weng et al., 2011). Most of the time, fracture geometries are not uniform (Webster et al., 2013, Gustavo et al., 2016), which can be as a

result of stress shadowing when multiple fractures are propagating simultaneously, heterogeneity of reservoir properties, or stress state induced by depletion.

Complex fracture geometries can be obtained using the fracture propagation model. In many circumstances, complex fracture geometries are modeling using DFN, which utilizes unstructured grids with grid refinement around fractures (Cipolla et al. 2011). However, this comes with high computational cost and instability in some cases. To be able to accommodate the complexity of fracture geometries while still using structured gridding discretization, Embedded Discrete Fracture Model (EDFM) has been developed. However, past studies mostly utilized EDFM mainly for reservoir simulation (Li et al. 2008, Xu 2015). This suggests that the geomechanical effect, which is very important when considering fracture propagation and interactions aspect, is still missing. In this study, the goal is to couple EDFM with a 3D geomechanics and fluid flow model to provides access to simulate complex fracture including the presence of natural fractures in a 3D reservoir under production to capture the changes of depletion-induced stress changes in both magnitude and orientation and perform production forecast based on structured gridding system. The obtained stress states can then be used to predict the geometry of newly created fractures, which is very useful for both refracturing and infill well completion.

1.2 Objectives

In order to optimize parent-infill well development in highly fractaured unconventional reservoirs , a 3D coupled fluid flow and geomechanics was to be developed. The overall goal is to utilize the developed model for field case studies to understand the effect of stress changes and

provide guidelines for developments in unconventional reservoirs to reduce production loss and improve completion/refracturing efficiency. Followings are sub-objectives of this study:

1. Develop a 3D coupled geomechanics and fluid flow capable of predicting depletion-induced stress change in a multi-payzones reservoir using a finite volume-based open source code (OpenFOAM).
2. Couple the developed model with EDFM to gain capability in simulating non-planar fracture geometries as well as complex fracture network containing multiple natural fractures using structured gridding system.
3. Upgrade the model from single-phase flow to two-phase flow to handle the problems involving water injection or reservoirs containing two-phase fluid and capillary effect.
4. Apply the developed model to study effectiveness of refracturing in parent well in highly fractured reservoir by investigating depletion-induced stress change.
5. Utilize the model for the study of infill well completion in multi-payzone reservoirs to determine the sequence of stacked pay and well spacing optimization in tightly spaced horizontal wells.

1.3 Literature review

1.3.1 Coupled geomechanics and fluid flow model

In order to accurately predict stress evolution due to reservoir depletion, a coupled model of fluid-flow and geomechanics capable of predicting stress change due to poroelastic effect is necessary. There are three types of models, an explicit method, a fully coupled method, and a sequentially implicit method. Results obtained from all three methods can be similar or different depending on how strong the geomechanical effect is. The explicit method simply solves fluid flow following by geomechanics. The calculation usually is only performed one time at each time step. The solutions obtained through this method can be acceptable if the smaller time steps are used (Dean at al. 2006) or if the pore volume compressibility is updated frequently during the

simulation. The fully coupled method solves fluid flow and geomechanics simultaneously resulting in a large system of equations and high computational cost but the solutions are the most reliable compared to other methods. Lee (2008) applied a fully coupled method in studying fluid flow in deformable porous media. The sequentially implicit method solves fluid-flow and geomechanics separately during the same time step, this produces a smaller system of equations resulting in lower computational time compared with the fully coupled method. Dean et al. 2006 suggests that solutions obtained from this method can be acceptable if a smaller tolerance is used, which may consequently yield higher computational cost. As discussed by Kim et al. (2011a and 2011b), the sequential method can mainly be divided into two main categories, i.e. solving geomechanics first or solving fluid-flow first. Both methods can yield either the same result or different results depending on the type of problem being solved. However, among all the methods fixed stress-split and undrained-split are found to be unconditionally stable. Fixed stress-split was used by Jha et al. (2014) to simulate multiphase flow and geomechanics of faulted reservoirs. Wang (2014) also used this method to develop reservoir simulator capable of simulating complex coupled poromechanical process on massively parallel computers.

1.3.2 Coupled geomechanics and fluid flow model in highly fractured reservoirs

The coupled reservoir-geomechanics model has widely been used as a main tool to capture rock deformation due to changes in reservoir pressure (injection or production). Rock deformation directly affects stress change in both magnitude and orientation, which is an important key when studying refracturing of infill well completion. Therefore, to accurately model stress change due to rock deformation and fracture aperture change as a result of reservoir depletion, researchers have developed several models to consider these effects including dual-porosity model, discrete

fracture network model as well as embedded fracture continuum appraoch. Each model has both advantages and disadvantages, which will be further discussed in the following subsections.

1.3.2.1 Dual porosity dual permeability model (DPDP)

The dual-porosity model is used as a tool to model two distinct continua containing reservoir and fractures mainly for naturally fractured reservoirs. The dual-porosity model was upgraded from a single porosity model that considers only flow in the reservoir and originally developed by Barenblatt et al. (1960). The model was later modified and introduced to the petroleum reservoir by Warren and Root (1963). The fracture has low storage capacity but high conductivity, while the matrix has high storage capacity but low conductivity. Kazemi et al. (1976) developed a single and multiple dual-porosity model for a two-dimensional radial system. Thomas et al. (1983) improved the model to 3D, three-phase for simulating naturally fractured reservoirs using pseudo-capillary pressure and relative permeability.

The model originally assumes that the communication between each grid block only occurs in the fracture, while each grid block in the matrix only communicates with fracture. Bai (1993) and Berryman and Wang (1995) modified the model by adding communication between each matrix block and the name was changed to Dual Porosity Dual Permeability model (DPDP) representing different porosity and permeability in matrix and fracture blocks. In addition, Multiple Interacting Continua (MINC) was developed (Berryman 2002) to consider multiple materials in the same grid blocks, which is very useful for multi-material reservoirs. Lim and Aziz (1994) improved matrix-fracture transfer function by implicitly solving the partial differential equation representing the flow between fracture and matrix.

To model depletion-induced stress change, the geomechanical part is coupled with the reservoir simulator. Bai et al. (1994) proposed a coupled geomechanics with dual-porosity model, which captures both matrix and fracture deformation. The system of equations becomes more complicated with geomechanical effect and the coefficient of each term appearing in the equations can be computed differently depending on how the equations are derived. Chen and Teufel (1997) summarized how the coefficients can be computed as suggested by several authors. Mehrabian (2014) applied dual porosity concept in deriving multi-porosity and multi-permeability and coupling with coupled geomechanics and fluid flow model for fluid-saturated and linearly elastic media. Kim et al. (2012) and Wang et al. (2017) coupled geomechanics with MINC for multi-material reservoirs. Change of fracture aperture directly affects fracture permeability and porosity.

1.3.2.2 Discrete Fracture Network Model (DFN)

Although the dual-porosity model is capable of simulating multiple fractures in the reservoir, it cannot capture explicit fracture geometries for both hydraulic and natural fractures. This is when the Discrete Fracture Network model (DFN) comes into play as it allows the fracture to be modeled explicitly according to its geometry obtained from fracture propagation model or predefined geometry. The model is mainly used to simulate complex fracture network (Min and Jing 2003, Sahimi 2011, Sun et al. 2011, Doe et al. 2014, Mi et al. 2016) and in some cases with multiple natural fractures (Offenberger et al. 2013). However, for the case of non-planar or complex fracture geometries, unstructured gridding or local grid refinement is required, resulting in higher computational cost and less computational stability for some cases containing multiple fractures and complex fracture geometries (Wang et al. 2016, Ding 2019, Hui et al. 2019). This makes the model becomes unpractical for some case studies. DFN was shown to provide similar or even better results compared to the dual-porosity model as demonstrated by Zhang et al. 2018.

Geomechanics is coupled with reservoir simulator to model rock deformation in the reservoir as well as capture fracture deformation as the fractures are modeled explicitly through grid refinement or unstructured gridding. (Rutqvist et al. 2002, Wang et al. 2015, Liu et al. 2018).

1.3.2.3 Embedded Fracture Continuum Approach (EFC)

Embedded Fracture Continuum was developed with the goal to improve the limitations of DFN. The idea is to apply the concept of Embedded Discrete Fracture Model (EDFM) and combine with the continuum model. The method is called fracture continuum approach (Boros et al. 2008, Hao et al. 2012). The main concept is having the fracture cells representing the actual fractures in the reservoir. Each fracture cell contains the equivalent porous medium with its own properties obtained from the calculation of fracture-matrix intersection. Fracture orientation and properties are incorporated in the calculation resulting in different properties in each fracture cell (Botros et al. 2008, Scheffler 2008). This method has also been coupled with geomechanics-fluid flow model (Figueiredo 2015, Yan et al. 2016). Embedded fracture continuum approach (EFC) was introduced by Dang et al. 2019 to study the coupled hydromechanical behavior of the fractured porous media. The idea is to explicitly model the fracture network based on fracture orientation and properties using fracture cell concept. These additional fracture cells are similar to EDFM concept but the mechanical properties are modified based on fracture orientation and how it is intersected with the matrix cells. This allows the model to be solely based on structured grids, which significantly improves computational time and cost compared to DFN. Equivalent poroelastic properties of each fracture cell can be determined with the adaption from the dual-porosity model following Oda's crack tensor (Rutqvist et al. 2013, Maghous et al. 2013, Wan and Eghbalian 2016) by modeling fracture and matrix compliance tensor separately to obtain fracture and matrix deformation.

1.3.3 Finite Volume Method (FVM) in coupled geomechanics and fluid flow

There are many types of numerical methods that can model coupled fluid-flow and geomechanics. Finite Element Method (FEM) is one of the methods used in many commercial software (ABAQUS, FLAC3D®) due to its capability in solving solid mechanics equation in both poroelastic and poroplastic formulations. Simulators used by both Roussel et al. (2013) and Gupta et al. (2012) are also based on FEM. However, as presented by Tang et al. (2015), Finite Volume Method (FVM), which has mainly been used in Computational Fluid Dynamics (CFD), can be a good alternative to FEM with its capability in handling both linear and nonlinear continuum solid mechanics (Jasak et al. 2000). A main feature of FVM is the solution being a cell-centered base, while FEM only handles solutions at edges of elements. FVM was originally used compared with FEM by Fryer et al. (1991). It was found that the solutions obtained from FVM are comparable with FEM. The conclusions suggest that FVM could have an advantage over FEM if the problem involves non-linear boundary or the deformation equations are solved in the context of thermal stress or phase change. Solutions of FVM were also compared with FEM by Fallah et al. (2000) for non-linear stress analysis and showed that FVM can be a reliable method for solving solid-mechanics-based problems. FVM can also couple fluid flow and solid body called solid-fluid interaction, in which a fluid domain and a solid domain interact at an interface (Demirdzic and Martinovic, 1993). FVM has mainly been used in multi-material problem (Tukovic, Ivankovic, and Karac, 2013), which is very useful for reservoir simulation due to its heterogeneous properties. Tang et al. (2015) adapted FVM using OpenFOAM (Open Source Field Operation and Manipulation) to model coupled poroelastoplasticity. The model contains both material nonlinearity and strong solid-fluid coupling effects based on implicit-explicit discretization. The developed model yields good agreement with analytical solutions.

When it comes to modeling crack opening, which involves the problems with discontinuities, classical FEM typically requires complicated mesing and mesh refinement might be necessary. This is when XFEM comes into play as it can handle discontinuity problems such as crack propagation using a fixed mesh. XFEM has also been coupled with EDFM to model complex fracture geometries using structured grids (Ren et al., 2017). The flow part is modeled using FVM through EDFM, while the solid deformation is handled via XFEM to address the discontinuous displacement field within the elements, which intersect the fractures. Although, XFEM allows the FEM to handle complex fracture geometries using structured grids through EDFM. The model still requires two different types of solver, one being the XFEM to solve solid deformation and another being the FVM to solve the pressure field, which increases the complexity of the solver. The reason is that FEM alone is generally proved to be difficult to handle multi-physics problems like fluid flow coupled with solid deformation (Demirdzic and Martinovic, 1993) even though there are commercial solfwares, i.e. COMSOL that are able to solve both fluid flow and solid deformation using FEM. The numerical techniques for fluid flow part may not be optimized resulting in higher computational cost. On the contrary, FVM which is well known for solving fluid flow and computational fluid dynamics (CFD), is proved to be comparable to FEM when solving solid deformation (Fryer et al., 1991, Fallah et al., 2000, Demirdzic and Martinovic, 1993). This allows the solver to be solely based on FVM to handle both fluid flow and solid deformation part, which reduces the complexity of the solver as the information to be exchanged between pressure and displacement field between two solvers (FVM and FEM) is no longer required. With the aforementioned reasons, FVM has been selected as a numerical technique for our study using the well-known open source code, OpenFOAM.

1.4 Scope of work

In this study, the goal is to address stress evolution induced by depletion in unconventional reservoirs with complex fracture geometry, which is important for infill well treatments and refracturing. Scope of work for each chapter is described as follows:

1. Chapter 2: Development of a 3D coupled two-phase flow and geomechanics with EDFM. The model is fully 3D and based on an open-source code, OpenFOAM using Finite Volume Method for discretization. The coupling model is based on a sequential method and is further modified from fixed-strain to fixed-stress split to ensure stability. EDFM is coupled with the model to open the possibility of simulating complex fracture geometry on structured gridding system which is versatile for reservoirs with multiple complex fractures.
2. Chapter 3: Utilize the coupled model to handle multiple natural fractures in a highly fractured reservoir for refracturing application based on Bakken data. Effects of natural fracture density, fracture spacing, differential stress, and reservoir permeability are to be studied to understand how each parameter affects stress change due to reservoir depletion.
3. Chapter 4: Utilize the coupled model to handle a reservoir with multiple payzones with and without natural fractures. This is for infill well completion in stacked pay. The reservoir is based on Permian basin data containing 6 payzones. Case studies include effect of parent well layout, fracture penetration, fracture geometries as well as presence of natural fractures. The goal is to understand how depletion in one payzone affects stress change in another payzone.
4. Chapter 5: Combine the coupled model with an in-house complex fracture propagation model to study how heterogeneous stress state induced by reservoir depletion affects fracture propagation created from an intill well. Effect of fracture geometry and natural fractures on stress evolution are to be observed. Well spacing between parent and infill wells is to be varied to see the effect on fracture propagation direction.

5. Chapter 6: The coupled model is to be upgraded to two-phase flow with the adaptation from Horgue (2014), which is based on the IMPES method and also includes capillary effect. The model was validated against analytical solution of Buckley-Leverett and Capillary-gravity equilibrium problems. Test cases were carried out to ensure capability of the model in terms of multiple fracture and complex fracture geometry modeling.
6. Chapter 7: Conclusions of each chapter and future work are discussed in this chapter.

CHAPTER 2: METHODOLOGY AND VALIDATION

2.1 Introduction

Stress changes associated with reservoir depletion is often observed in the field. Stress evolution within and surrounding drainage areas can greatly affect further reservoir developments, such as completion of infill wells and refracturing. Previous studies mainly focus on bi-wing planar fracture geometry, which limits the possibility of investigating stress evolution due to complex fracture geometry. This chapter introduces the development of a novel and efficient coupled fluid flow and geomechanics model with Embedding Discrete Fracture Model (EDFM) to characterize stress evolution associated with depletion in unconventional reservoirs with complex fracture.

Coupled geomechanics and fluid-flow was developed based on the well-known fixed-stress split, which is unconditionally stable and computationally efficient to simulate how stress changes during reservoir depletion. EDFM was coupled to the model to gain the capability of simulating complex fracture geometries using structured grids. The model was validated against classical Terzaghi's and Mandel's problems. Local grid refinement was used as a benchmark when comparing results from EDFM for fractures with 0^{o} and 45^{o} angles of inclination. Following that, the model was used to analyze stress distribution and reorientation in reservoirs with three different fracture geometries, planar (90^{o} angle of inclination), 60^{o} inclination, and non-planar fracture geometries. The results indicate that created fracture geometry has a significant effect on stress distribution and reorientation induced by depletion.

Part of this section is reprinted with permission from "Development of efficiently coupled fluid flow and geomechanics models to predict stress evolution in unconventional reservoirs with complex fracture geometry" by Sangnimnuan, A., Li, J., Wu, K., 2018. SPE Journal. Copyright [2018] by Society of Petroleum Engineers.

2.2 Methodology

2.2.1 Coupled geomechanics and fluid flow model

Coupled fluid-flow and geomechanics is based on biot's theory (Biot, 1941, 1955), describing the poroelastic effect in isothermal linear isotropic poroelastic material, which can be used to model a reservoir. The governing equations for this coupled system comes from mass conservation and linear-momentum balance. Mechanical deformation can be expressed as

$$\nabla \cdot \sigma + \rho_b g = 0, \quad \text{(2.1)}$$

where σ is total stress tensor (rank-2), ρ_b is single-phase fluid bulk density. g is gravitational acceleration. Combining with Biot's theory, which describes total stress in porous media in terms of effective stress, which is written in terms of strain and fluid pressure. Relationship between stress and strain with poroelastic effect from Kim et al. (2011a and 2011b) can be written as

$$\sigma - \sigma_0 = C_{dr} : \varepsilon - b(p - p_0)I, \quad \text{(2.2)}$$

where subscript 0 refers to reference state, C_{dr} is a rank-4 elastic tensor (details of C_{dr} as well as operation $C_{dr} : \varepsilon$ can be found in Appendix C), I is a rank-2 identity tensor, p is fluid pressure, b is the Biot coefficient, and ε is linearized strain tensor, which can be written in terms of displacement as

$$\varepsilon = \frac{1}{2}(\nabla u + \nabla^T u), \quad \text{(2.3)}$$

where u is a displacement vector containing 3 components. Mass conservation equation can be written in terms of change of fluid pressure and strain rate as follows

$$\frac{1}{M}\frac{\partial p}{\partial t} + b\frac{\partial \varepsilon_v}{\partial t} + \nabla \cdot V = q, \quad \text{(2.4)}$$

where $\varepsilon_v = tr(\varepsilon)$ is the volumetric strain. V is a fluid flow rate, q is a source or sink term, M is the Biot modulus, and *u* is a displacement vector containing 3 components. Relationship between Biot modulus and Biot coefficient can be shown as

$$\frac{1}{M} = \phi c_f + \frac{b-\phi}{K_s}, \quad \text{..... (2.5)}$$

$$b = 1 - \frac{K_{dr}}{K_s}, \quad \text{..... (2.6)}$$

where c_f is fluid compressibility, K_s is bulk modulus of solid grain, ϕ is porosity, and K_{dr} is drained bulk modulus, which can be computed from drained rock properties, i.e. Young's modulus (E) and Poisson's ratio (ν) and according to Kim et al. (2011b), K_{dr} can be chosen to achieve an optimal convergence rate for the fixed-stress iterative coupling

$$K_{dr} = \frac{E(1-\nu)}{(1+\nu)(1-2\nu)}. \quad \text{..... (2.7)}$$

Volumetric mean total stress is trace of the stress tensor ($\sigma_v = \frac{1}{3}\, tr\sigma$). With the relationship between volumetric stress and strain, Eq. (2.2) can be rewritten as

$$(\sigma_v - \sigma_{v,0}) + b(p - p_0) = K_{dr}\varepsilon_v. \quad \text{..... (2.8)}$$

Fluid flow rate can be written in terms of pressure through Darcy's law as

$$V = -\frac{k}{\mu_f}(\nabla p - \rho_b g), \quad \text{..... (2.9)}$$

where μ_f is fluid viscosity, k is matrix permeability (rank-2 tensor). Substitute Eq. (2.9) in Eq. (2.4), which represents fluid pressure change due to strain rate and neglect gravitational term, Eq. (2.4) becomes

$$\frac{1}{M}\frac{\partial p}{\partial t} + b\frac{\partial \varepsilon_v}{\partial t} - \nabla \cdot \frac{k}{\mu_f}(\nabla p) = q. \quad \text{..... (2.10)}$$

Eqs. (2.2) and (2.10) are called fixed-strain split (Kim et al., 2011b), in which the equations are solved in terms of strain. Fixed-strain represents the sequential method that geomechanics and fluid flow equations are solved separately starting by solving Eq. (2.10) first and then Eq. (2.2) using relationship in Eq. (2.1). Iteration stops when convergent criteria are reached on both equations. As demonstrated by Kim et al. (2011a), this method is not stable for high coupling strength ($\tau = \frac{b^2 M}{K_{dr}} > 1$). Thus, Eq. (2.10) is modified by writing volumetric strain in terms of volumetric strength as

$$\left(\frac{1}{M} + \frac{b^2}{K_{dr}}\right)\frac{\partial p}{\partial t} + \frac{b}{K_{dr}}\frac{\partial \sigma_v}{\partial t} - \nabla \cdot \frac{k}{\mu_f}(\nabla p) = q. \quad \text{..... (2.11)}$$

Eq. (2.11) is called fixed-stress split and is unconditionally stable. K_{dr} can also be expressed in terms of first and second Lame constant (λ and μ) as

$$\mu = \frac{E}{2(1+\nu)}, \quad \text{..... (2.12)}$$

$$\lambda = \frac{\nu E}{(1+\nu)(1-2\nu)}. \quad \text{..... (2.13)}$$

Substitute Eqs. (2.11), (2.12), (2.13), and (2.2) in Eq. (1) and neglect gravitational term, relationship between displacements and pressure under the momentum balance condition can finally be obtained,

$$\nabla \cdot [\mu \nabla \mathrm{u} + \mu \nabla u^T + \lambda I tr(\nabla u)] + \nabla \cdot \sigma_0 - b\nabla p + b\nabla p_0 = 0. \quad \text{..... (2.14)}$$

Eq. (2.11) can also be written in terms of displacement as

$$\left(\frac{1}{M} + \frac{b^2}{K_{dr}}\right)\frac{\partial p^n}{\partial t} - \frac{b^2}{K_{dr}}\frac{\partial p^{n-1}}{\partial t} + b\frac{\partial(\nabla \cdot u)}{\partial t} - \nabla \cdot \frac{k}{\mu_f}(\nabla p^n) = q, \quad \text{..... (2.15)}$$

where n is the current time step and n-1 is the previous time step. Eqs. (2.14) and (2.15) are solved through an iteration loop to obtain displacement and pressure as shown in Figure 2.1, detail of discretization and how to solve each equation will be discussed in section 2.2.3.

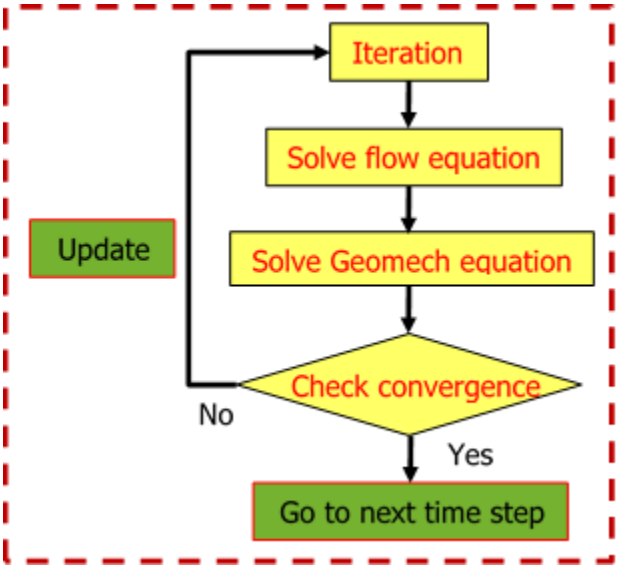

Figure 2.1. Diagram showing fixed-stress method for fluid-flow and geomechanics (Sangnimnuan et al. 2018a).

Porosity and permeability can be updated at the end of every time step, One of the models that has been widely used is shown in Eq. (2.16).

$$\frac{\partial \phi}{\partial t} = \frac{b-\phi}{K_s}\frac{\partial p}{\partial t} + (b-\phi)\frac{\partial(\nabla \cdot u)}{\partial t}. \quad \text{..... (2.16)}$$

The permeability is expressed in terms of porosity and also updated at every time step. The relationship between permeability and porosity change is expressed in Eq. (2.17). The ϕ_0 and k_0 are initial porosity and permeability respectively and γ is obtained from experiment.

$$k = k_0 exp\left[\gamma\left(\frac{\phi}{\phi_0} - 1\right)\right]. \quad \text{..... (2.17)}$$

Since our model can include not only the zero-displacement boundary condition, but also the traction boundary condition for the geomechanics equation. For the traction boundary condition, displacements at boundaries are computed from traction boundary and are then applied to solve for the entire displacement field. The traction boundary equation is obtained by setting Eq. (1) equal to traction value rather than zero,

$$\nabla \cdot [\mu \nabla u + \mu \nabla u^T + \lambda I tr(\nabla u)] + \nabla \cdot \sigma_0 - b\nabla p + b\nabla p_0 = T, \quad \text{..... (2.18)}$$

where T is the traction at the boundaries and pressure gradient term represents the force acting on the surface as a result of pressure diffence across the cells.

2.2.2 Coupled geomechanics and fluid flow model with Embedded Discrete Fracture model

In this section, Embedded Discrete Fracture Model (EDFM) is implemented to the coupled model to efficiently simulate complex fracture geometry without using unstructured grids. As mentioned by Xu et al. (2016), EDFM has been developed with the concept to honor the accuracy of discrete fracture models (DFMs) while keeping the efficiency offered by structured grids. The idea is to completely separate fracture from the matrix domain and have them communicate through transmissibility. It is worth to mention that deformation inside fracture is not considered for EDFM and deformations from matrix (reservoir) and fracture are combined together. Both fracture and matrix domains have the same grid size. Volume of fracture segment (V_f) represented in fracture domain can be computed as,

$$V_f = S_{seg} w_{f,} \quad \text{..... (2.19)}$$

where S_{seg} is the area of the fracture segment perpendicular to the fracture aperture and w_f is the fracture aperture. Pore volume of fracture (ϕ_f) domain, which represents the ratio between fracture segment contained in the cell to the total cell volume will have to be assigned as

$$\phi_f = \frac{S_{seg} w_f}{V_b}, \quad \text{..... (2.20)}$$

where V_b is the bulk volume of the cell assigned to the fracture segment. Next important parameter is transmissibility, which represents the flow from fracture to matrix domain and can be defined as

$$q_{f-m} = \lambda_t T_{f-m} \Delta p, \quad \text{..... (2.21)}$$

where $q_{f\text{-}m}$ is flow between fracture and matrix cell, λ_t is the relative mobility, $T_{f\text{-}m}$ is transmissibility between fracture and matrix, and Δp is pressure difference between fracture and matrix cell.

For connections between two fracture cells, as discussed by Xu et al. (2016), transmissibility can be expressed as

$$T_{f-f} = \frac{T_1 T_2}{T_1 + T_2}, \quad \text{..... (2.22a)}$$

$$T_1 = \frac{k_{f1} w_{f1} L_{int}}{d_{f1}}, T_2 = \frac{k_{f2} w_{f2} L_{int}}{d_{f2}}, \quad \text{..... (2.22b)}$$

where $T_{f\text{-}f}$ is transmissibility between fracture cell 1 (T_1) and cell 2 (T_2), k_{f1} and k_{f2} are permeability inside fracture cell 1 and 2 respectively, w_{f1} and w_{f1} are width of fracture cell 1 and 2 respectively, L_{int} is length of the intersection line, and d_{f1} and d_{f2} are the weighted average of the normal distances from the centroids of the sub-segments (on both sides) to the intersection line.

The transmissibility factor between matrix and fracture segment ($T_{f\text{-}m}$) depends on the matrix permeability and fracture geometry. Eq. (2.22a) can be modified incorporating normal vector between fracture and matrix as

$$T_{f-m} = \frac{2A_f(\bar{\bar{K}} \cdot \vec{n}) \cdot \vec{n}}{d_{f-m}}, \quad \text{..... (2.23)}$$

where A_f is area of the fracture segment on one side, $\overline{\overline{K}}$ is matrix permeability tensor, $\vec{n}$ is a normal vector of the fracture plane, and $d_{f\text{-}m}$ is average normal distance from matrix to fracture, which can be calculated as

$$d_{f-m} = \frac{\int_V x_n dV}{V_c}, \quad \text{..... (2.24)}$$

where x_n is distance from matrix to fracture cell, V_c is cell volume. Transmissibility term is then added to Eq. (2.15) to account for flow associated with fracture as

$$\left(\frac{1}{M} + \frac{b^2}{K_{dr}}\right)\frac{\partial p^n}{\partial t} - \frac{b^2}{K_{dr}}\frac{\partial p^{n-1}}{\partial t} + b\frac{\partial(\nabla \cdot u)}{\partial t} - \nabla \cdot \frac{k}{\mu_f}(\nabla p^n) + \lambda_t T_{f-m}({p_f}^n - p^n) = 0. \quad \text{..... (2.25)}$$

Similarly, conservation in fracture can be written as

$$\frac{1}{M_f}\frac{\partial {p_f}^n}{\partial t} - \nabla \cdot \frac{k_f}{\mu_f}\left(\nabla {p_f}^n\right) + \lambda_t T_{f-m}\left(p^n - {p_f}^n\right) = q. \quad \text{..... (2.26)}$$

Eq. (2.26) is added to the system of equations to solve for fracture pressure (p_f), M_f is biot modulus inside the fracture domain calculated using modified porosity obtained from Eq. (2.20), and k_f is fracture permeability. With the absence of strain rate term in Eq. (2.26), both hydraulic and natural fractures modeled using Eqs. (2.25) and (2.26) are assumed to be open throughout the entire production period. This suggests that there is no change in pore volume of fracture domain, only change of pore volume in matrix domain is considered. This assumption is based on the fact that total rock deformation is dominated by deformation in the matrix domain. The deformation inside

the fracture due to fracture closure may affect change of stress around the fracture but should not affect change of stress in the area outside SRV region.

In addition, the minimum grid size used to model each fracture should have at least the same size as fracture length meaning that the grid size in the longitudinal direction of the fracture should be equal to or larger than the fracture length. If the fracture length is smaller than the grid size, the errors might occur. Therefore, grid refinement may be required in some cases where the fractures are very small. However, if the fracture network does not cover the entire reservoir, the grid refinement is only required for area where fractures are located.

2.2.3 Numerical model

As stated in section 1, OpenFOAM has been used as a main solver for our model. Discretization is based on finite volume method (FVM), which is up to second-order accuracy and consists of time and space. Time discretization is implicit method and first-order accuracy, while spatial discretization consists of implicit and explicit methods, in which the majority is based on Gaussian linearization method. Discretization was discussed in Tian et al. (2015), which can be written in terms of integral form representing control volume (∂V) of each cell. Geomechanics Eq. (2.14) can be rewritten using Gauss's theorem to convert volume integral to surface integral as

$$\oint_{\partial V} ds \cdot [(2\mu + \lambda)\nabla u] = -\oint_{\partial V} ds \cdot \{\mu \nabla u^T + \lambda I tr(\nabla u) - (\mu + \lambda)\nabla u\} + \oint_{\partial V} ds \cdot (bpI) - \oint_{\partial V} ds \cdot [bp_0 I + \sigma_0], \quad \text{..... (2.27)}$$

The term in the left of Eq. (2.27) is an implicit surface diffusion term, the first term in the right is explicit surface diffusion term, following by explicit pressure coupling term, and explicit

constant term representing initial state, respectively. In addition, the fluid flow of Eq. (2.25) can be rewritten as

$$\int_V \left\{\left(\frac{1}{M}+\frac{b^2}{K_{dr}}\right)\frac{\partial p^n}{\partial t}\right\}dV - \oint_{\partial V} ds\cdot\left(\frac{k}{\mu_f}\nabla p^n\right) - \int_V \left\{\lambda_t T_{f-m} p^n\right\}dV = \int_V \left\{\frac{b^2}{K_{dr}}\frac{\partial p^{n-1}}{\partial t}\right\}dV - \oint_{\partial V} ds\cdot\frac{\partial u}{\partial t} - \int_V \left\{\lambda_t T_{f-m} {p_f}^n\right\}dV, \quad \text{..... (2.28)}$$

The first term in the left is an implicit time derivative of pressure. The second term is an implicit diffusion team and the last time is an implicit part of the flow transmissibility term. The first term in the right is an explicit term representing pressure from the previous time step, the second term is an explicit displacement coupling term, and last term is an explicit part of flow transmissibility term. Fluid flow equation inside fractures (Eq. (2.26)) can be similarly discretized as Eq. (2.28).

$$\int_V \left\{\frac{1}{M_f}\frac{\partial {p_f}^n}{\partial t}\right\}dV - \oint_{\partial V} ds\cdot\left(\frac{k_f}{\mu_f}\nabla {p_f}^n\right) - \int_V \left\{\lambda_t T_{f-m} {p_f}^n\right\}dV = -\int_V \left\{\lambda_t T_{f-m} p^n\right\}dV + \int_V q dV, \quad \text{...... (2.29)}$$

Traction boundary condition can also be discretized in the same manner as Eq. (2.27) with implicit and explicit splits but only at the boundary surfaces. With the discretization, a system of five equations consisting of three displacement equations, fluid-flow equations in matrix and fractures with 5 unknowns (i.e. u_x, u_y, u_z, p, and p_f) can then be solved sequentially using iterative method. Effective stress and total stress can be computed after obtaining displacement components and pressure using Eq. (2.2). Details of implicit and explicit discretization for each term can be found in the following subsections.

2.2.3.1 Discretization of implicit terms

Following Tian et al. 2015, implicit diffusion term (Laplacian terms) from geomechanics equation can be discretized as

$$\oint_{\partial V_P} ds \cdot [(2\mu + \lambda)\nabla u] = \sum_{f=1}^{F} \left(2\mu_f + \lambda_f\right) n_f \cdot [\nabla u]_f S_f,$$

……... (2.30)

where F is for the number of faces of V_P. With the assumption of linear variation across face *f*, the face center gradient $[\nabla u]_f$ can be evaluated as

$$n_f \cdot [\nabla u]_f = |n_f| \frac{u_N - u_P}{[d_f]}.$$

…… (2.32)

Similarly, the pore pressure diffusion term can be discretized as follows

$$\oint_{\partial V_P} ds \cdot \left(\frac{k}{\mu_f} \nabla p_f\right) = \sum_{f=1}^{F} \frac{k}{\mu_f} n_f \cdot (\nabla p)_f S_f = \sum_{f=1}^{F} \frac{k}{\mu_f} \left(|n_f| \frac{p_N - p_P}{|d_f|}\right) S_f.$$

…… (2.33)

The volume integral of the time derivative of *p* is calculated using the midpoint rule and a first-order implicit Euler method as shown below

$$\int_{V_P} \left(\frac{1}{M} + \frac{b^2}{K_{dr}}\right) \frac{\partial p}{\partial t} dV = \int_{V_P} \left(\frac{1}{M} + \frac{b^2}{K_{dr}}\right) \frac{p - p^0}{\Delta t} dV = \left(\frac{1}{M} + \frac{b^2}{K_{dr}}\right) \frac{p_P - {p^0}_P}{\Delta t} V_P,$$

……. (2.34)

Where the upper index *o* represents the old-time step value. Finally, an explicit part of the flow transmissibility term can be simply expressed as

$$\int_{V_P} \{\lambda_t T_{f-m} p\}\, dV = \lambda_t T_{f-m} p V_P.$$

…….……..…….. (2.35)

2.2.3.2 Discretization of explicit terms

The explicit surface diffusion terms (coupling terms) in Eq. (2.14) can be approximated the same way as Eq. (2.28)

$$\oint_{\partial V_P} ds \cdot \{\mu \nabla u^T + \lambda I tr(\nabla u) - (\mu + \lambda)\nabla u\}$$

$$= \sum_{f=1}^{F} n_f \cdot \{\mu [\nabla u^T]_f + \lambda I tr[\nabla u]_f - (\mu + \lambda)[\nabla u]_f\} S_f.$$

(2.36)

As opposed to the implicit discretization, the face-center gradient $[\nabla u]_f$ will be calculated from linear interpolation of the cell center gradients obtained from the previous iteration as shown below

$$[\nabla u]_f = f_x [\nabla u]_P + (1 - f_x)[\nabla u]_N, \ldots\ldots\ldots\ldots\ldots\ldots\ldots\ldots\ldots\ldots \text{(2.37)}$$

Where $f_x = |n_f|/|d_f|$ is the interpolation factor and the cell center gradient value. $[\nabla u]_P$ and $[\nabla u]_N$ can be evaluated using the least square fit approach based on the available distribution of *u*.

The explicit gradient terms are related to the nonlinearity and pressure coupling terms in Eq. (2.27). The discretization is based on linear variation of the values across the face (i.e. linear interpolation approach)

$$\oint_{\partial V} ds \cdot (bpI) - \oint_{\partial V} ds \cdot [bp_0 I + \sigma_0]$$

$$= \sum_{f=1}^{F} n_f [f_x (bpI - bp_0 I - \sigma_0)_P + (1 - f_x)(bpI - bp_0 I - \sigma_0)_N]\ S_f,$$

..… (2.38)

where all the cell center values shown above are evaluated from the previous iterative values. The explicit displacement coupling term is differentiated with respect to both time and space and can be expressed as follows

$$\oint_{\partial V} ds \cdot \frac{\partial u}{\partial t} = \oint_{\partial V_P} ds \cdot \left(\frac{u - u^o}{\Delta t}\right) = \frac{1}{\Delta t} \sum_{f=1}^{F} n_f \cdot \left(u_f - {u^o}_f\right) S_f$$

$$= \frac{1}{\Delta t} \sum_{f=1}^{F} n_f . [f_x u_P + (1 - f_x) u_N] S_f - \frac{1}{\Delta t} \sum_{f=1}^{F} n_f . [f_x {u^o}_P + (1 - f_x) {u^o}_N] S_f,$$

(2.39)

Where u_P and u_N are evaluated from the current available iterative value. Similarly, the explicit pressure term from previous time step and the explicit part of the flow transmissibility can be expressed as

$$\int_{V_P} \left\{\frac{b^2}{K_{dr}} \frac{\partial p^{n-1}}{\partial t}\right\} dV = \frac{b^2}{K_{dr}} \left(\frac{p^{n-1} - p^{n-2}}{\Delta t}\right) V_P,$$

$$\int_{V_P} \{\lambda_t T_{f-m} p_f\}\, dV = \lambda_t T_{f-m} p_f V_P.$$

…….... (2.40)

2.2.3.3 Traction boundary conditions

The traction boundary condition in FVM is discretized into displacement gradients of the control volumes on the boundary patches based on Cauchy's stress theorem. The similar Implicit-Explicit split and iteration method are to be applied on the boundary as the inner solution domain as shown below

$$(2\mu + \lambda)n_b \cdot [\nabla u]_b = T_b - \{\mu[\nabla u]_b \cdot n_b + \lambda tr([\nabla u]_b)n_b - (\mu + \lambda)n_b \cdot [\nabla u]_b\} + \{b(p_b - p_{0b}) - \sigma_{0b}\}n_b, \tag{2.41}$$

Where n_b is the outward-pointing boundary face area vector, T_b is the traction on the boundary, and the variables with lower index b are values on boundary face. Following this method, the traction boundary will be iteratively updated until both the convergence of the inner solution domain and the convergence of the boundaries are obtained.

2.3 Validation

The validation part is divided into two sub-sections. The first part is the coupled fluid-flow with geomechanics model and the second part is the implementation of EDFM in our coupled model.

2.3.1 Coupled fluid-flow with geomechanics model

The coupled model has been validated with classical poroelasticity problems consisting of Terzaghi's (1-D) (Figure 2.2a) and Mandel's (2-D) (Figure 2.2b) problems. It was assumed that the isothermal porous media composes of single-phase fluid and solid and behaves as linear poroelastic.

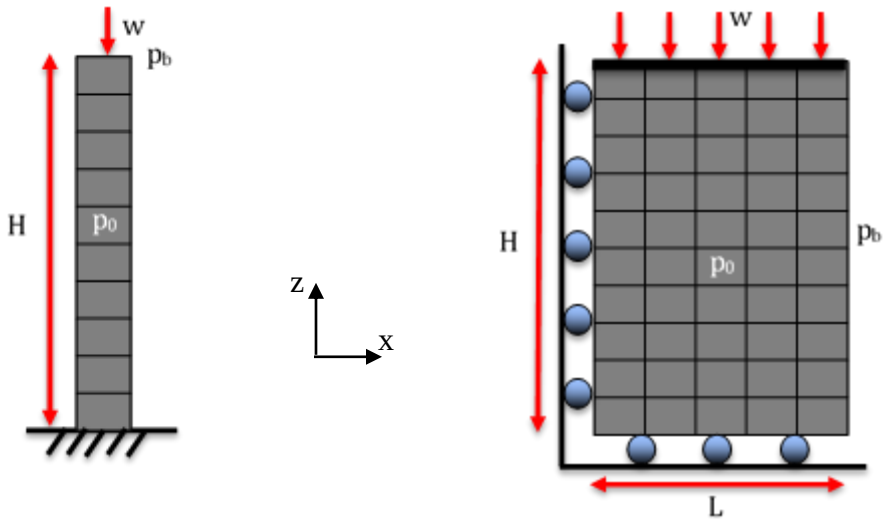

(a) Terzaghi's problem (b) Mandel's problem

Figure 2.2. Diagram for Terzaghi's problem (a) and Mandel's problem (b) (Sangnimnuan et al. 2018a).

2.3.1.1 Terzaghi's problem

Terzaghi's problem deals with 1-D consolidation of fluid-saturated column with a drainage boundary at the top domain and a no-flow boundary at the bottom domain. A constant load (w) is applied instantaneously at time t = 0. Problem geometry is shown in Figure 4a. Column height, H = 15 ft, is subdivided into 10 grid blocks of uniform size z = 1.5 ft. Gravity effect is neglected for this problem. Poroelastic parameters used for this problem are shown in Table 2.1. Initial pressure (p_0) is 1450 psi and displacement is zero everywhere. 2900 psi load (w) is applied on top of the domain while zero displacement boundary condition is applied on the bottom of the domain. Fluid is only allowed to flow out at top of the domain with boundary pressure 1450 psi and no flow on the bottom of the domain. As shown in Figure 2.3, solution for vertical displacement computed by

our model (dots) is compared against the analytical solution (lines) specified in detail in Appendix A.

Parameter	Value	Unit
Young's modulus (E)	1.45×10^5	psi
Poisson's ratio (ν)	0	-
Biot's coefficient (b)	1	-
Reservoir permeability (k)	50	md
Reservoir porosity (ϕ)	0.25	-
Fluid compressibility (c_f)	2.76×10^{-5}	psi^{-1}
Fluid viscosity (μ_f)	1	cp

Table 2.1. Parameters for Terzaghi's problem (Sangnimnuan et al. 2018a).

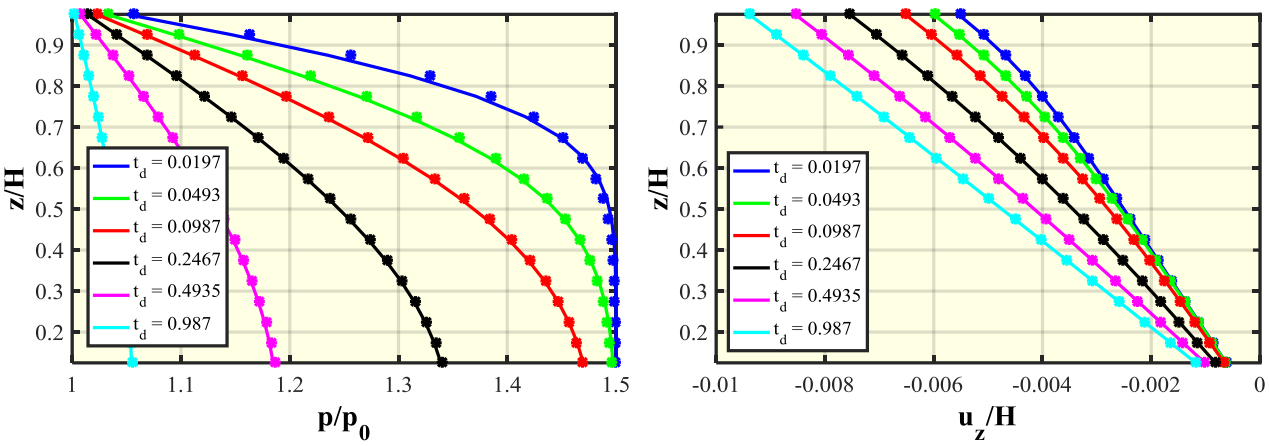

(a) Pressure plot at various times

(b) Displacement in x direction plot at various times

Figure 2.3. Comparison of numerical solution (dots) for pressure (a) and displacement (b) with analytical solution (lines) along z-direction at different characteristic times (Sangnimnuan et al. 2018a).

Figure 2.3 shows a comparison between analytical and numerical solutions for both pressure (p) and vertical displacement (u_z) at various characteristic times ($t_d = \frac{kt}{\mu(\emptyset c_f + \frac{1}{K_{dr}})L^2}$). A

good agreement was obtained for both pressure and displacement at early and late time. Initially, pressure along the column increases to about 1.5 times of initial pressure and then decreases as the fluid flows out at the bottom of the domain. Linear displacement along z-direction increases with time as there is less pressure to support the column.

2.3.1.2 Mandel's problem

The Mandel's problem deals with 2-D consolidation of fluid-saturated slab sandwiched between two rigid, frictionless, impermeable plates with compressive force being applied on both sides (Mandel 1953). Traction free is applied on both left and right boundary with fluid being allowed to flow out. A main feature of this classical problem is the Mandel-Cryer effect (Cryer 1963), which is the instant increase of pressure at the middle of the slab because two-way coupling between fluid-flow and solid deformation. To achieve this, uniform vertical displacement (in z-direction) along x-direction must be maintained at all times. This can be done by modeling a stiff plate (impervious material) on top of porous material (Lee I.S. 2008) or using time-dependent displacement boundary condition calculated from analytical solution (Wang, 2014). In this case, rather than modeling a stiff plate, geometry in Figure 2.2b (length in y-direction is longer than x-direction like a column) was used to ensure uniform vertical displacement. Due to the symmetry of this problem, the simulation was run only one-quarter of the domain by assigning left and bottom boundary as no flow for fluid part, and roller boundary as shown in figure 2.2b (zero normal displacement) for geomechanics part. The domain has 30 ft length (x-direction) and 300 ft height (z-direction) with 20 grid blocks along x-direction and 200 grid blocks along z-direction. Detail of parameters used in this problem are shown in Table 2.2. Initial pressure (p_0) is 0 psi including pressure at boundary (p_b) and displacement in both x and z-direction are zero everywhere. 616 psi load (w) is uniformly applied on top of the domain, zero displacement in normal direction is used

for left and bottom of the domain to represent symmetry boundary, and the right boundary of the domain is traction free. Fluid is only allowed to flow out on right boundary with boundary pressure being set as 0 psi and on other boundaries being no-flow. Solution for pressure, x-displacement along x-direction, and the vertical stress along z-direction computed obtained through our model are compared against the analytical solution (lines). The analytical solution is provided in detail in Appendix A.

Parameter	Value	Unit
Young's modulus (E)	6.52×10^4	psi
Poisson's ratio (ν)	0	-
Biot's coefficient (b)	1	-
Reservoir permeability (k)	50	md
Reservoir porosity (ϕ)	0.25	-
Fluid compressibility (c_f)	2.76×10^{-6}	psi^{-1}
Fluid viscosity (μ_f)	1	cp

Table 2.2 Parameters used in the calculation of Mandel's problem (Sangnimnuan et al. 2018a).

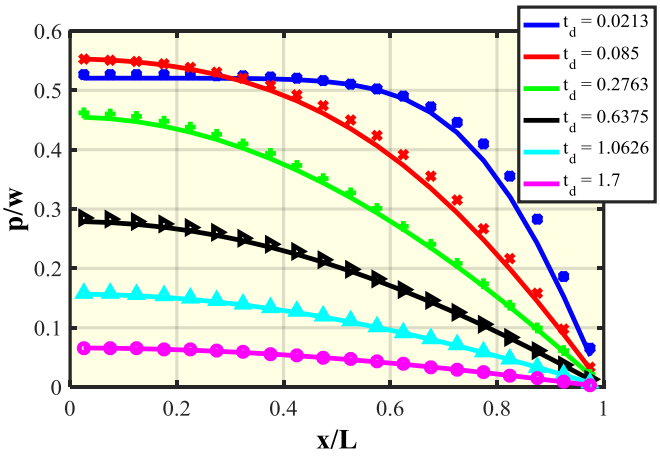

(a) Pressure plot at various times

Figure 2.4. Comparison of numerical solution (dots) for pressure (a), horizontal displacement (u_x) (b) and vertical stress (σ_{yy}) (c) with the analytical solution (lines) along x-direction at various characteristic times (Sangnimnuan et al. 2018a).

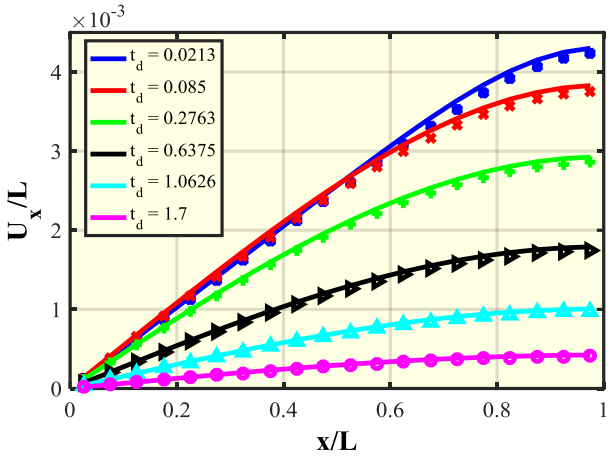

(b) Displacement plot in x direction at various times

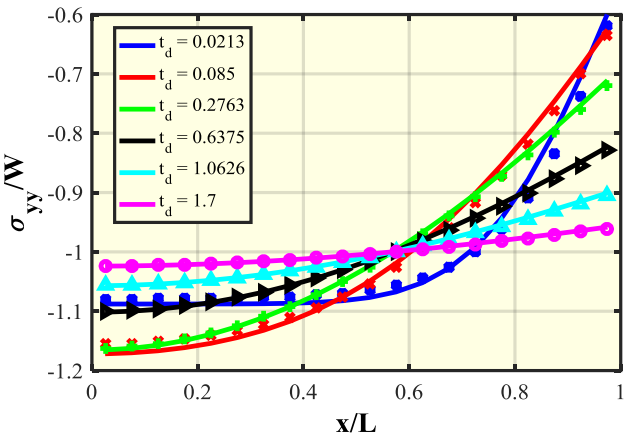

(c) Stress in y-direction plot at various times

Figure 2.4. Continued.

Figure 2.4 shows a comparison between analytical (lines) and numerical solutions (dots) for pressure (p), vertical stress (σ_{yy}), and horizontal displacement (u_x) at various characteristic times (t_d). Our model produces similar solutions compared with the analytical solution at both early and late time. Initially, a uniform pressure, 313 psi, which is about half of the load being applied on top boundary, is generated due to Skempton effect (Skempton, 1954). Mandel-Cryer effect can then be observed at t_d = 0.085, illustrating a rise in pressure of about 10%. After this

point, pressure starts to decrease due to the flow boundary until it reaches an initial value, which is p = 0 psi at late time. Vertical stress (y-direction) increases larger than the external load (w) at the center due to Mandel-Cryer effect. As pressure starts to decrease, σ_{yy} approaches a uniform value, which is the value of external load (w). The largest horizontal displacement (u_x) can be observed at the right boundary as the plate is fixed at the center. u_x for the entire domain decreases to zero with time due to fluid flowing out from the domain.

2.3.2 The coupled model with EDFM

Our coupled geomechanics-fluid flow with EDFM using uniform structure grids is validated against local grid refinement for 0^o angle of inclination fracture and refined grid for 45^o angle of inclination fracture on 2-D reservoir. Figure 2.5 shows fracture geometry on local grid refinement and refined grid (zoom-in area around fracture) with L_x = 2420 ft and L_y = 1820 ft with N_x = 121, N_y = 95 for 0^o angle of inclination fracture and N_x = 347, N_y = 317 for 45^o angle of inclination fracture. For the EDFM case, a uniform grid was used with N_x = 121, N_y = 91 for both 0^o and 45^o angle of inclination fracture. Parameters used are shown in Table 2.3. Initially, stress in x-direction is 4600 psi and stress in y-direction is 4500 psi. Initial reservoir pressure is 4000 psi.

Quantity	Value	Unit
Young's modulus (E)	$1x10^6$	psi
Poisson's ratio (ν)	0.3	-
Biot's coefficient (b)	0.7	-
Reservoir permeability (k)	10	md
Reservoir porosity (ϕ)	0.05	-
Fluid compressibility (c_f)	$2x10^{-4}$	psi^{-1}
Fluid viscosity (μ_f)	0.6	cp

Table 2.3. Parameters used in calculation for a single fracture test problem (Sangnimnuan et al. 2018a).

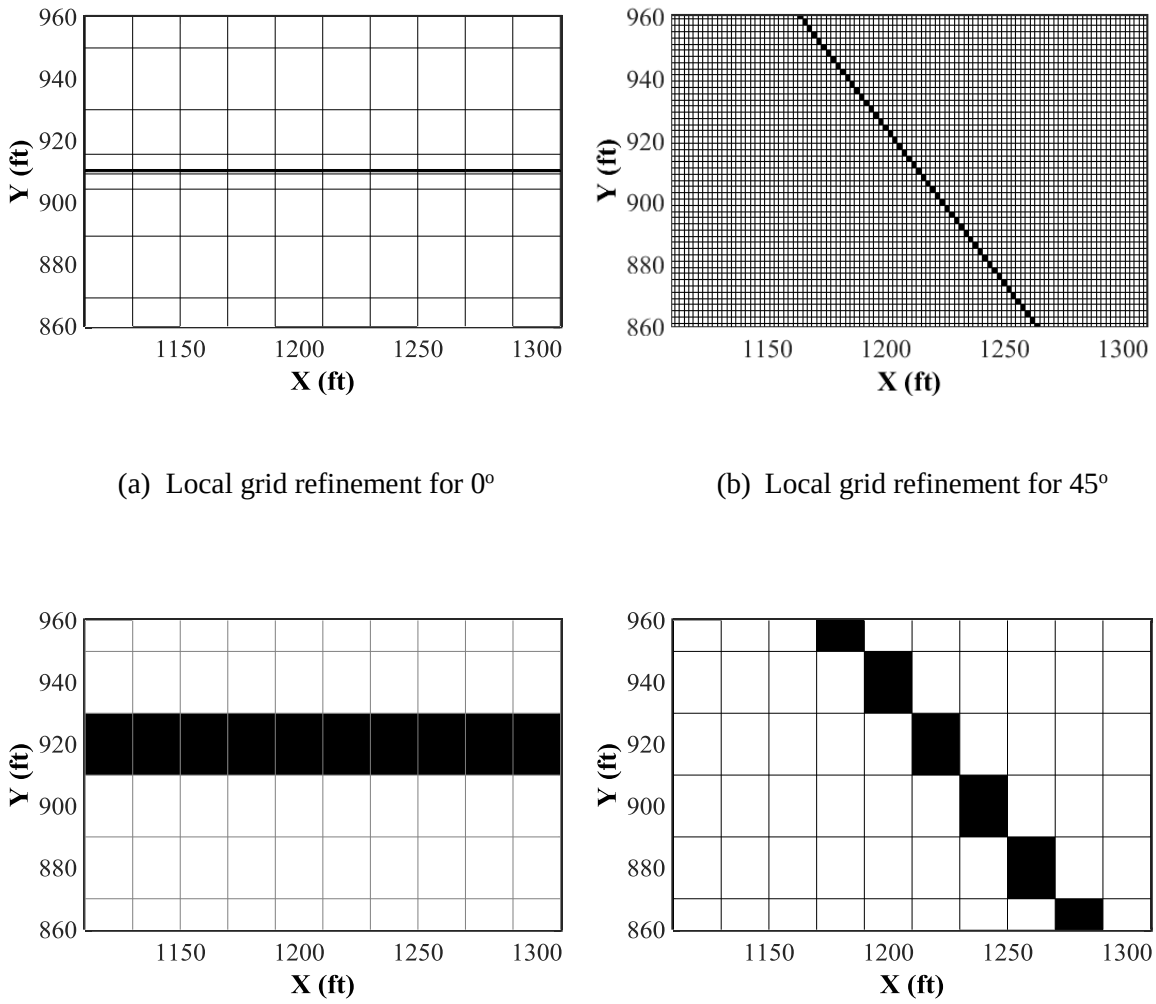

(a) Local grid refinement for 0º

(b) Local grid refinement for 45º

(c) Grid structure for 0º EDFM

(d) Grid structure for 45º EDFM

Figure 2.5. Grid structure (zoom-in area around fractures) for 0º grid refinement (a), 0º EDFM (c), 45º grid refinement (b), and 45º EDFM angle of inclination (d) (Sangnimnuan et al. 2018a).

Figures 2.6 and 2.7 provide a comparison between local grid refinement and our model for reservoir pressure (p) (a, b), σ_{xx} (c, d), and σ_{yy} (e, f) distribution for 0º and 45º cases. σ_{yy} and σ_{xx} are current reservoir stresses after depletion. As shown in figures, the difference between our model and local grid refinement is insignificant for both 0º and 45º cases. Pressure is observed being depleted in elliptical shape due to its geometry. σ_{xx} increases on top and bottom parts of the

domain to support pressure depletion in x-direction, while σ_{yy} increases on right and left parts of the domain to support pressure depletion in y-direction. The flow rate for all 4 cases is calculated using Peaceman's equation with 0.25 ft well radius. Comparison in Figure 2.8 yields a good matching among all cases with 0^o having a slightly higher flow rate due to larger depletion area. This implies that angle of inclination plays an important role in well performance. In addition, our model provides a significant improvement in computational efficiency. Although this cannot be observed in 0^o case as number of cells is very similar for our model and local refinement, 45^o case reduces computational time from 4 hours of local refinement to 0.5 hour of our model. This is important for future studies where complex fracture geometry is considered.

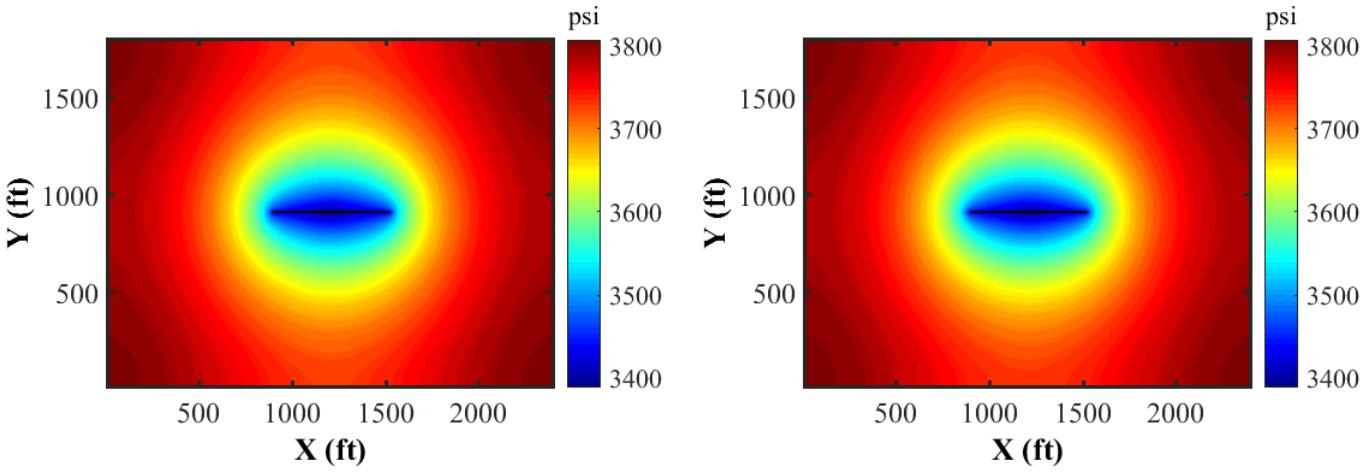

(a) Pressure distribution for local grid refinement

(b) Pressure distribution for our model

Figure 2.6. Comparison between our model (right) and local grid refinement (left) of 0^o angle of inclination for pressure distribution (a, b), σ_{xx} distribution (c, d), and σ_{yy} distribution (e, f) at 100 days of production (Sangnimnuan et al. 2018a).

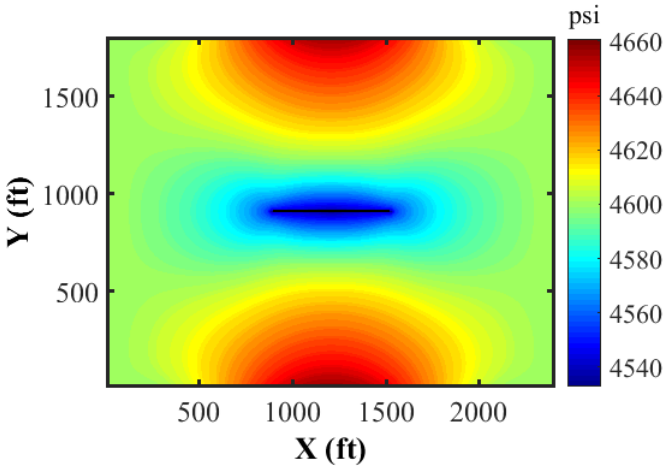

(c) σ_{xx} distribution for local grid refinement

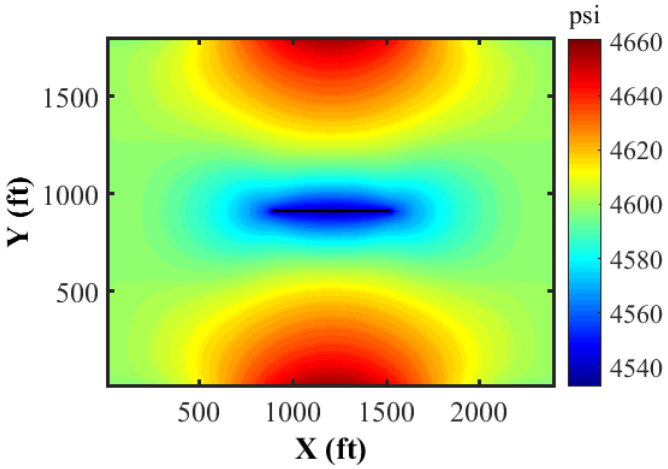

(d) σ_{xx} distribution for our model

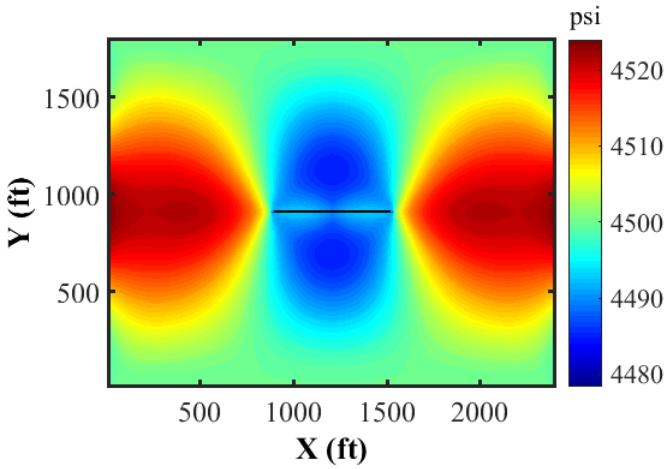

(e) σ_{yy} distribution for local grid refinement

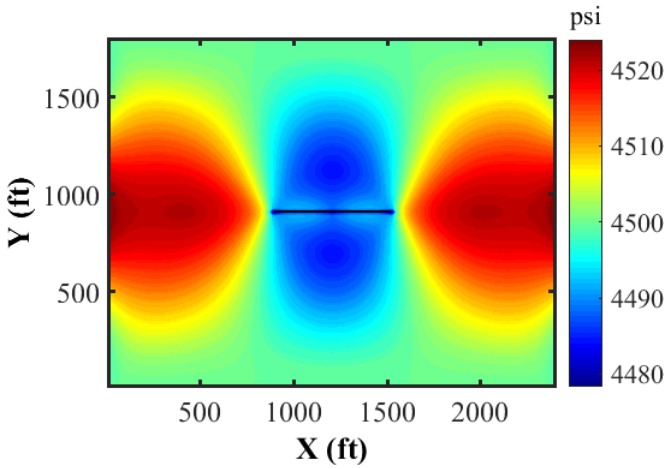

(f) σ_{yy} distribution for our model

Figure 2.6. Continued.

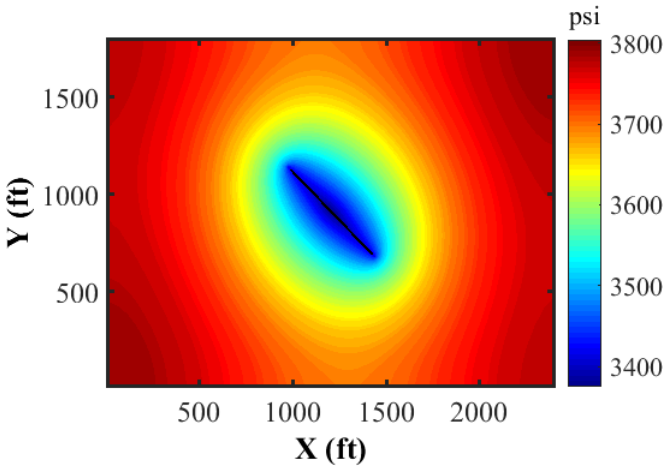

(a) Pressure distribution for local grid refinement

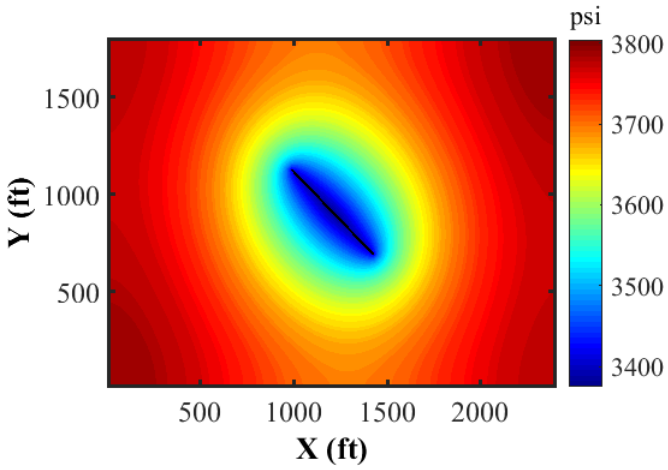

(b) Pressure distribution for our model

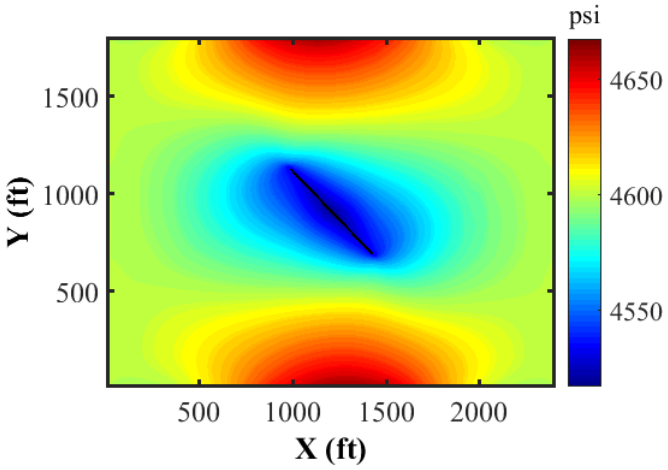

(c) $\boldsymbol{\sigma}_{xx}$ distribution for local grid refinement

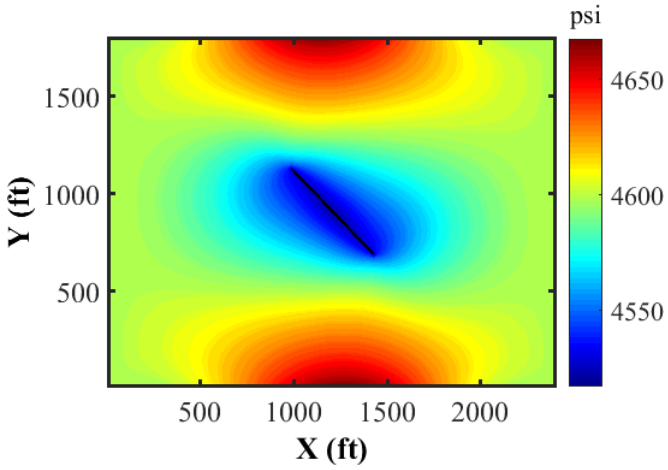

(d) $\boldsymbol{\sigma}_{xx}$ distribution for our model

Figure 2.7. Comparison between our model (right) and local grid refinement (left) of 45^{o} angle of inclination for pressure distribution (a, b), σ_{xx} distribution (c, d), and σ_{yy} distribution (e, f) at 100 days of production (Sangnimnuan et al. 2018a).

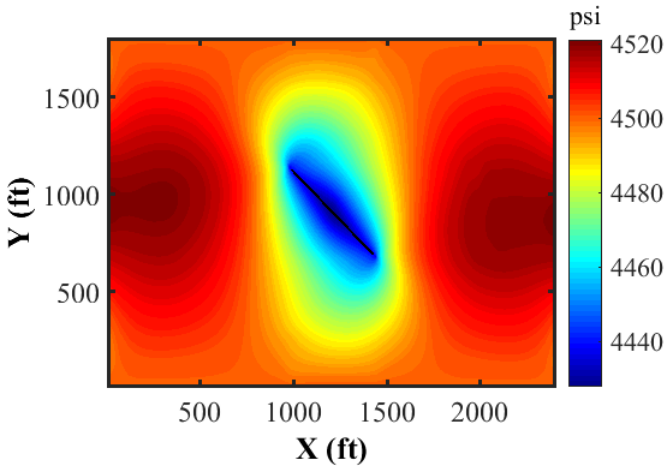

(e) σ_{yy} distribution for local grid refinement

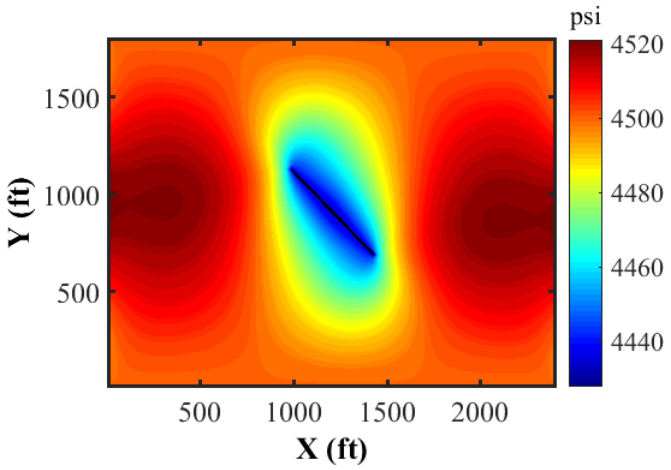

(f) σ_{yy} distribution for our model

Figure 2.7. Continued.

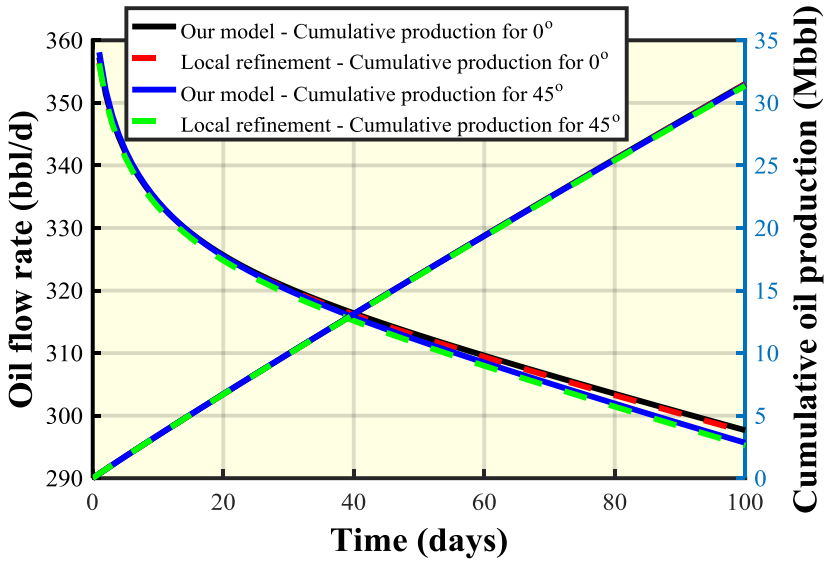

Figure 2.8. Flow rate comparison between our model and local grid refinement for 0^o and 45^o angle of inclination for 100 days of production (Sangnimnuan et al. 2018a).

2.4 Case studies

In this section, the focus is on studying the effects of fracture geometry on stress distribution and reorientation in the field. Boundary condition needs to be appropriately chosen in

order to accurately simulate actual conditions in the field. In the following sub-section, the effects of boundary conditions were investigated to illustrate the role that boundary conditions play in flow-stress calculation.

2.4.1 Effect of boundary condition

In this section, pressure and stress distribution was compared between constrained and unconstrained boundary conditions. A similar comparison was done by Dean et al. (2006) with the focus on reservoir pressure and surface subsidence compared between constrained and unconstrained boundary conditions. Reservoir and fracture geometry are shown in Figure 2.9. Table 2.4 provides parameters used in the simulation. This set of parameters is based on the Bakken reservoir, which was given in Roussel et al. (2013). The domain has 755 ft length (L_x), 755 ft width (L_y), and 100 ft height (L_z). The domain was discretized to 151 cells in x and y directions and 1 cell in z-direction. The constrained boundary condition has 11,000 psi applied on the boundary in x-direction, 11,500 psi applied on the boundary in y-direction, 13,000 psi applied on the top boundary in z-direction, and zero displacement on the bottom boundary. The unconstrained boundary condition has zero displacements on all boundaries, except the top boundary in z-direction with 13,000 psi traction stress. No flow boundary is applied on all 6 boundaries to contain fluid from flowing out, thus, pressure in the reservoir can only decrease due to production. A similar comparison was done by Dean et al. (2006).

Quantity	Value	Unit
Young's modulus (E)	$2x10^6$	psi
Poisson's ratio (ν)	0.2	-
Biot's coefficient (b)	0.7	-
Reservoir permeability (k)	0.304	μd
Reservoir porosity (ϕ)	0.05	-
Fluid compressibility (c_f)	$2.18x10^{-5}$	psi^{-1}
Wellbore radius (r_w)	0.25	ft
Fluid viscosity (μ_f)	0.25	cp
Initial pressure (p_0)	$1x10^4$	psi
Initial stress in x-direction ($\sigma_{xx,0}$)	$1.1\ x10^4$	psi
Initial stress in y-direction ($\sigma_{yy,0}$)	$1.15\ x10^4$	psi
Initial stress in z-direction ($\sigma_{zz,0}$)	$1.3\ x10^4$	psi
Fracture spacing	50	ft

Table 2.4. Parameters used for testing different boundary conditions on multi fractures test problems and case studies for different fracture geometries (Sangnimnuan et al. 2018a)..

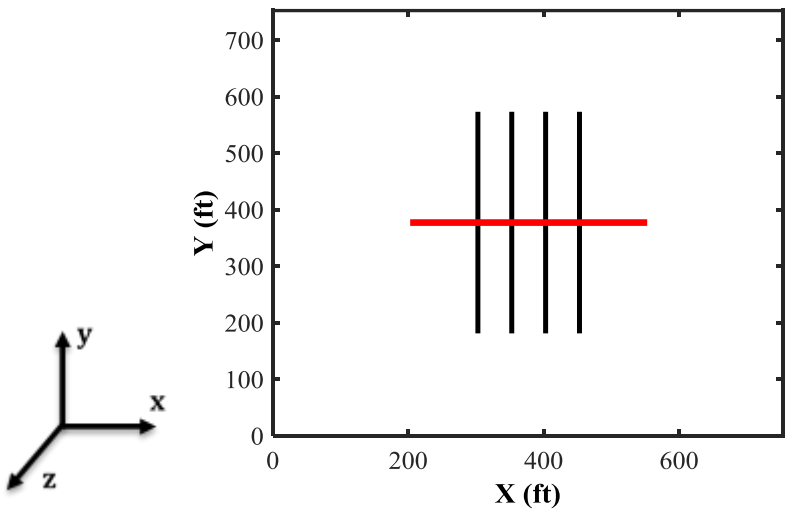

Figure 2.9. Reservoir geometry with 4 planar fractures (Sangnimnuan et al. 2018a).

Figure 2.10 illustrates the comparison of pressure with the direction of maximum horizontal stress (σ_{Hmax}), σ_{xx}, and σ_{yy} distributions between constrained and unconstrained boundary conditions at 5 years of production. White dash lines on top of pressure distribution in

Figures 10a and 10b represent the orientation of σ_{Hmax}. The difference in pressure distribution is insignificant. However, contour plots of σ_{xx} and σ_{yy} show a significant difference between the two conditions. There is about 1000 psi stress difference in the area near the boundaries. The constrained boundary condition allows stress to change at all boundaries, while the unconstrained boundary condition enforces stress at the boundaries to remain constant. Therefore, when pressure decreases, stress at the boundaries increases to support boundary force from unconstrained boundary condition. Distribution at fracture area is shown to be not so much different between constrained and unconstrained boundary conditions, which results in small difference in stress reorientation (Figures 2.10a and 2.10b).

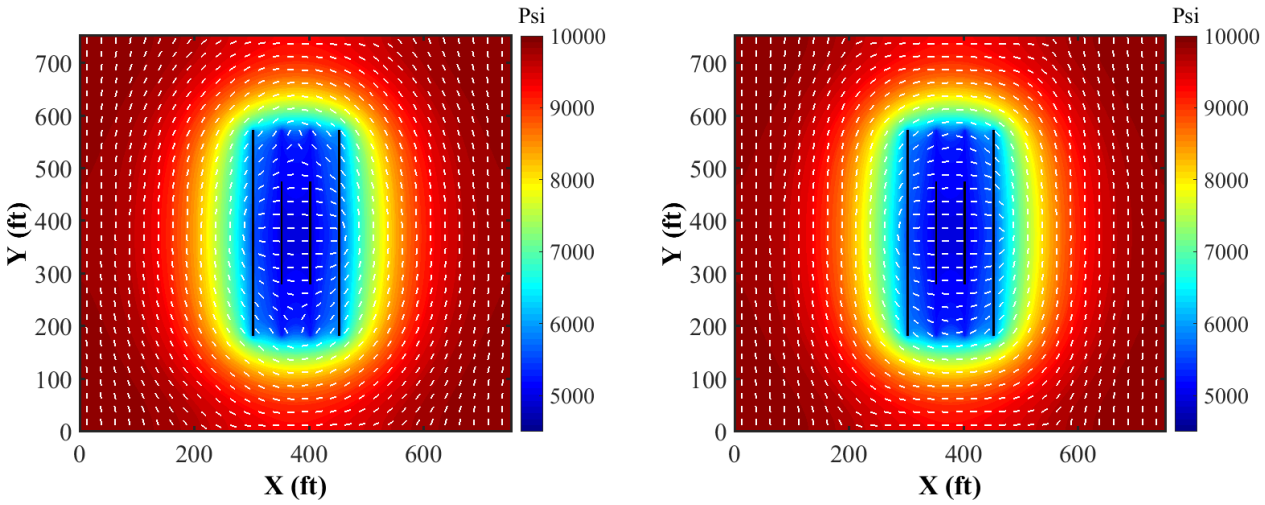

(a) Pressure distribution for the unconstrained boundary condition

(b) Pressure distribution for the constrained boundary condition

Figure 2.10. Comparison between constrained (right) and unconstrained (left) for pressure distribution (top), σ_{yy} distribution (middle), and σ_{xx} distribution (bottom) at 5 years of production (Sangnimnuan et al. 2018a).

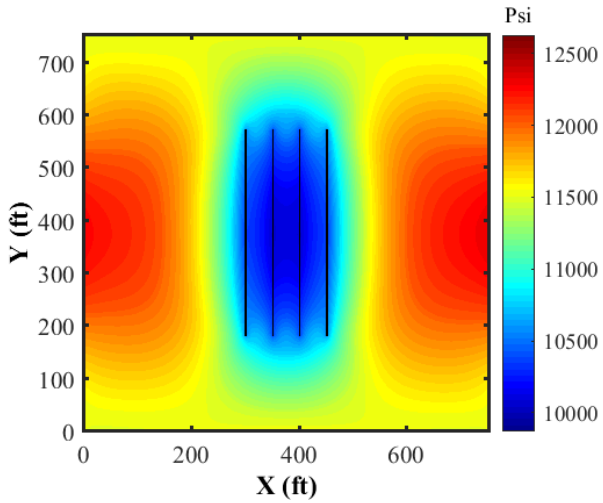

(c) σ_{yy} distribution for the unconstrained boundary condition

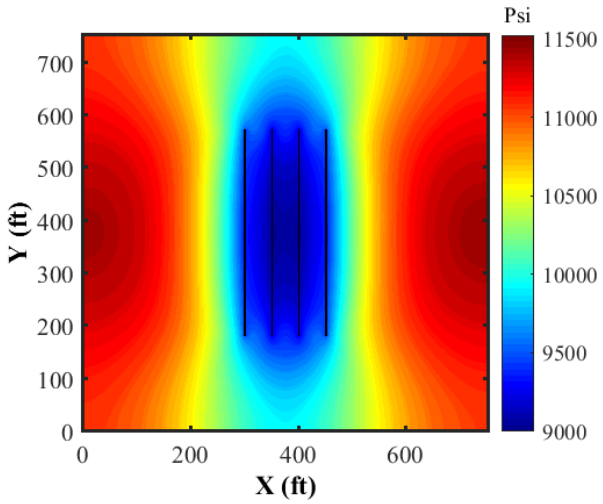

(d) σ_{yy} distribution for the constrained boundary condition

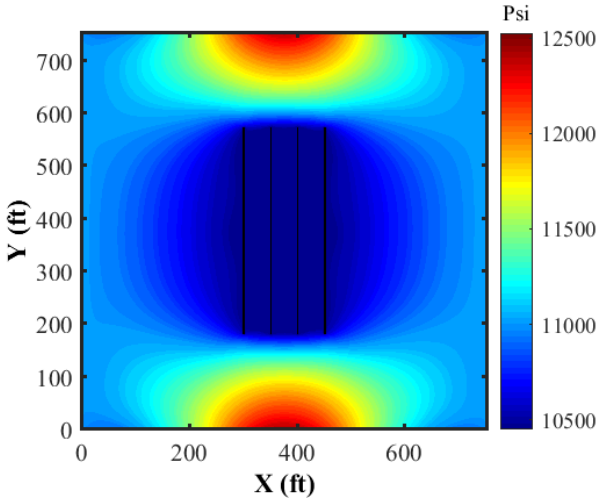

(e) σ_{xx} distribution for the unconstrained boundary condition

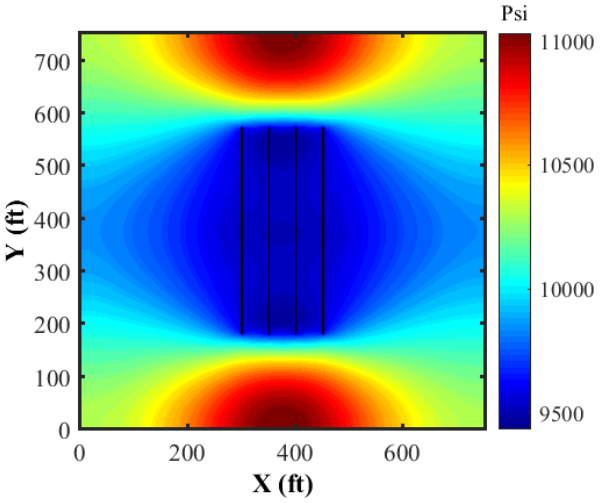

(f) σ_{xx} distribution for the constrained boundary condition

Figure 2.10. Continued.

Flow rate and average reservoir pressure remain the same for both cases (Figure 2.11). From the analysis, it was found that boundary conditions primarily have great effects on stresses near the boundary and almost no influence on stresses within the drainage area. Since the focus is only on a group of 4 fractures from a well with a multi-stage fracturing treatment, the constrained

boundary condition is a better choice in this case as it allows stress at all boundaries to change over time. Constraining displacements in normal direction are a result of production from adjacent fractures or wells. If the entire reservoir that covers multiple perforations, as well as large area of reservoir, were to be studied, unconstrained boundary might be a better option as stress at all boundaries is expected to remain constant.

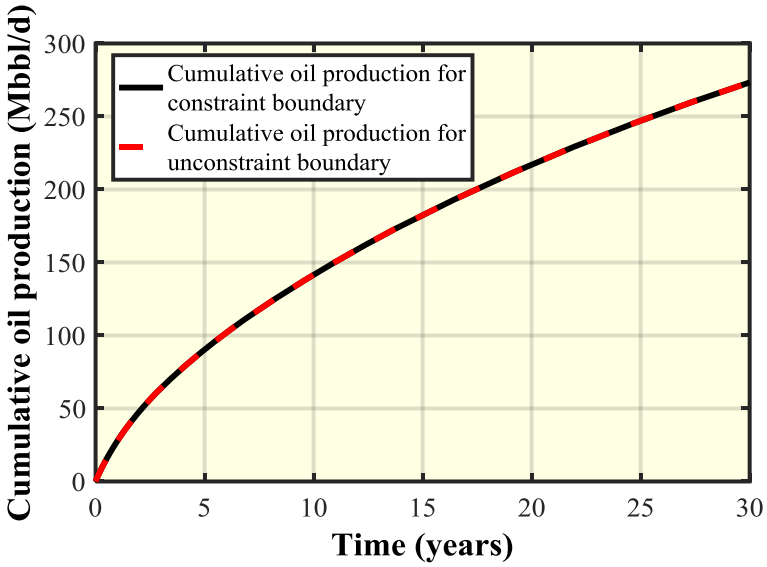

Figure 2.11. Flow comparison between constrained and unconstrained boundary conditions (Sangnimnuan et al. 2018a).

2.4.2 Effect of fracture geometry

In this section, the interest is based on how fracture geometries affect stress distribution and reorientation as well as production rate using the constrained boundary condition as discussed in section 5.1. With the implementation of EDFM in our coupled geomechanics and fluid-flow model, the code is capable of simulating stress change due to depletion in the reservoir with complex fracture geometry. Fracture geometries in this study consist of planar (90^o angle of inclination), 60^o inclination, and non-planar fracture geometries. Fracture with 60^o misaligned

angle was chosen as in some situations horizontal wells are not drilled along the direction of the least principal stress. When fracture interaction has great effects on multiple fracture propagation, non-planar fracture geometry can be generated in the field. The non-planar fracture geometry was obtained using our in-house fracture propagation model, which predicts fracture propagation incorporating stress-shadowing effects. In order to make comparisons, all three geometries have been created with the same surface area. The same set of parameters as well as reservoir size in section 2.3 is used for this section to represent simulation in Bakken reservoir. Figures 2.12 and 2.13 show pressure distribution with the direction of σ_{Hmax} and σ_{yy} - σ_{xx} of the three fracture geometries at 1 and 5 years of production.

As shown in Figure 2.12, all three cases have different drainage areas. Non-planar fracture geometry has the largest depleted area following by 60^o inclination and planar fracture geometries. This directly affects the production rate, which corresponds to the size of the depleted area as shown in Figure 2.13. Non-planar fracture geometry has the largest area resulting in highest production, following by planar fracture geometries and 60^o inclination, respectively. There is almost no difference in production between the planar fracture and 60^o inclination geometry, which is a result of similar drainage size. Another observation from these plots is direction of maximum horizontal stress, which originally is in y-direction (fracture propagation direction). After 1-year production, some angle changes around fracture tips for all three cases start to appear. In addition, after 5-year production, more angle changes, especially at the depleted area, can be observed. Stress reversal (stress rotates 90^o from its original orientation) can mainly be observed at the inner fractures around depleted area for planar fracture geometry. Similarly, stress rotates 60^o from its original orientation for 60^o inclination fracture geometry, becoming perpendicular to fracture

orientation. This is due to the shape of depleted area, which will be further discussed in section 2.5.

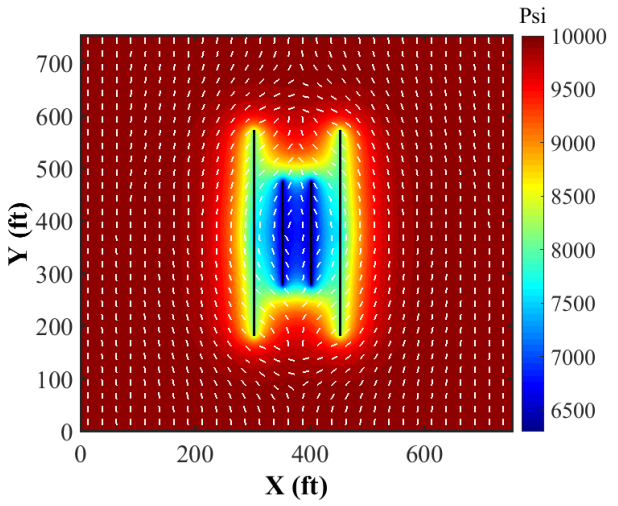

(a) Pressure distribution for planar fracture geometry with direction of maximum horizontal stress at 1 year

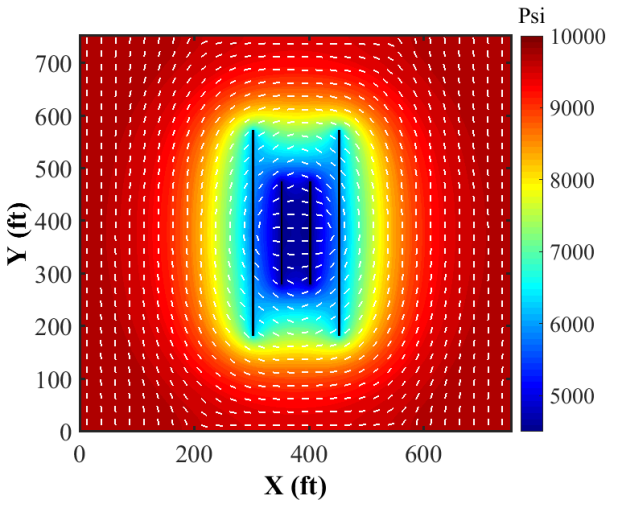

(b) Pressure distribution for planar fracture geometry with direction of maximum horizontal stress at 5 year

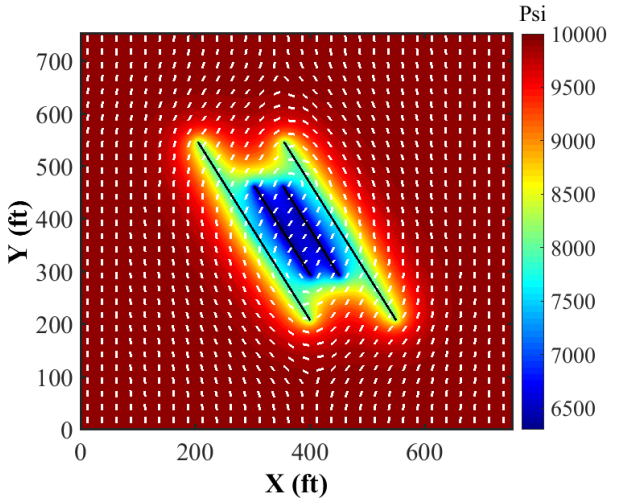

(c) Pressure distribution for 60º fracture geometry with direction of maximum horizontal stress at 1 year

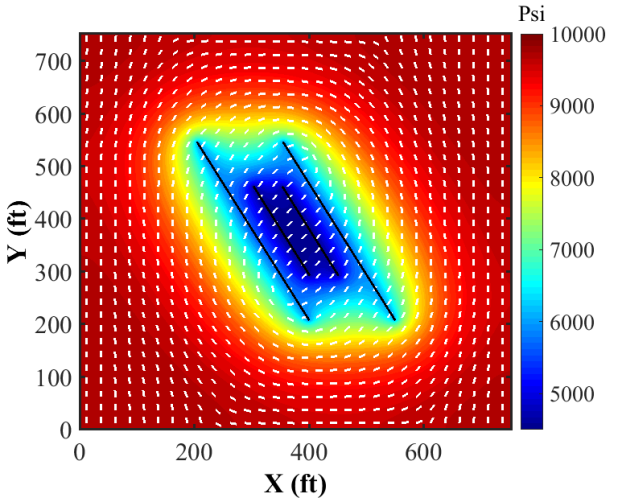

(d) Pressure distribution for 60º fracture geometry with direction of maximum horizontal stress at 5 year

Figure 2.12. Pressure distribution with the direction of maximum horizontal stress of planar (a, b), 60º inclination (c, d), and non-planar (e, f) fracture geometries at 1 and 5 years (Sangnimnuan et al. 2018a).

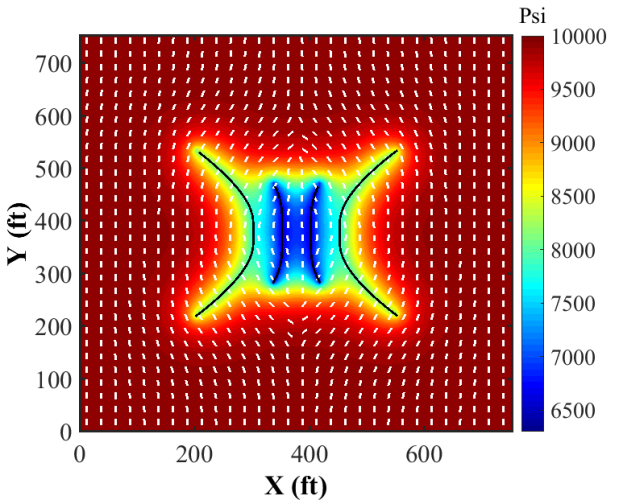

(a) Pressure distribution for non-planar fracture geometry with direction of maximum horizontal stress at 1 year

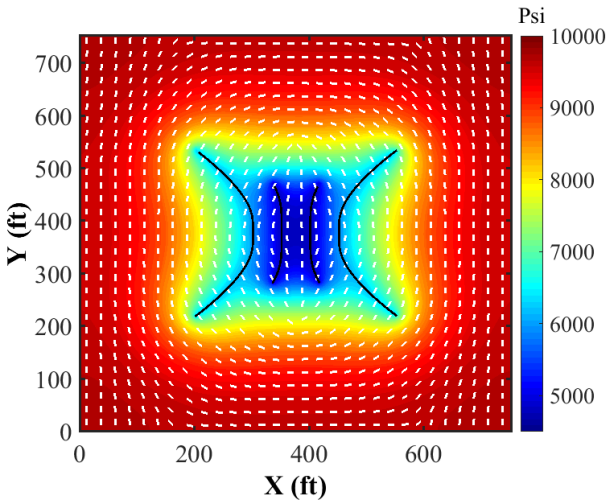

(f) Pressure distribution for nonplanar fracture geometry with direction of maximum horizontal stress at 1 year

Figure 2.12. Continued.

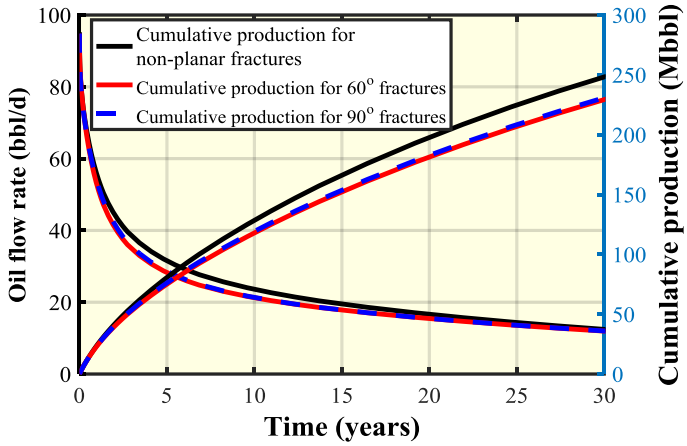

Figure 2.13. Flow rate and cumulative production comparison between planar fracture, 60o fracture, and non-planar fracture geometries (Sangnimnuan et al. 2018a).

Furthermore, stress reversal can be observed at the top and bottom area of fractures for all three cases after 5 years of production. This is due to a reduction in stress difference (σ_{yy}-σ_{xx}) as shown in Figure 2.14, which represents the distribution of stress difference at 1-year and 5-year production times. Originally, σ_{yy} is 500 psi larger than σ_{xx}. After depletion, σ_{yy} decreases more in

top and bottom area, while σ_{xx} in these areas stays almost the same. Consequentially, the difference between σ_{yy} and σ_{xx} becomes less than its original value. In some areas, σ_{yy} can become smaller than σ_{xx}. In contrast, σ_{xx} decreases more at right and left boundaries, while σ_{yy} remains the same. Thus, in this location the difference between σ_{yy} and σ_{xx} becomes larger than its original difference. In the drainage area near fractures, the three different fracture geometries generate significant difference of σ_{yy}-σ_{xx} distribution. Both σ_{xx} and σ_{yy} decrease with reservoir pressure. σ_{yy} reduces faster than σ_{xx} as a function of depletion. However, decrease rate of σ_{xx} and σ_{yy} is distinct for different fracture geometries. Decrease rate difference of σ_{xx} and σ_{yy} is much larger for planar fracture geometry than non-planar fracture geometry. Updated stress difference (σ_{yy}-σ_{xx}) of non-planar fracture geometry is greater than that of planar fracture geometry, which implies that the difference of decrease rate of σ_{xx} and σ_{yy} is smaller for non-planar fracture geometry. Once σ_{yy} becomes smaller than σ_{xx}, stress reversal will occur.

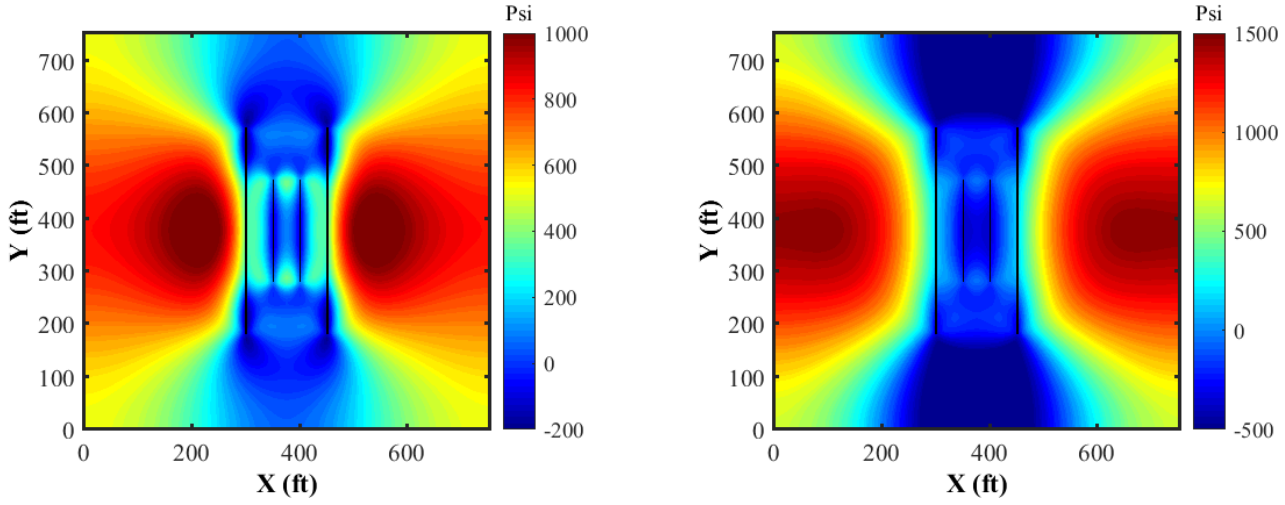

(a) σ_{yy}-σ_{xx} distribution for planar fracture geometry at 1 year

(b) σ_{yy}-σ_{xx} distribution for planar fracture geometry at 5 years

Figure 2.14. $\sigma_{yy} - \sigma_{xx}$ distribution of planar (a, b), 60^o degree inclination (c, d), and non-planar (e, f) fracture geometries at 1 and 5 years (Sangnimnuan et al. 2018a).

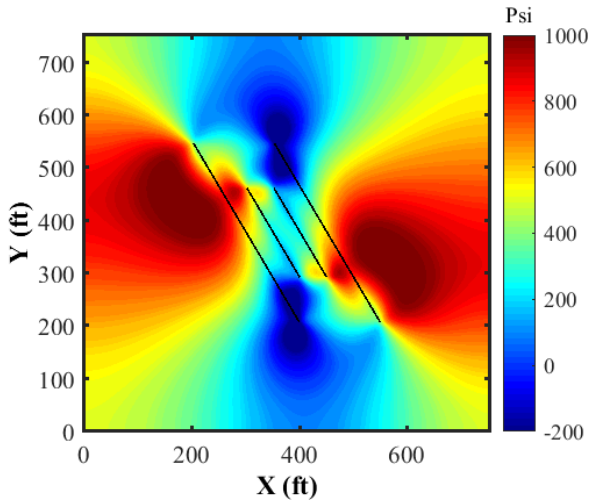

(c) σ_{yy}-σ_{xx} distribution for planar fracture geometry at 1 year

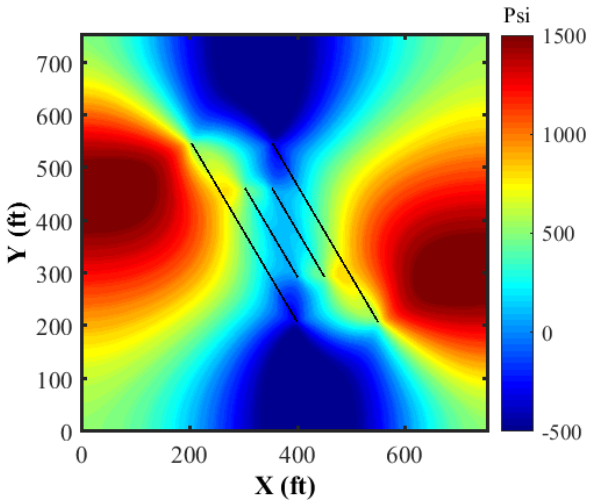

(d) σ_{yy}-σ_{xx} distribution for planar fracture geometry at 5 years

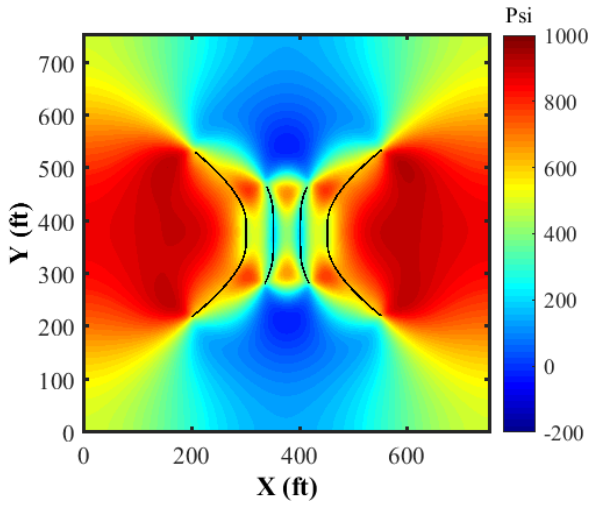

(e) σ_{yy}-σ_{xx} distribution for planar fracture geometry at 1 year

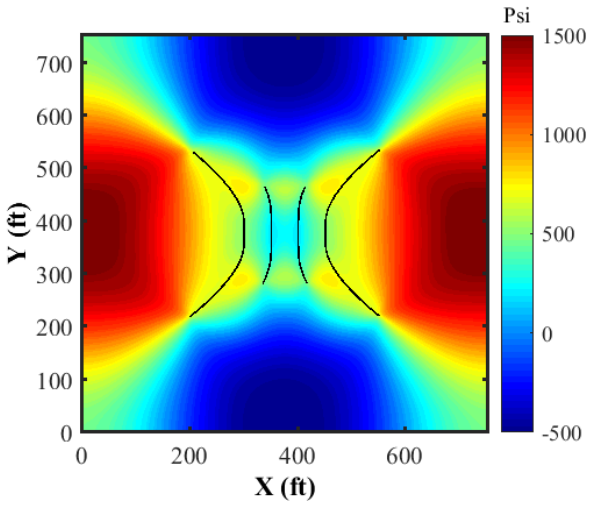

(f) σ_{yy}-σ_{xx} distribution for planar fracture geometry at 5 years

Figure 2.14. Continued.

2.4.3 Effect of differential stress ($\sigma_{xx,0}$ - $\sigma_{yy,0}$)

Differential Stress (DS) is defined as the difference of two horizontal principal stresses in the reservoir before depletion. As two principal stresses are initially in x and y directions, DS is the

difference between $\sigma_{xx,0}$ and $\sigma_{yy,0}$. DS plays an important role in stress reorientation as the smaller it is, the higher chance that reorientation will occur. In this section, DS is 500 psi, which is a base case in section 5.2, 250 psi and 100 psi. In order to study how new fractures would propagate during refracturing or completion of infill wells while existing fractures are under production, it is important to be able to predict stress reorientation, which defines direction of new fracture propagation. $\sigma_{xx,0}$, $\sigma_{yy,0}$ are the initial reservoir stresses before depletion. While σ_{yy}, σ_{xx} are current reservoir stresses after depletion. $\Delta\sigma_{yy}$, $\Delta\sigma_{xx}$, and $\Delta\sigma_{xy}$ are stress changes induced by depletion. The relationship between stresses can be expressed as shown in Eq. 2.42.

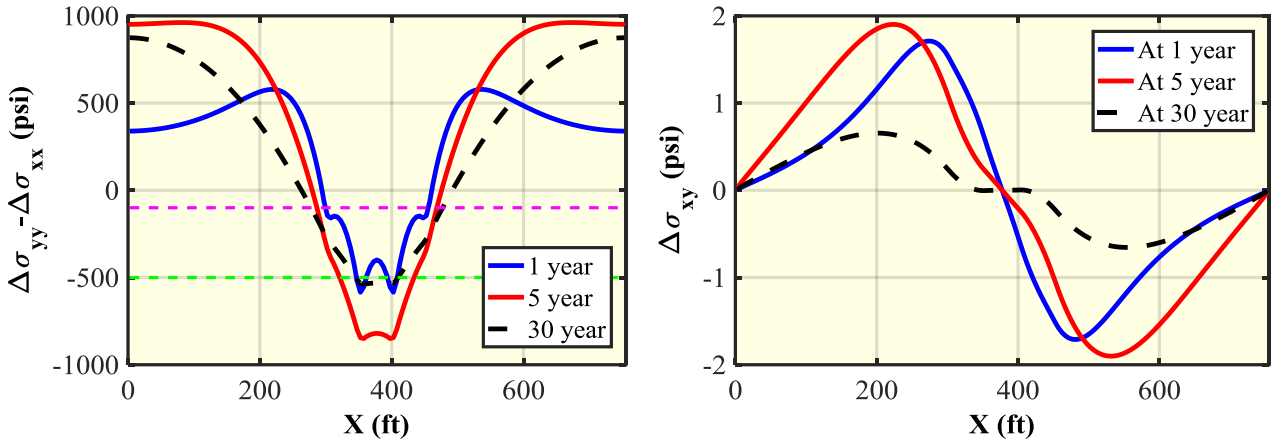

(a) $\Delta\sigma_{yy} - \Delta\sigma_{xx}$ for planar fracture geometry at different times

(b) $\Delta\sigma_{xy}$ for planar fracture geometry at different times

Figure 2.15. On the left, change of differential stress along the center of the well for 3 different geometries (a, c, e) at different times. On the right, shear stress along the center of the well for 3 different geometries (b, d, f) at different times (Sangnimnuan et al. 2018a).

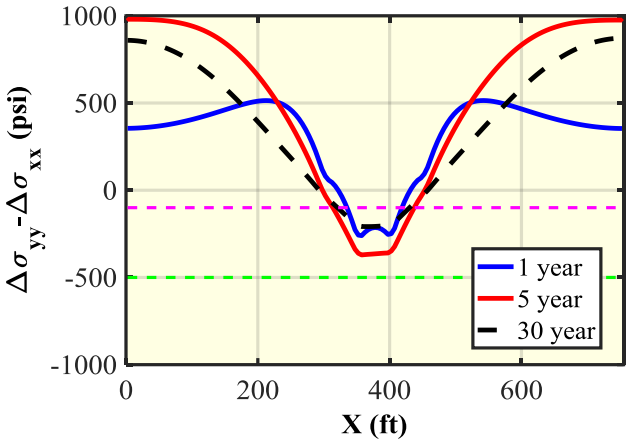

(c) $\Delta\sigma_{yy} - \Delta\sigma_{xx}$ for 60° inclination fracture geometry at different times

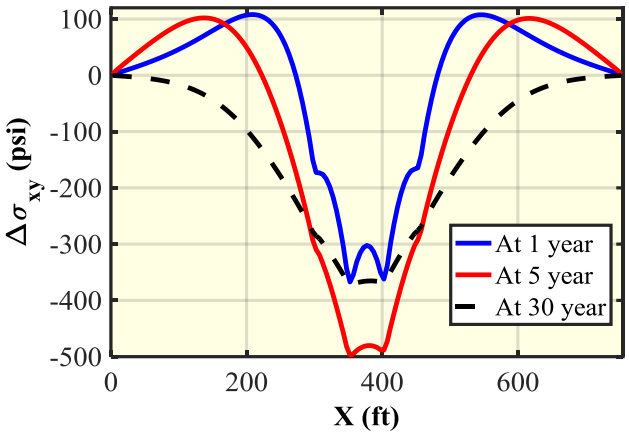

(d) $\Delta\sigma_{xy}$ for 60° inclination fracture geometry at different times

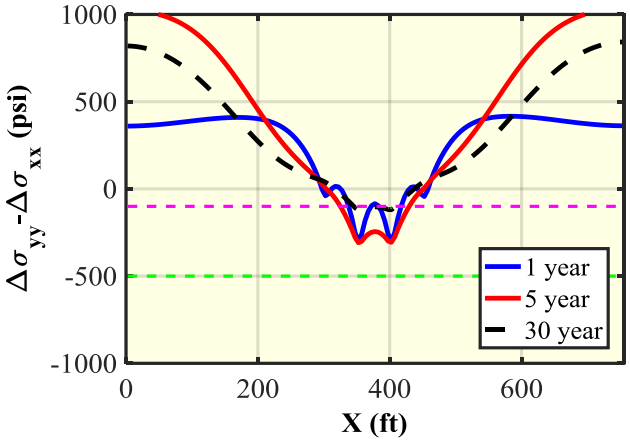

(e) $\Delta\sigma_{yy} - \Delta\sigma_{xx}$ for non-planar fracture geometry at different times

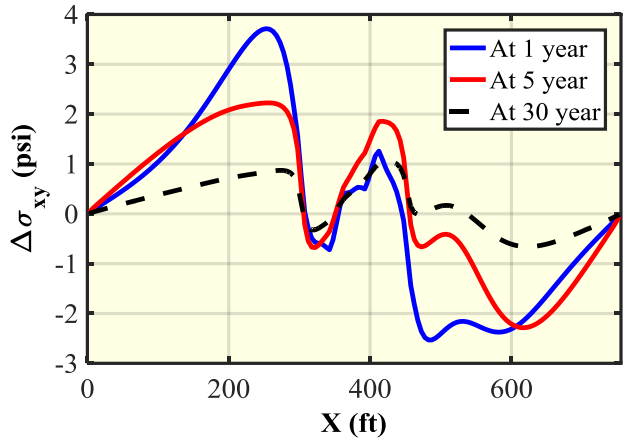

(f) $\Delta\sigma_{xy}$ for non-planar fracture geometry at different times

Figure 2.15. Continued.

$$\sigma_{yy} - \sigma_{xx} = \sigma_{yy,0} + \Delta\sigma_{yy} - \sigma_{xx,0} - \Delta\sigma_{xx}$$

$$\sigma_{yy} - \sigma_{xx} = (\sigma_{yy,0} - \sigma_{xx,0}) + \Delta\sigma_{xx} - \Delta\sigma_{yy}$$

$$\sigma_{yy} - \sigma_{xx} = DS + \Delta\sigma_{xx} - \Delta\sigma_{yy}, \quad \text{..... (2.42)}$$

Figure 2.15 illustrates induced stress difference ($\Delta\sigma_{yy}$ - $\Delta\sigma_{xx}$) plotted along x-direction at y = 377.5 ft for all 3 geometry cases at 1, 5, and 30 years. According to Eq. (2.30), this plot can be applied for any initial DS as it is written in terms of DS, which is a constant value. $\sigma_{yy} - \sigma_{xx}$ is an updated stress difference after production and only changes when DS changes for a specific $\Delta\sigma_{yy}$ - $\Delta\sigma_{xx}$. If the initial DS is 0 psi, any areas of the plot that is below 0 represent stress reversal. The same mechanism applies for other different stresses i.e. 100 psi (pink line) and 500 psi (green line).

A very small magnitude of induced shear stress ($\Delta\sigma_{xy}$) is observed on planar and non-planar fracture geometries (2.15b and 2.15f). The inclination fracture geometry produces a large shear stress as a result of the inclination of fractures causing stress to rotate to 60^o. Since the magnitude of induced shear stress is small compared to induced horizontal stresses, the main factor that causes stress to reorient is the difference between $\Delta\sigma_{xx}$ and $\Delta\sigma_{yy}$. Therefore, the focus is on induced stress difference $\Delta\sigma_{yy}$ - $\Delta\sigma_{xx}$ as it directly affects the calculation of reorientation.

For planar fracture geometry (Figure 2.15a), stress reorientation between inner fractures can be observed from DS = 0 psi up to around 500 psi at 1 year and 850 psi at 5 years. It was also observed that stress reorienting back after 30 years of production. This result corresponds to section 2.4.2, in which stress reorientation at the depleted area can be observed the most in planar fracture geometry. Angle change of maximum horizontal stress (σ_{Hmax}) can be found in Figure 2.16 for DS = 100 and 500 psi. This aligns with plots of $\Delta\sigma_{yy}$ - $\Delta\sigma_{xx}$ as both cases reorient 90 degree at the depleted area between two inner fractures.

On the other hand, for 60^o inclination fracture geometry (Figure 2.15c), no reorientation can be observed at all for DS = 400 psi or more. This implies that if the original DS is 500 psi, which is our base case, there will be no stress reorientation. After a 30-year production, stress starts

to reorient back just like planar fracture geometry. Figure 2.16 shows orientation change at DS = 100 and 500 psi, which confirms that only small orientation change occurs at DS = 500 psi (Figures 2.16a, 2.16c, 2.16e) for planar and 60^o inclination fracture geometries. No change can be observed for non-planar fracture geometry. Larger orientation change occurs at DS = 100 psi for all three geometries, especially in the region between inner fractures (Figures 2.16b, 2.16d, 2.16f). The maximum angle change for 60^o inclination fracture geometry is only 53^o, which is very close to initial fracture direction (60^o), but in a perpendicular direction. While maximum angle change for the other two cases is 90^o or fully reversed.

Similarly, no stress reorientation is observed on non-planar fracture geometry (Figure 2.15e) for any DS above 250 psi. At DS = 100 psi, some reorientation can be observed, but the area is small compared with planar and 60^o inclination fracture geometry. It can be seen from Figure 2.15 that there is no reorientation at all for DS = 500 psi even after 30 years of production. However, for DS = 100 psi, reorientation can be observed between inner fractures from 1 year to 30 years of production. This corresponds to Figures 2.15e, where $\Delta\sigma_{yy}$ - $\Delta\sigma_{xx}$ is below zero in between inner fractures.

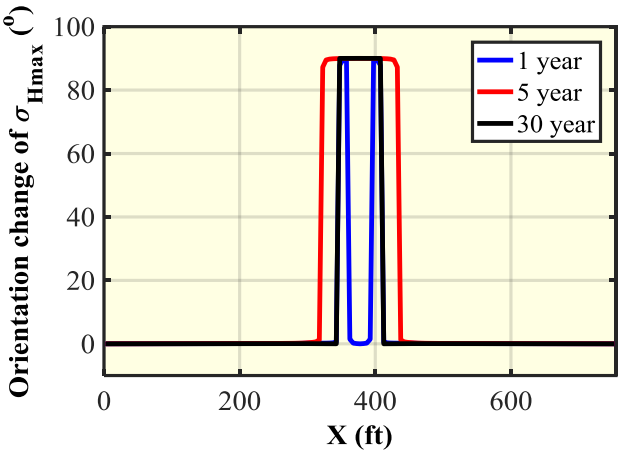

(a) Orientation change of $\boldsymbol{\sigma}_{Hmax}$ for planar fracture geometry at DS = 500 psi

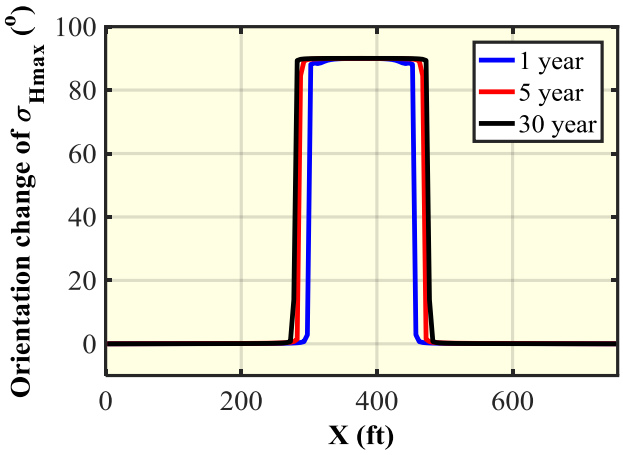

(b) Orientation change of $\boldsymbol{\sigma}_{Hmax}$ for planar fracture geometry at DS = 100 psi

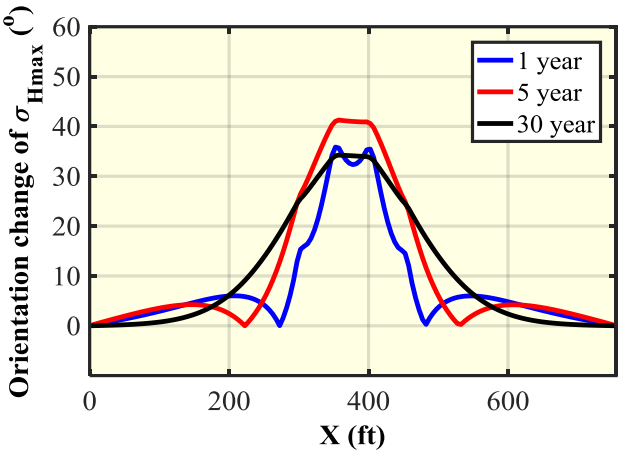

(c) Orientation change of $\boldsymbol{\sigma}_{Hmax}$ for 60° inclination fracture geometry at DS = 500 psi

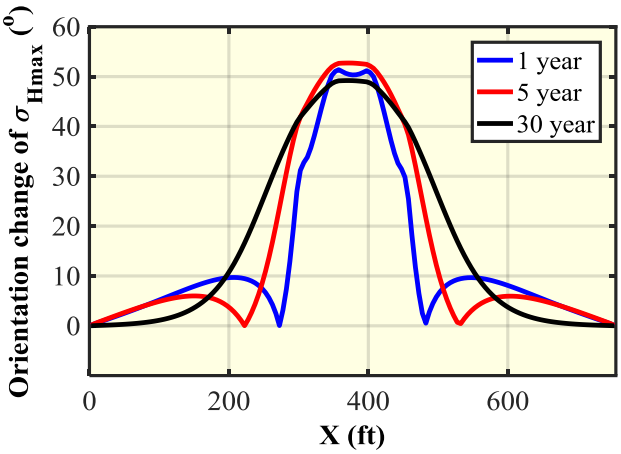

(d) Orientation change of $\boldsymbol{\sigma}_{Hmax}$ for 60° inclination fracture geometry at DS = 100 psi

Figure 2.16. Orientation change along x-direction at y = 377.5 ft for planar fracture geometry (a, b), 60° inclination fracture geometry (c, d), and non-planar fracture geometry (e, f) at different production times for DS = 100 psi and 500 psi (Sangnimnuan et al. 2018a).

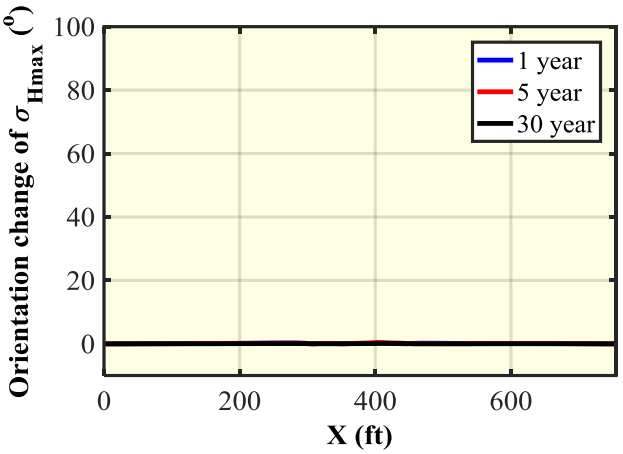

(e) Orientation change of $\boldsymbol{\sigma}_{Hmax}$ for non-planar fracture geometry at DS = 500 psi

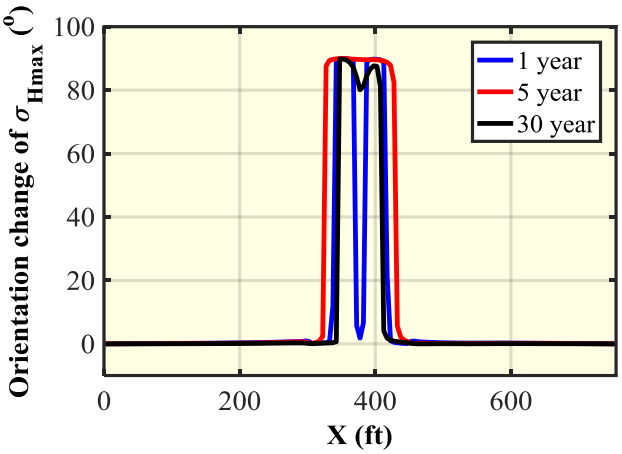

(f) Orientation change of $\boldsymbol{\sigma}_{Hmax}$ for non-planar fracture geometry at DS = 100 psi

Figure 2.16. Continued.

As mentioned in section 2.4.2, stress reorientation occurs when σ_{yy} becomes smaller than σ_{xx}. This phenomenon can be observed in the depleted area that has different depletion rates in x and y directions (rectangular shape). A large reduction in y-direction causes σ_{yy} to decrease faster than σ_{xx} and finally become less than σ_{xx} creating stress reorientation. Depletion in rectangular shape can be observed in planar and 60^o inclination fracture geometries. While the squared shape of drainage area can be observed in non-planar fracture geometry, which results in small difference in stress change in x and y directions and small likelihood of stress reorientation. It is noted that stress can rotate back if σ_{yy} becomes larger than σ_{xx} again. It is possible to observe this phenomenon around the fracture area, especially between inner fractures. This is because both σ_{xx} and σ_{yy} decrease at different rates at different production periods.

2.5 Conclusions

Geomechanics and fluid-flow finite volume-based model has been successfully developed using a fixed stress method to ensure stability for high coupling strength problems and coupled

with EDFM to simulate the poroelastic effect of complex fracture geometry in unconventional reservoirs. This opens the possibility to simulate multiple hydraulic fractures in reservoirs with highly complex fracture geometries to study stress evolution during depletion. The model was validated against classical poroelastic problems as well as local grid refinement to ensure accuracy for coupled geomechanics and fluid-flow with EDFM. The constrained boundary condition was chosen to represent actual conditions in the field. The simulations were run for three different types of geometries using parameters from Bakken reservoir. Different fracture geometries result in different shapes of depleted area as well as stress redistribution and reorientation. Decrease rates of two horizontal principal stresses are distinct for different fracture geometries. Rectangular shape with longer drainage dimension in y-direction can be found in planar fracture geometry. Squared shape with similar drainage dimension in both x and y directions can be found in non-planar fracture geometry. The shape of depleted area has a significant impact on stress changes in x and y directions and stress reorientation. Rectangular shape yields largest stress reorientation, while squared shape has a much smaller likelihood to create stress reorientation. Large induced shear stress can be observed in inclined fracture geometries. Reorientation observed from these cases tend to be the same angle as created fractures. In addition, differential stress (DS) also plays an important role in stress reorientation. The smaller the DS, the higher chance of stress to reorient. The results simulated by our model indicate that it is important to simulate fracture geometry as close as what actually is in the reservoir in order to accurately predict stress redistribution and reorientation rather than simulating planar fracture geometry, which can easily be simulated using typical coupled geomechanics and fluid flow simulator. It is crucial for understanding how stress in reservoir changes after a period of production time for applications of refracturing and completion treatments of infill wells. These findings can provide not only a fundamental guideline

for selecting best candidates to perform refracturing and optimizing fracturing design of infill wells, but also a tool to predict direction of new fracture propagation.

CHAPTER 3: STRESS CHANGE ANALYSIS NEAR WELLBORE REGION (FOR REFRACTURING)

3.1 Introduction

Refracturing has been an appealing technique to mitigate flow rate decline. To optimize refracturing performance, it is crucial to understand stress redistribution due to poroelastic effect, which determines candidate selection, timing, and effectiveness of refracturing. Understanding how stress redistributes and evolves is a key to success in refracturing. The main phenomenon affecting stress change is the poroelastic effect, which relates pressure change to stress change.

There have been many studies using coupled geomechanics and fluid flow model to predict stress evolution and redistribution due to reservoir depletion for refracturing or infill well treatments. Rezaei et al. (2017) developed a transient poroelastic displacement discontinuity model to study the problem of hydraulic fracture propagation towards depleted zones to determine optimum refracturing timing and volume for fluid injection to successfully perform refracturing in order to protect parent fractures from getting damaged by child fractures. The protection can be achieved by increasing pore pressure through fluid injection as concluded by Miller et al. (2016). Another way to protect parent fractures is to reduce the time period between the first and second well for refracturing. Pankaj et al. (2016) investigated stress evolution in Eagle Ford and concluded that time is a vital component in determining the effectiveness of the refracturing strategy as the benefit from refracturing can be obtained at a certain period of time of the well-producing life.

Part of this section is reprinted with permission from "Development of Efficiently Coupled Fluid Flow and Geomechanics Model for Refracturing Optimization in Highly Fractured Reservoirs" by Sangnimnuan, A., Li, J., Wu, K. and Holditch S., 2018. *SPE* Hydraulic Fracturing Technology Conference. Woodlands, Texas, USA, 23-25 January. Copyright [2018] by Society of Petroleum Engineers.

Another factor affecting the alteration of stress field is presence of natural fractures which has been studied only by a few literatures. Forand et al. (2017) studied natural fracture distribution in Delaware and Midland Basins and found that Delaware Wolfcamp typically has two orthogonal fracture sets. This has become the objective of this chapter, which is to predict stress redistribution due to depletion and optimize timing and locations for refracturing in reservoirs with complex hydraulic and natural fractures.

In this chapter, pressure and stress distribution due to depletion in a highly fractured reservoir are predicted using the coupled fluid flow and geomechanics model with Embedding Discrete Fracture Model (EDFM). Synthetic cases with multiple natural fractures were created to study the effects of natural fractures, fracture spacing, natural differential stress, and reservoir permeability on stress evolution. Change in stress distribution is to be observed from the study. The critical time to perform refracturing is also to be determined for different scenarios as the critical time is one of the important factor to consider. Beyond the critical timing, the child fractures may not be able to propagate towards intact areas at all and may damage parent fractures as a result of the reversal of maximum horizontal stress.

3.2 Model implementation for cases with multiple natural fractures

To be able to simulate multiple complex natural fractures, the model is to be modified. Each additional fracture domain is created to represent each fracture orientation in the reservoir that contains multiple hydraulic and natural fractures. For example, if only hydraulic fractures are considered in the simulation (Figure 3.1) and they are all propagated perpendicular to the well, then only one fracture domain is required; however, if two different natural fracture orientations exist in the reservoir along with stimulated hydraulic fractures (Figure 3.2), then three fracture

domains (one for hydraulic fractures and two for natural fractures) are required, meaning that not only p_f will be solved, but also p_{nf1} and p_{nf2}. p_{nf1} is pressure inside natural fracture domain 1 and p_{nf2} is pressure inside natural fracture domain 2. Eqs. (2.23) and (2.24) will also have to be modified incorporating flow transmissibility from natural fracture domain 1 and 2. If more orientations of natural fracture set are to be simulated, more mass conservation equations will be added to the system of equations. Therefore, a generic version of the system of equations can be written by modifying Eqs. (2.23) and (2.24) as shown in Eqs. (3.1) and (3.2) for the reservoir and hydraulic fracture respectively.

$$\left(\frac{1}{M}+\frac{b^2}{K_{dr}}\right)\frac{\partial p^n}{\partial t}-\frac{b^2}{K_{dr}}\frac{\partial p^{n-1}}{\partial t}+b\frac{\partial(\nabla\cdot u)}{\partial t}-\frac{k}{\mu_f}(\nabla^2 p^n)+\lambda_t T_{f-m}({p_f}^n-p^n)+\sum_{i=1}^{N}\lambda_t T_{nfi-m}({p_{nfi}}^n-p^n)\ =0. \quad \text{……...……...……} \quad (3.1)$$

$$\frac{1}{M_f}\frac{\partial {p_f}^n}{\partial t}-\frac{k_f}{\mu_f}\left(\nabla^2 {p_f}^n\right)+\lambda_t T_{f-m}\left(p^n-{p_f}^n\right)+\sum_{i=1}^{N}\lambda_t T_{f-nfi}\left({p_{nfi}}^n-{p_f}^n\right)\ =q. \quad \text{...…...} \quad (3.2)$$

Where T_{nfi-m} is transmissibility between the matrix and natural fracture domain i. T_{f-nfi} is transmissibility between hydraulic fractures and natural fracture domain i. N is the number of natural fracture sets. Conservation equations inside natural fracture domains can be written in the same matter as Eqs. (3.2).

$$\frac{1}{M_f}\frac{\partial {p_{nfi}}^n}{\partial t} - \frac{k_f}{\mu_f}\left(\nabla^2 {p_{nfi}}^n\right) + \lambda_t T_{nfi-m}\left(p^n - {p_{nfi}}^n\right) + \lambda_t T_{f-nfi}\left({p_f}^n - {p_{nfi}}^n\right) + \sum_{i,j=1, j \text{ not equal to } i}^{N} \lambda_t T_{nfi-nfj}\left({p_{nfj}}^n - {p_{nfi}}^n\right) = 0. \quad \ldots\ldots\ldots\ldots\ldots\ldots\ldots\ldots (3.3)$$

Where $T_{nfi\text{-}nfj}$ is transmissibility between natural fracture set i and set j, p_{nfi} is pressure in natural fracture set i, and p_{nfj} is pressure in natural fracture set j. As mentioned in the previous chapter, natural fractures are assumed to be open throughout the entire production period and effect of sliding is not considered in the model. Therefore, the contribution from natural fractures is mainly from pressure depletion as the fluid can flow through the fractures and some of the fractures are connected to hydraulic fractures. Eqs. (3.1), (3.2), and (3.3) are to be solved together through the sequential method to obtain pressure and displacement in the matrix, the pressure in the hydraulic fractures, and pressure in each natural fracture set. Eq. (3.3) is to be added to the system of equations if there are two or more natural fracture orientations. Model discretization can be carried out the same way as discussed in chapter 2 for Eqs. (3.1), (3.2), and (3.3).

3.3 Boundary effect in a field-scale reservoir

Boundary effect plays an important role in reservoir modeling specifically in geomechanics part as the change of stress in magnitude and orientation is directly caused by not only reservoir depletion but boundary conditions. Typically, geomechanics simulator uses either constrained or unconstrained boundary condition depending on the reservoir size. This study was shown in chapter 2, in which it was found that the difference between the two boundary conditions is insignificantly and there is no difference in terms of production. However, reservoir size is another important factor that should be considered in a field-scale reservoir simulation. On one hand, if

the reservoir size is too small, stress changes observed around SRV region obtained from the coupled geomechanics and fluid flow model may not be accurate due to boundary condition. On the other hand, if the reservoir size is too large, the computational cost will be very expensive even though the result is much more accurate. Therefore, the reservoir size should be selected properly based on production time and in-situ differential stress which directly affect stress changes.

In this section, the reservoir used in the study has 11 stages with each stage having 4 perforation clusters and 100 ft spacing between each cluster. The well is placed at the center of the reservoir along x-direction as shown in Figure 3.1. Due to stress shadowing effects, 2 inner fractures are to be about half-length of 2 outer fractures in each stage. Reservoir size is 5105 ft (L_x) × 1805 ft (L_y) × 100 ft (L_z) with the number of grid cells being 1021 (N_x) × 361 (N_y) × 1 (N_z) in x, y, and z-direction, respectively. No flow boundary condition was applied on all six boundaries for fluid flow. For the geomechanics part, traction boundary was applied on the top boundary in the z-direction, while constrained boundary condition (zero displacements in a normal direction) was applied for the rest of the boundaries to allow stress changes at the boundaries as the reservoir is depleted.

All parameters used in this study can be found in Table 1 in Roussel et al. (2013), which represents liquid-rich shale development found in the Bakken reservoir. The only difference is that this study includes natural fractures to represent high permeability or Stimulated Reservoir Volume (SRV) instead of increased permeability in Stimulated Reservoir Volume (SRV) region. Positive stress represents compression and negative represents tension.

Quantity	Value	Unit
Young's modulus (E)	$2x10^6$	psi
Poisson's ratio (ν)	0.2	-
Biot's coefficient (b)	0.7	-
Reservoir permeability (k)	300	nd
Reservoir porosity (ϕ)	0.05	-
Fluid compressibility (c_f)	$2.18x10^{-5}$	psi^{-1}
Fracture permeability (k_f)	2000	md
Wellbore radius (r_w)	0.25	ft
Fluid viscosity (μ_f)	0.25	cp
Initial pressure (p_0)	$1x10^4$	psi
Bottomhole pressure (p_b)	$0.3\ x10^4$	psi
Initial stress in x direction ($\sigma_{hmin,0}$)	$1.15\ x10^4$	psi
Initial stress in y direction ($\sigma_{Hmax,0}$)	Vary	psi
Initial stress in z direction ($\sigma_{zz,0}$)	$1.3\ x10^4$	psi
Differential stress (varies for each case)	500, 900, 1300	psi
Fracture spacing	30-200	ft

Table 3.1. Parameters used for all case studies (Sangnimnuan et al. 2018b).

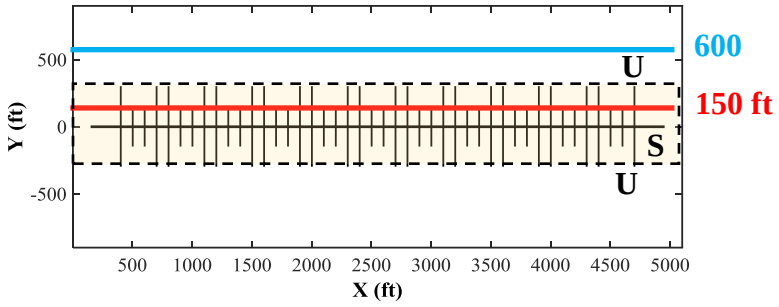

Figure 3.1. The configuration of a well with 11 production stages and 4 perforation clusters per stage. Locations to plot orientation change along x-direction at y = 150 ft and 600 ft from well, are also shown in this figure.

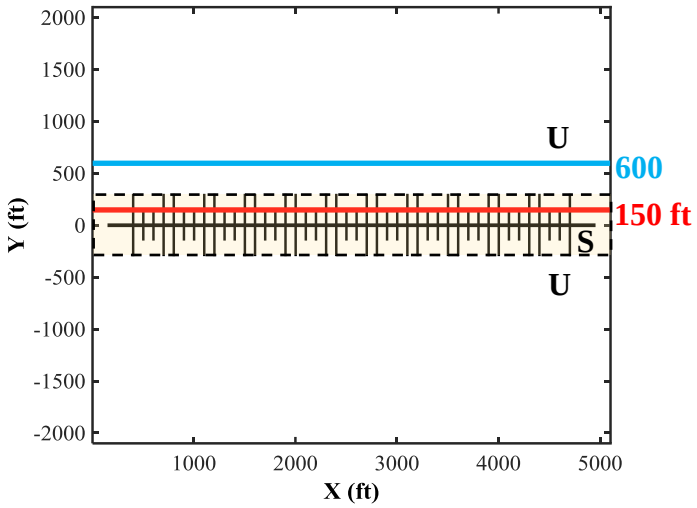

Figure 3.2. The configuration of a well with 11 production stages and 4 perforation clusters per stage. Locations to plot orientation change along x-direction at y = 150 ft and 600 ft from well, are also shown in this figure.

Reservoir shown in Figure 3.1, in which the distance in y-direction from fracture tip to each boundary in y-direction is only 600 ft or equals fracture length, is to be compared with a full-size reservoir case, in which distance from fracture tip to each boundary in y-direction is 3 times larger than fracture length to ensure that boundary condition would not affect our results in terms of stress redistribution. Orientation change along x-direction at y = 150 ft and 600 ft from well is to be studied. The lines shown in red and blue respectively in Figures 3.1 and 3.2. The goal of this comparison is to quantify how stress redistribution of our base case, which is likely to be affected by boundary condition, differs from a full-size reservoir case, which has no effect from boundary condition. Configuration for a full-size reservoir is shown in Figure 3.2. Regions S and U shown in Figure 3.2 represent inside and outside SRV region respectively.

Pressure distribution with the direction of maximum horizontal principal stress as well as orientation change of σ_{Hmax} along x-direction at 150 ft (within SRV region) and 600 ft (outside SRV region) from the well in y-direction for our base case (small reservoir) are compared with a

full-size reservoir case as shown in Figures 3.3 and 3.4 for differential stress (DS) of 500 and 900 psi (base case) at 0.5 and 5 years of production respectively. Figures 3.3e and 3.3f, show orientation change of σ_{Hmax} along x-direction inside and outside SRV region at 0.5 year of production. It shows that there is almost no difference between our base case and full-size reservoir case inside SRV (region S). However, for the area outside SRV (region U), a significant difference can be observed for a case with DS = 500 psi (Figures 3a and 3c), while a case with DS = 900 psi shows no difference (Figures 3.3b and 3.3d).

At 5 years of production, a case with DS = 500 psi shows good agreement both in region S and U compared with a full-size reservoir case at the same condition as shown in orientation change of σ_{Hmax} along x-direction (Figure 3.4e). Overall stress redistributions for both cases are also very similar (Figures 3.4a and 3.4c) as pressure depletion in region S is large enough to bring down σ_{Hmax} to be smaller than σ_{min} for the entire reservoir domain. On the other hand, small differences in region U can be observed in a case with DS = 900 psi. Figure 3.4d reveals that stress in region U is already rotated 90^o for entire region due to pressure depletion in region S and boundary effect, while a full-size reservoir case (Figure 3.4b) only shows partial stress reversal mostly in the center area of region U with the farthest distance from fracture tip (area close to boundary) having the least stress reversal. This supports the fact that the larger the DS, the less stress redistribution as it is harder for σ_{Hmax} to become smaller than σ_{hmin}.

For a small reservoir size (base case), pressure depletion in region S has a big impact on stress redistribution in region U as the distance between fracture tip and reservoir boundary is very short. The effect can be observed at early time (0.5 year) when DS is low (500 psi) and later time (5 years) when DS is higher (900 psi). However, for region S, there is no difference between our base case and full-size reservoir case for both DS = 500 and 900 psi as well as both 0.5 year and 5

years, meaning that our base case (small reservoir size) is suitable to study stress redistribution due to pressure depletion inside SRV region. When it comes to stress redistribution outside the SRV region, it is not always the case that the small reservoir would yield a correct result since it is subject to DS and production time. Therefore, in order to accurately study stress redistribution of small reservoir cases for in-fill well treatment and refracturing in reservoir with multiple wells and small well spacing, it is necessary to ensure that not only stress redistribution inside SRV region, but also outside SRV is accurate. Results at DS = 900 psi indicate that boundary condition only affects stress redistribution at a later time and only outside SRV region, and the effect is not significant (Figure 3.4f) compared with the 500-psi DS case, in which boundary condition yields a completely different result (Figure 3.3e). Since most of the cases in this study are based on DS = 900 psi (base case), it is acceptable to study stress redistribution using small reservoir size. If the study were projected to cases with smaller DS, boundary effect may have to be taken into consideration and a larger reservoir size may be required when studying stress redistribution for refracturing and in-fill well treatments in order to obtain accurate and reliable results.

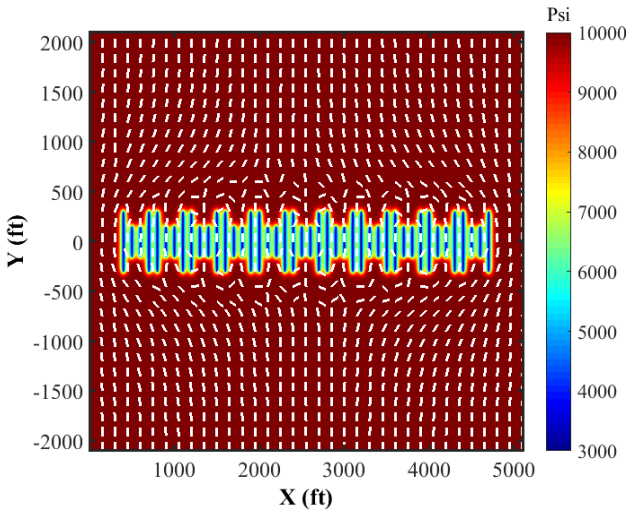

(a) Pressure distribution for large reservoir case with direction of maximum horizontal principal stress for DS = 500 psi

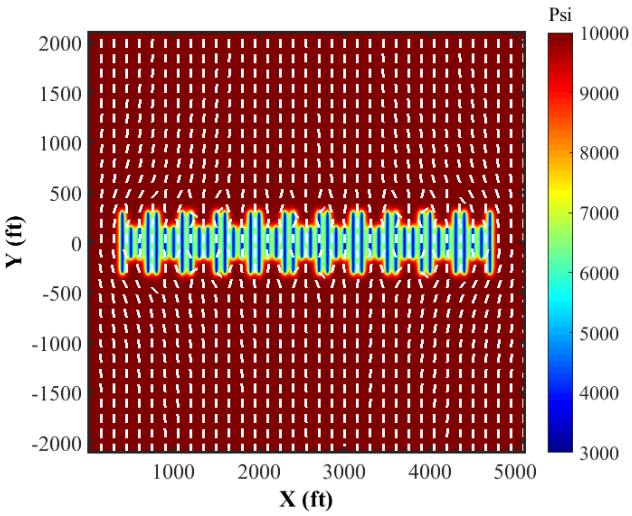

(b) Pressure distribution for large reservoir case with direction of maximum horizontal principal stress for DS = 900 psi

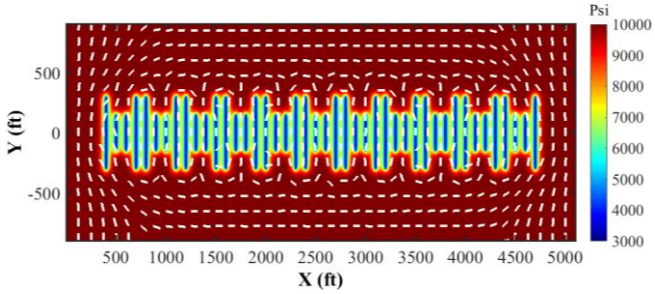

(c) Pressure distribution for small reservoir case with direction of maximum horizontal principal stress for DS = 500 psi

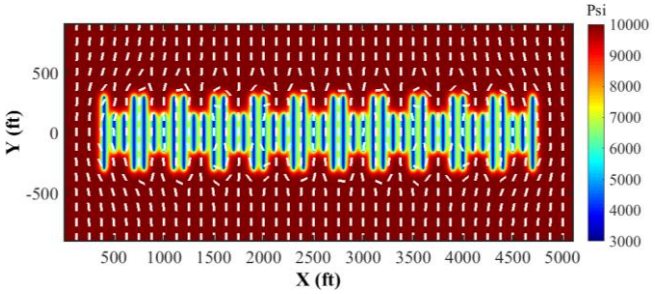

(d) Pressure distribution for small reservoir case with direction of maximum horizontal principal stress for DS = 900 psi

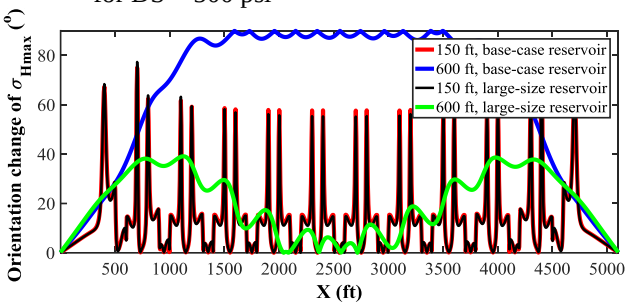

(e) Orientation change of maximum horizontal principal stress for small and large reservoir case along x-axis at different distances from the well for DS = 500 psi

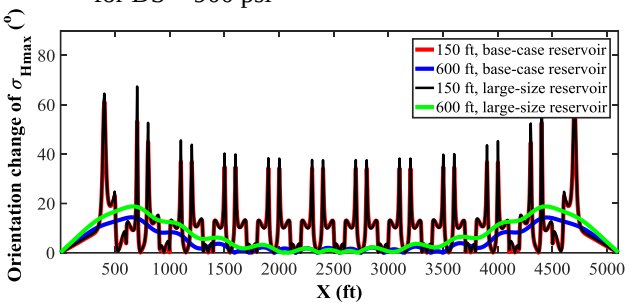

(f) Orientation change of maximum horizontal principal stress for small and large reservoir case along x-axis at different distances from the well for DS = 900 psi

Figure 3.3. Pressure distribution and orientation change of maximum horizontal principal stress for small and large reservoir cases at DS = 500 psi (a,c,e) and 900 psi (b,d,f) at 0.5 years of production.

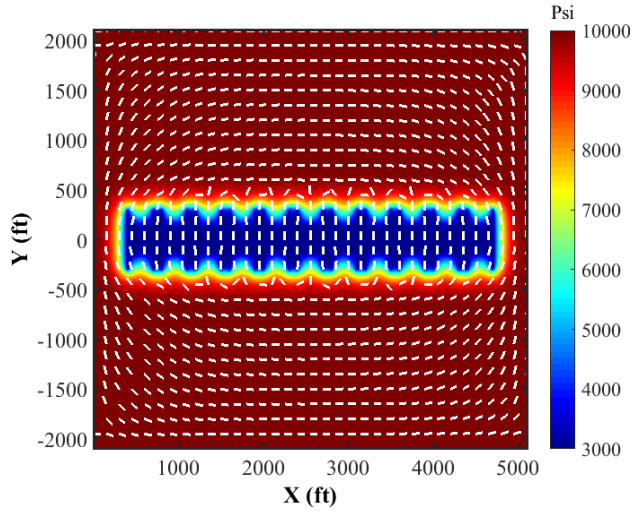

(a) Pressure distribution for large reservoir case with direction of maximum horizontal principal stress for DS = 500 psi

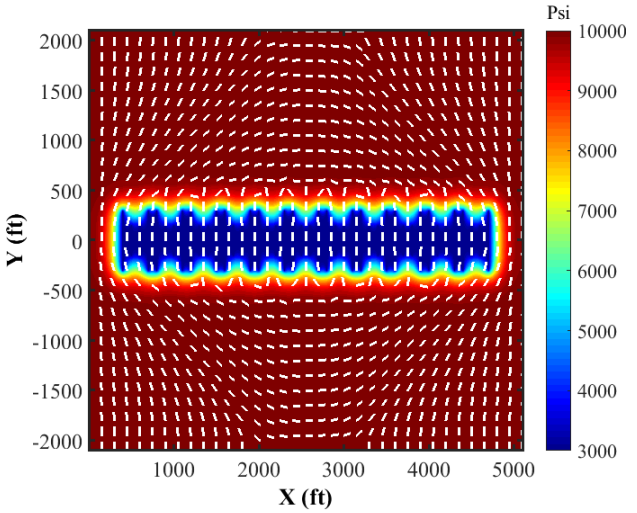

(b) Pressure distribution for large reservoir case with direction of maximum horizontal principal stress for DS = 900 psi

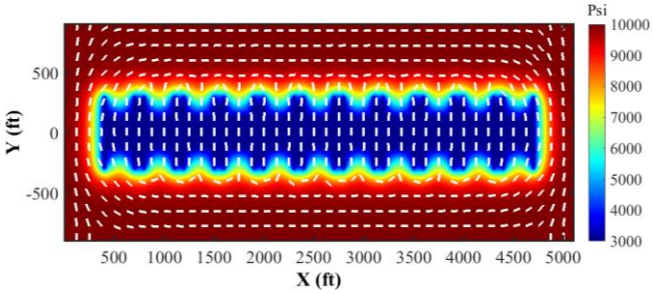

(c) Pressure distribution for base case with direction of maximum horizontal principal stress for DS = 500 psi

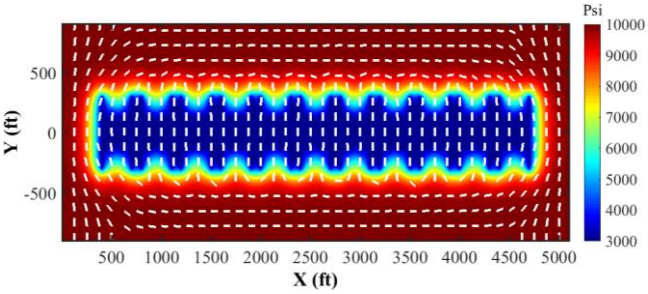

(d) Pressure distribution for base case with direction of maximum horizontal principal stress for DS = 900 psi

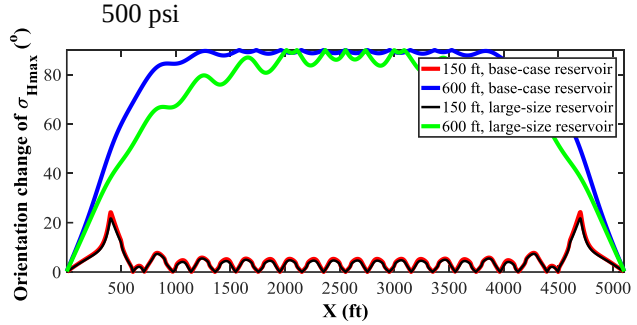

(e) Orientation change of maximum horizontal principal stress for small and large reservoir cases along x-axis at different distances from the well for DS = 500 psi

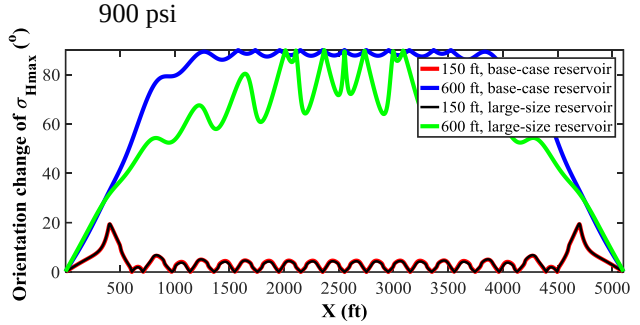

(f) Orientation change of maximum horizontal principal stress for small and large reservoir cases along x-axis at different distances from the well for DS = 900 psi

Figure 3.4. Pressure distribution and orientation change of maximum horizontal principal stress for small and large reservoir cases at DS = 500 psi (a,c,e) and 900 psi (b,d,f) at 5 years of production.

3.4 Case studies

The case studies include the effect of natural fractures and density of natural fractures, the effect of hydraulic fracture spacing, the effect of differential stress, and effect of reservoir permeability. Figure 3.5 shows the overall configuration of the reservoir (left figure) which is similar to Figure 3.1 with 4 lines in different colors representing different distances (150 ft, 300 ft, 450 ft, and 600 ft) in the y-direction from well. Zoom-in of middle stage (right figure) shows different points (A, B, C, D, E, and F) that are used to monitor stress evolution at different locations in the reservoir over time. Two red lines in zoom-in figure separate simulated region (S region), which has higher depletion due to fractures (SRV) than the unstimulated region (U region). Reservoir permeability is uniform and constant for entire reservoir. The main focus of this study is at the middle stage (zoom-in figure) for all cases as it has the least effect on left and right boundary conditions. In the following sub-section, the effect of natural fractures was investigated to illustrate the roles natural fractures play in stress redistribution and evolution.

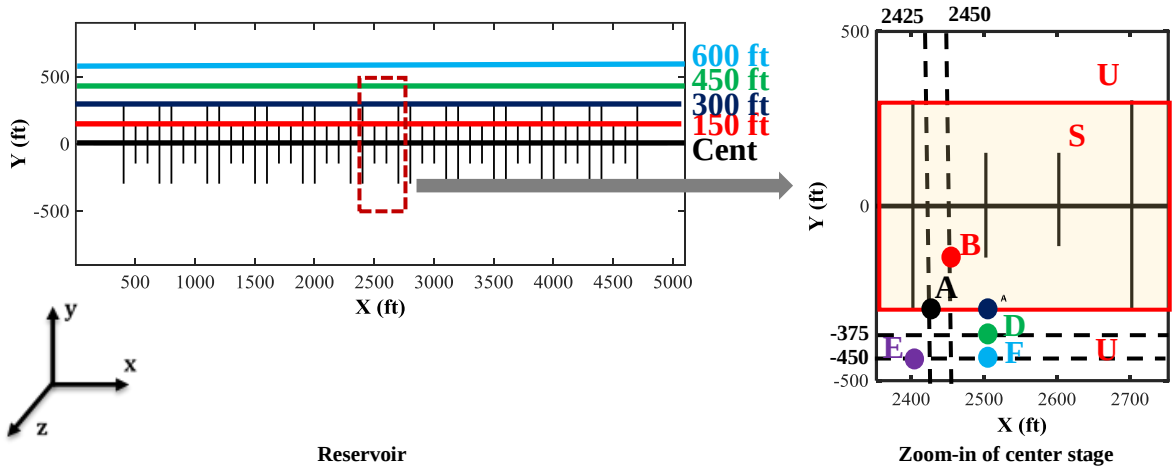

Figure 3.5. Locations to plot orientation change along x-direction at y = 0 ft, 150 ft, 300 ft, 450 ft, and 600 ft from well, and locations to observed stress evolution (Sangnimnuan et al. 2018b).

3.4.1 Effect of natural fractures and natural fracture density

In this section, pressure distribution as well as stress redistribution in the reservoir were compared for the case without and with natural fractures. For cases with natural fractures, 3 different densities of natural fractures were considered; low density with 100-ft spacing (360 fractures), mid-density (1700 fractures), and high density (2400 fractures) as shown in Figure 3.6. Natural fracture distribution for all 3 designs were generated using a stochastic realization method developed by Wu (2014) based on natural fracture lengths, spacing, and density. The accuracy of natural fracture distribution can be improved if more information, such as analysis of core samples, is available. Mid-density natural fracture case is used as a base case when making a comparison.

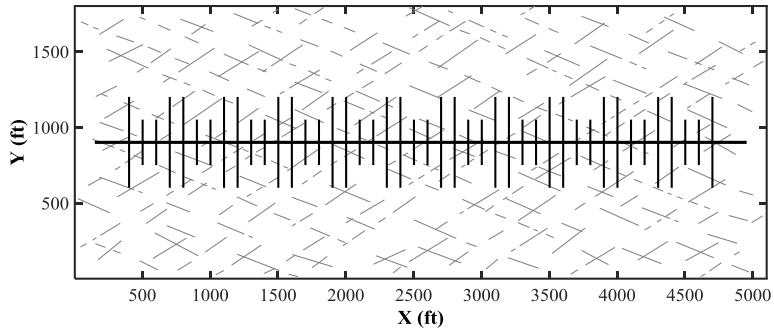

(a) Low-density natural fracture distribution

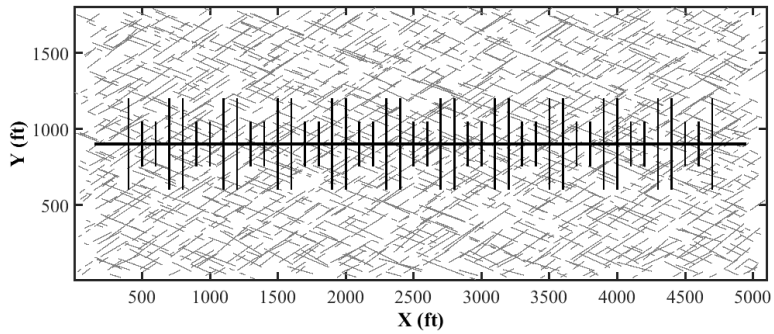

(b) Mid-density natural fracture distribution

Figure 3.6. Three different designs of natural fracture distribution (low density (a), mid-density (b), and high density (c)) (Sangnimnuan et al. 2018b).

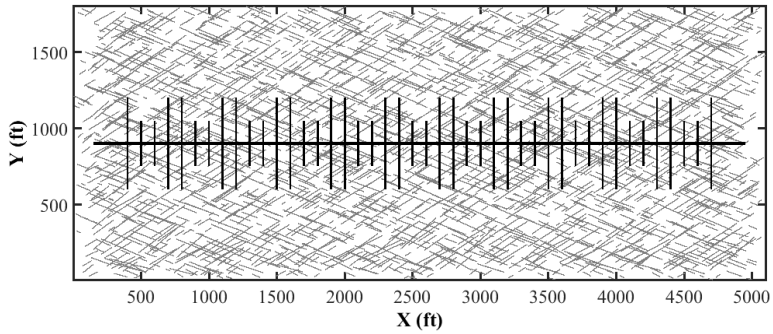

(c) High-density natural fracture distribution

Figure 3.6. Continued.

Figure 3.7 compares pressure distribution with the direction of maximum horizontal principal stress at 0.5 and 1 year of production for cases without natural fractures and with different natural fracture densities. White dash lines on top of pressure distribution in all plots represent the orientation of maximum horizontal principal stress (σ_{Hmax}). Figures 3.7a and 3.7b show how stress evolves due to reservoir depletion as time progresses from 0.5 to 1 year. At early time (0.5 year), stress reversal, which occurs when σ_{Hmax} becomes smaller than σ_{hmin}, can only be observed in region U (Figure 3.7a). This is due to higher depletion on these longer hydraulic fractures compared with the shorter ones resulting in the higher reduction of σ_{Hmax} around tips of longer hydraulic fractures in region U, while σ_{hmin} does not change as there is no pressure change along x-direction. In addition, stress reversal can also be observed on each hydraulic fracture as pressure depletes much faster in y-direction which is the direction of σ_{Hmax} than that in x-direction. At 1 year of production, all stresses in region U have rotated 90^o as the depletion in region S is sufficiently high to lower value of σ_{Hmax} in region U. However, stress reversal along each hydraulic fracture can no longer be observed as the depleted area fractures start to merge with each other, creating a larger reduction in pressure along x-direction than y-direction. The same phenomenon can be observed when natural fractures are considered in the simulation. In contrast with the case

without natural fractures, stress reversal at 0.5 years in region U occurs randomly, depending on which areas in region S have high depletion. This is highly subject to locations of natural fractures. As more natural fractures are present, less stress reversal is observed in region S at all times. Among all three natural fracture densities, the low-density case (Figure 3.7c) shows the most stress reversal, followed by Figures 3.7e (mid-density) and 3.7g (high-density) respectively, which has almost no stress reversal even as early as at 0.5 year as natural fractures connect depleted area of each hydraulic fracture together. Less stress reversal can be observed in region S for all three natural fracture cases when compared with case without natural fracture. Figures 3.7d, 3.7f, and 3.7h illustrate similar results as the case without natural fractures at 1 year of production.

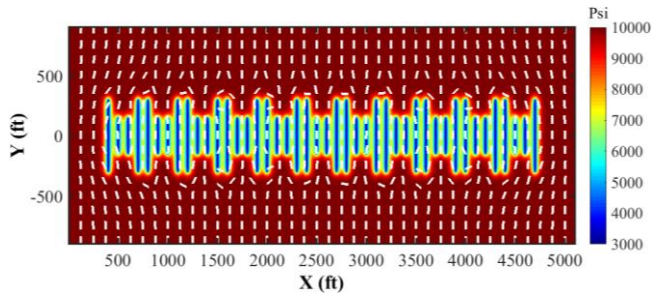

(a) Pressure distribution for case without natural fractures with direction of S_{Hmax} at 0.5 year

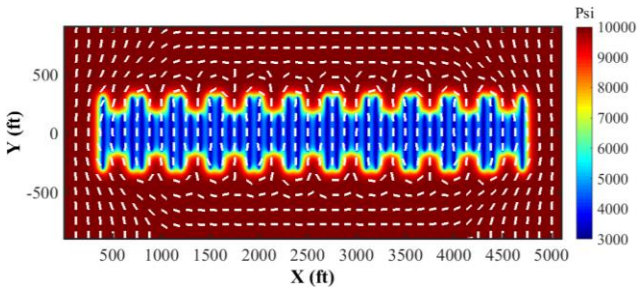

(b) Pressure distribution for case without natural fractures with direction of S_{Hmax} at 1 year

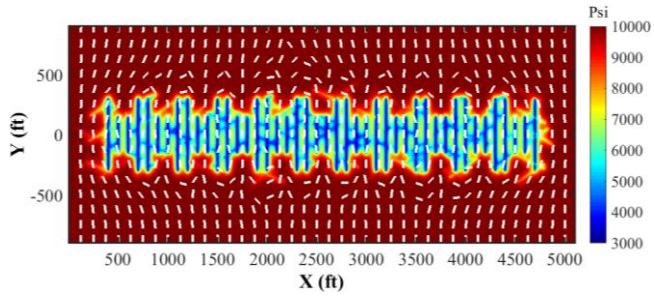

(c) Pressure distribution for low-density natural fractures with direction of S_{Hmax} at 0.5 year

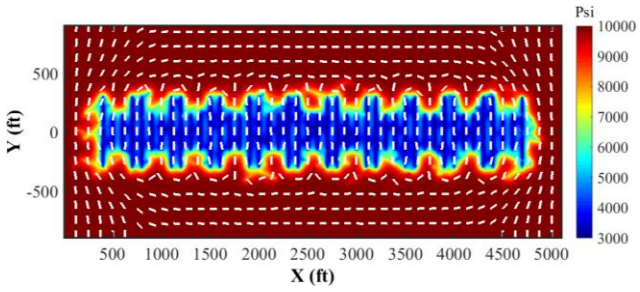

(d) Pressure distribution for low-density natural fractures with direction of S_{Hmax} at 1 year

Figure 3.7. Pressure distribution with the direction of maximum horizontal principal stress for the case without natural fractures (a, b), low density (c, d), mid-density (e, f), and high-density natural fractures (g, h) at 0.5 and 1 year (Sangnimnuan at el. 2018b).

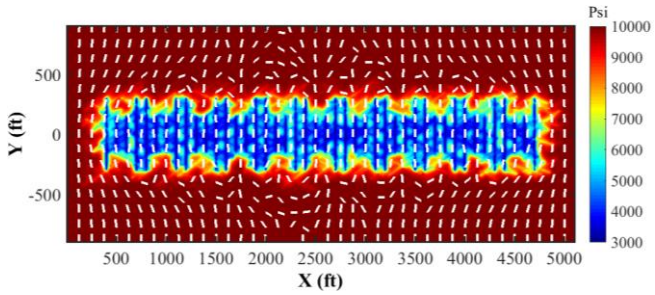

(e) Pressure distribution for mid-density natural fractures with direction of S_{Hmax} at 0.5 year

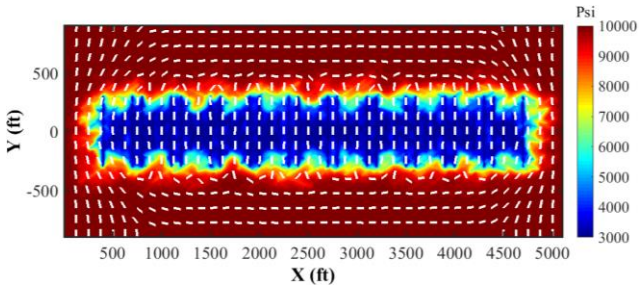

(f) Pressure distribution mid-density natural fractures with direction of S_{Hmax} 1 year

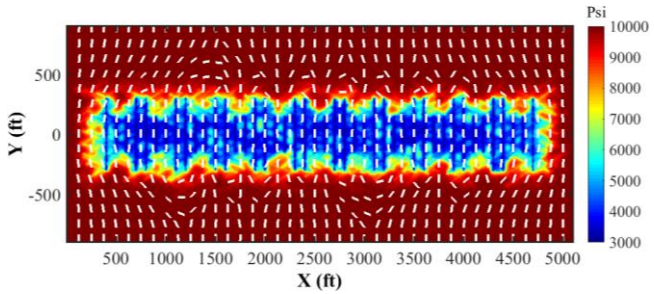

(g) Pressure distribution for high-density natural fractures with direction of S_{Hmax} at 0.5 year

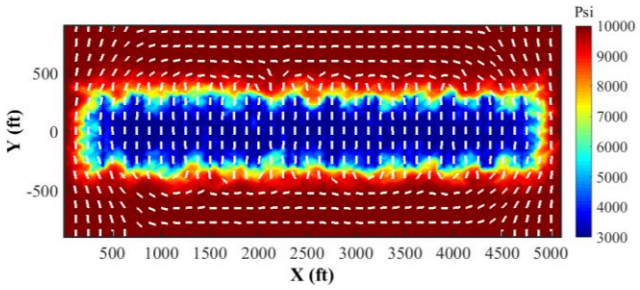

(h) Pressure distribution for high-density natural fractures with direction of S_{Hmax} at 1 year

Figure 3.8. Continued.

Figure 3.8 shows the time evolution of orientation change of σ_{Hmax} for all 4 cases at different monitoring points (see Figure 3.3 for the location of each point). Points A, B, and C were selected to monitor stress evolution in region S, while points D, E, and F were selected for region U. Points A and B are for refracturing between fractures in the same stage in region S. Points C, D, E, D are for refracturing on the same location as original fractures at different production regions (S and U). Solid lines in Figure 3.8 represent monitoring points in region U, while dash lines represent monitoring points in region S. In accordance with Figures 3.8a and 3.8b, more stress redistribution can be observed in region S (dash lines) at early time (0.5 year), while stress redistribution in region U can be observed after 0.5 year up until around 1 year (solid lines), where stress completely rotates 90^o. This phenomenon applies to Figures 3.8a, 3.8b, 3.8c, and 3.8d with

the difference being that the more natural fractures, the less stress reorientation can be observed in region S. Similar to region S, stress reorientation is less in region U when the number of natural fractures increases. This also results in stress rotating back to its original direction after a certain period of production time as shown in Figure 3.8d for the case of high-density natural fractures. Stresses at points E and F start to rotate back after 2 years of production.

Results observed from Figures 3.8a, 3.8b, 3.8c, and 3.8d suggest that there exists a critical time when refracturing can be performed successfully. After the critical time, new fractures from refracturing between fractures in the same stage (points A and B) or at the same location as original fractures (points C, D, E, and F) may not be able to propagate to un-depleted areas in reservoir as stress in region U is already rotated 90^o (points E and F). For example, in Figure 3.8a, stress at points E and F rotate almost 90^o at around one-year of production, which indicates that if refracturing is performed before this time, a new fracture can easily propagate to region U. However, after 1 year, it is unlikely for refracturing to be successful as new fractures will propagate to depleted areas in the reservoir. On the other hand, at high-density natural fractures (Figure 3.8d), it is still possible to perform refracturing after the critical time (2 years of production) as stress at points E and F start to rotate back to its original direction. This critical time varies depending on the distribution and density of natural fractures in the reservoir. Not only the critical time but also refracturing locations can be determined from this plot. For instance, in cases of high-density natural fractures (Figure 3.8d), if refracturing is performed between original fractures (points A and B), a new fracture can easily propagate out. On the other hand, if refracturing is performed at the same location as original fractures (points C, D, E, and F), new fractures may get caught by stress reversal in region U and will not be able to propagate to un-depleted areas. This is also subject to the time that refracturing is performed.

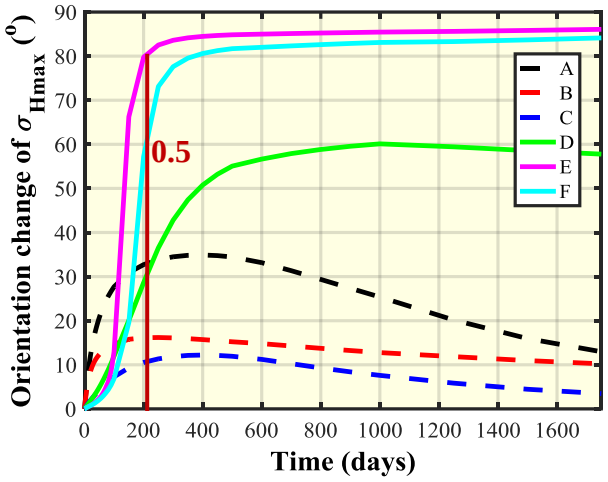

(a) Time evolution of orientation change of σ_{Hmax} for case without natural fractures

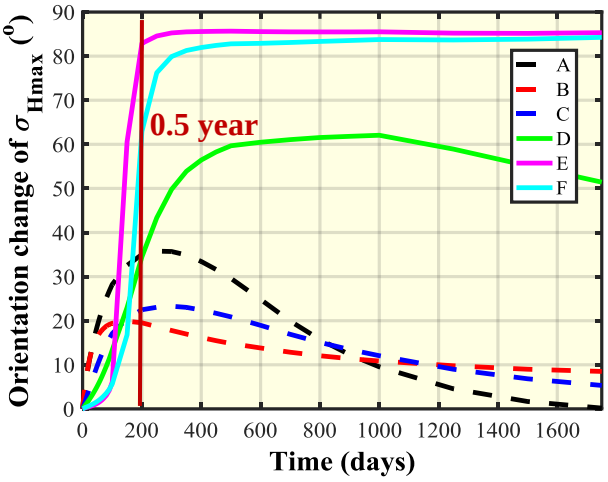

(b) Time evolution of orientation change of σ_{Hmax} for low-density natural fractures

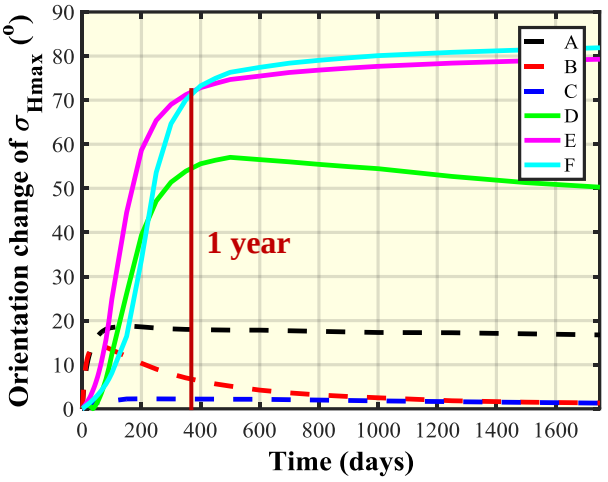

(c) Time evolution of orientation change of σ_{Hmax} for mid-density natural fractures

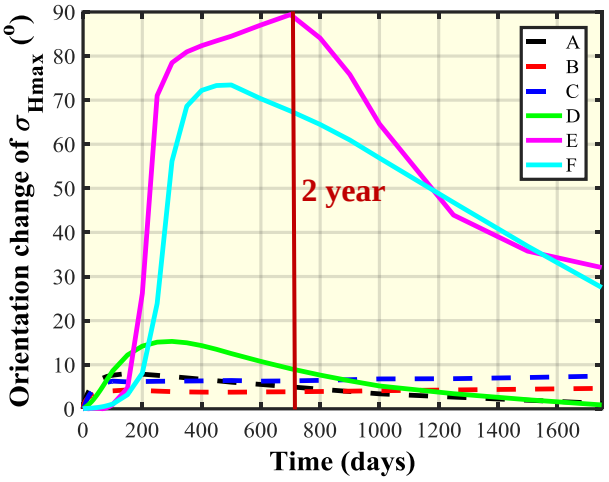

(d) Time evolution of orientation change of σ_{Hmax} for high-density natural fractures

Figure 3.8. Time evolution of orientation change of maximum horizontal principal stress for the case without natural fractures (a), low density (b), mid-density (c), and high-density natural fractures (d) (Sangnimnuan at el. 2018b).

Orientation change of σ_{Hmax} along x-direction at different distances from well in y-direction can be seen in Figures 3.9 and 3.10. Figures 3.9a, 3.9c, and 3.9e illustrate orientation change of σ_{Hmax} along x-direction at different times (0.5, 1, and 5 years) for the case without natural fractures and Figures 3.9b, 3.9d, and 3.9f are for mid-density natural fracture case. Initially, stress

reorientation can be found at all fracture locations and at almost all distances from wellbore (0 to 600 ft) As time progresses, stresses in region S (0-150 ft) start to rotate back, while stresses in region U (300 to 600 ft) completely rotate 90^{o}. At 5 years, less stress reorientation can be observed in region S and orientations in region U at 300 ft from well begin to rotate back. A similar phenomenon can be observed for mid-density natural fractures. However, stress redistribution is not uniform and does not have any pattern as this is subject to natural fracture distribution. More stress reversal can be observed at far distances from the wellbore (region U) as time progresses. Also, stress starts to rotate back in some areas in region U at 5 years due to the presence of natural fractures, which decreases σ_{hmin} in region U resulting in σ_{Hmax} becoming larger than σ_{hmin} again. This implies that refracturing can still be performed successfully after the critical time has passed if a specific location is selected for refracturing. For the case of lower natural fracture density (Figures 3.10a, 3.10c, and 3.10e), more stress redistribution can be observed in U region even as early as 0.5 year with similar trend as the case without natural fractures (Figures 3.9a, 3.9c, and 3.9e), while at higher natural fracture density (Figures 3.10b, 3.10d, and 3.10f), less stress reorientation is observed. For the same reason as the case of mid-density natural fracture in Figure 3.8f, stresses rotate back in some areas at 5 years for both cases with lower and higher natural fracture densities (Figures 3.10e and 3.10f). Results shown in Figures 3.9 and 3.10 together with results from Figure 3.8 provide critical insights into how natural fractures alter stress distribution during the production and how much this stress distribution differs from the case without natural fractures. This can be used as a guideline in determining time and location for refracturing in highly fractured reservoirs.

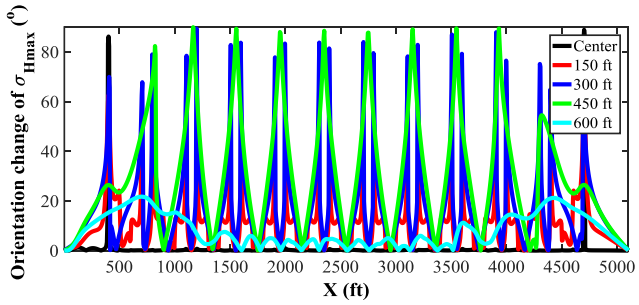

(a) Orientation change of maximum horizontal principal stress for case without natural fractures along x-axis at different distances from well at 0.5 year

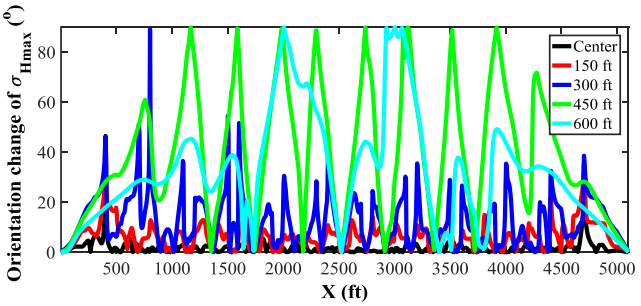

(b) Orientation change of maximum horizontal principal stress for mid-density natural fractures along x-axis at different distances from well at 0.5 year

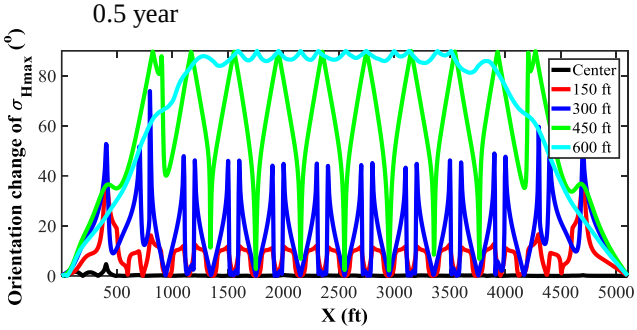

(c) Orientation change of maximum horizontal principal stress for case without natural fractures along x-axis at different distances from well at 1 year

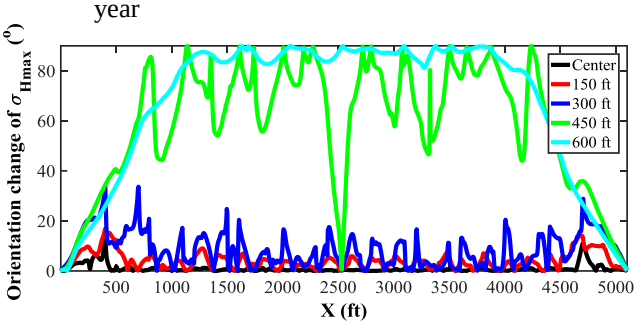

(d) Orientation change of maximum horizontal principal stress for mid-density natural fractures along x-axis at different distances from well at 1 year

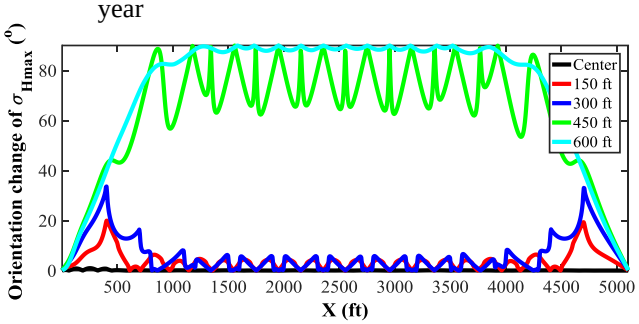

(e) Orientation change of maximum horizontal principal stress for case without natural fractures along x-axis at different distances from well at 5 years

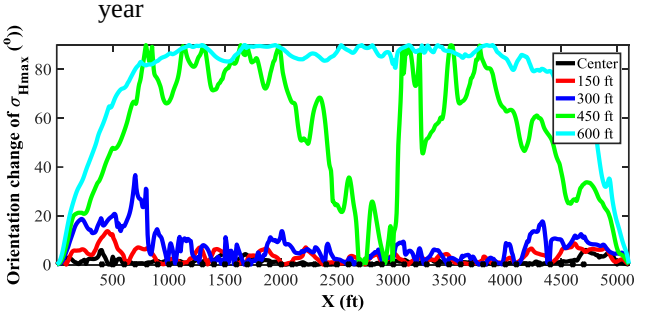

(f) Orientation change of maximum horizontal principal stress for mid-density natural fractures along x-axis at different distances from well at 5 years

Figure 3.9. Orientation change of maximum horizontal principal stress along x-direction at different distances from well in the y-direction at 0.5, 1, and 5 years for the case without natural fractures (a, c, e) and mid-density natural fracture (b, d, f) (Sangnimnuan at el. 2018b).

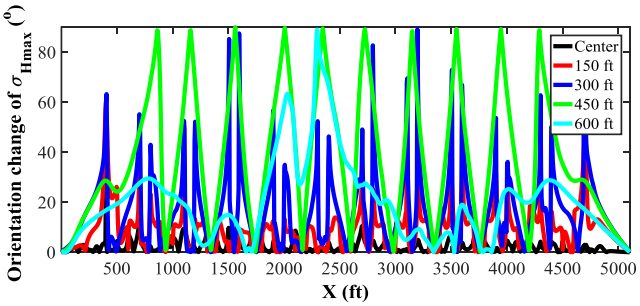

(a) Orientation change of maximum horizontal principal stress for low-density natural fractures along x-axis at different distances from well in y-direction at 0.5 year

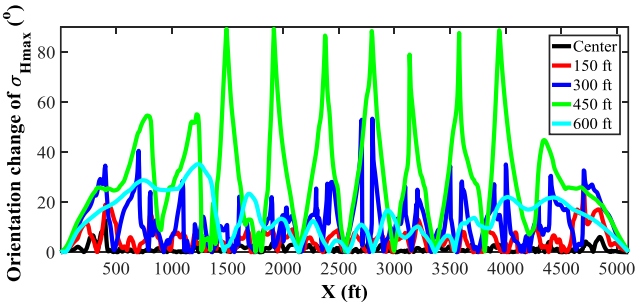

(b) Orientation change of maximum horizontal principal stress for high-density natural fractures along x-axis at different distances from well in y-direction at 0.5 year

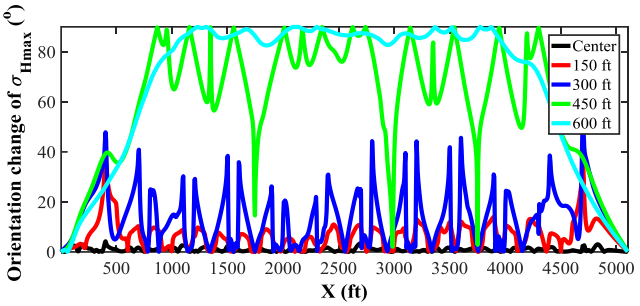

(c) Orientation change of maximum horizontal principal stress for low-density natural fractures along x-axis at different distances from well in y-direction at 1 year

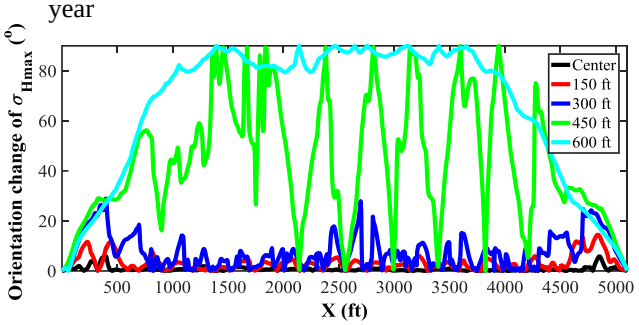

(d) Orientation change of maximum horizontal principal stress for high-density natural fractures along x-axis at different distances from well in y-direction at 1 year

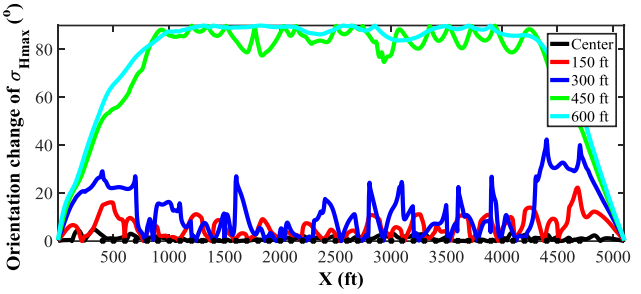

(e) Orientation change of maximum horizontal principal stress for low-density natural fractures along x-axis at different distances from well in y-direction at 5 years

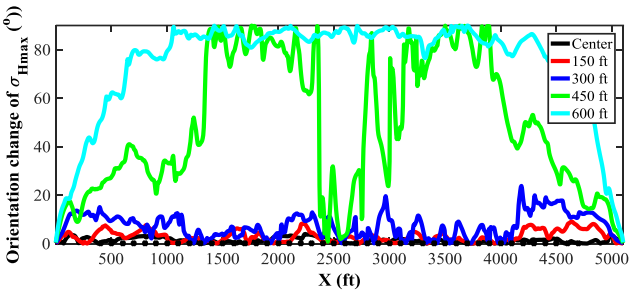

(f) Orientation change of maximum horizontal principal stress for high-density natural fractures along x-axis at different distances from well in y-direction at 5 years

Figure 3.10. Orientation change of maximum horizontal principal stress along x-direction at different distances from well in the y-direction at 0.5, 1, and 5 years for low-density (a, c, e) and high-density natural fracture (b, d, f) (Sangnimnuan at el. 2018b).

Cumulative oil production for all 4 cases studied in this section is shown in Figure 3.11. The case with no natural fractures has the lowest production, while the case with the highest natural

fracture density has the highest production. Natural fractures help increase production compared with the case without natural fractures from 8% (360 natural fractures) to 42% (2400 natural fractures) depending on natural fracture density by enlarging the size of the depleted area in the reservoir and increasing the production rate.

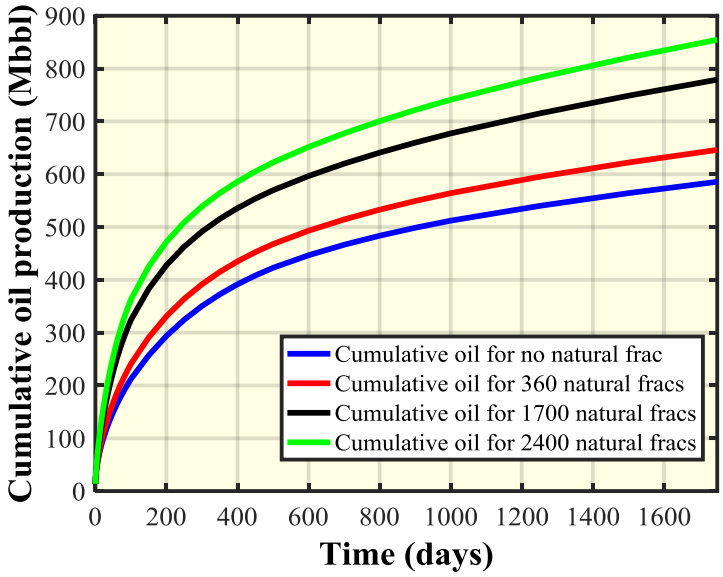

Figure 3.11. Cumulative oil production for multiple cases, case without natural fractures, low density (360 fractures), mid-density (1700 fractures), and high-density natural fracture (2400 fractures) (Sangnimnuan at el. 2018b).

3.4.2 Effect of hydraulic fracture spacing

In this section, pressure distribution and stress redistribution in a reservoir with mid-density natural fracture (base case) was compared at different hydraulic fracture spacing, i.e. 200 ft, 100 ft, 50 ft, and 30 ft as shown in Figure 3.12. Spacing is increased to 200 ft compared with the previous section and reduced to 50 ft and 30 ft with the two inner fractures in each stage being shorter than outer ones due to stress shadowing effects. This is to see how stress redistribution changes at larger and smaller spacing. It is common to perform refracturing in a well with small

spacing (30 ft) as smaller spacings allow more perforation clusters per stage and thus more production gain. Performing refracturing between two short spacing fractures can be challenging as stress around the fractures might completely reverse (stress reversal), resulting in a new fracture intersecting original fractures during refracturing. For a 200-ft spacing case, the results were compared with Roussel et al. (2013) as reservoir properties and configuration used in our simulations are similar to the one used by Roussel except that two inner fractures are shorter than two outer fractures due to stress shadowing effects on each stage, while Roussel used uniform fracture lengths for the entire well. In addition, natural fractures are included in our study, while Roussel used k_{srv} to represent faster depletion in SRV region.

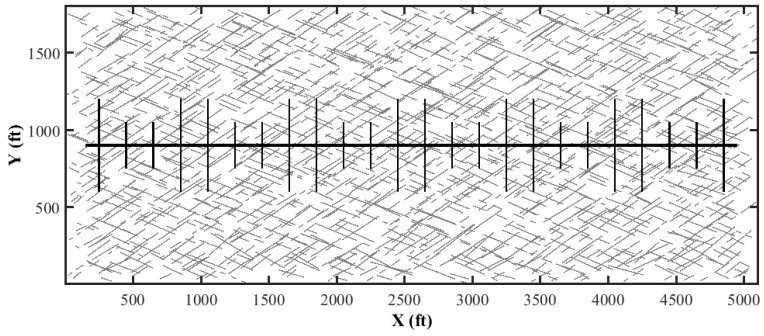

(a) Configuration of 200-ft spacing with mid-density natural fracture

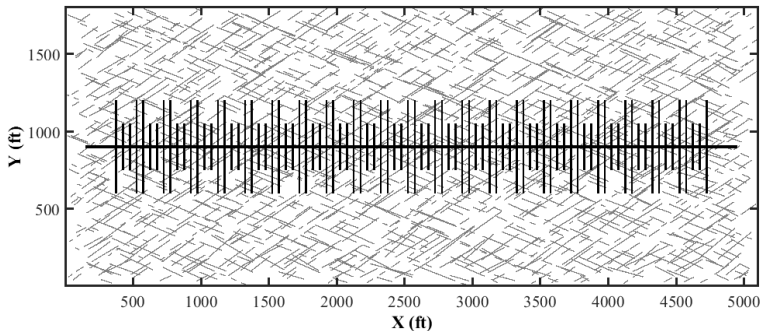

(b) Configuration of 50-ft spacing with mid-density natural fracture

Figure 3.12. 3 Different designs of hydraulic fracture spacing (200 ft (a), 50 ft (b), and 30 ft (c)) (Sangnimnuan et al. 2018b).

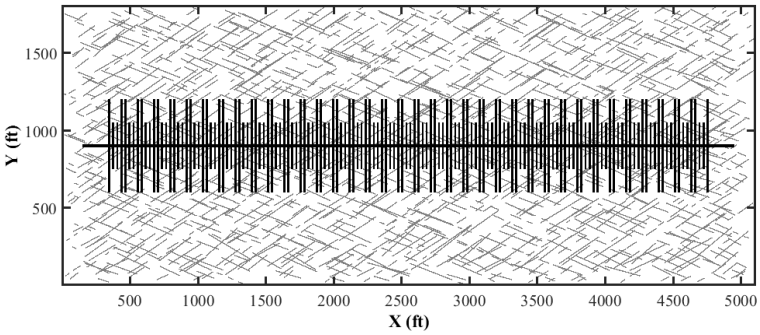

]

(c) Configuration of 30-ft spacing with mid-density natural fracture

Figure 3.13. Continued.

It can be observed that there is no stress reorientation at 0.5 year of production for a 200-ft spacing case (Figures 3.13a) as pressure depletion in region S is not sufficiently high to make σ_{Hmax} becomes smaller than σ_{hmin} in region U, while stress reorients 90^o in region U (outside SRV) at 1 year of production due to more depletion. There is also no stress reorientation in each hydraulic fracture because the depleted areas are connected together by natural fractures. Results of a 200-ft spacing show a significant difference compared with results obtained by Roussel et al. (2013), in which stress reversal can be observed along each hydraulic fracture in SRV region (region S), while our results do not show any reorientation at 0.5 year of production inside SRV region. This is due to the presence of natural fractures, which connect together the depleted area of each hydraulic fracture, thus changing size and shape from rectangular shape with longer side in y-direction to rectangular shape with longer side in x-direction. As discussed in previous section, stress reorientation can only occur when shape of depleted area is longer in y-direction as σ_{Hmax} can become smaller than σ_{hmin}. However, at 1 year of production, our result shows good agreement with Roussel's, in which stress outside SRV region (region U) completely reorients as the depletion inside SRV region (region S) is large enough to lower σ_{Hmax} in region U. On the other hand, for the small spacing cases (Figures 3.13c and 3.13e), a complete stress reversal in region U

can be observed as early as 0.5 year due to a large number of hydraulic fractures creating fast depletion in region S at early time.

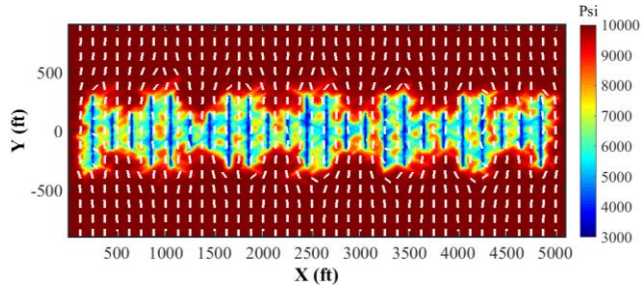

(a) Pressure distribution for 200 ft spacing with direction of maximum horizontal principal stress at 0.5 year

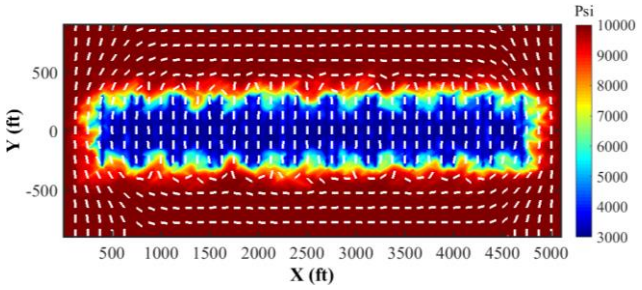

(b) Pressure distribution for 200 ft spacing with direction of maximum horizontal principal stress at 1 year

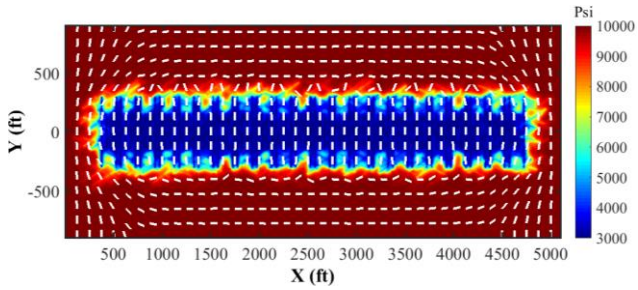

(c) Pressure distribution for 50 ft spacing with direction of maximum horizontal principal stress at 0.5 year

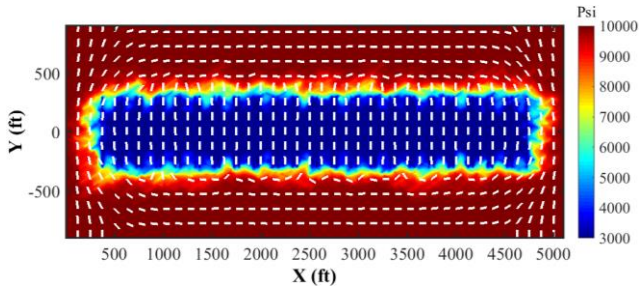

(d) Pressure distribution for 50 ft spacing with direction of maximum horizontal principal stress at 1 year

Figure 3.13. Pressure distribution with the direction of maximum horizontal principal stress for 200 ft spacing (a, b), 50 ft spacing (c, d), and 30 ft spacing at 0.5 and 1 year (Sangnimnuan et al. 2018b).

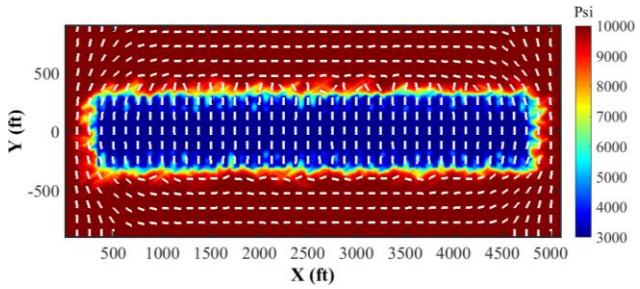

(e) Pressure distribution for 30 ft spacing with direction of maximum horizontal principal stress at 0.5 year

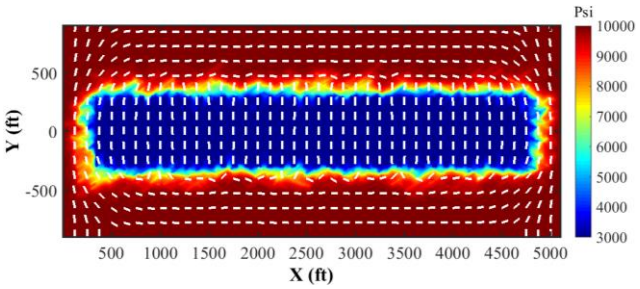

(f) Pressure distribution for 30 ft spacing with direction of maximum horizontal principal stress at 1 year

Figure 3.14. Continued.

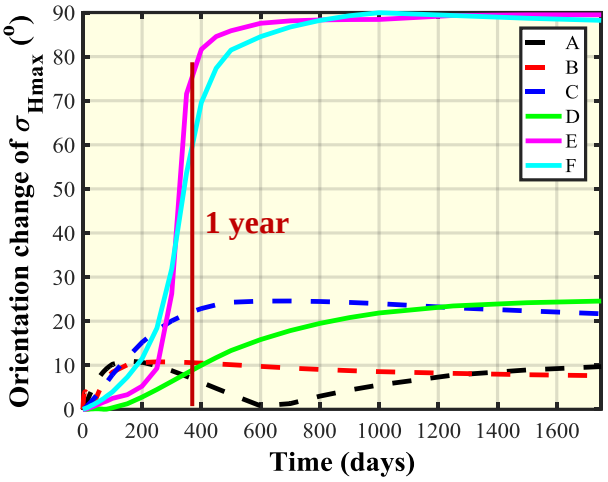

(a) Time evolution of orientation change of σ_{Hmax} for 200 ft spacing

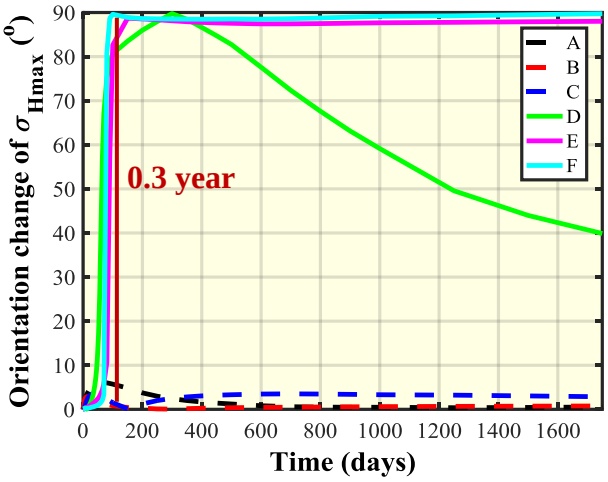

(b) Time evolution of orientation change of σ_{Hmax} for 30 ft spacing

Figure 3.14. Time evolution of orientation change of maximum horizontal principal stress for 200 ft spacing (a) and 30 ft spacing (b) (Sangnimnuan et al. 2018b).

Figures 3.14a and 3.14b illustrate the time evolution of orientation change of σ_{Hmax} at different monitoring points (Figure 3.3) for cases with 200-ft and 30-ft spacing. At 200-ft fracture spacing (Figure 3.14a), small stress reorientations along each fracture can be observed in region S until after 1 year of production, when stress reversal can be observed in region U. Similarly, for the case of 100-ft spacing from the previous section (Figure 3.8c), more orientation changes can

be observed in region S and stress reversal can be observed at points D, E, and F at around 1 year of production onwards. Lastly, for the 30-ft spacing case, stress reversal in region U occurs at an early time (0.3 years) and stays reversed as time progresses. This suggests that shorter spacing or more hydraulic fractures increase depletion rate inside SRV region, resulting in fast stress reversal outside SRV region. Orientation change of σ_{Hmax} along x-direction at different distances from well in y-direction can be seen in Figure 3.15. A small stress reorientation can be observed in Figures 3.15a (200-ft spacing) in both region S and U, which represent orientation of σ_{Hmax} at 0.5 year of production, while at 1 and 5 years, more stress reorientation can be observed in region U. Stress reorientations diminish in region S, which corresponds to Figures 3.13a and 3.13b. Figures 3.15b and 3.15d (30-ft spacing) clearly show stress reversal in region U with almost no reorientation in region S due to depletion area along each hydraulic fracture being connected, compared with 200-ft spacing (Figure 3.15a). However, at 5 years (Figures 3.15e and 3.15f), stresses in region U start to rotate back to their original direction at some locations, depending on the distribution of natural fractures. The locations in region S, where there is less pressure depletion, yield small reduction in σ_{Hmax}, which may not be large enough to overcome reduction in σ_{hmin}.

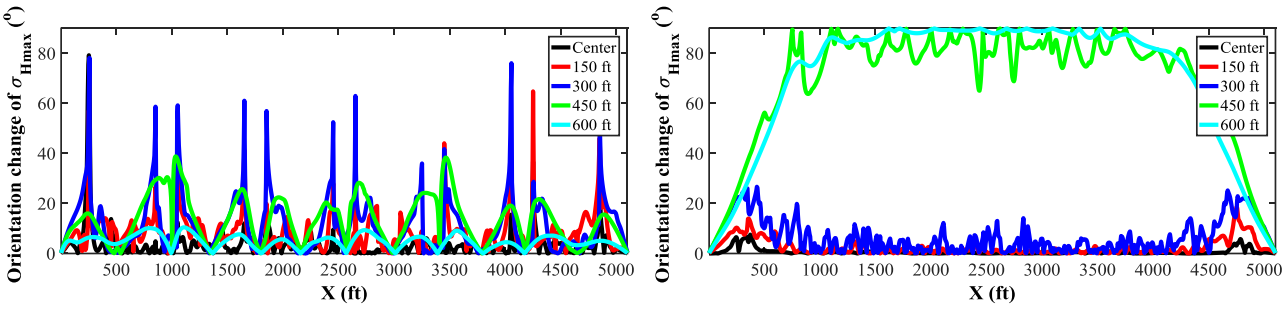

(a) Orientation change of maximum horizontal principal stress for 200 ft along x-axis at different distances from well in y-direction at 0.5 year

(b) Orientation change of maximum horizontal principal stress for 30 ft along x-axis at different distances from well in y-direction at 0.5 year

Figure 3.15. Orientation change of maximum horizontal principal stress along x-direction at different distances from well in the y-direction at 0.5, 1, and 5 years for 200 ft spacing (a, c, e) and 30 ft spacing (b, d, f) (Sangnimnuan et al. 2018b).

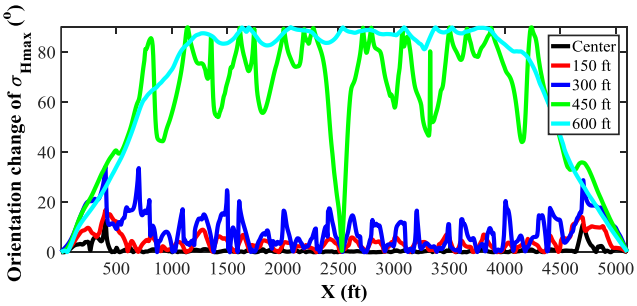

(c) Orientation change of maximum horizontal principal stress for 200 ft spacing along x-axis at different distances from well in y-direction at 1 year

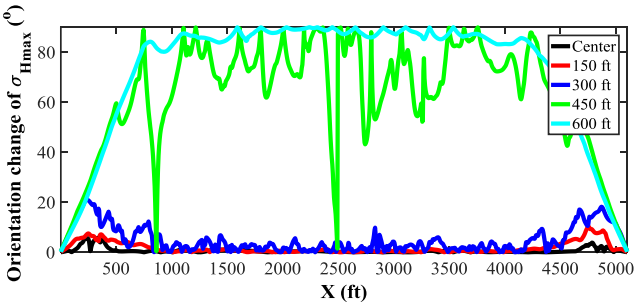

(d) Orientation change of maximum horizontal principal stress for 30 ft spacing along x-axis at different distances from well in y-direction at 1 year

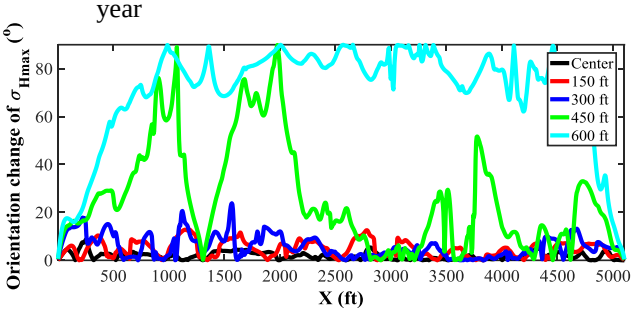

(e) Orientation change of maximum horizontal principal stress for 200 ft spacing along x-axis at different distances from well in y-direction at 5 years

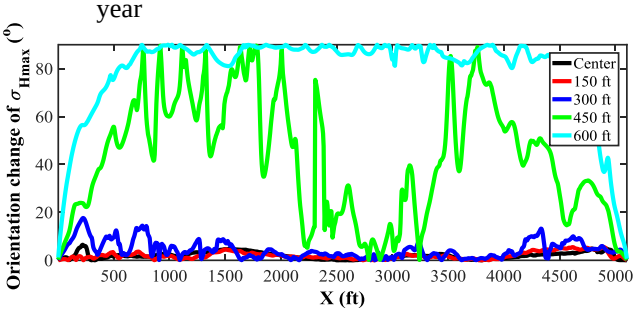

(f) Orientation change of maximum horizontal principal stress for 30 ft spacing along x-axis at different distances from well in y-direction at 5 years

Figure 3.16. Continued.

Cumulative oil production for all 3 cases studied in this section in comparison with the base case (100 ft spacing) from the previous section is shown in Figure 3.16. The case with the smallest spacing (30 ft) yields highest production and the case with the largest spacing (200 ft) corresponds to the lowest production due to less number of hydraulic fractures. At 5 years of production, the change in production is 140% when reducing fracture spacing from 200 ft to 30 ft without natural fractures. With the natural fractures, production gain from 200 ft to 30 ft is 128%, meaning that natural fractures contribute to production gain when reducing fracture spacing. Similarly, the larger the spacing, the more contribution from natural fractures as shown in the 30-

ft spacing case, 28% production gain can be observed, while 40% production gain can be expected when considering a 200-ft spacing case.

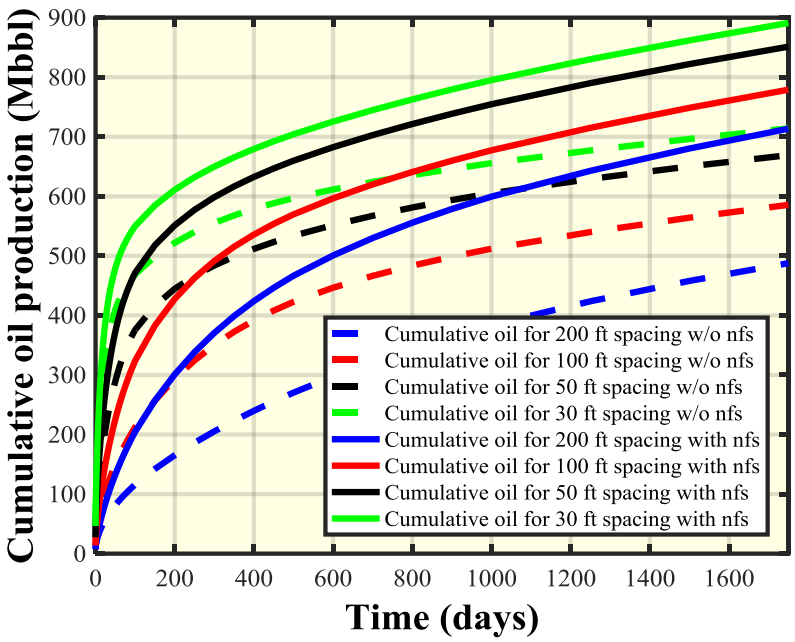

Figure 3.16. Cumulative oil production for 200 ft spacing, 100 ft spacing, 50 ft spacing, and 30 ft spacing (Sangnimnuan et al. 2018b).

3.4.3 Effect of differential in-situ stress

In this section, stress redistribution in a reservoir with mid natural fracture density (1700 natural fractures) is to be compared at different differential in-situ stresses (DS), i.e. 100 psi, 200 psi, and 500 psi as differential in-situ stress plays an important role in stress redistribution. Direction maximum horizontal stress is calculated based on induced differential stress and induced shear stress due to depletion.

Generally, induced shear stress is relatively smaller, hence here only induced normal stresses was analyzed to investigate orientation change of stresses. But when calculating updated orientation after depletion in this study, induced shear stress is also considered. In this study, maximum

horizontal stress is in y-direction, and minimum horizontal stress is in x-direction. Once stress in y-direction (σ_{yy}) becomes smaller than stress in x-direction (σ_{xx}), maximum horizontal stress would be close to rotate 90^o (stress reversal). This phenomenon is important as it allows prediction of propagation during refracturing whether child fractures would hit parent fractures or propagate to un-depleted area in order to ensure production gain from refracturing.

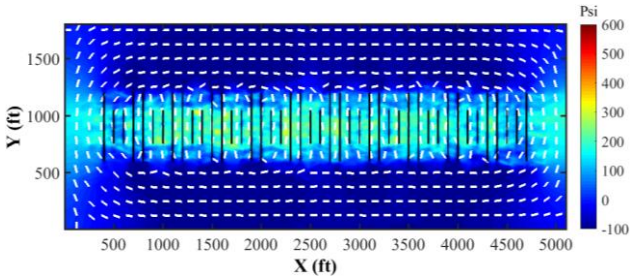

(a) σ_{Hmax}-σ_{hmin} distribution for DS = 100 psi with direction of maximum horizontal stress at 0.5 year

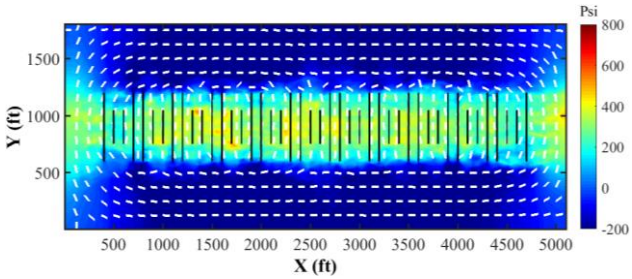

(b) σ_{Hmax}-σ_{hmin} distribution for DS = 100 psi with direction of maximum horizontal stress at 1 year

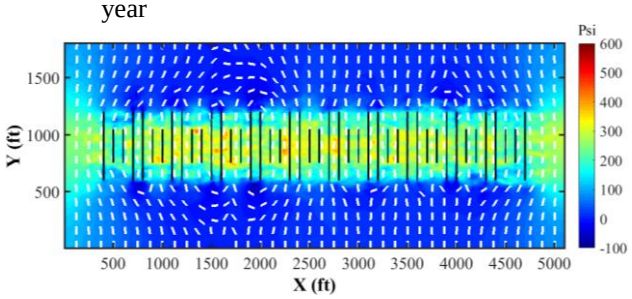

(c) σ_{Hmax}-σ_{hmin} distribution for DS = 200 psi with direction of maximum horizontal stress at 0.5 year

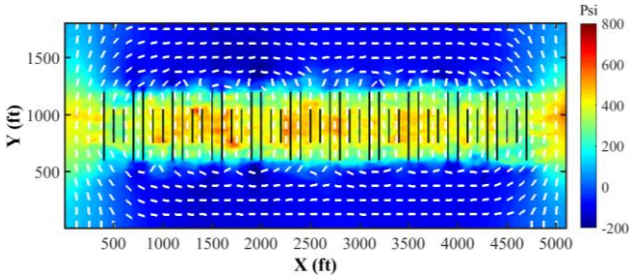

(d) σ_{Hmax}-σ_{hmin} distribution for DS = 200 psi with direction of maximum horizontal stress at 1 year

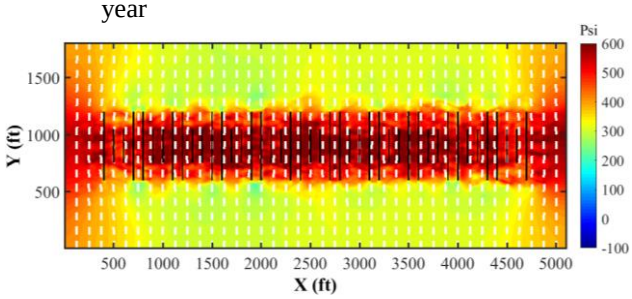

(e) σ_{Hmax}-σ_{hmin} distribution for DS = 500 psi with direction of maximum horizontal stress at 0.5 year

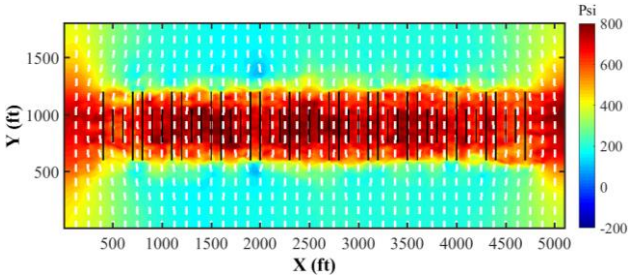

(f) σ_{Hmax}-σ_{hmin} distribution for DS = 500 psi with direction of maximum horizontal stress at 1 year

Figure 3.17. σ_{Hmax}-σ_{hmin} distribution with direction of maximum horizontal stress for DS = 100 psi (a, b), 200 psi (c, d), and 500 psi at 0.5 and 1 year (e, f) (Sangnimnuan et al. 2018b).

Figure 3.17 shows σ_{yy} - σ_{xx} distribution for all 3 differential in-situ stresses as well as the direction of maximum horizontal stress at 0.5 and 1 year. According to Figures 3.17a, 3.17c, and 3.17e, there is a significant difference among the three differential stresses. At 100-psi DS, stress reorientation occurs as early as 0.5 year in region U (regions with negative value or σ_{yy} is smaller than σ_{xx}), while at 200-psi DS (base case), reorientation can only be observed in some locations corresponding to high depletion areas in region S. For 500-psi DS, no reorientation occurs as it is much harder for σ_{yy} to become smaller than σ_{xx} both in region S or region U. At 1 year, stresses in region U for 200-psi DS (Figure 3.16d) start to rotate, while 500-psi DS still yields no reorientation.

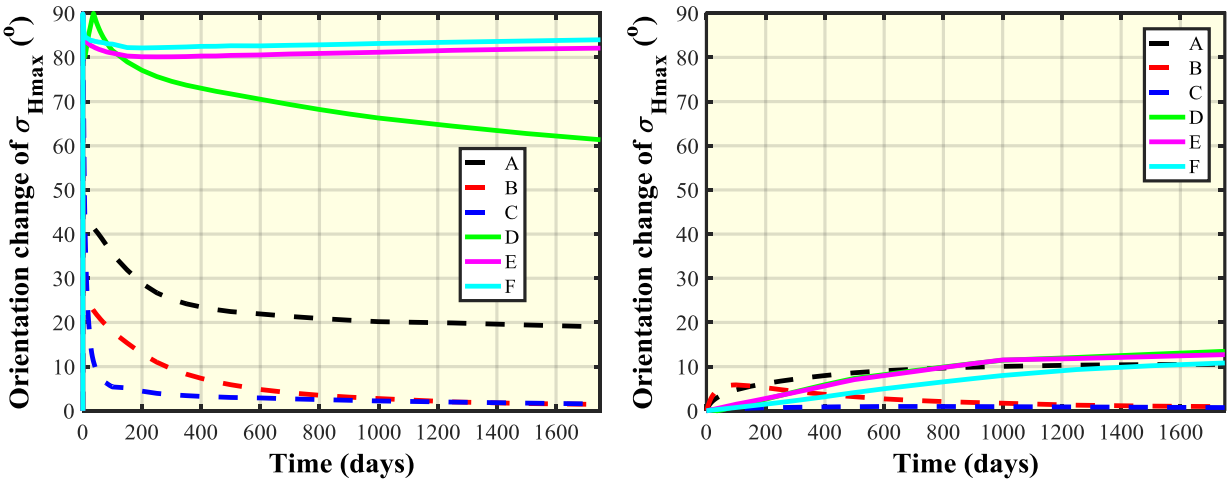

(a) Time evolution of orientation change of $\boldsymbol{\sigma}_{Hmax}$ for DS = 100 psi

(b) Time evolution of orientation change of $\boldsymbol{\sigma}_{Hmax}$ for DS = 500 psi

Figure 3.18. Time evolution of orientation change of maximum horizontal stress for Ds = 100 psi (a) and DS = 500 psi (b) (Sangnimnuan et al. 2018b).

The differences among three differential stresses can be emphasized more on time evolution of orientation change of σ_{Hmax} as shown in Figures 3.18a and 3.18b. For 100-psi DS,

stress reversal can be observed in region U at the very beginning of production and stay the same for the entire production period. In addition, more stress reorientation is observed in region S compared with 200-psi DS (Figure 3.8c). However, for 500-psi DS, almost no stress reorientation can be observed even at 600 ft away from the well center (region U), which is in good agreement with the result from Figure 3.17f, where almost no regions with negative values or regions with stress reorientation.

Figure 3.19 illustrates induced stress difference ($\Delta\sigma_{yy}$ - $\Delta\sigma_{xx}$) plotted along x-direction at different distances from well in the y-direction at 0.5, 1, and 5 year. Calculation of $\Delta\sigma_{yy}$ - $\Delta\sigma_{xx}$ can be expressed as

$$\sigma_{yy} - \sigma_{xx} = \sigma_{yy,0} + \Delta\sigma_{yy} - \sigma_{xx,0} - \Delta\sigma_{xx}$$

$$\sigma_{yy} - \sigma_{xx} = (\sigma_{yy,0} - \sigma_{xx,0}) + \Delta\sigma_{yy} - \Delta\sigma_{xx}$$

$$\sigma_{yy} - \sigma_{xx} = DS + \Delta\sigma_{yy} - \Delta\sigma_{xx}, \quad \text{..... (3.4)}$$

According to Eq. (3.4), this equation can be applied for any initial DS ($\sigma_{yy,0} - \sigma_{xx,0}$), which is a constant value. $\sigma_{\text{Hmax}} - \sigma_{\text{hmin}}$ is an updated stress difference after production and only changes when DS changes for a specific $\Delta\sigma_{yy}$ - $\Delta\sigma_{xx}$. If the initial DS is 0 psi, any area in the plot that is below 0 represents stress reversal. The same mechanism applies for other different stresses, i.e. 100 psi (scarlet dash line), 200 psi (purple dash line), and 500 psi (olive dash line) in Figure 3.19.

As shown in Figures 3.19a, 3.19b, and 3.19c, lines representing well center (0 ft), and 150 ft (region S) are far above 0 meaning that it is impossible for stresses in this area to completely rotate 90^{o} even at 100-psi DS and as early as 0.5 year of production due to presence of natural fractures. On the other hand, stresses in region U (300 ft, 450 ft, and 600 ft) can easily rotate when

DS is reduced from 500 psi to 200 psi and 100 psi. In addition, as time progresses, more reorientation can be observed in region U even at 500-psi DS, where stress reversal occurs at far distance from well (600 ft). Results observed from this section suggest that the critical time can be as early as 0.5 years if DS is as low as 100 psi. However, as DS increases to 500 psi, the critical time is pushed back to as late as 5 years. This directly affects how refracturing should be performed. For instance, if DS in the field is large (~500 psi), it is not necessary to perform refracturing at an early time compared with DS = 100 psi, where refracturing should be performed at an early time to make sure that child fractures will propagate to un-depleted areas in the reservoir and avoid fracture hit. This statement is solely based on reservoir properties used in this simulation, had the reservoir properties changed, the critical time would have totally changed i.e. stress reversal may be observed at DS = 500 psi.

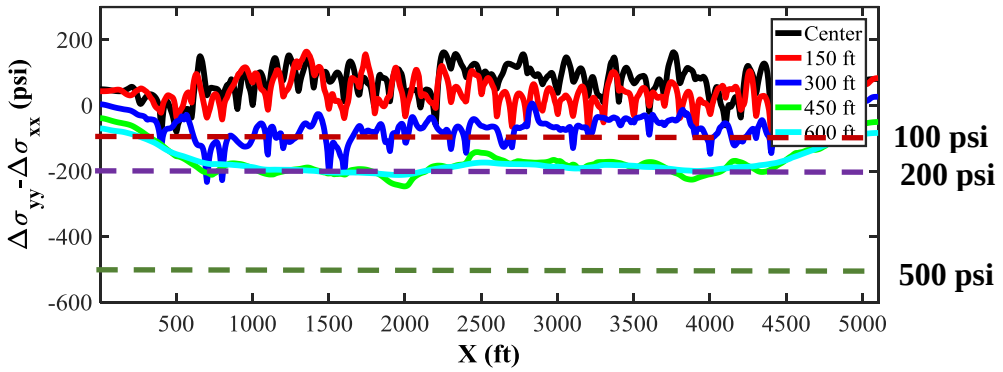

(a) $\Delta\sigma_{yy} - \Delta\sigma_{xx}$ for 100 ft spacing with mid fracture density (1700 fracs) at different differential in-situ stress (100, 200, and 500 psi) at 0.5 years.

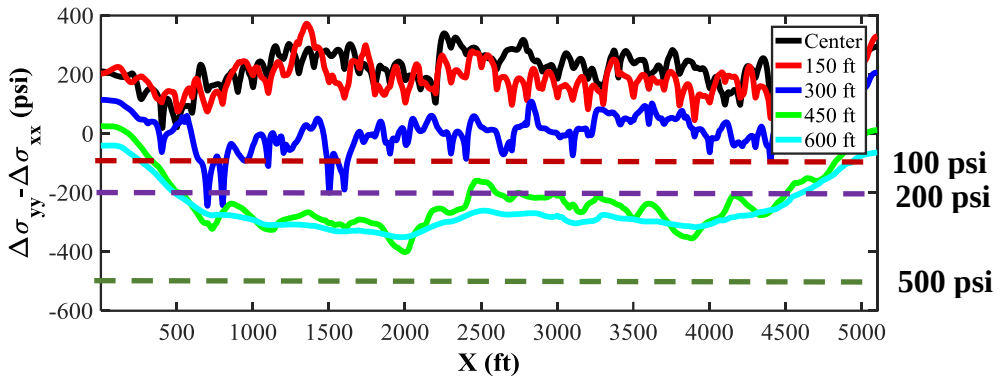

(b) $\Delta\sigma_{yy} - \Delta\sigma_{xx}$ for 100 ft spacing with mid fracture density (1700 fracs) at different differential in-situ stress (100, 200, and 500 psi) at 1 year.

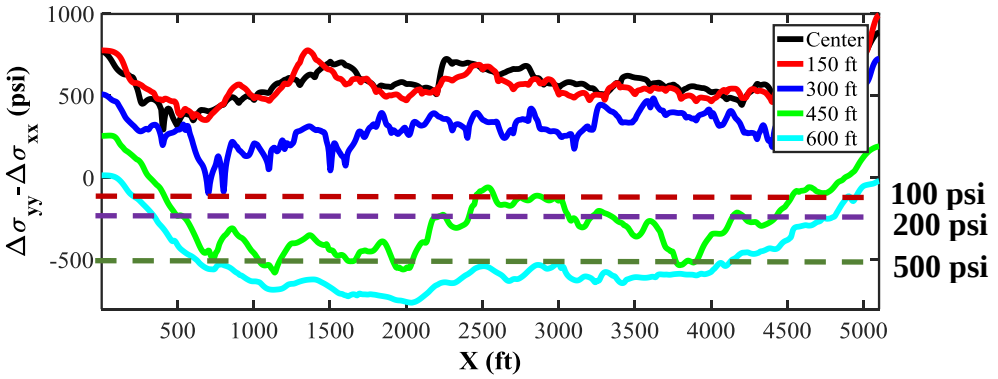

(a) $\Delta\sigma_{yy} - \Delta\sigma_{xx}$ for 100 ft spacing with mid fracture density (1700 fracs) at different differential in-situ stress (100, 200, and 500 psi) at 5 years.

Figure 3.19. Different differential in-situ stress along the x direction at different distances from the well in the y direction at 0.5 (a), 1 (b), and 5 year (c) for DS = 100 psi, 200 psi, and 500 psi (Sangnimnuan et al. 2018b).

3.4.4 Effect of reservoir permeability

In this section, stress redistribution in a reservoir with mid natural fracture density (1700 natural fractures) at low reservoir permeability (30 nd) is compared with the base case, in which reservoir permeability is 300 nd. A low reservoir permeability yields a low depletion rate, leading to unique stress redistribution especially around fracture area, where the depleted shape is totally

different from the base case. Figure 3.20 shows pressure distribution for low permeability case as well as the direction of maximum horizontal principal stress (dash line) at 0.5 and 1 year.

It can be observed from Figure 3.20a that stress reorientation is delayed at low reservoir permeability due to a decrease in production rate in region S. As mentioned in the previous section for a 200-ft spacing case, if production rate is not high enough, σ_{Hmax} in region U would not drop below σ_{hmin} and thus no stress reversal occurs. In contrast to the low reservoir permeability case, Figure 3.7e, which represents our base case, shows some stress redistribution in region U at 0.5 years as a result of faster depletion. As time progresses to 1 year, stress reversal can be observed in the U region as shown in Figure 3.20b, which is similar to Figure 3.7f, pointing that reservoir permeability plays an important role in the critical time. To support this statement, Figure 3.21 suggests that time taken for stress at points E and F to rotate almost 90^o is 3 years, which is longer than the case with higher permeability that takes only 1 year (Figure 3.8c). In addition, more stress reorientation can be observed at points A, B, and C for this low permeability case compared with the base case (Figure 3.8c) as a result of reduction in production rate. The slower the production rate, the more reorientation can be observed on each hydraulic fracture as the shape of depleted area is maintained as a rectangular shape with longer length in y-direction (Sangnimnuan et al., 2018).

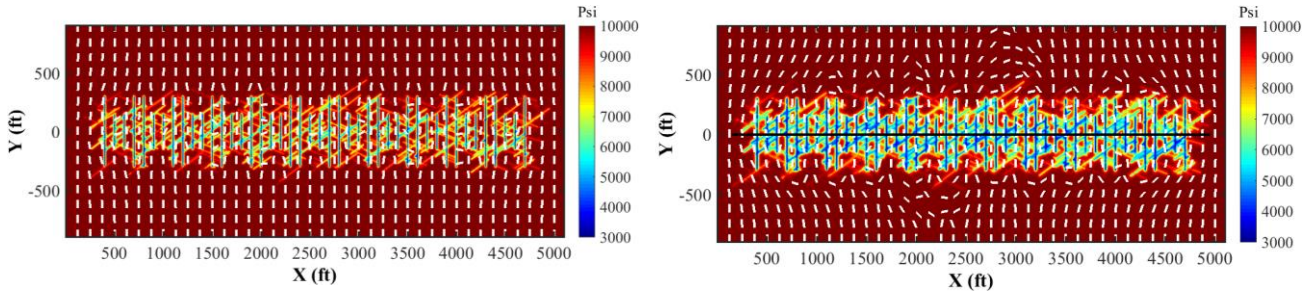

(a) Pressure distribution for reservoir permeability = 30 nd with direction of maximum horizontal principal stress at 0.5 year

(b) Pressure distribution for reservoir permeability = 30 nd with direction of maximum horizontal principal stress at 1 year

Figure 3.20. Pressure distribution with direction of maximum horizontal principal stress for low reservoir permeability at 0.5 (a) and 1 year (b) (Sangnimnuan et al. 2018b).

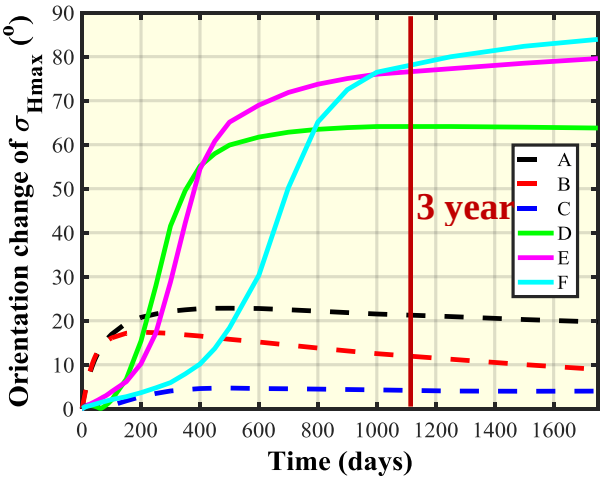

Figure 3.21. Evolution of orientation change of maximum horizontal principal stress for low reservoir permeability (Sangnimnuan et al. 2018b).

Figure 3.22a shows more stress reorientation observed in region S at 0.5 years (center, 150 ft, and 300 ft from well in y-direction) compared with Figure 3.9b. This result is in good agreement with Figures 3.20a and 3.21. At 1 year, stresses in region S start to rotate back, while stresses in region U (300 ft, 450 ft, and 600 ft) completely rotate 90° as shown in Figure 3.22b. This is similar to Figure 3.9d except that more reorientation can be observed in region S (Figure 3.22b). Less stress redistribution is observed towards 5 years of production in region S for both low

permeability (Figure 3.22c) and high permeability cases (Figure 3.9f). This is due to the same reason mentioned previously, which is the depleted area on each hydraulic fracture connecting to each other, creating a larger depleted area. As a result, the shape of the depleted area has changed from rectangular with the longer direction in y-direction to rectangular with the longer direction in x-direction, creating a higher reduction in σ_{hmin}, while σ_{Hmax} does not change much, yielding a very small to no stress reorientation. This suggests that there is a possibility of new fractures intersecting original fractures at an early time (0.5 to 1 year), if refracturing location is not selected properly, as stress reversal can be observed at some locations in region S. However, if refracturing is performed later (5 years), new fractures may not be able to propagate to un-depleted area as stress in region U already rotated 90^o just like the high permeability case (base case). Therefore, the critical time and locations must be carefully selected especially in low permeability reservoirs.

Cumulative oil production for a case with low reservoir permeability is compared with a case with high reservoir permeability for both cases; with and without natural fractures as shown in Figure 3.23. Without natural fractures, production increases by around 50% when permeability is enhanced from 30 nd to 300 nd. However, only 41% production increase is observed when increasing permeability 10 times for the case with natural fractures. This is due to the presence of natural fractures, which significantly increase production rate even at low permeability case, by increasing the size of the depleted area.

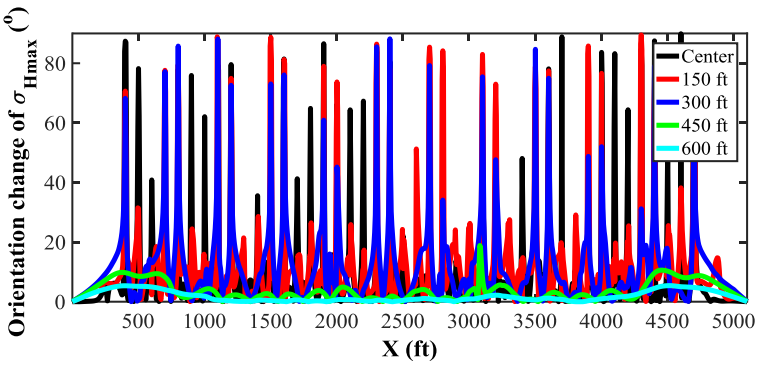

(a) Orientation change of maximum horizontal principal stress for low permeability reservoir (30 nd) along x-axis at different distances from well in y-direction at 0.5 year

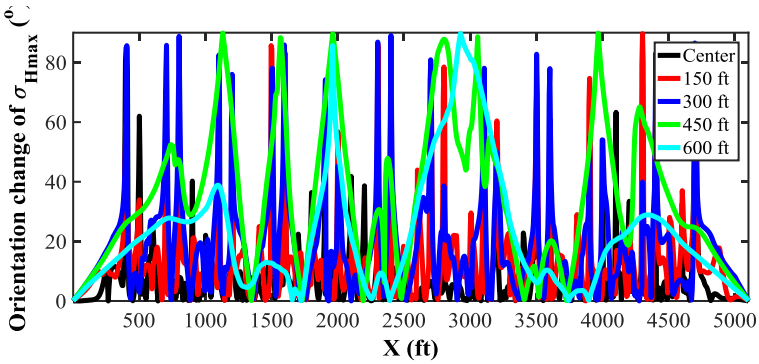

(b) Orientation change of maximum horizontal principal stress for low permeability reservoir (30 nd) along x-axis at different distances from well in y-direction at 1 year

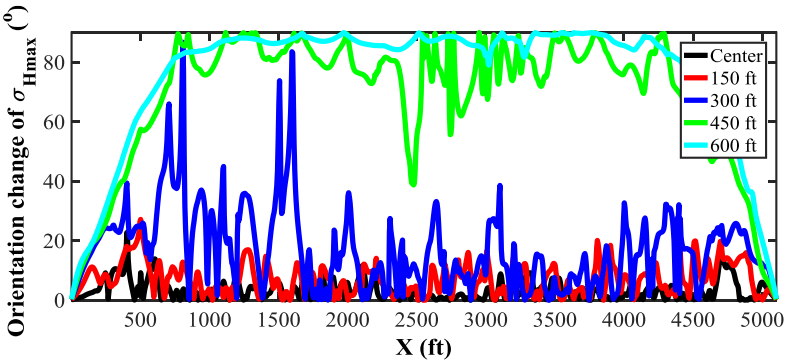

(c) Orientation change of maximum horizontal principal stress for low permeability reservoir (30 nd) along x-axis at different distances from well in y-direction at 5 years

Figure 3.22. Orientation change of maximum horizontal principal stress along x-direction at different distances from well in the y-direction with low reservoir permeability at 0.5 (a), 1 (b), and 5 years (c) (Sangnimnuan et al. 2018b).

Cumulative oil production for a case with low reservoir permeability is compared with a case with high reservoir permeability for both cases; with and without natural fractures as shown in Figure 3.23. Without natural fractures, production increases by around 50% when permeability is enhanced from 30 nd to 300 nd. However, only 41% production increase is observed when increasing permeability 10 times for the case with natural fractures. This is due to the presence of natural fractures, which significantly increase production rate even at low permeability case, by increasing the size of the depleted area.

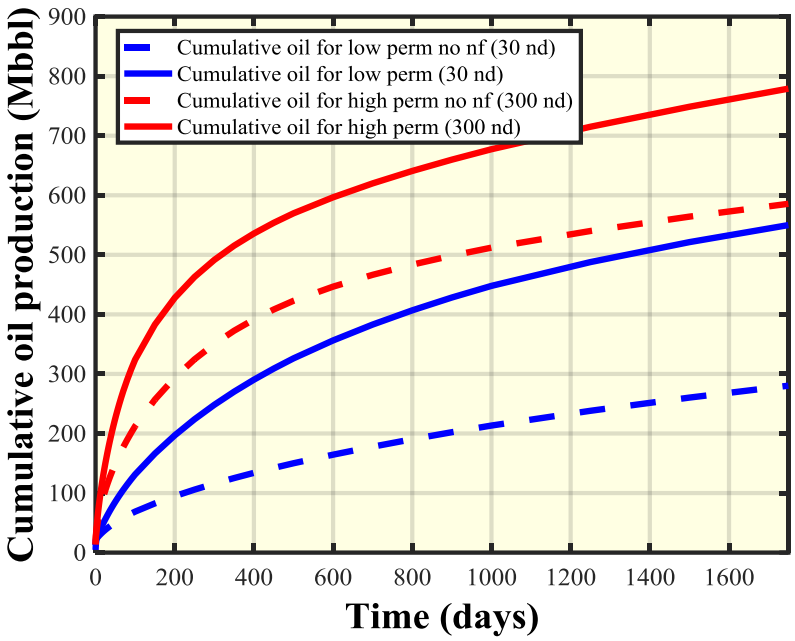

Figure 3.23. Cumulative oil production for low permeability reservoir (30 nd) and base case (300 nd) (Sangnimnuan et al. 2018b).

3.5 Conclusions

The EDFM with geomechanics and fluid flow was further modified from the one described in chapter 2 to be able to simulate multiple natural fractures representing a highly fractured reservoir for refracturing application. The modified model was used to simulate the poroelastic

effect in a highly fractured reservoir with heterogeneous natural fracture distribution to study stress redistribution and evolution for refracturing in unconventional reservoirs with limited size. Effect of boundary condition has been studied due to reservoir size used in this study and it was found that boundary conditions do affect stress redistribution more or less depending on reservoir properties; specifically DS. It is acceptable to use small size reservoirs for our base case as boundary effect is insignificant. Case studies are based on liquid-rich shale reservoir data and involve variations of parameters, affecting stress evolution; i.e. density of natural fractures, hydraulic fracture spacing, as well as reservoir permeability. The key conclusions can be summarized as below:

1. Different natural fracture densities produce distinct stress fields and stress evolution. The presence of natural fractures changes the shape of the depleted area from rectangular with longer distance in y or σ_{Hmax} direction to rectangular with longer distance in x or σ_{hmin} direction, resulting in less stress reorientation and more complex stress distribution in SRV region. However, stress reversal can still be observed outside the SRV region just like the case without natural fractures.
2. The presence of natural fractures, large fracture spacing, and low reservoir permeability can cause a delay in stress reorientation. Stress can also rotate back to its original direction depending on natural fracture distribution, hydraulic fracture spacing, and reservoir permeability.
3. Differential in-situ stress (DS) is also important when it comes to stress redistribution as the smaller the DS, the easier the stress would redistribute. Stress reversal occurs as early as 0.5 years and at any distance from well outside SRV region at low DS (100 psi), while at high DS

(500 psi), stress reversal can only be observed at a later time (5 years) and only at distance 600 ft in the y-direction from well based on case studies in this paper.

4. Results from Roussel et al. (2013), which uses k_{srv} instead of modeling natural fractures, suggest that stress reorientation can occur inside SRV region at early time (0.5 year), which is different from our 200-ft case, where almost no stress redistribution can be observed inside SRV region due to presence of natural fractures. However, at 1 year of production onwards, our result is in good agreement with Roussel's, in which stress redistribution can only be observed outside the SRV region.
5. Natural fractures also contribute to production. The presence of natural fractures results in less production increase when reducing hydraulic fracture spacing from 200 to 30 ft. At larger spacing (200 ft), natural fractures contribute more to production gain compared with small spacing (30 ft). On the other hand, natural fractures contribute less to production gain when increasing reservoir permeability from 30 nd to 300 nd.
6. There exists a critical time during production when refracturing can be performed successfully. This critical time is subject to natural fracture distribution, fracture spacing, differential in-situ stress, and reservoir permeability. Beyond this time, a new fracture from refracturing between original fractures in the same stage or at the same location as original fractures may not be able to propagate to undepleted areas in the reservoir and may intersect original fractures due to stress reversal. If refracturing time is predetermined, well candidates can then be selected based on well configuration, heterogeneity of the reservoir as well as reservoir properties. Optimum refracturing locations can subsequently be chosen in order to ensure the success of refracturing and maximizing production gain.

The results obtained from our model indicate that it is important to include natural fractures when simulating stress evolution for refracturing and infill well completion in unconventional reservoirs as most of these reservoirs are highly fractured. Natural fractures increase depleted size and shape and thus change the critical time as well as optimum location to perform refracturing, which is totally different from the case without natural fractures. Other factors, i.e. hydraulic fracture spacing, differential in-situ stress, and reservoir permeability should also be taken into consideration when a well is selected to perform refracturing. These findings can provide not only a fundamental guideline for candidate selection when refracturing in order to optimize production gain, but also open a new possibility for understanding how stress evolves throughout the production period in highly fractured reservoirs.

CHAPTER 4: STRESS CHANGE ANALYSIS IN A MULTI-PAYZONE RESERVOIR (FOR INFILL WELL COMPLETION)

4.1 Introduction

Growth in a number of newly drilled wells in unconventional reservoir development results in tightly spaced horizontal wells, which consequently creates well interference (fracture hits) between parent and infill wells. This directly affects the production performance of both parent and infill wells. In order to minimize this effect, it is sometimes more preferable to place an infill well in a different pay zone. However; due to the poroelastic effect, pressure depletion from the parent well also affects stress distribution in different pay zones and yet only a few literatures focus on this effect. The main objective of this chapter is to predict temporal and spatial evolution of stress field for the Permian basin using an in-house 3D reservoir-geomechanics model and propose guidelines for determining sequence of stacked pay.

In this chapter, a 3D reservoir containing multiple payzones based on Permian basin data is to be simulated. The depletion-induced stress change in each payzone is to be observed in this study. The study includes effect of well layout (parent wells located in same (Wolfcamp B2) and different payzone (Wolfcamps A2 and B2), fracture penetration (to another payzone), fracture geometry, and presence of natural fractures. Boundary effect is included by increasing reservoir size to include non-payzone part. The results observed in this study is to be adjust sequence of stacked pay, which may have to be changed from lateral to vertical well layout and mitigate well interference to improve production performance.

Part of this section is reprinted with permission from "Impact of Parent Well Depletion on Stress Changes and Infill Well Completion in Multiple Layers in Permian Basin" by Sangnimnuan, A., Li, J., Wu, K., and Holditch S, 2019. Unconventional Resources Technology Conference, Denver Colorado, USA, 22-24 July, whose permission is required for further use.

4.2 Case studies

The main focus of this study is on the effect of reservoir depletion on stress reorientation in a multi-zone reservoir based on Permian basin data. The reservoir consists of 6 pay zones, Wolfcamps A1-A3, and B1-B3. Parent wells are located in layers B2 and A2. Each well consists of 5 stages with 4 fractures per stage. The fracture spacing is 15 m. Distance between two wells measured in the horizontal direction is 300 m. For geomechanics part, the constraint boundary condition is applied to 5 boundaries including two in the x-direction, two in the y-direction and one in the z-direction. Overburden stress is applied on the top of the reservoir. No flow boundary is applied to all 6 boundaries for fluid flow part. Numbers of cells in x, y, and z directions are 311, 641, and 8 respectively with Dx = 1.5 m, Dy = 1.5 m, and Dz = reservoir thickness in each layer. Only one cell in the z-direction is used in all layers but B2, in which 3 cells are used. Schematic diagram of the reservoir and reservoir properties can be found in Figure 4.1 and Tables 4.1 and 4.2.

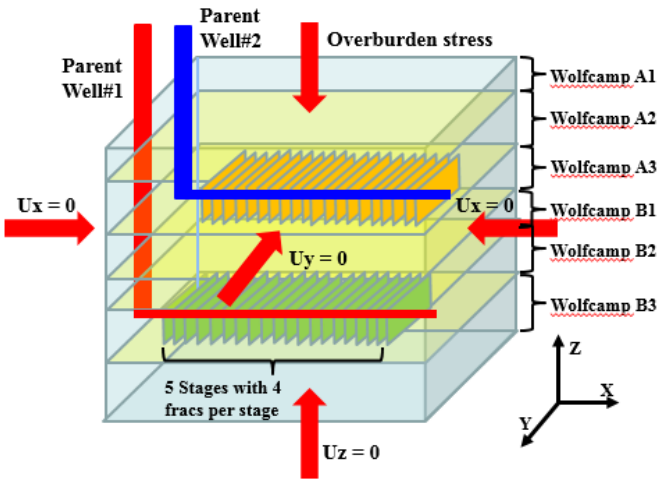

Figure 4.1. 3D diagram of the reservoir used in this study (Sangnimnuan et al. 2019b).

Rock Formation (Wolfcamp)	Young's Modulus (GPa)	Thickness (m)	Porosity (%)	Perm (nd)
A1	22.4	4.77	6.46	57.3
A2	20.8	13.6	5.59	61
A3	20	8.29	6.23	210
B1	20.7	4.68	9.09	449
B2	21.4	22.25	9.3	561
B3	21.7	28.91	7.44	372

Table 4.1. Rock properties at different layer (Sangnimnuan et al. 2019b).

Input Parameter	Unit	Value
Initial reservoir pressure (p)	MPa	32.8
Bottomhole pressure (p_b)	MPa	6.89
Fluid viscosity (μ_f)	Pa.s	0.001
Fluid compressibility (c_f)	Pa^{-1}	3e-9
Poisson's ratio (ν)	-	0.26-0.29
Biot's coefficient (b)	-	1
Initial stress in x direction ($S_{xx,0}$)	MPa	41.34
Initial stress in y-direction ($S_{yy,0}$)	MPa	44.1
Initial stress in z direction ($S_{zz,0}$)	MPa	55.12
Overburden stress (S_{zz})	MPa	55.12
Initial differential stress (DS)	MPa	2.76

Table 4.2. Reservoir properties applied to all layers (Sangnimnuan et al. 2019b).

Case studies include the effect of well layout in which parent wells are to be located in different layers, B2 and A2 (case 1) and the same layer, B2 (case 2), fracture penetration (case 3), fracture length (case 4), and natural fractures (case 5). The two-parent wells are to be located in layer A2 and B2 for all cases except case 2, in which both wells are to be located in layer B2 as shown in Figure 1 and will be under production for 5 years. Fractures from both parent wells were created using our in-house complex fracture propagation model (Wu and Olson, 2015a and 2015b) based on reservoir properties shown in Tables 1 and 2. Fracture half-length is around 108 m for the longer ones and the shorter ones are about one-third to half of the longer ones. Fractures are in the direction of S_{Hmax} or S_{yy} direction and perpendicular to the direction of S_{hmin} or S_{xx} direction as

shown in Figure 4.2. The initial magnitude of S_{Hmax} is the same as S_{yy} and S_{hmin} is the same as S_{xx} Infill well is to be placed in the layer A3 between 2 parent wells as shown in Figure 3b. Change of orientation of S_{Hmax} and magnitude of S_{xx} is to be observed along the path of target infill well at different times. In addition, change of stress orientation along fracture tips in the layer B2 is also observed for cases 1 and 2 to better understand fracture hits induced by parent well in different well layouts.

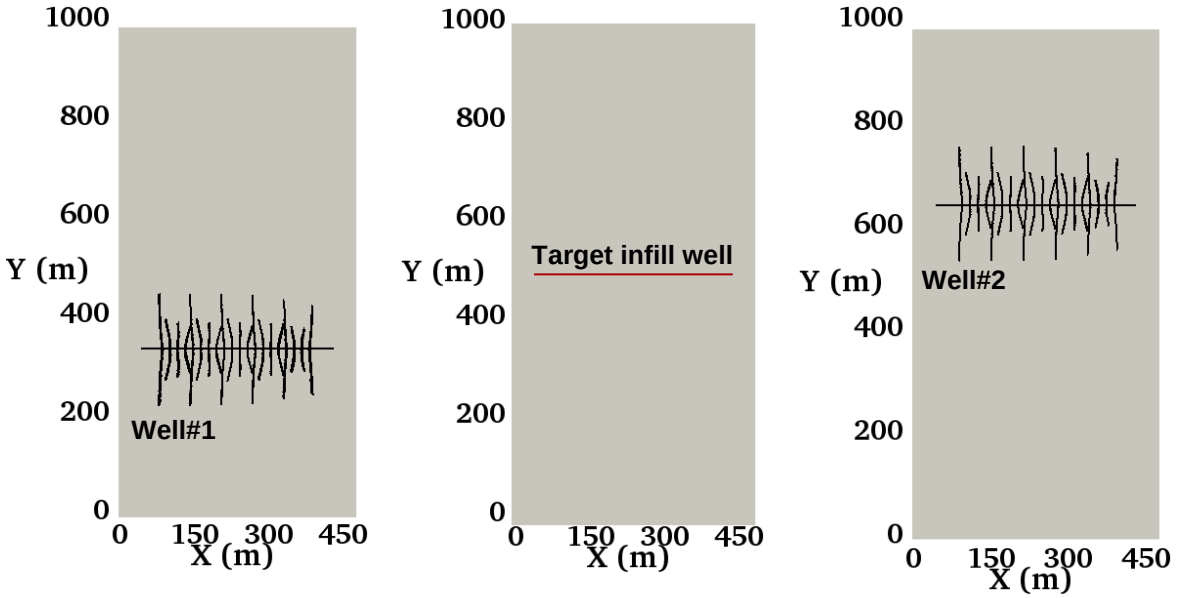

a) Cross-section of layer B2 for case 1

b) Cross-section of layer A3 for case 1

c) Cross-section of layer A2 for case 1

Figure 4.2. Well configuration in 2D at different layers for all cases but case 2 including location of target infill well in layer A3 (Sangnimnuan et al. 2019b).

4.2.1 Case 1: Two parents well located in different payzones

One parent well is located in layer B2 and another is in A2 with the well spacing being 300 m. The fractures are assumed to be contained in the same layer as the well and have the same height as layer thickness. The 3D schematic diagram for well layout and fracture locations can be shown in Figure 4.3. Pressure distribution showing depleted zone (SRV) around fractures in well#1

in the 3D plot after 5 years of production along with the direction of S_{Hmax} in layer B2 can be found in Figure 4.4.

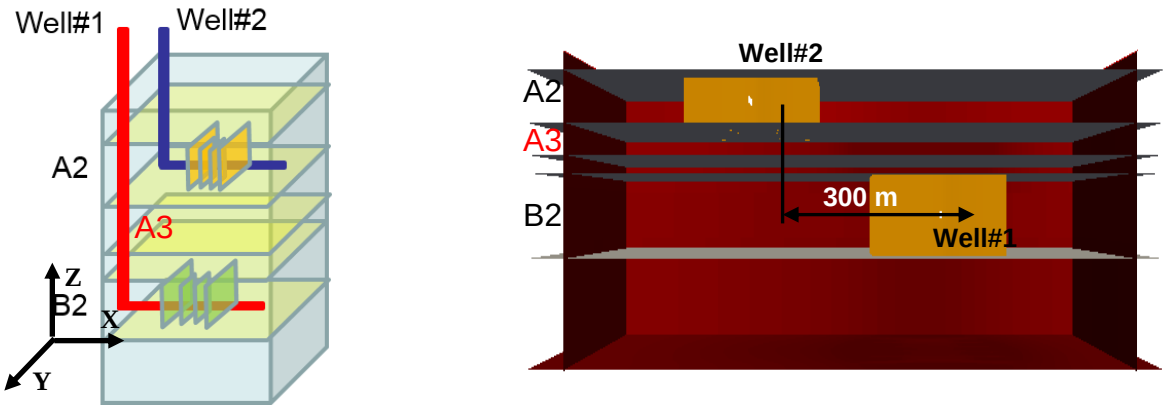

a) 3D Schematic diagram

b) Y-Z plane of reservoir showing fractures of both wells

Figure 4.3. 3D schematic diagram of well layout for case 1 (Sangnimnuan et al. 2019b).

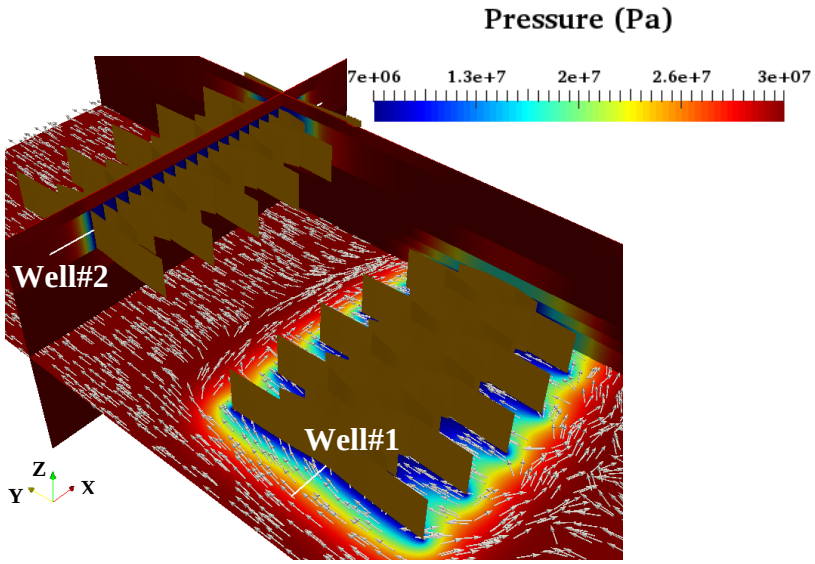

Figure 4.4. 3D pressure distribution showing fracture geometries for both wells with orientation of S_{Hmax} (shown in white dash lines) in layer B2 (Sangnimnuan et al. 2019b).

Figure 4.5 depicts the orientation of S_{Hmax} in layer B2 for well#1 after 2 and 5 years of production. Dash lines shown in the figure represent the orientation of S_{Hmax} and the color gradients

represent the magnitude of S_{xx} in which the initial magnitude is 41.34 MPa (refer to Table 4.2). Stress reversal or 90^o change in orientation of S_{Hmax} can be observed along each fracture at 2 years as a result of a decrease in S_{yy} and S_{xx}. Once S_{yy} becomes smaller than S_{xx} stress reversal occurs, meaning that the decrease in S_{yy} is much larger than S_{xx}. Stress reversal around the fracture tips can also be observed, which suggests the possibility of fracture hits once the fractures from infill well that is completed in the same layer (B2) reach the SRV zone. In contrast, increase in S_{xx} magnitude can be observed in layer A2 while the present well (well#2) is only located in layer A2, indicating the effect of reservoir depletion on stress reorientation in different layers. This is because the reservoir is being depleted in layer A2 but causing a change in the magnitude of S_{xx} in layer B2. After 5 years of production, strong stress reversal can be observed around fracture tips (Figures 4.4 and 4.5) due to larger depletion in the SRV zone, while stress inside SRV zone reverts back to its original direction as S_{xx} becomes smaller than S_{yy}. Detailed discussion regarding mechanism of stress reorientation due to reservoir depletion can be found in Sangnimnuan et al. (2018b).

Reservoir depletion in layers B2 and A2 causes the change in magnitude of S_{xx} and in orientation of SHmax as shown in Figure 4.6. Specifically, after 2 years of production, there is an increase in S_{xx}, which can be observed in the areas parallel to the well#1 (B2) and well#2 (A2). Since there is barely any stress reorientation in these areas, it implies that Syy also increases. This is to support the decrease of pressure in layers B2 and A2, where parent wells are located. After 5 years of production, both S_{xx} and S_{yy} start to decrease as the entire reservoir starts to deplete more not only just layers B2 and A2. Some of the orientation changes can be observed along the target infill zone (location of target infill zone can be found in Figure 2b) due to less decrease of S_{xx}

compared to S_{yy}. Results observed from this case suggest that fractures from infill well in layer A3 will only be affected by stress reorientation only after 5 years of production.

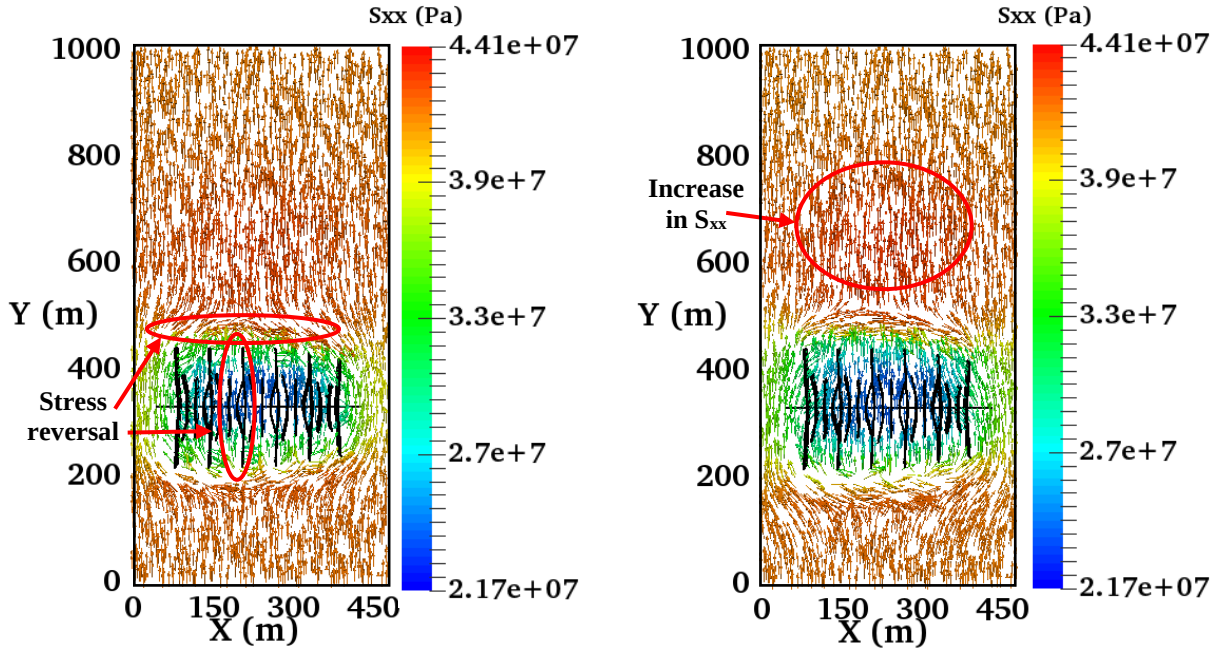

a) Orientation of S_{Hmax} in layer B2 after 2 years

b) Orientation of S_{Hmax} in layer B2 after 5 years

Figure 4.5. Orientation of S_{Hmax} in the layer B2 after 2 years and 5 years of production (Sangnimnuan et al. 2019b).

Reservoir depletion in layers B2 and A2 causes the change in magnitude of S_{xx} and in orientation of SHmax as shown in Figure 4.6. Specifically, after 2 years of production, there is an increase in S_{xx}, which can be observed in the areas parallel to the well#1 (B2) and well#2 (A2). Since there is barely any stress reorientation in these areas, it implies that Syy also increases. This is to support the decrease of pressure in layers B2 and A2, where parent wells are located. After 5 years of production, both S_{xx} and S_{yy} start to decrease as the entire reservoir starts to deplete more not only just layers B2 and A2. Some of the orientation changes can be observed along the target infill zone (location of target infill zone can be found in Figure 2b) due to less decrease of S_{xx}

compared to S_{yy}. Results observed from this case suggest that fractures from infill well in layer A3 will only be affected by stress reorientation only after 5 years of production.

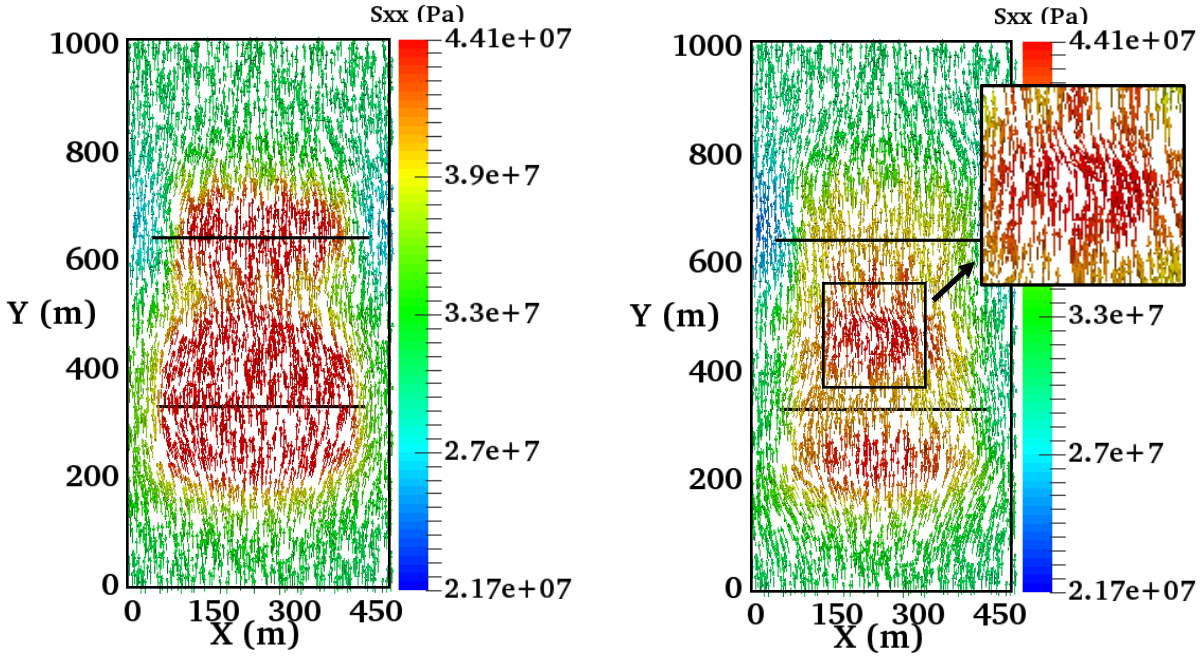

a) Orientation of S_{Hmax} in layer A3 after 2 years b) Orientation of S_{Hmax} in layer A3 after 5 years

Figure 4.6. Orientation of S_{Hmax} in the layer A3 after 2 and 5 years of production (Sangnimnuan et al. 2019b).

4.2.2 Case 2: Two-parent wells located in the same payzone

In this case, two-parent wells are located in the same layer (B2) with the same well spacing (300 m). The goal is to understand how changing the well layout from vertical to lateral will affect stress reorientation. A 3D schematic diagram for well layout and fracture locations is shown in Figure 4.7. Pressure distribution showing depleted zone (SRV) around fractures in well#1 and well#2 in 3D after 5 years of production along with the direction of S_{Hmax} in layer B2 can be found in Figure 4.8.

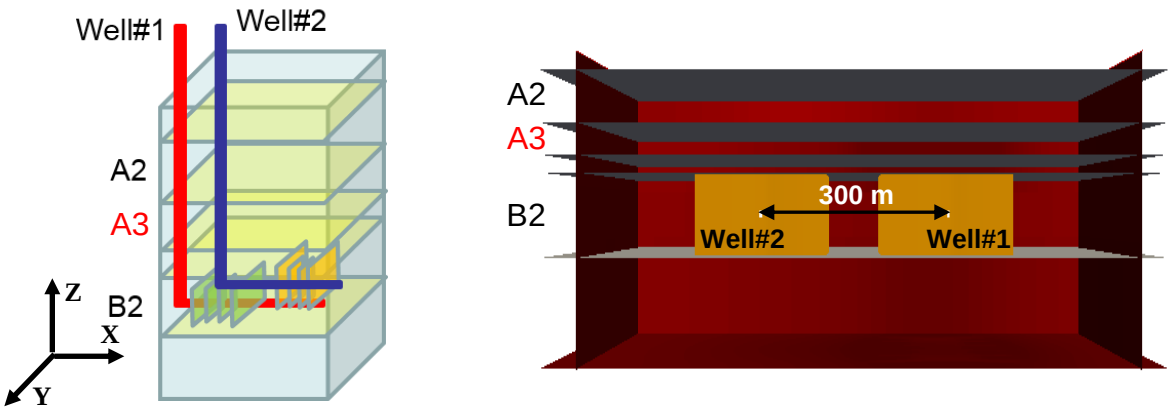

a) 3D Schematic diagram b) Y-Z plane of reservoir showing fractures of both wells

Figure 4.7. 3D schematic diagram of well layout for case 2 (Sangnimnuan et al. 2019b).

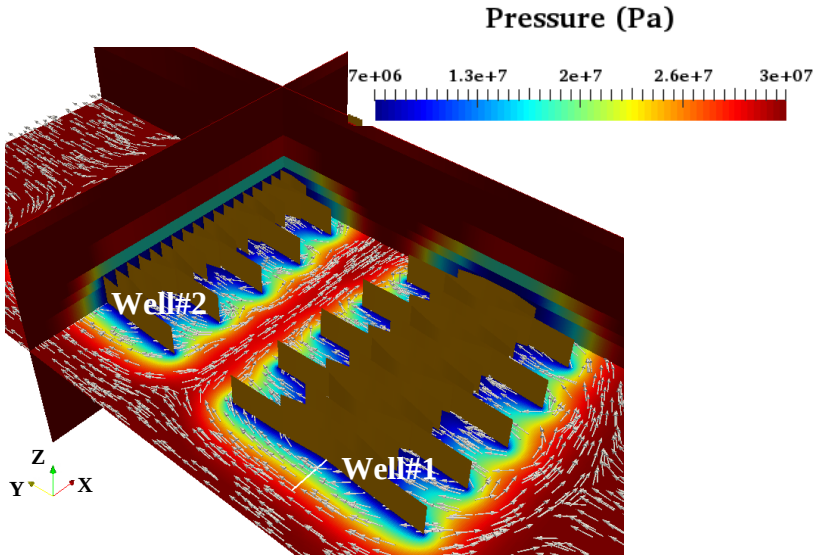

Figure 4.8. 3D pressure distribution showing fracture geometries for both wells with orientation of S_{Hmax} (shown in white dash lines) in layer B2 (Sangnimnuan et al. 2019b).

Similar to case 1, the orientation of S_{Hmax} in layer B2 for both well#1 and well#2 is shown in Figure 4.9. Dash lines shown in the figure represent the orientation of S_{Hmax} and the color gradients represent the magnitude of S_{xx}. Stress reversal or 90° change in orientation of S_{Hmax} can be observed along each fracture at 2 years as a result of a decrease in S_{yy} and S_{xx}. Having two wells depleted at the same time causes much more noticeable stress reversal around fracture tips at the

zone between the two wells compared to case 1, which contains only one well in layer B2. Pressure reduction in SRV zone directly reduces the magnitude of S_{yy} in this zone, resulting in a decrease in S_{Hmax} in the zone between two wells leading to stress reversal. After 5 years of production, the results are similar to case 1, in which stronger stress reversal can be observed in the area between two wells and stress reversal inside SRV zone is no longer present.

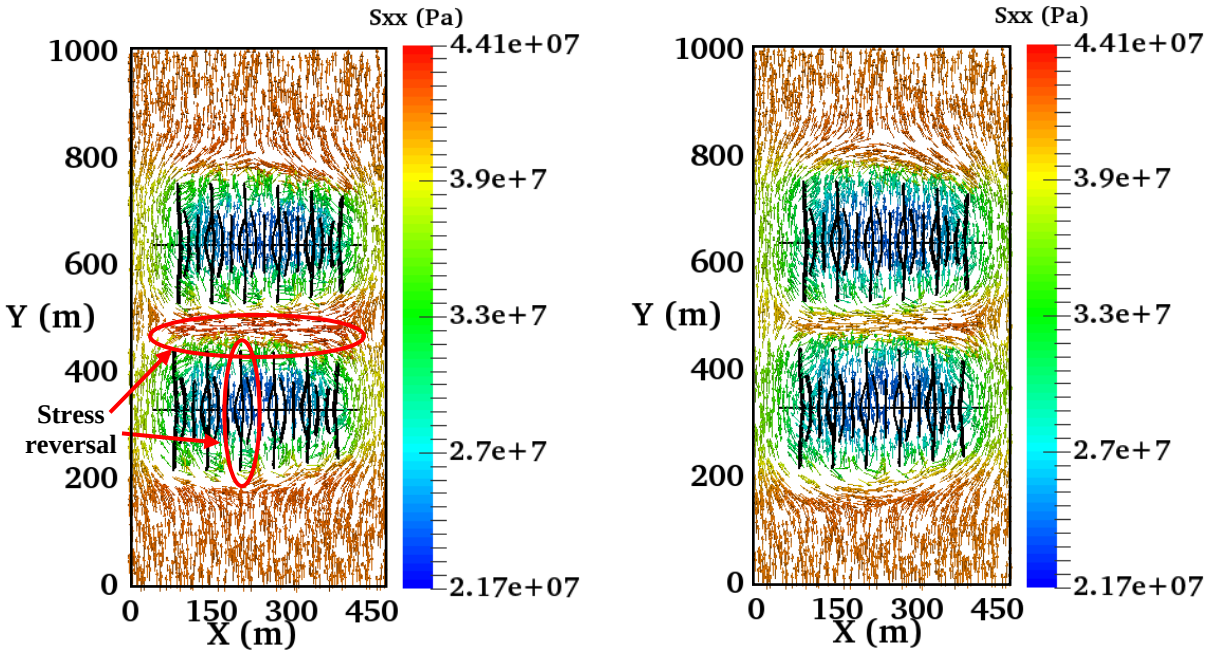

a) Orientation of S_{Hmax} in layer B2 after 2 years b) Orientation of S_{Hmax} in layer B2 after 5 years

Figure 4.9. Orientation of S_{Hmax} in the layer B2 after 2 years and 5 years of production (Sangnimnuan et al. 2019b).

Stress reorientation can also be observed in layer A3 despite not having any producing well there. This is due to reservoir depletion in layer B2, which causes the change of S_{xx} in magnitude and S_{Hamx} in orientation in this layer as shown in Figure 4.10. After 2 years of production, increase in S_{xx} can be observed in layer A3 to support the decrease of pressure in layers B2. No stress reversal can be observed at this time just like case 1 as S_{yy} is still larger than S_{xx}. However, after 5 years of production, both S_{xx} and S_{yy} start to decrease as the reservoir depletes more not only just

layers B2 and A2. Stress reversal can be seen along the target infill zone in layer A3, which is similar to layer B2 suggesting that S_{yy} decreases at a faster rate than S_{xx} and eventually becomes smaller than S_{xx}. The trend of stress reorientation in layer A3 for this case is similar to case 1 except that stress reversal can be observed as a result of producing two wells at the same layer.

Figure 4.11 provides a quantitative comparison between case 1 and case 2 for orientation change of S_{Hmax} and change in the magnitude of S_{hmin} along with target infill well in layer A3. After 2 years of production, orientation change for both cases are insignificant as also shown in Figures 4.5 and 4.9; however, after 5 years of production, orientation change for case 2 becomes almost 90^o at the middle, while case 1 still shows small change. This can be confirmed with the plot of S_{hmin}, in which case 2 shows a much larger increase in S_{hmin} (around 2.5 MPa in the middle) causing stronger stress reorientation compared to case 1. Results observed from this case suggest that producing two-parent wells in different layers causes less influence in other layers that are not yet under production (layers A1, A3, B1, and B3), which seems to be a better option for infill well completion in multi-zone reservoirs.

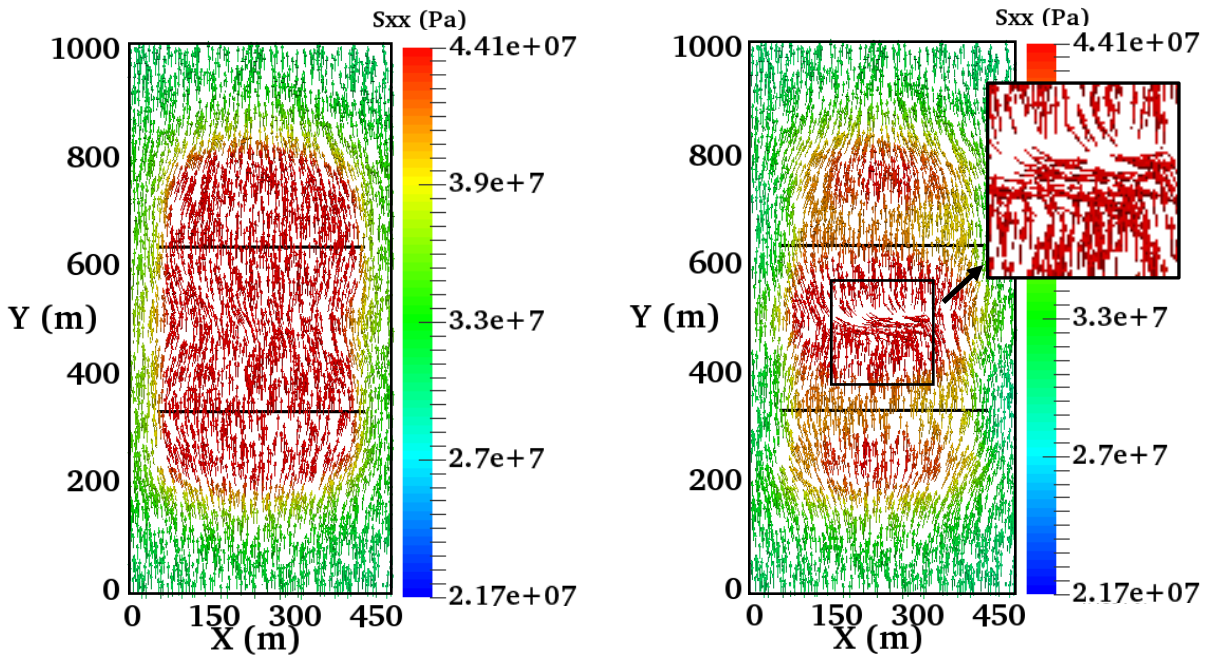

a) Orientation of S_{Hmax} in layer A3 after 2 years b) Orientation of S_{Hmax} in layer A3 after 5 years

Figure 4.10. Orientation of S_{Hmax} in the layer A3 after 2 and 5 years of production (Sangnimnuan et al. 2019b).

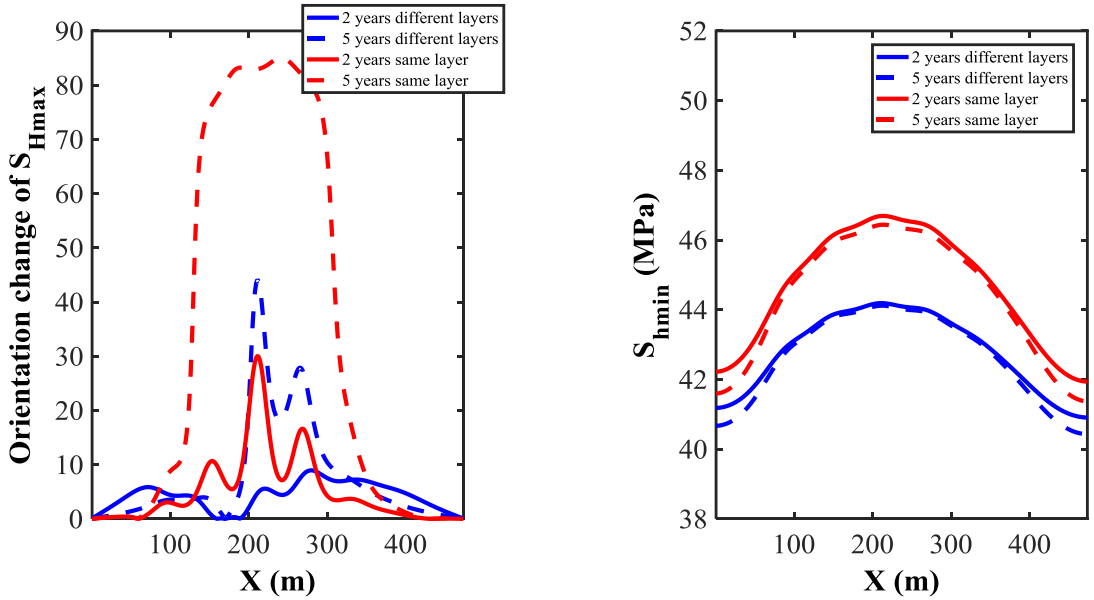

a) Orientation of S_{Hmax} along target infill well b) Magnitude of S_{hmin} along target infill well

Figure 4.11. Orientation change of S_{Hmax} and magnitude of S_{hmin} along target infill well in layer A3 at different times for case 1 and case 2 (Sangnimnuan et al. 2019b).

4.2.3 Case 3: Effect of fracture penetration

In this case, fractures configuration and layout are the same as case 1 but the fractures in layer B2 are assumed to penetrate to layer B1 due to weak bedding (Tang et al., 2017, 2018) as shown in Figure 13. For the previous two cases, it is assumed that the stress barrier does exist and prevents fractures in layer B2 from propagating upwards and penetrating to another zone. The aim of this case is to study how the penetration of fractures affect stress reorientation in layer A3.

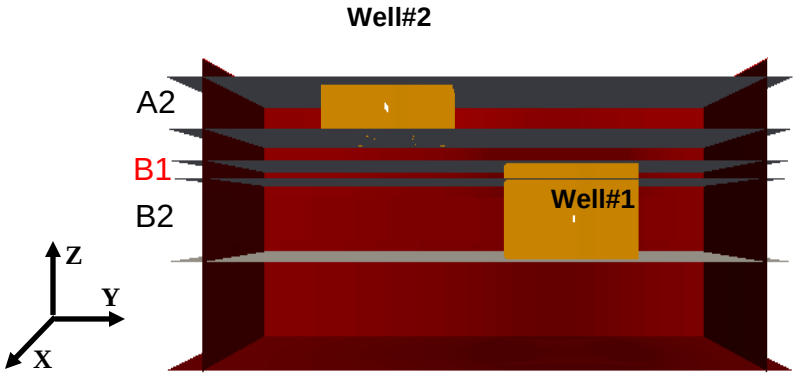

Figure 4.12. Y-Z plane for fractures of both wells case 3 (Sangnimnuan et al. 2019b).

Penetrated fractures yield a larger depletion rate in layer B1, which eventually causes the increase in S_{xx} as shown in Figure 4.13. The Figure shows the orientation of S_{xx} along with the magnitude of S_{xx} after 2 and 5 years of production. As mentioned in previous cases, increase in S_{xx} is a result of pressure depletion in layer A2 and B1 (only for this case due to fracture penetration). Only small changes of orientation can be observed after 2 years of production especially in the target infill well zone (between two-parent wells). However, stress reversal can be observed after 5 years of production in the same zone. This is due to larger depletion along with both wells (from layer B2 and A2) causing S_{yy} to decrease faster than S_{xx} in the target infill zone. The results observed from this case suggest that fracture penetration plays a significant role in stress orientation in different layers and can redirect fractures from infill well to propagate to undesired areas of the reservoir. A quantitative comparison in terms of change in orientation of

S_{Hamx} and magnitude of S_{hmin} in layer A3 between case 1 and case 2 can be shown in Figure 4.14. Orientation change is minimal after 2 years of production for both cases. On the other hand, orientation change for case 3 becomes much stronger compared to case 1 and stress reversal can be observed (Figures 4.13b and 4.14a). Despite having completely different orientation of S_{Hmax} after 5 years of production, both cases yield similar stress change in magnitude (Figure 4.14b) at both 2 and 5 years of production. This confirms that orientation change, in this case, is not caused by the increase in S_{hmin} but rather the decrease of S_{yy}. The large decrease in S_{yy} is mainly due to faster depletion rate in layers B2 and B1 (fracture penetration from B2). Results observed from this case suggest that fracture penetration negatively contributes to stress reorientation in multi-layer reservoirs and should be included in the study if the stress barrier does not exist.

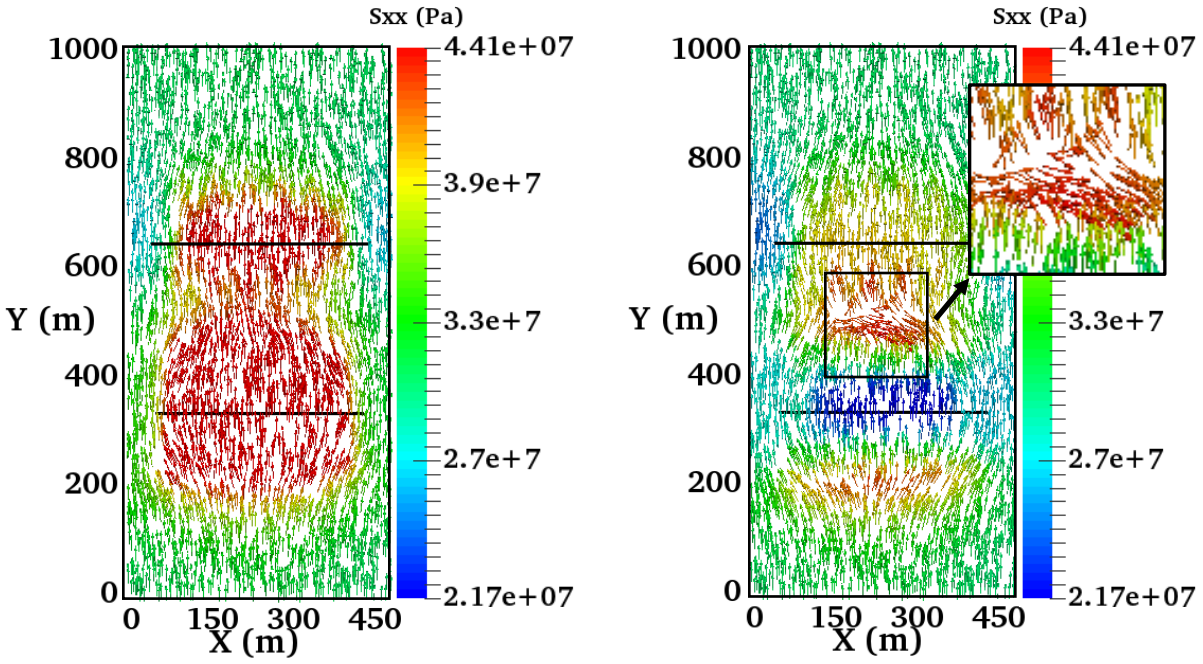

a) Orientation of S_{Hmax} in layer A3 after 2 years b) Orientation of S_{Hmax} in layer A3 after 5 years

Figure 4.13. Orientation of S_{Hmax} in the layer A3 after 2 and 5 years of production (Sangnimnuan et al. 2019b).

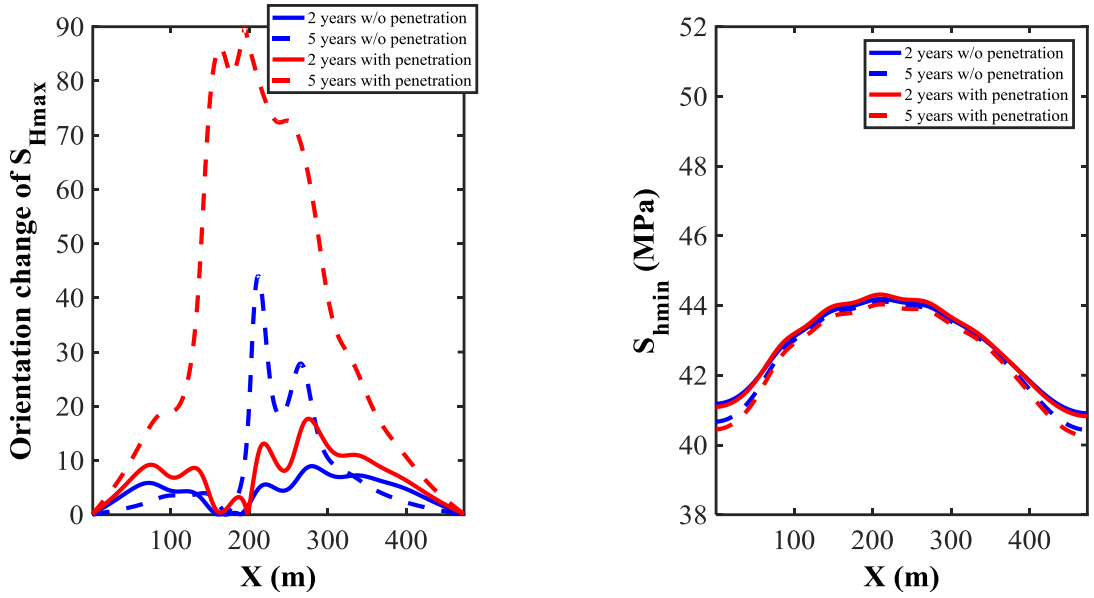

a) Orientation of S_{Hmax} along target infill well b) Magnitude of S_{hmin} along target infill well

Figure 4.14. Orientation change of S_{Hmax} and magnitude of S_{hmin} along target infill well in layer A3 at different times for case 1 (no penetration) and case 3 (with penetration) (Sangnimnuan et al. 2019b).

4.2.4 Case 4: Effect of fracture length

Effect of fracture length on stress reorientation in multi-zone reservoirs is to be studied in this section. The Well layout is the same as case 1 where one well is located in layer B2 and another is in A2. Fractures were created in the same manner as case 1 except that the leak-off coefficient in fracture propagation model is reduced by half, yielding longer fracture length. Short and long fractures can be observed in the same stage due to stress shadowing effect. The average of fracture half-length for longer fractures is around 219 m. while the average half-length for longer fractures in case 1 is only 108 m. Y-Z plane showing well locations as well as fracture geometries can be found in Figures 4.15 and 4.16, respectively.

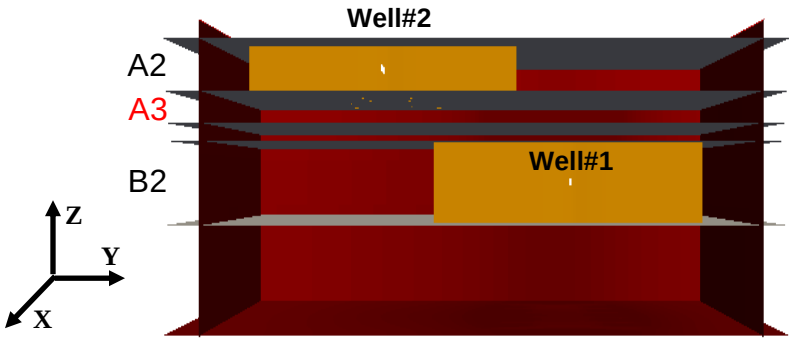

Figure 4.15. Y-Z plane of fractures of both wells for case 4 (Sangnimnuan et al. 2019b).

Figure 4.16 shows the orientation of S_{Hmax} and magnitude of S_{xx} in layer B2 and A2 after 2 years of production. Overall stress reorientation is similar to case 1, in which stress reversal can be observed around fracture tips and along each fracture. Stress reversal observed in this case is due to a decrease rate of S_{yy}, which is much faster than S_{xx} along each fracture. This can also cause fracture hits if infill well is completed in the same layer (B2). S_{xx} also increases in layer B2 to support pressure depletion in layer A2. This observation is similar to all other previous cases. After 5 years of production, stress reversal along each fracture can still be observed mostly at the outer fractures (most left and most right ones), meaning that S_{yy} still decreases at a faster rate than S_{xx}. The presence of stress reversal suggests a completely different result from case 1, in which stress reversal no longer exists at 5 years. This largely because of the length of the fracture, which allows S_{yy} to decrease at a faster rate than S_{xx} for a longer period of time compared to case 1. The result observed in this case suggests that infill well completion may have to be performed after at a later time (after 5 years) compared to case 1 if the fracture length becomes longer in order to avoid fracture hits.

When it comes to stress orientation in layer A3, a very small change of orientation can be observed along target infill well zone (Figure 4.17a) even after 5 years of production compared with case 1 as a result of fracture overlapping between wells in layers A2 and B2. This result

causes a significant increase in both S_{xx} and S_{yy} to support pressure depletion in both layers A2 and B2 preventing stress reorientation to occur. Figure 18b shows a large increase of S_{xx} along with target infill well in layer A3 compared to case 1 at both 2 and 5 years of production.

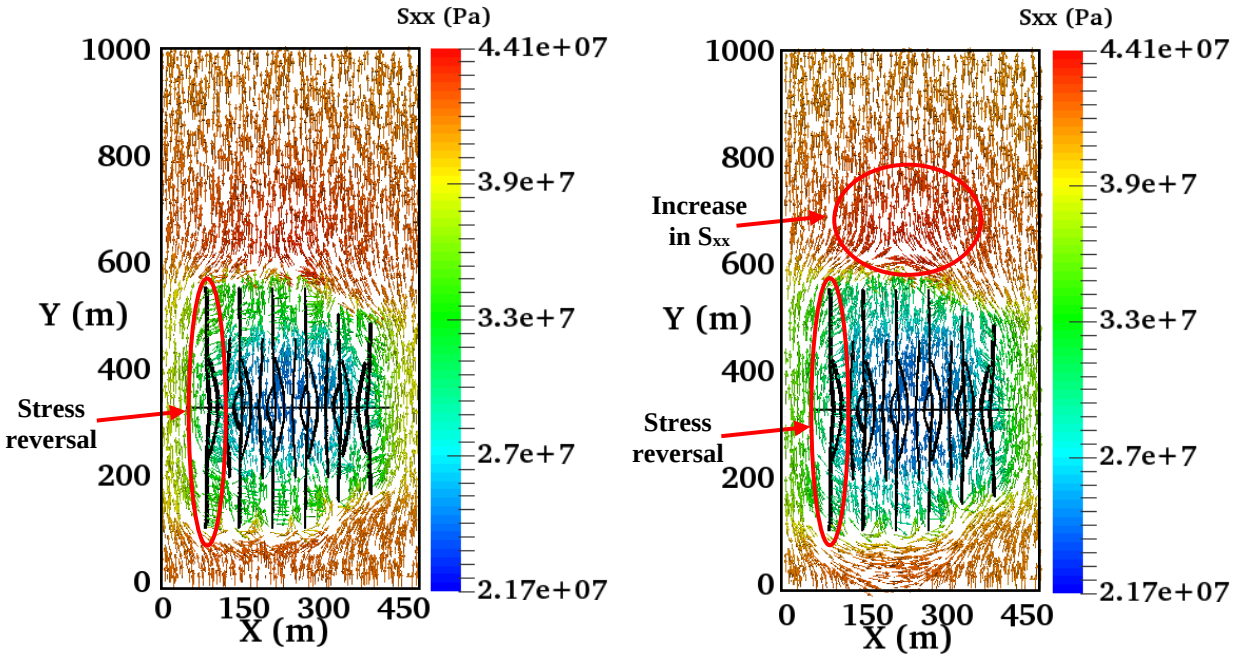

a) Orientation of S_{Hmax} in layer A2 after 2 years b) Orientation of S_{Hmax} in layer B2 after 5 years

Figure 4.16. Orientation of S_{Hmax} in layer B2 after 2 years and 5 years of production (Sangnimnuan et al. 2019b).

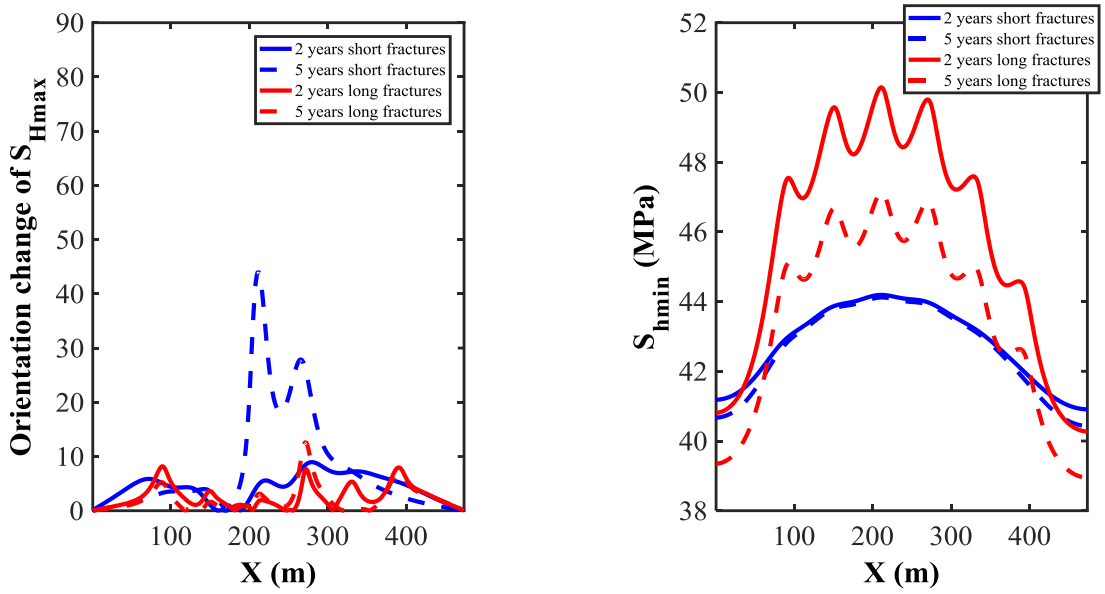

a) Orientation of S_{Hmax} along target infill well b) Magnitude of S_{hmin} along target infill well

Figure 4.17. Orientation change of S_{Hmax} and magnitude of S_{hmin} along target infill well in layer A3 at different times for case 1 (shorter fractures) and case 4 (longer fractures) (Sangnimnuan et al. 2019b).

4.2.5 Case 5: Effect of natural fractures

In this case, the reservoir is assumed to contain several activated natural fractures, which directly affects the heterogeneity of stress field after production. Natural fractures were included when simulating the propagation of hydraulic fractures from parent well, resulting in much more complex fracture geometries. The average fracture half-length is around 108 m, which is similar to case 1. One parent well is located in layer B2 and another is in layer A2. Y-Z plane showing well locations and fracture geometries in the X-Y plane can be found in Figures 4.18 and 4.19, respectively.

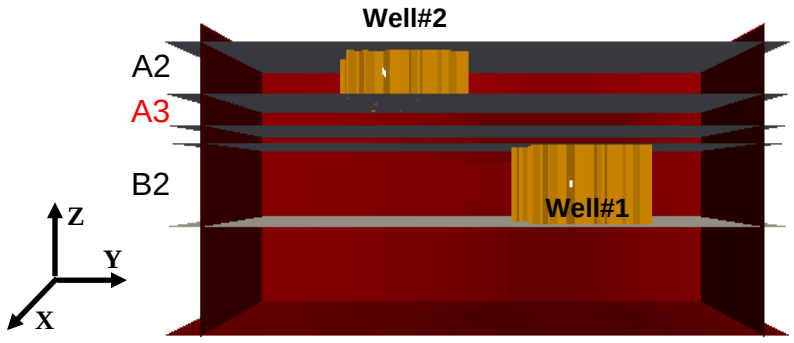

Figure 4.18. Y-Z plane of fractures of both wells for case 5 (Sangnimnuan et al. 2019b).

Active natural fractures can be observed in Figure 4.19, showing pressure distribution in layers B2 and A2 after 2 years of production along with hydraulic fractures. Active natural fractures are more noticeable in layer A2 due to its low reservoir permeability. These natural fractures not only change fracture geometries but also creates a more complex stress field as shown in Figure 4.20. Similar to previous cases, Figure 4.20 depicts the orientation of S_{Hmax} and magnitude of S_{xx} after 2 and 5 years of production in Wolfcamp B2. Even as early as 2 years of production, no stress reversal along each fracture is observed considering everything else but fracture geometry is the same as case 1, in which stress reversal can be easily observed at 2 years. Incorporating natural fractures in the fracture propagation and reservoir-geomechanics model yields more complex fracture geometries, and thus increasing depletion rate. Consequently, this reduces both S_{xx} and S_{yy} at a similar rate, preventing stress reversal to occur. However, stress reversal can still be observed only along fracture tips at both 2 and 5 years of production.

As shown in Figure 4.21, orientation change of S_{Hmax} along target infill well in layer A3 becomes stronger when natural fractures are incorporated in the simulation at both 2 and 5 years of production in comparison to case 1. A significant increase of stress reorientation along target infill well after 5 years of production can be observed even though the magnitude of S_{hmin} is similar to case 1 (Figure 4.21b). This confirms that natural fractures help increase depletion rate, causing

S_{yy} outside SRV zone to decrease faster than S_{xx}, and thus creating stress reversal. Based on this result, incorporating natural fractures is important for highly fractured reservoirs as the stress reorientation in multiple layers can change significantly.

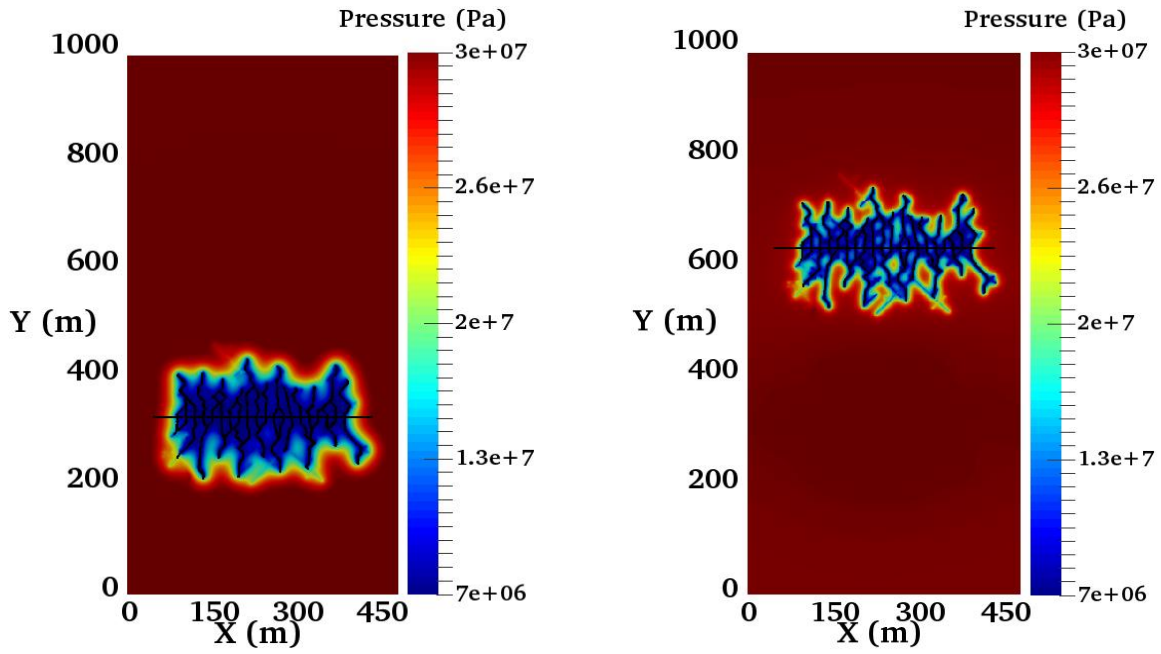

a) Pressure distribution in layer B2 after 2 years

b) Pressure distribution in layer A2 after 2 years

Figure 4.19. Pressure distribution in layers B2 and A2 after 2 years of production (Sangnimnuan et al. 2019b).

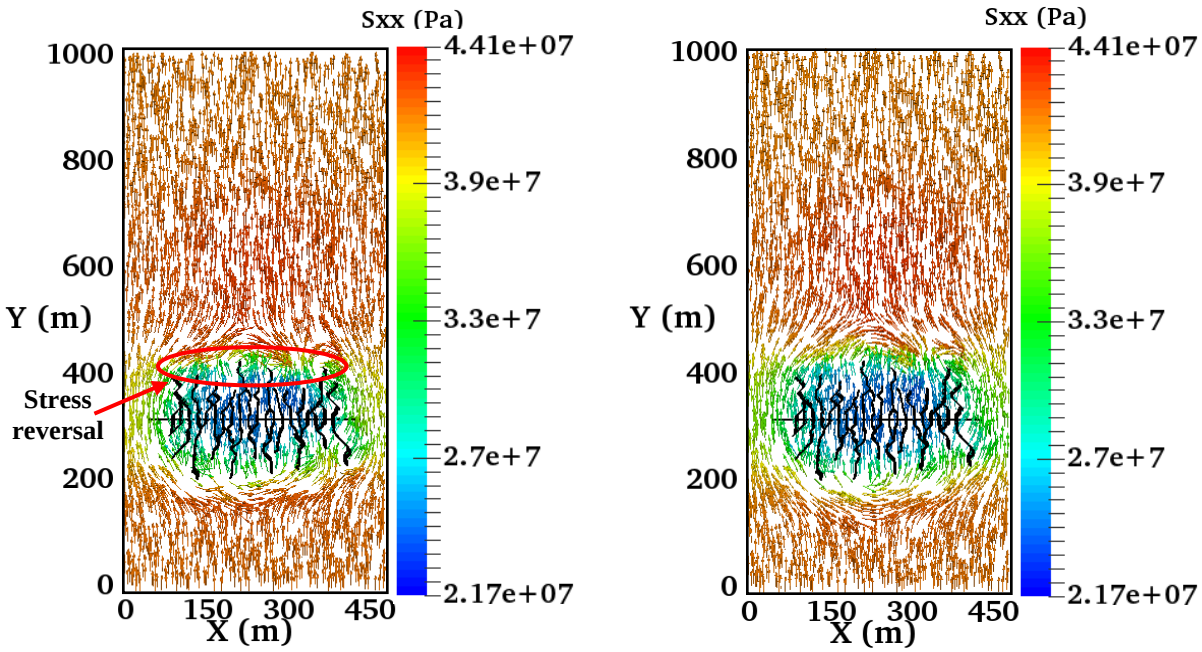

a) Orientation of S_{Hmax} in layer B2 after 2 years b) Orientation of S_{Hmax} in layer B2 after 5 years

Figure 4.20. Orientation of S_{Hmax} after 2 and 5 year production (Sangnimnuan et al. 2019b).

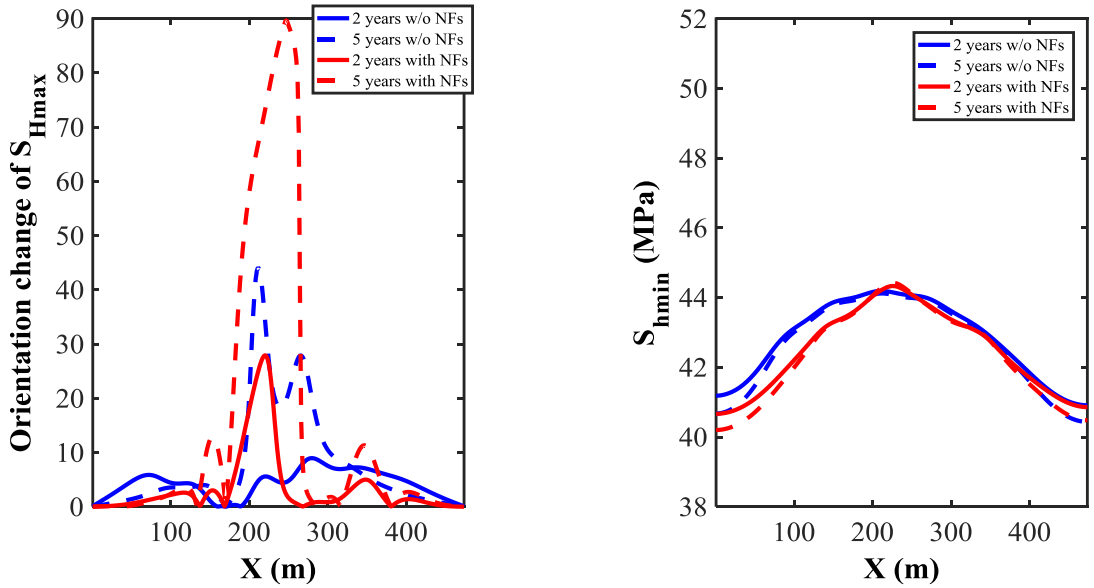

a) Orientation of S_{Hmax} along target infill well b) Magnitude of S_{hmin} along target infill well

Figure 4.21. Orientation change of S_{Hmax} and magnitude of S_{hmin} along target infill well in layer A3 at different times for case 1 (shorter fractures) and case 3 (longer fractures) (Sangnimnuan et al. 2019b).

4.3 Boundary effect

In order to ensure that the results obtained from all case studies are accurate and the boundary effect does not cause any significant difference, an additional study was carried out. The reservoir is now partitioned to include both payzoned and non-payzoned part and assumed to be located at 10,000 ft from the ground level (10,000 ft at top of payzone). The reservoir is enlarged to cover the non-payzone in x, y, and z directions. The payzone is the same as shown in Figure 4.1 in terms of size and configuration. Two well configurations (cases 1 and 2) were included in the study. The goal is to observe change of stress field in terms of magnitude and direction under production in the payzone. Number of cells in x, y, and z directions are 329, 659, and 12 respectively with Dx and Dy varying from 150 to 1.5 m. and Dz is reservoir thickness varying from 600 to 12.3 m. Three layers of non-payzone were added on top and one layer on the bottom of the reservoir (see Figure 4.23 for detailed dimensions). Total number of cells increases from 1.59M to 2.6M. Simulation time has increased from 45 mins to 120 mins for simulation of 5 years production. Zero permeability is applied to the non-payzone. Porosity and Poisson's ratio are the similar for the payzone and non-payzone assuming drained condition. Young's Modulus on the top and bottom layers in the non-payzone is about 1.5 times larger than those in the payzone. Stress gradients of 0.8 psi/ft, 0.64 psi/ft and 0.6 psi/ft are applied to the entire reservoir for vertical, maximum, and minimum horizontal stress respectively. Reservoir properties for non-payzone can be found in Table 4.3. No flow boundary is used for 6 boundaries for fluid flow part and constraint boundary is applied for 5 boundaries with overburden stress applied on the top boundary for geomecanical part. Reservoir configuration including both payzone and non-payzone is shown in Figure 4.22 with blue region being the payzone and the red is for non-payzone. Figure 4.23 shows details of reservoir layout in 3D and 2D including locations of wells and fractures.

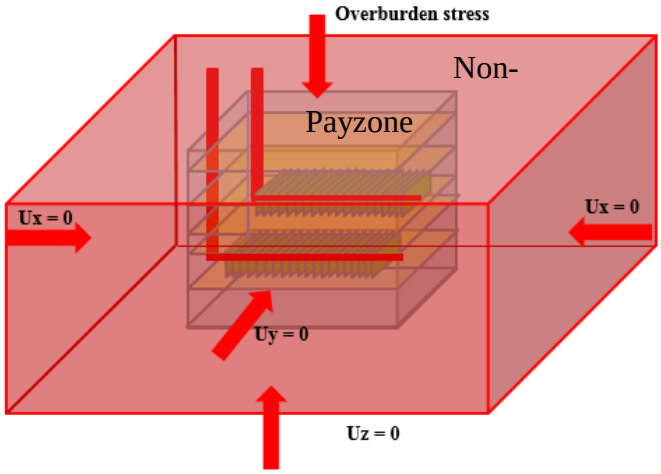

Figure 4.22. Reservoir configuration containg both payzone and non-payzone.

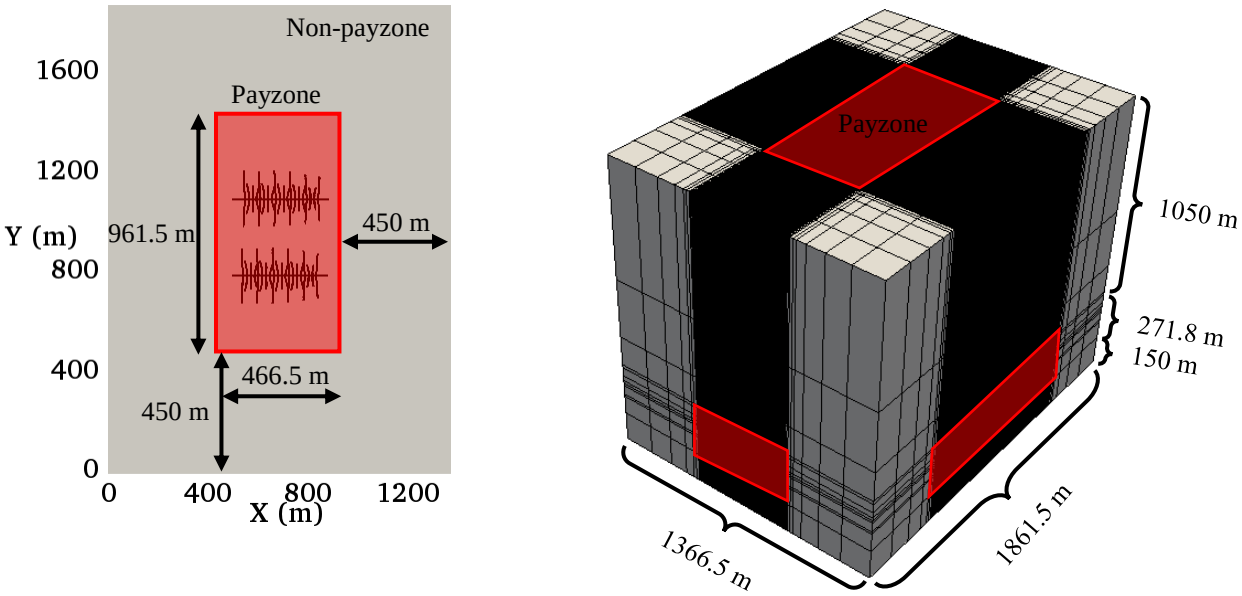

Figure 4.23. Reservor layout in 2D (left) and 3D (right).

Input Parameter	Payzone	Non-payzone
Young's Modulus (GPa)	Vary	30
Poisson's ratio (-)	Vary	0.26
Permeability (nd)	Vary	0
Porosity (%)	Vary	6.46

Table 4.3. Reservoir properties applied to non-payzone

4.3.1 Case 1A: Two wells are located in a different layer

The set-up of this case is similar to well configuration in case 1 with the payzone located in the middle of the reservoir as showin already in Figure 4.23. Figures 4.24 shows Y-Z plane showing well locations.

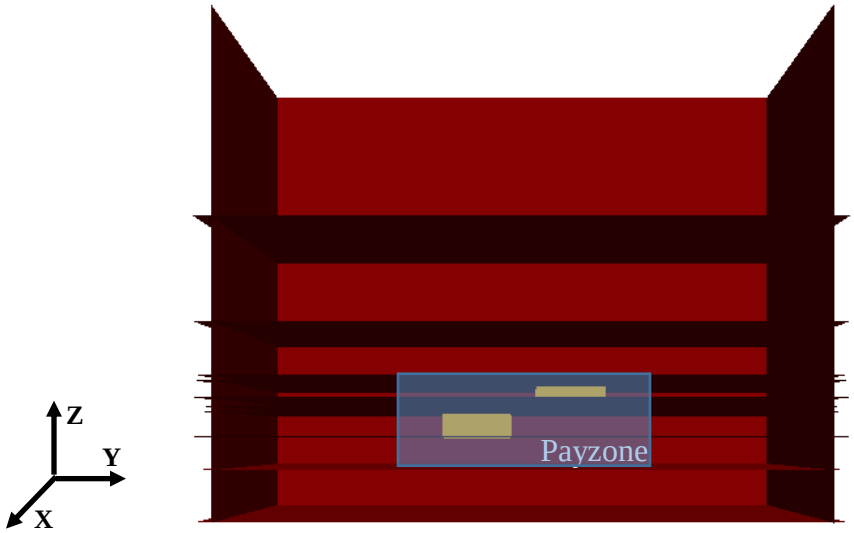

Figure 4.24. Y-Z plane of reservoir showing fractures of both wells that are located in different layers.

Pressure distribution along with the change of S_{Hmax} orientation has been observed in the layers A2 and B2 where the parent wells are located and layer A3 where the infill well is to be located. A comparison of pressure distribution with orientation of S_{Hamx} between this case and the case 1 from section 4.2.1 in layers B2 and A2 is shown in Figure 4.25 and 4.26 respectively. Additionally, a comparison of S_{xx} distribution in the layers B2 and A2 is shown in Figure 4.27 and 4.28 respectively. The results suggest that there is no diference in terms of pressure and stress distrubiton between the two cases in both layers A2 and B2; however, a small difference in orientation change can be observed around the fracture tips both in layers A2 and B2 due to the

presence of the non-payzone. This difference can be neglected if the initial differential in-situ stress is larger since there will be no orientation change at all.

Figures 4.29 and 4.30 show a comparion of S_{xx} and S_{yy} distribution with the direction of S_{Hmax} in the layer A3 respectively, which is the layer for the target infill well. The results show more orientation changes along the target infill zone even though the trend of stress distribution for both cases are very similar. The main difference is the stress magnitude, in which both S_{xx} and S_{yy} in case 1A is about 5% smaller than case 1 for the region parallel to the well in the layer B2. While S_{xx} and S_{yy} in case 1A is about 2% larger than case 1 for the region parallel to the well in the layer A2. In addition, a comparison of magnitude of S_{Hmax} and S_{hmin} (initial S_{hmin} is 41.3 MPa and S_{Hmax} is 44.1 MPa) as well as pressure (initial pressure is 32.8 MPa) along the target infill well between case 1 and 1A are shown in Figure 4.31a, 4.31b, and 4.31C respectively in both 2 and 5 years of production. The increase in pressure in the layer A3 can be observed to support the decrease in pressure in layers A2 and B2 during reservoir production. This leads to the increase in S_{xx} along the target infill well for both cases 1 and 1A. However, only a small increase in S_{yy} can be observed for case 1, while a decrease in S_{yy} can be observed for case 1A. The difference is mainly due to the presence of non-payzone, which reduces the pressure rise in the layer A3 as the top part of the reservoir is larger and becomes less stiff. This reduces the magnitude of S_{yy} in case 1A causing stress reorientation as the S_{yy} becomes smaller than S_{xx}. This explains why more stress orientation can be observed in the case 1A. On the other hand, the difference of orientation change in layers B2 and A2 is insignificant as the pressure decrease at the similar rate for cases 1 and 1A. As the time progresses, pressure starts to dissipate resulting in the decrease in S_{yy} in both cases 1 amd 1A, while no significant change in S_{xx} can be observed.

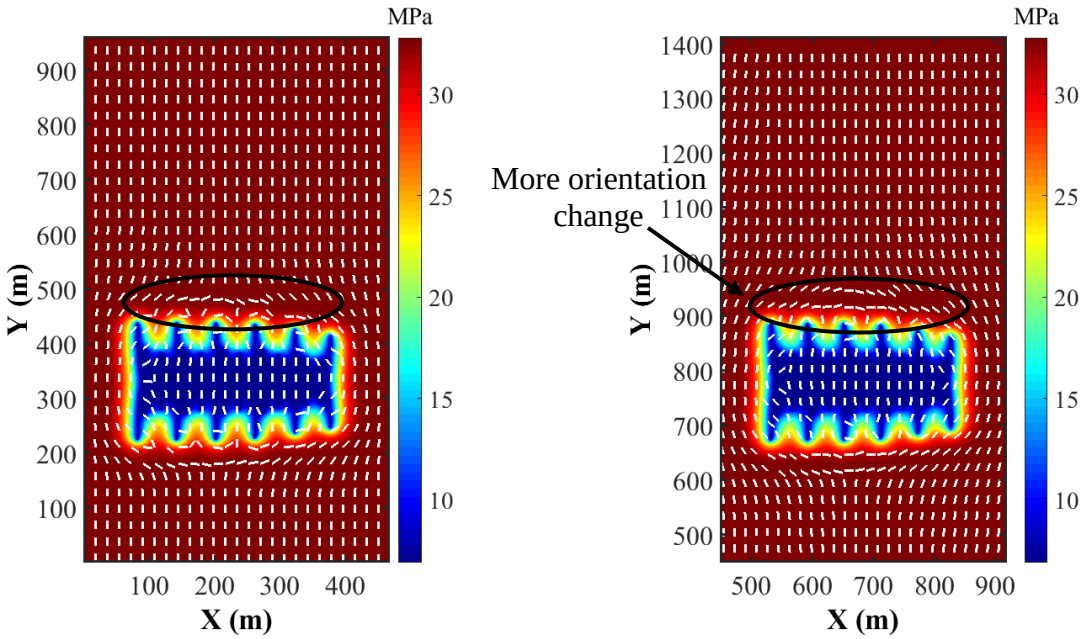

a) Pressure distribution for case 1. b) Pressure distribution for case 1A.

Figure 4.25. Pressure distribution in layer B2 after 2 years of production for cases 1 and 1A.

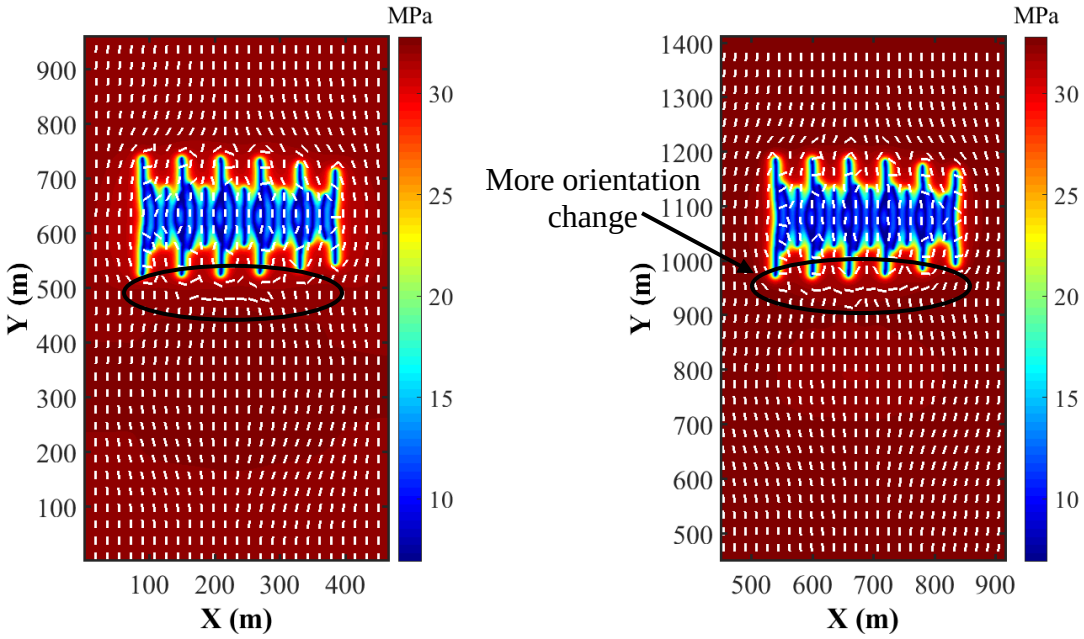

a) Pressure distribution for case 1. b) Pressure distribution for case 1A.

Figure 4.26. Pressure distribution in layer A2 after 2 years of production for cases 1 and 1A.

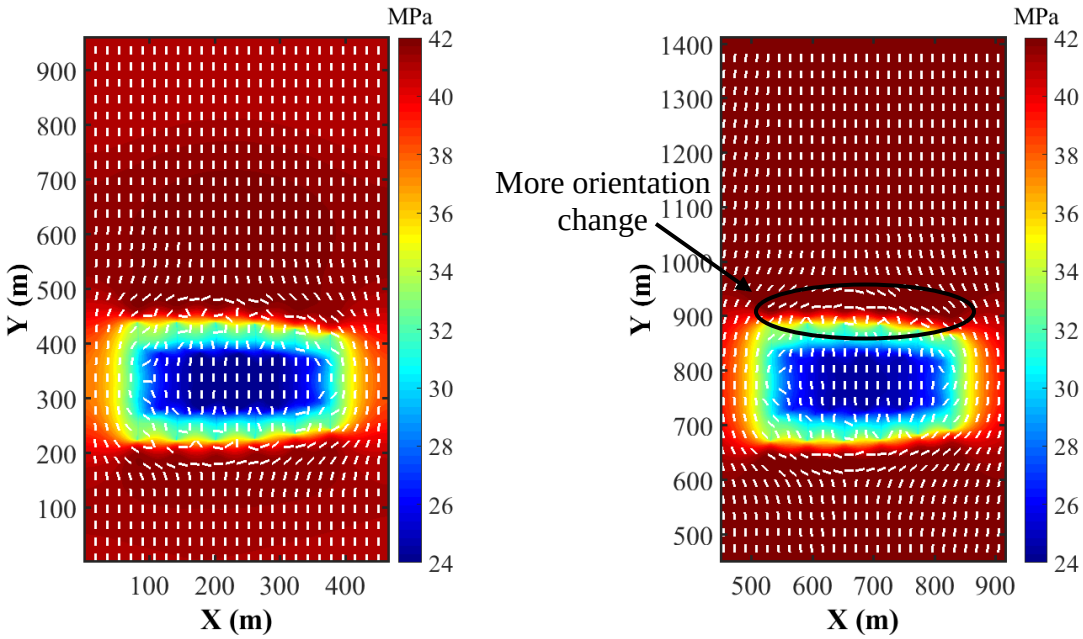

a) S_{xx} distribution for case 1.

b) S_{xx} distribution for case 1A.

Figure 4.27. S_{xx} distribution in layer B2 after 2 years of production for cases 1 and 1A.

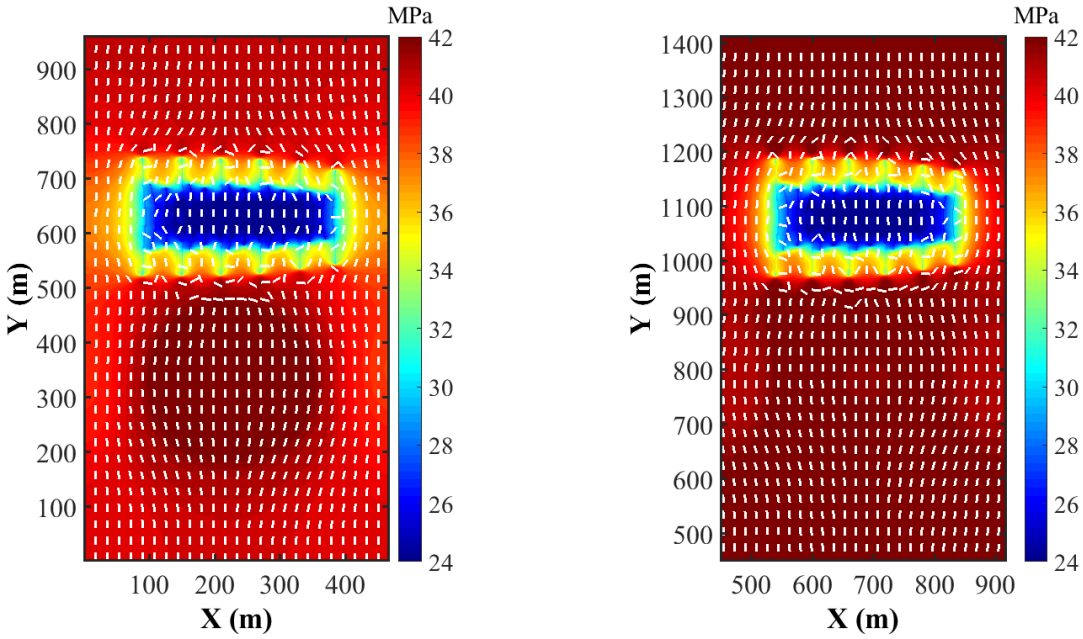

a) S_{xx} distribution for case 1.

b) S_{xx} distribution for case 1A.

Figure 4.28. S_{xx} distribution in layer B2 after 2 years of production for cases 1 and 1A.

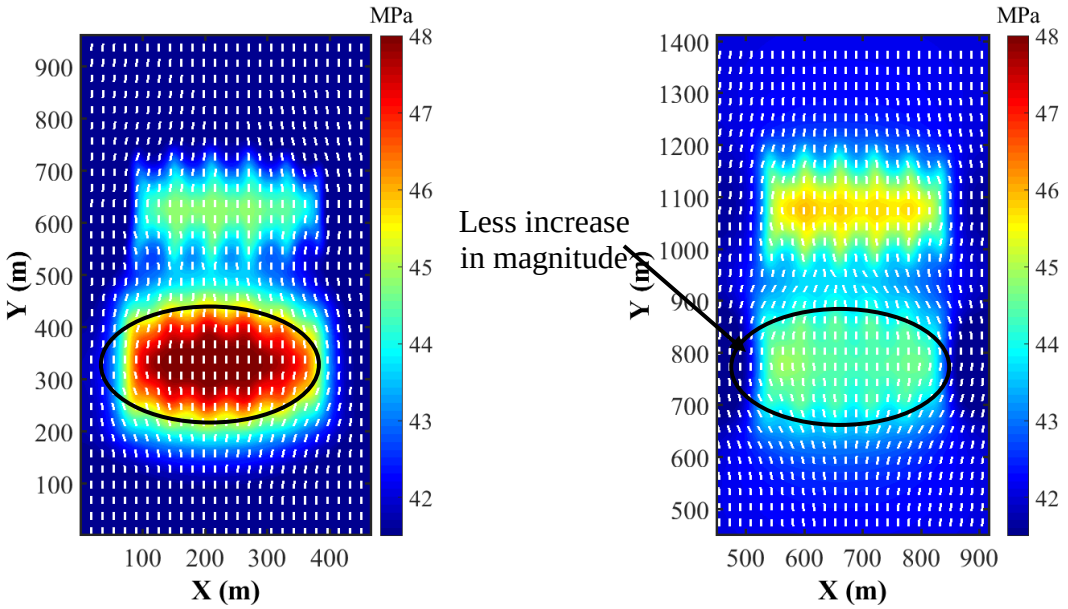

a) S_{xx} distribution for case 1. b) S_{xx} distribution for case 1A.

Figure 4.29. S_{xx} distribution in layer A3 after 2 years of production for cases 1 and 1A.

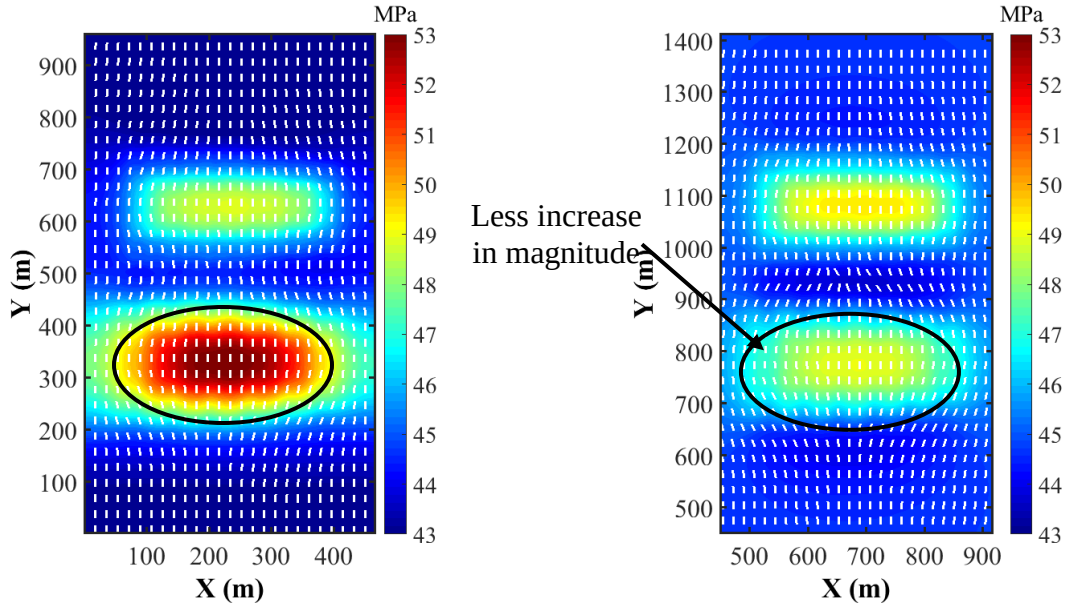

a) S_{yy} distribution for case 1. b) S_{yy} distribution for case 1A.

Figure 4.30. S_{yy} distribution in layer A3 after 2 years of production for cases 1 and 1A

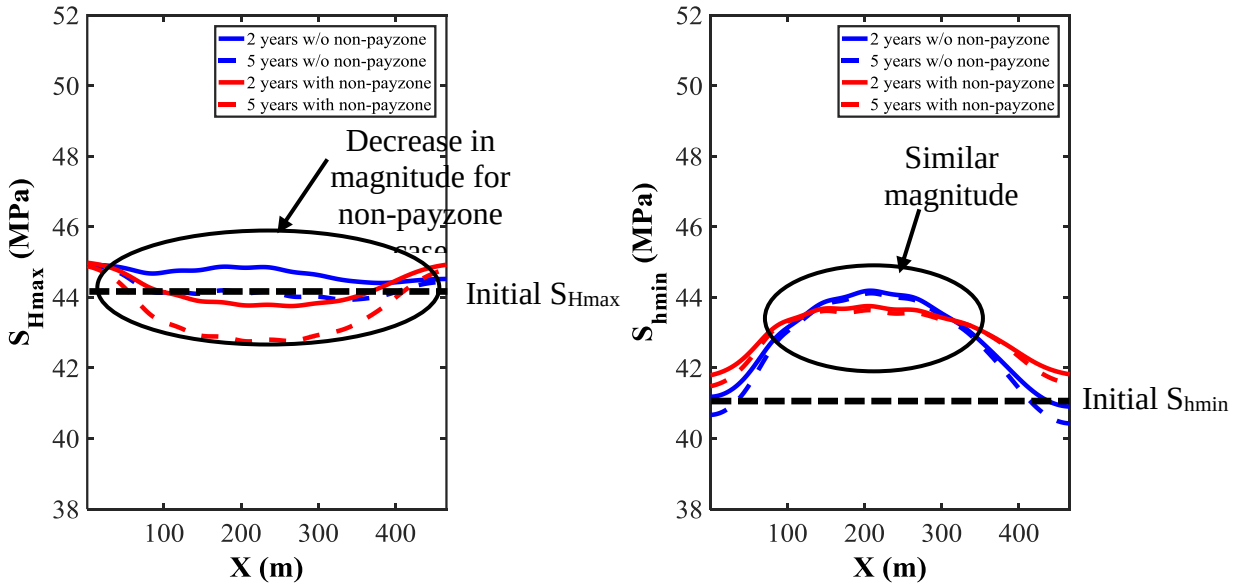

a) Magnitude of S_{Hmax} along target infill well b) Magnitude of S_{hmin} along target infill well

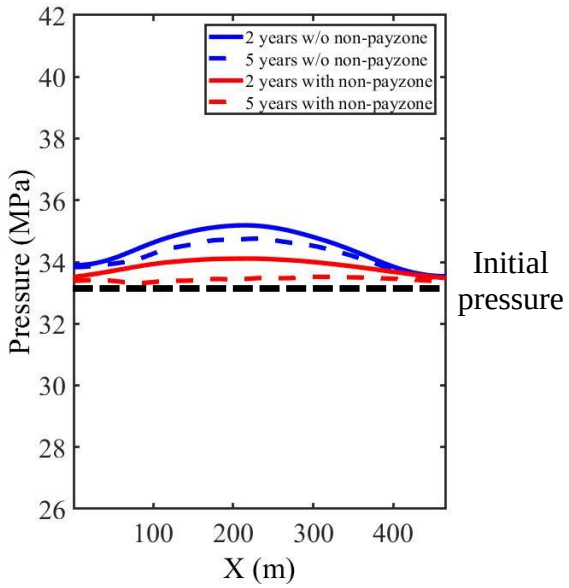

c) Pressure along target infill well

Figure 4.31. Magnitude of S_{Hmax} and S_{hmin} and pressure along target infill well in layer A3 at different times for case 1 (w/o non-payzone) and case 1A (with payzone).

4.3.2 Case 2A: Two wells are located in the same layer

The set-up of this case is similar to well configuration in case 2 with the payzone located in the middle of the reservoir as showin already in Figure 4.23. Figures 4.32 depicts a Y-Z plane showing well locations.

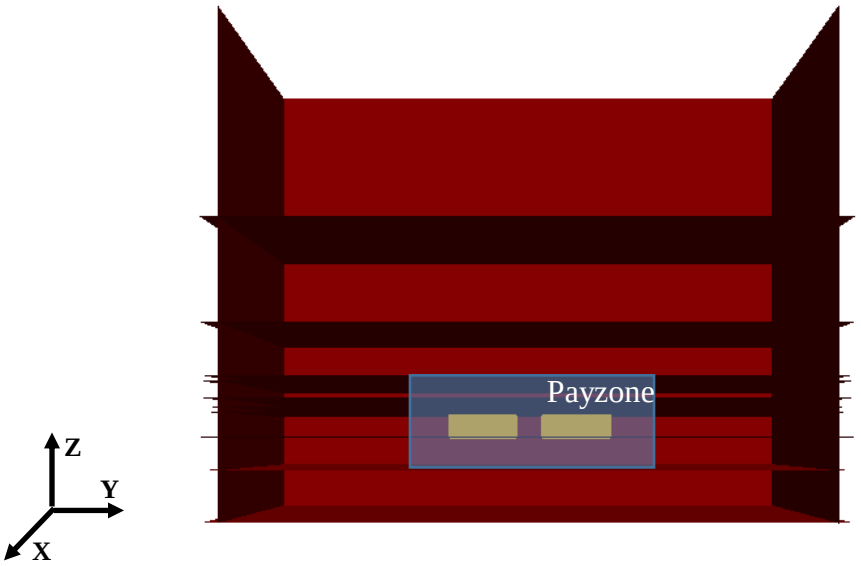

Figure 4.32. Y-Z plane of reservoir showing fractures of both wells that are located in the same layer.

Similar to the previous case, case 2A is compared with case 2 (section 4.2.2) in terms of pressure and stress distribution. Figure 4.33 compares pressure distribution after 2 years of protection in the layer B2 between case 2 and 2A. More orientation change around fracture tips can be observed in case 2A, where non-payzone is present. However, the difference is not very significant and overall result is very similar between both cases as can be observed in Figures 4.34 for S_{xx} distribution. As opposed to the layer B2, a significant diffence in both magnitude of S_{xx} and S_{yy} and orientation of S_{Hmax} can be observed in the layer A3 as shown in Figures 4.35 and 4.36. The locations that are parrell with the well locations in the layer B2 yield a larger increase in both S_{xx} and S_{yy} for case 2 (about 6% for S_{xx} and 8% for S_{yy}) compared to case 2A . This observation

is similar to the previous case due to the presence of non-payzone reducing the increase in pressure in the layer A3 as the pressure can dissipate more in case 2A.

Figure 4.37 provides a comparison between case 2 and 2A for both magnitude of S_{xx} and S_{yy} as well as pressure along the target infill zone. A large pressure increase can be observed in case 2 (13.6% increase), which is significantly larger than those obtained from case 2A (3% increase). This is mainly due to the presence of non-payzone in case 2A, which allows more pressure dissipation and hence reducing pressure increase in the layer A3. The increase in pressure in case 2 is also much larger than case 1 as the two parent wells are located in the same layer causing faster depletion rate in the layer B2, which in turn requires larger pressure increase in the layer A3. Pressure increase in layer A3 leads to a large increase of S_{xx}, which is about 12% for case 2 and 6% for case 2A. S_{yy} also increases about 5% for case 2 and decreases about 2.5% for case 2A, which results in stress reversal along the target infill zone. In addition, as the time progresses to 5 years, pressure starts to drop leading to the reduction in both S_{xx} and S_{yy}, which eventually creates more stress reorientation. In addition, due to the smaller in magnitude of S_{xx} in both case 1A and 2A, the fractures created during the completion will be easier to open allowing the well to gain more production.

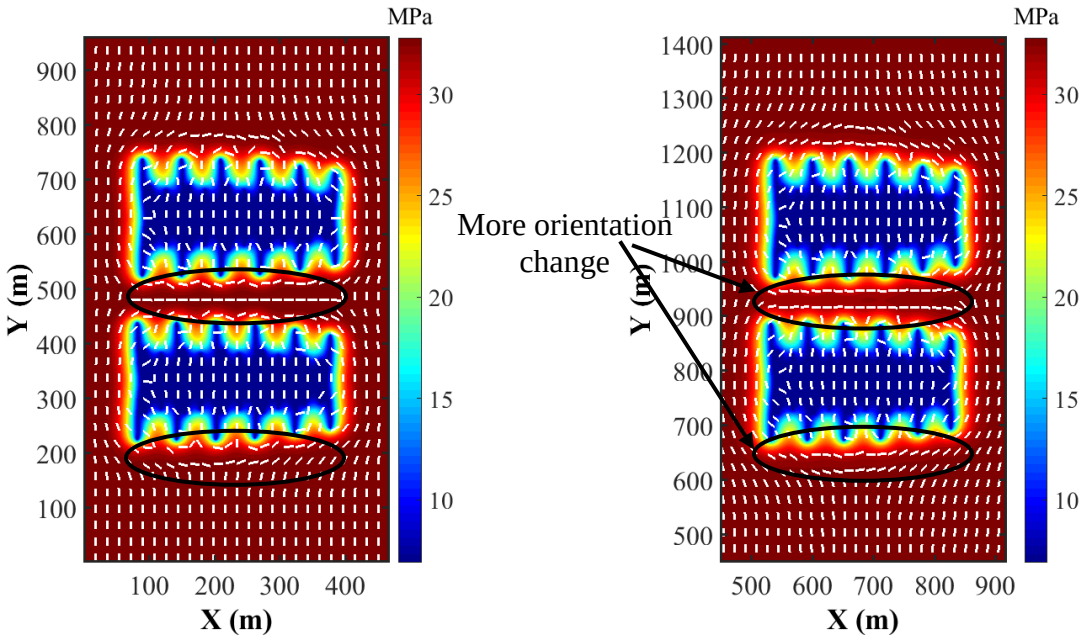

a) Pressure distribution for case 2. b) Pressure distribution for case 2A.

Figure 4.33. Pressure distribution in layer A2 after 2 years of production for cases 2 and 2A.

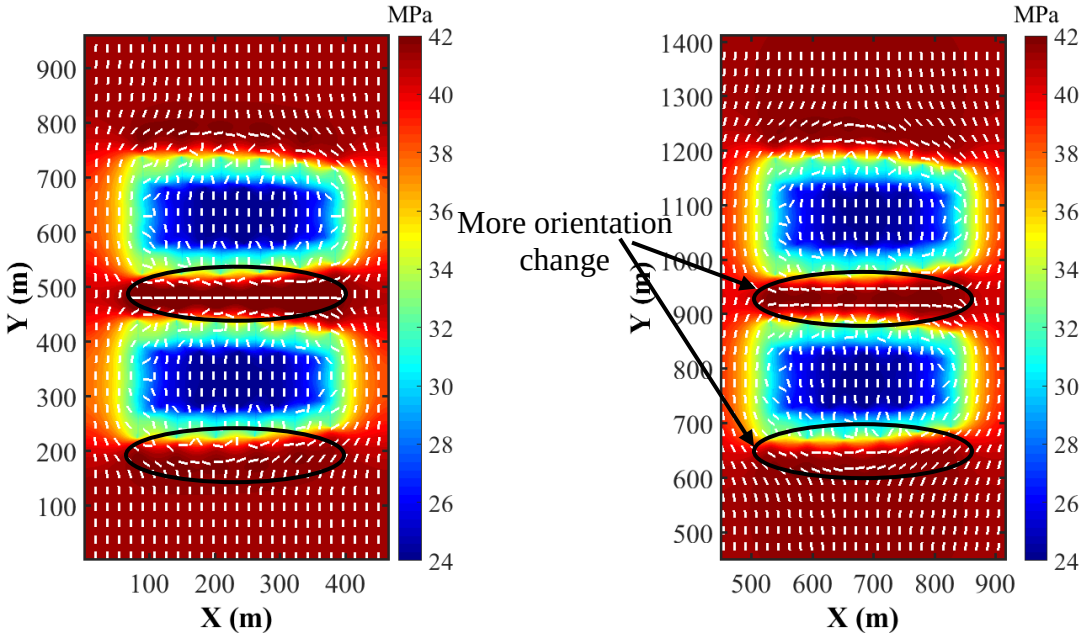

a) S_{xx} distribution for case 2. b) S_{xx} distribution for case 2A.

Figure 4.34. Pressure distribution in layer A2 after 2 years of production for cases 2 and 2A.

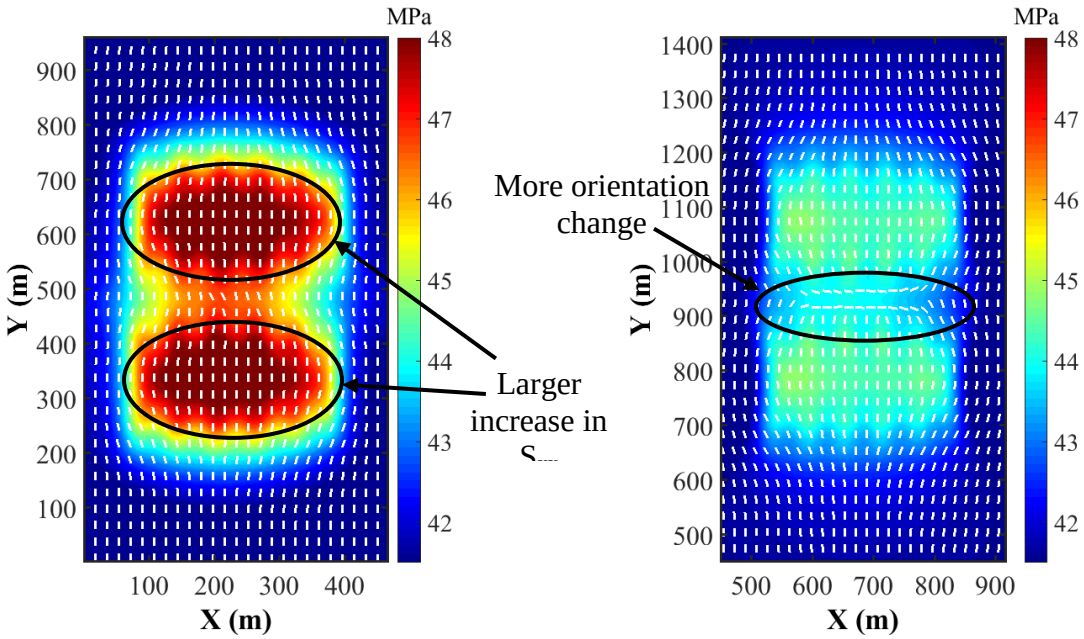

a) S_{xx} distribution for case 2.

b) S_{xx} distribution for case 2A.

Figure 4.35. S_{xx} distribution in layer A3 after 2 years of production for cases 2 and 2A.

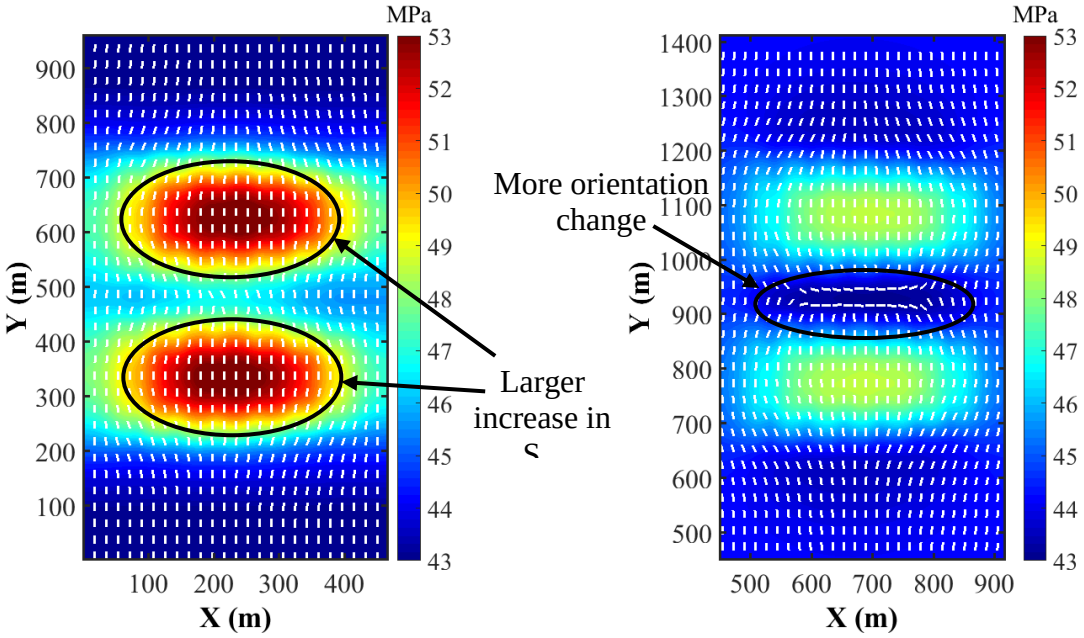

a) S_{yy} distribution for case 2.

b) S_{yy} distribution for case 2A.

Figure 4.36. S_{yy} distribution in layer A3 after 2 years of production for cases 2 and 2A.

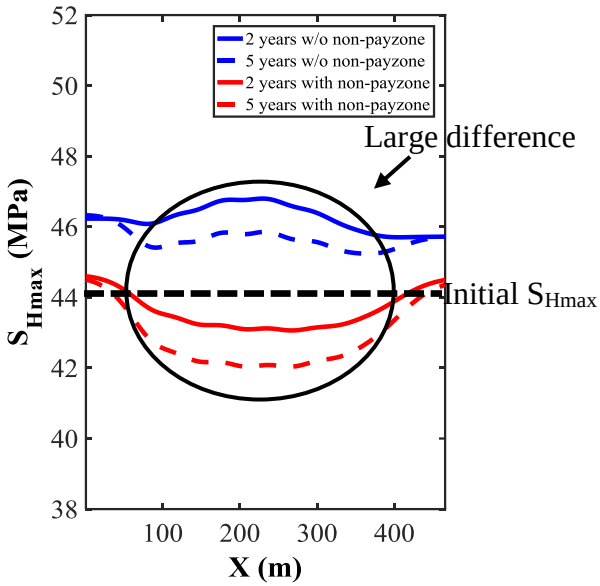

a) Magnitude of S_{Hmax} along target infill well

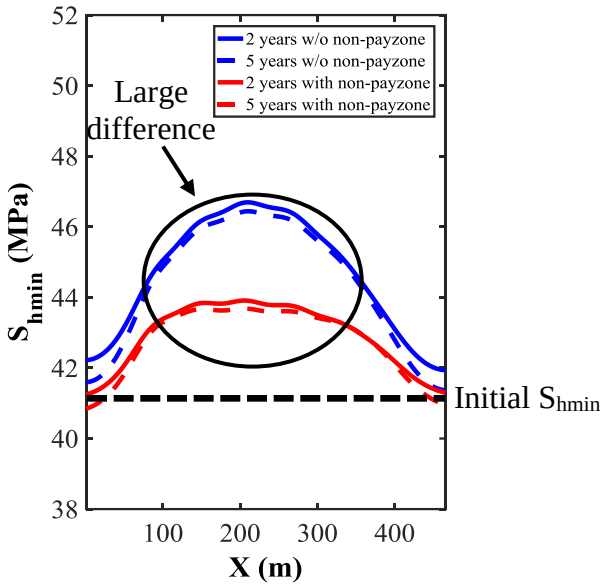

b) Magnitude of S_{hmin} along target infill well

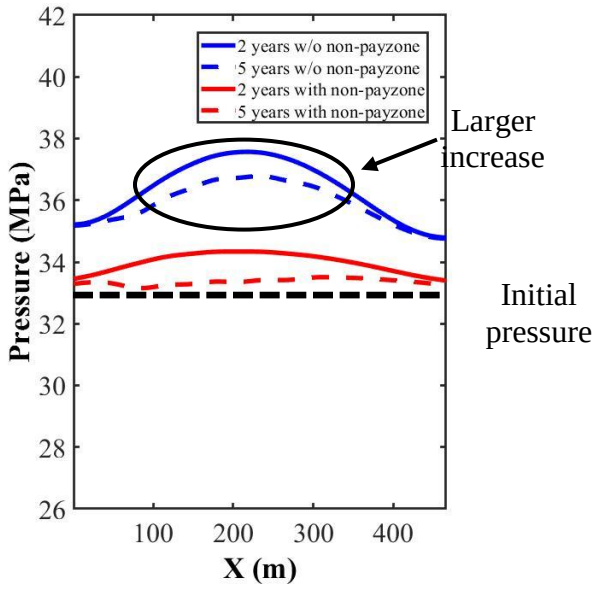

c) Pressure along target infill well

Figure 4.37. Magnitude of S_{Hmax} and S_{hmin} and pressure along target infill well in layer A3 at different times for case 2 (w/o non-payzone) and case 2A (with payzone).

The results observed in this study suggest that including non-payzone in the study can play a significant effect in terms of stress change in both magnitude and orientation in multiple-layer reservoirs. Boundary effect can vary from one layer to another depending on whether that layer is under production or not. For example, the layer that contains the well under production is most likely to have minimal effect as the depletion is the major factor that controls stress change in that layer. However, the layers that do not contain any production well can be affected by the presence of non-payzone resulting in smaller increase in stress magnitude and more stress orientation due to a smaller increase in pressure compared with the case without non-payzone. This suggests that if the study mainly focuses on the the layers under production, it is not necessary to include the non-payzone in the simulation due to its high computational cost and small difference in stress change. However, if the study involves the layers that are not under production but will be in the future, it is better to include the non-payzone in the simulation to minimize the boundary effect and be able to obtain accurate results in terms of stress change in both magnitude and direction for field operations.

4.3.3 Comparison between different sizes of non-payzone

Since different sizes of non-payzone might yield different stress distribution, a few variations of boundary size is to be studied in this section to obtain the optimized size that does not change the solution of stress field. First, only lateral non-payzone is to be considered and compared with the case base (case 1), then the vertical non-payzone is to be considered with different height varying from 550 m, 1050 m (case 1A) and 1550 m. Results can be shown in the following subsections.

4.3.3.1 Effect of lateral non-payzone

In this case, only lateral non-payzone (case 1B) is included and the vertical non-payzon in both top and bottom reservoir is neglected, meaning that only 8 layers considered in this study. Comparions between case 1B and the base case (case 1) in both S_{xx} and S_{yy} distribution is shown in Figs. 4.38 and 4.39 respectively. The results after 2 years of production suggest that the increase in S_{xx} and S_{yy} in the area parallel to the well in the layer B2 is very similar between both cases; however, the increase in S_{xx} is slightly larger for the area parallel to the well in the layer A2 for case 1B as a result of lateral non-payzone.

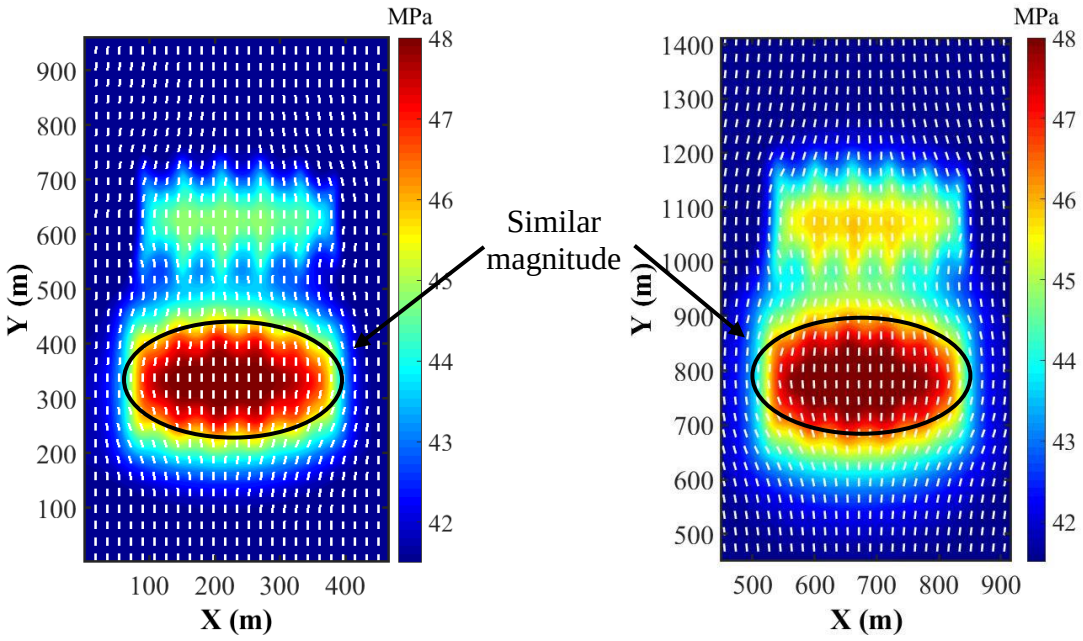

a) S_{xx} distribution for case 1.

b) S_{xx} distribution for case 1B.

Figure 4.38. S_{xx} distribution in layer A3 after 2 years of production for cases 1 and 1B.

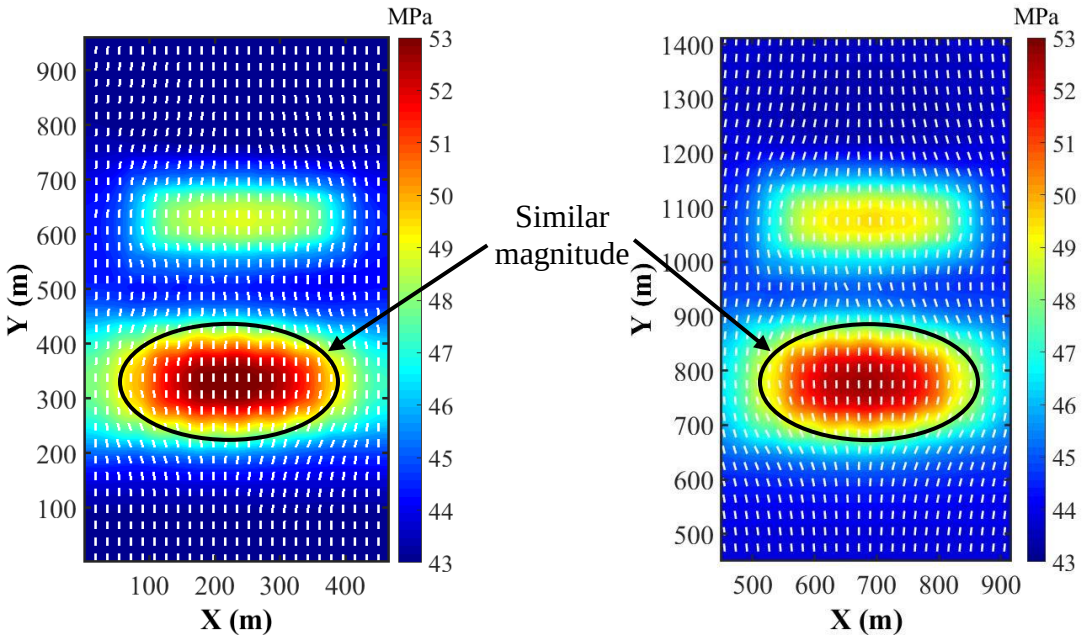

a) S_{yy} distribution for case 1. b) S_{yy} distribution for case 1B.

Figure 4.39. S_{yy} distribution in layer A3 after 2 years of production for cases 1 and 1B.

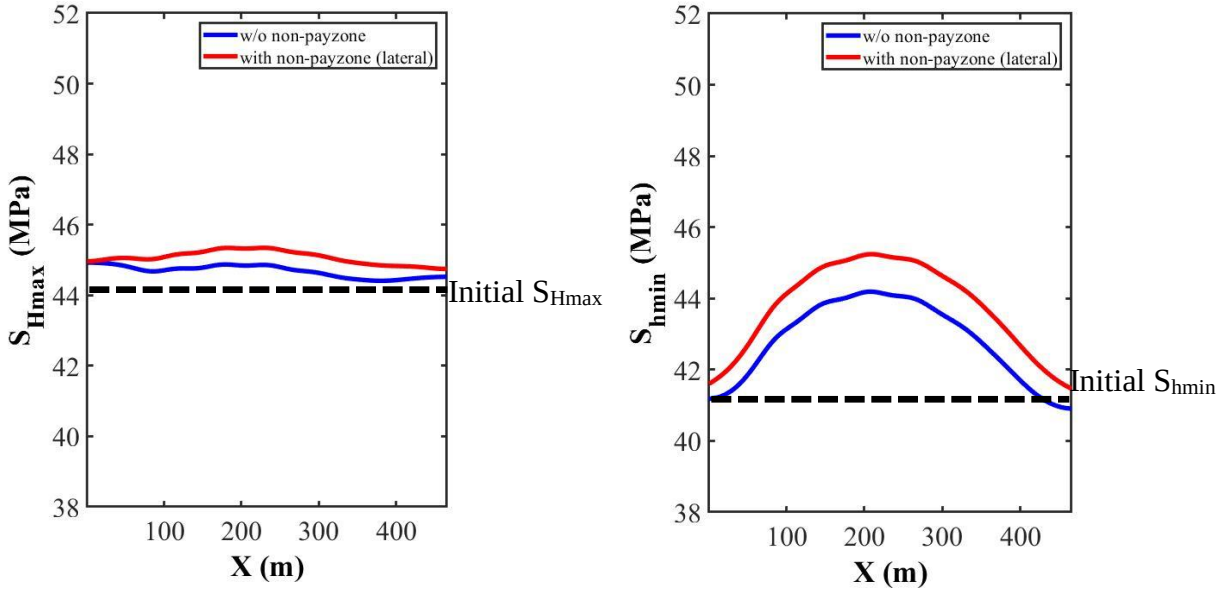

a) Magnitude of S_{Hmax} along target infill well b) Magnitude of S_{hmin} along target infill well

Figure 4.40. Magnitude of S_{Hmax} and S_{hmin} along target infill well in layer case 1 and case 1B.

Comparions of S_{Hmax} and S_{hmin} along target infill well in layer A3 also show that the trend of stress increase is very similar with the case with lateral non-payzone having a slightly larger stress magnitude but not so significant to change the orientation as the orientation of S_{Hmax} observed in Fig. 4.39 is very similar between both cases. The results obtained from this comparison suggest that the difference in the stress magnitude observed in the layer A3 is mainly due to the presence of vertical non-payzone as the presence of lateral non-payzone plays little to no effect on the stress change in the non-producing layer (A3).

4.3.3.2 Effect of vertical non-payzone

In this section, size of vertical non-payzone on top of the reservoir is to be varied from 550 m (case 1C), 1050 m (case 1A), and 1550 m (case 1D). The non-payzone under reservoir is maintained the same for The goal is to find the optimized size since the larger the vertical size, the higher the computational cost. Therefore, it is important to properly include the vertical non-payzone size to obtain the correct solution in terms of pressure and stress field in producing and non-producing layer and optimize computational cost. Reservoir layout can be shown in Fig. 4.41.

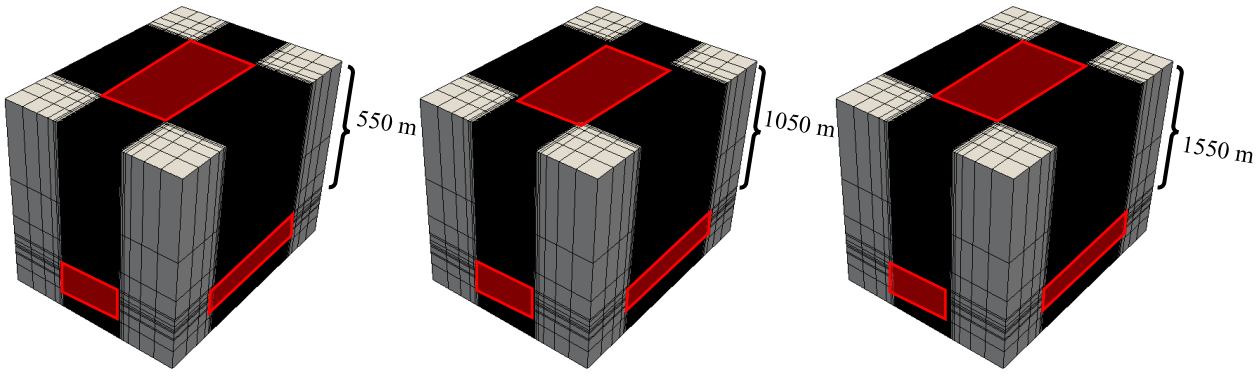

Case 1C, 550m Case 1A, 1050m Case 1D, 1550m

Figure 4.41. Reservor layout 3D of all 3 cases

Figs. 4.42 and 4.43 show S_{xx} and S_{yy} distribution after 2 years of production of 3 cases. The plots suggest that case 1C yield distinct results compared to cases 1A and 1D, implying that the smaller vertical non-payzone causes a smaller increase in S_{xx} and S_{yy} in the non-producing layer (A3) compared to the cases with larger vertical non-payzone (1A and 1D). On the other hand, the results obtained from case 1A and 1D are very similar with almost no difference in terms of magnitude of S_{xx} and S_{yy}. This means that it is not necessary to increase the vertical non-payzone to be as larger as 1550 m as the 1050m non-payzone is larger enough to provide consistent results, while the 550m non-payzone is too small and can still yield inconsistent results. However, when it comes to orientation change along target infill well, there is no diference between all 3 cases, confirming that the presence of vertical non-payzone mainly affects stress magnitude.

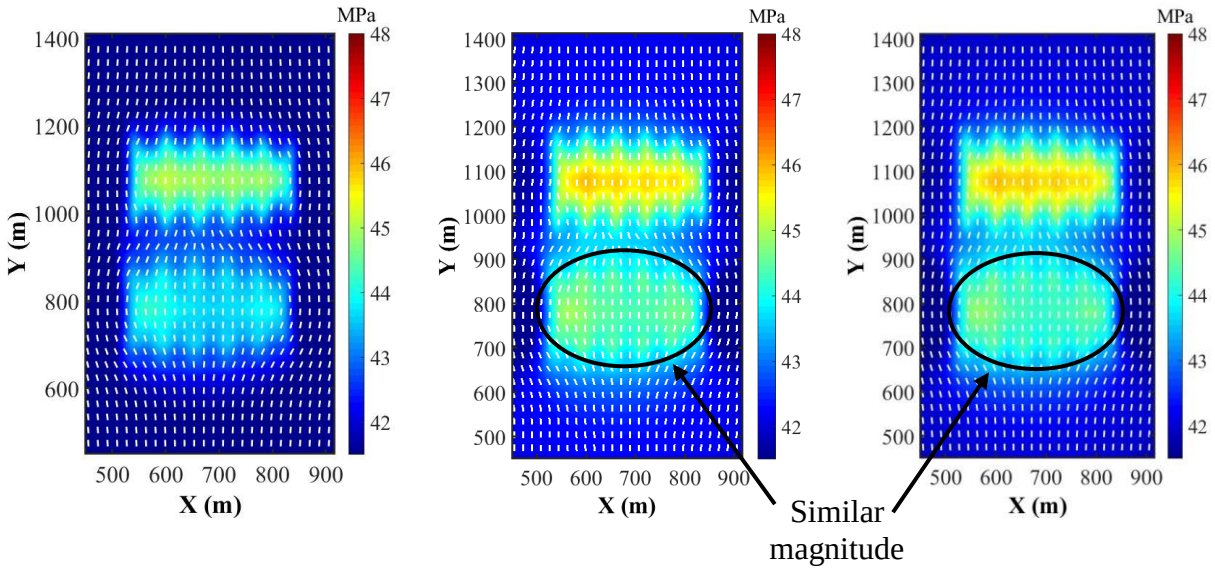

a) S_{xx} distribution for case 1C b) S_{xx} distribution for case 1A a) S_{xx} distribution for case 1D

Figure 4.42. S_{xx} distribution in layer A3 after 2 years of production for cases 1C, 1A, and 1D.

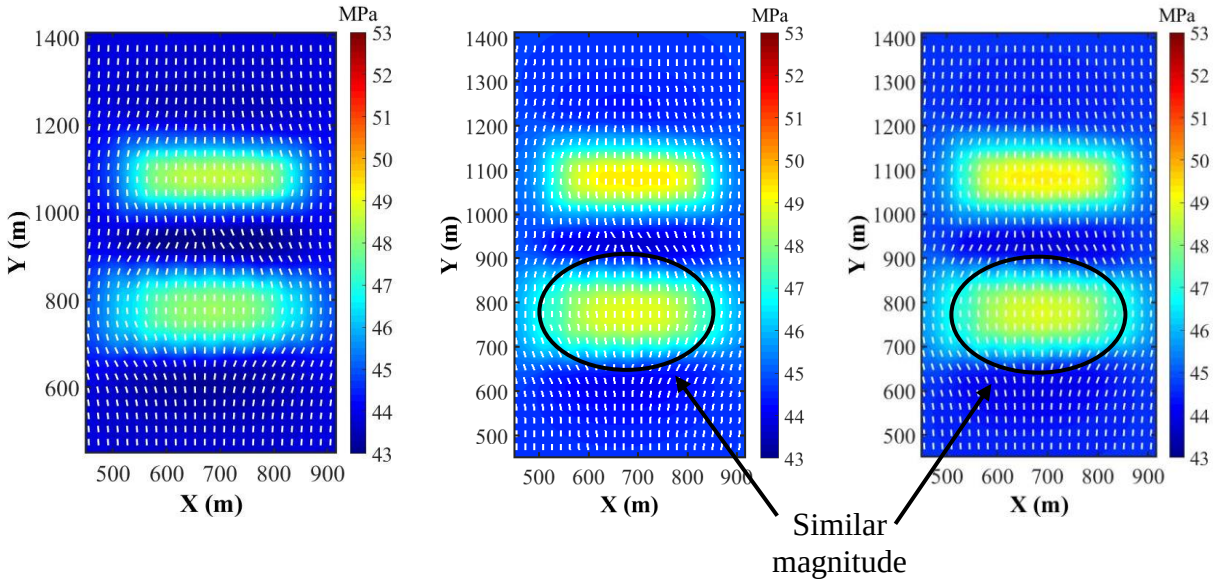

a) S_{yy} distribution for case 1C b) S_{yy} distribution for case 1A a) S_{yy} distribution for case 1D

Figure 4.43. S_{yy} distribution in layer A3 after 2 years of production for cases 1C, 1A, and 1D

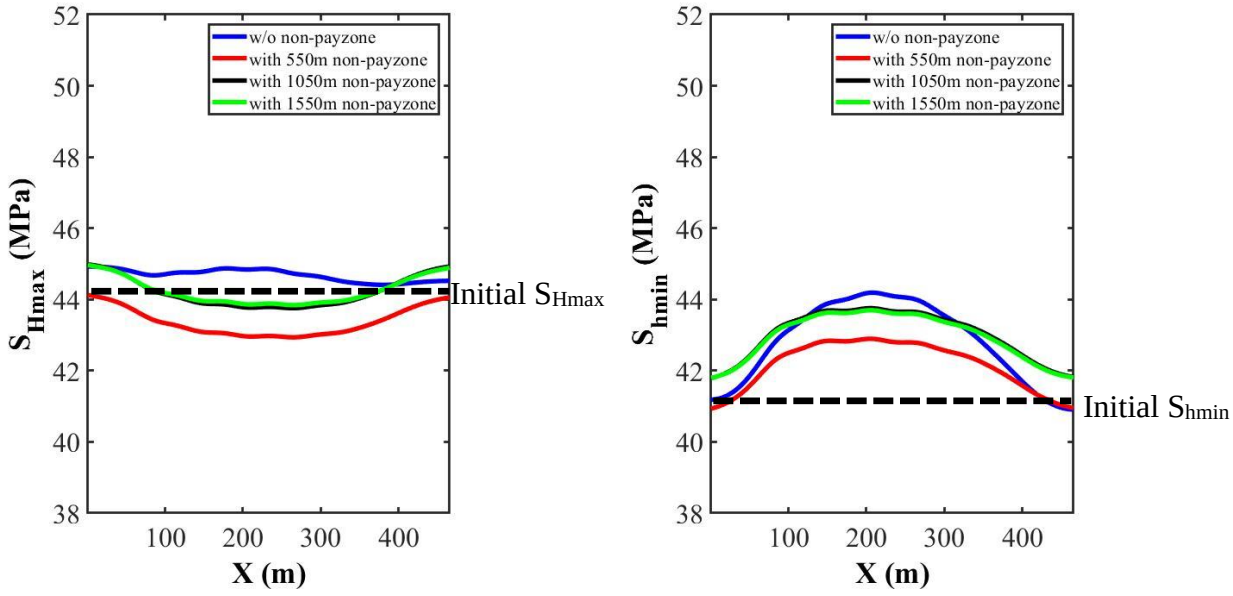

a) Magnitude of S_{Hmax} along target infill well b) Magnitude of S_{hmin} along target infill well

Figure 4.44. Magnitude of S_{Hmax} and S_{hmin} along target infill well in layer case 1 and case 1B.

In addition to stress distrubtion plots, the change of S_{Hmax} and S_{hmin} magnitude along target infill well has been compared between the 3 cases with the base case (case 1). Fig 4.44 suggests that case 1C produces a distinct result in both S_{Hmax} and S_{hmin} compared to cases 1A and 1D, which is in a good agreement with stress distribution shown in Figs. 4.42 and 4.43. This confirms that a sufficient height of vertical non-payzone should be included in the simulation, which is 1050 m in this case, to ensure the effect of non-payzone has been incorporated and the solution obtained from the simulation is correc, while the computational cost is optimized.

4.4 Conclusions

In this chapter, the coupled reservoir-geomechanics-EDFM model was utilized to investigate depletion-induced stress reorientation in a reservoir with multiple pay zones based on Permian Basin data. Fracture geometries used in the study were created using our in-house fracture propagation model. The effect of well layout, fracture penetration, fracture length, and natural fractures were studied. Results observed from all the cases suggest that depletion from a parent well affects stress reorientation outside SRV zone not only in the same layer but also in other layers that do not contain any production well. Followings are detailed conclusions drawn from this study:

1. Placing two-parent wells in the same layer is likely to cause more stress change than placing them in different layers. Therefore, from this aspect, the vertical well layout is a better option to mitigate stress change induced by depletion in both parent well's and infill well's layer and fracture hits.

2. Fracture penetration increases the depletion rate in the penetrated layer, resulting in more stress reorientation along target infill zone at a later time (5 years). The result suggests that

infill well completion should be performed at an earlier time (2 years) for maximized production gain.

3. Longer fracture length can cause fracture overlapping as shown in case 3, in which target infill zone in layer A3 is occupied by fractures from well#1 in layer B2 and from well#2 in layer A2. This significantly reduces stress reorientation along target infill zone. Hence, based on this study, case 3 is a better candidate for infill well completion compared to case 1.

4. If a reservoir is highly fractured and includes activated natural fractures, it is important to consider natural fractures as they elevate depletion rate in parent wells and create more stress reorientation along target infill zone. This suggests that infill well should be performed at an earlier time compared to the case without natural fractures.

5. If the infill well is to be completed in the same layer as the parent well for the vertical well layout, performing infill well completion at a later time (5 years) might be a better option. This is because of the presence of stress reversal around fracture tips, which helps prevent fractures from infill well to interact with fractures from parent well.

6. Presence of non-payzone can play an important role in multi-payzone reservoirs in terms of stress change. However, only the non-producing layers (layers without a well), which may be a good candidate for infill well completion, is affected and yields a significant change in stress magnitude and orientation, while the effect is minimal on the producing layer

7. The change of stress field in the non-producing layer is mainly due to the presence of the vertical non-payzone since the lateral non-payzone yields almost on difference in terms of

depletion-induced stress change. Optimum height of vertical non-payzone should be obtained and used in the simulation to ensure the correctness of the solutions as well as optimize computational cost.

CHAPTER 5: COUPLED FLUID FLOW AND GEOMECHANICS WITH A COMPLEX FRACTURE PROPAGATION MODEL

5.1 Introduction

To efficiently and economically develop hydrocarbon from unconventional reservoirs, horizontal wells are getting closer and closer to each other. As more wells are drilled, fractures propagating from a well are more likely to connect with fractures in adjacent wells and fracture hits are induced. Fracture hits are becoming a common phenomenon and has received significant attention because it directly affects well performance of both parent and infill wells. To improve performance, much work has been done to investigate stress change induced by parent-well depletion and fracture growth in infill wells. Recently, behaviors of fracture growth in infill wells also been studied by fracture propagation models. Most of recent published work focuses on planar fracture geometry in both parent and infill wells. However, multi-stage multiple fractures were generally created in the field to develop unconventional reservoirs.

Hence in this chapter, stress change induced by depletion of a parent well with five stages considering stress shadowing effects between and within stages is to be investigated. Subsequently, multiple fracture growth in infill wells based on the heterogeneous stress state is to be analyzed. Effect of fracture geometries consisting of short fractures, long fractures, and complex fracture created with presence of natural fractures is to be investigated to understand how it affects fracture geometry created from the infill well. In addition, well spacing is to be varied to find the optimized spacing that still allows the infill well fractures to to access undepleted zone.

Part of this section is reprinted with permission from "Fracture Hits Analysis for Infill-Parent Well Development" by Sangnimnuan, A., Li, J., Wu, K., 2019. American Rock Mechanics Association. Copyright [2019] by American Rock Mechanics Association.

5.2 Model description

As stated in the introduction part, the coupled fluid flow and geomechanics model is to be coupled with a complex fracture propagation model. Since the former has been described in chapter 2, only the latter will be discussed in this chapter.

An in-house, complex fracture propagation model was used to simulate multi-stage hydraulic fracturing propagation and characterize complex fracture geometry in unconventional reservoirs. The model was initially developed by Wu (2014) and extended to field application of multi-stage fracturing. This model is a pseudo-3D model and couples rock deformation and fluid flow in the fracture and wellbore. Fracture height growth is determined by an equilibrium height growth model. Our model employed a simplified three-dimensional displacement discontinuity method (simplified 3D DDM) proposed by Wu and Olson (2015a) to model rock deformation. This simplified method considered the 3D effects of limited fracture height and greatly enhanced computational efficiency compared with true 3D DDM. The method can accurately determine fracture opening, shearing, and the non-local three-dimensional stress interaction for single and multi-fracture cases. To simulate dynamic fracture propagation, the simplified 3D DDM was coupled with fluid flow in the fractures and horizontal wellbore (Wu and Olson, 2015b). Leak-off is modeled by Carter's model. Fluid flow in the wellbore is analogous to the flow of electric current through an electrical circuit network, applying Kirchoff's first and second laws. The total fluid injected into the horizontal wellbore is assumed to be constant. Partitioning of flow rate into each fracture is dynamically calculated in such a way that the wellbore pressure is constrained to gradually decrease along the lateral due to wellbore friction.

To generate natural fracture distribution, the model employs stochastic realization methods. Length of natural fractures follows a power-law distribution. When a hydraulic fracture encounters a natural fracture, the propagation direction of the hydraulic fracture is determined by induced stresses at the tips of hydraulic fractures, rock properties, reservoir stresses, and mechanical properties of natural fractures. When hydraulic fractures cross through natural fractures, fracture fluid can leak into natural fractures and elevate pore pressure within natural fractures. The model uses the finite difference method to simulate diffusivity of fracture fluid in the natural fractures. When pore pressure within a natural fracture segment reaches a certain value and satisfy the shear failure criterion, the natural fracture segment can be activated. Due to the rough asperities on the surface of the natural fracture segment, shear dilation is induced and transmissivity along the fracture can be greatly increased.

5.3 Case studies

5.3.1 Reservoir and input data

In this study, reservoir properties are based on the Permian basin, consisting of Wolfcamps A1-A3 and Wolfcamps B1-B3. Parent well is located in Wolfcamp B2 due to its large thickness and high permeability and consists of 5 fracture stages with each stage having 4 perforation clusters with 15 m fracture spacing. Reservoir properties were obtained from field data and are the same as those used in chapter 4 (Table 4.1 and 4.2) except that the initial differential stress used in this study is 4.4 MPa yielding initial stress in y-direction being 45.74 MPa. Schematic diagram of the reservoir used in this study is shown in Figure 5.1.

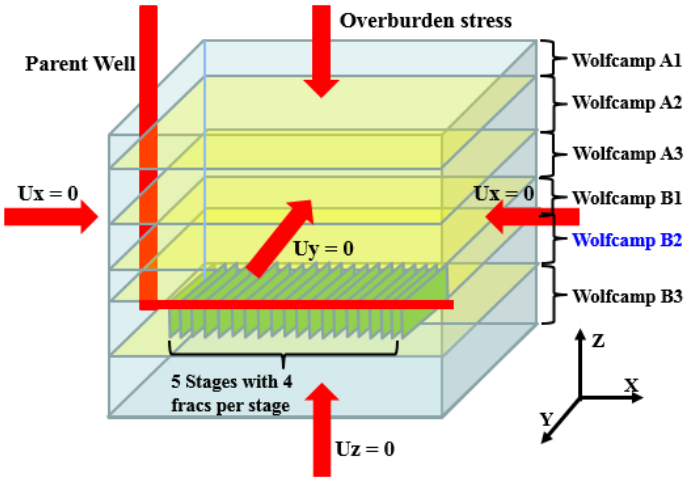

Figure 5.1. Schematic diagram showing the Permian basin reservoir in 3D used in this study (Sangnimnuan et al. 2019a).

The reservoir consists of 6 payzones (Wolfcamps A1-A3 and B1-B3) with each payzone having one cell in Z direction. Numbers of cells in X, Y, and Z directions are 271, 481, and 6 respectively. The location of the parent well in Wolfcamp B2 can be shown in Figure 2 for 3 different cases (2a, 2b, and 2c) in the 2D plot.

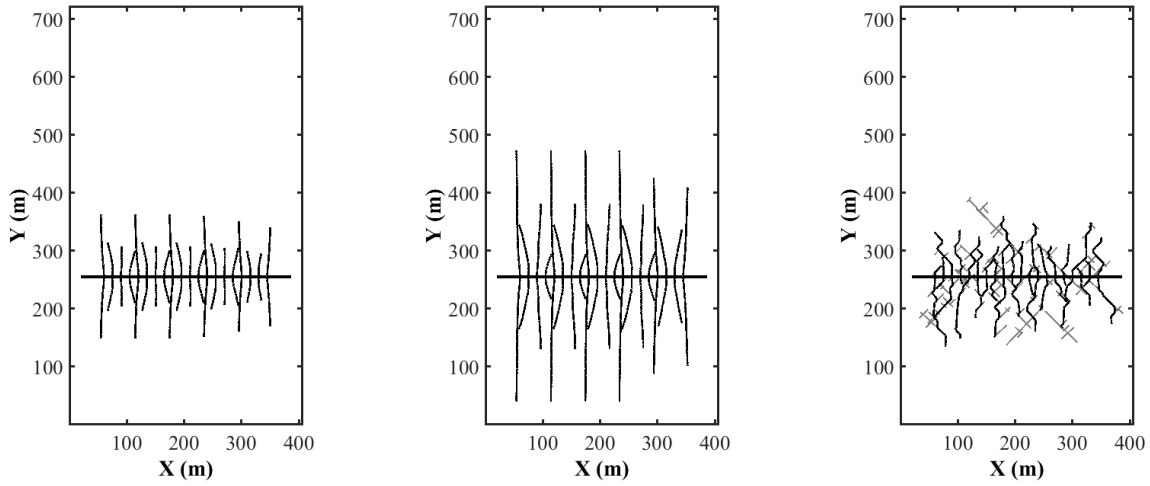

a) Case 1. b) Case 2. c) Case 1.

Figure 5.2. Schematic diagram in 2D on Wolfcamp B2 showing fracture geometries for case 1(a), 2 (b), and 3 (c) (Sangnimnuan et al. 2019a).

No flow boundary condition is applied on all 6 boundaries for fluid flow part and zero displacement in normal direction to the plane is applied to 5 boundaries for geomechanics, while the top boundary was applied with overburden stress of 55 MPa. Initial differential stress is 4.4 MPa. Hydraulic fractures were created using the complex fracture propagation model as described in section 5.2 based on homogeneous stress field. Figure 5.2a depicts fracture geometries for case 1 or base case with fracture half-length being 108 m for the longer ones and 45 m for the shorter ones. While fracture geometries for case 2 are shown in Figure 5.2b, in which leak-off coefficient is reduced by half yielding longer fracture length (219 m for the longer ones and 45 m for the shorter ones) at the same injection time. Short fractures observed in case 1 and 2 are due to stress shadowing effect, which shortens the length of inner fractures in each stage. Fracture height is assumed to be the same as the thickness of Wolfcamp B2, which is 22.25 m. Natural fractures were also generated and included in case 3 (Figure 5.2c) using the model described in section 5.2. This creates much more complex fracture geometries despite having homogeneous stress field.

In order to investigate frac hits, infill well is placed in the same payzone as parent well, which is Wolfcamp B2 and fractures are created using updated pressure and stress field obtained from the coupled geomechanics and fluid flow as described in chapter 2. Exiting fractures from parent well are assumed to be static during propagation of infill well fractures, meaning that there will be no actual interactions between parent well and infill well fractures since the input used in fracture propagation model is only an updated stress and pressure field. Fracture geometries obtained from the fracture propagation model can suggest the possibility of fracture hits between parent well and infill well fractures based on location of fracture tips after completion is finished. Furthermore, since the fracture propagation model is based on boundary element method, it is completely meshless or remeshing is not required to model infill well fractures. However, if the

scope of this work were to include production forecast of infill well, EDFM will be implemented to model complex fracture geometries obtained from infill well completion and hence, no grid refinement is required.

Infill well contains single-stage fracture having 4 perforation clusters with 15 m fracture spacing. Spacing between parent and infill well is varied from 150, 180, and 210 m to study infill well fracture propagation and asymmetrical fracture geometries induced by pressure sink from parent well.

5.3.2 The case without natural fractures

As stated in 5.3.1, there are 2 cases without natural fractures, one with shorter fracture length (case 1) and the other with longer fracture length (case 2).

5.3.2.1 Case 1: Shorter fracture length

Pressure and S_{xx} distribution at 2 and 5 years of production can be found in Figures 5.3 and 5.4 respectively. The plots also include width distribution of fractures generated using the model in section 5.2.

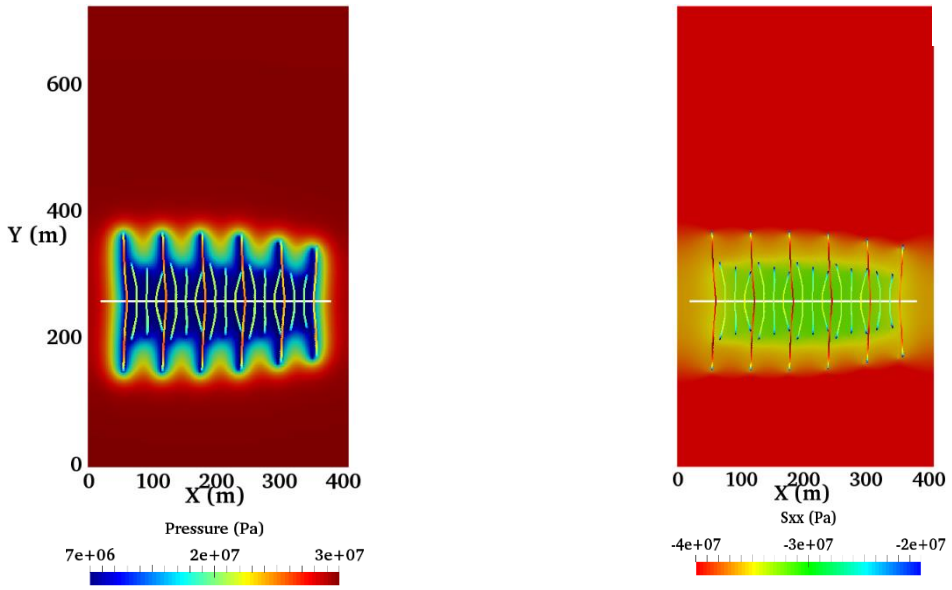

a) Pressure distribution b) S_{xx} distribution

Figure 5.3. Pressure (a) and S_{xx} (b) distribution after 2 years of production of case 1 (Sangnimnuan et al. 2019a).

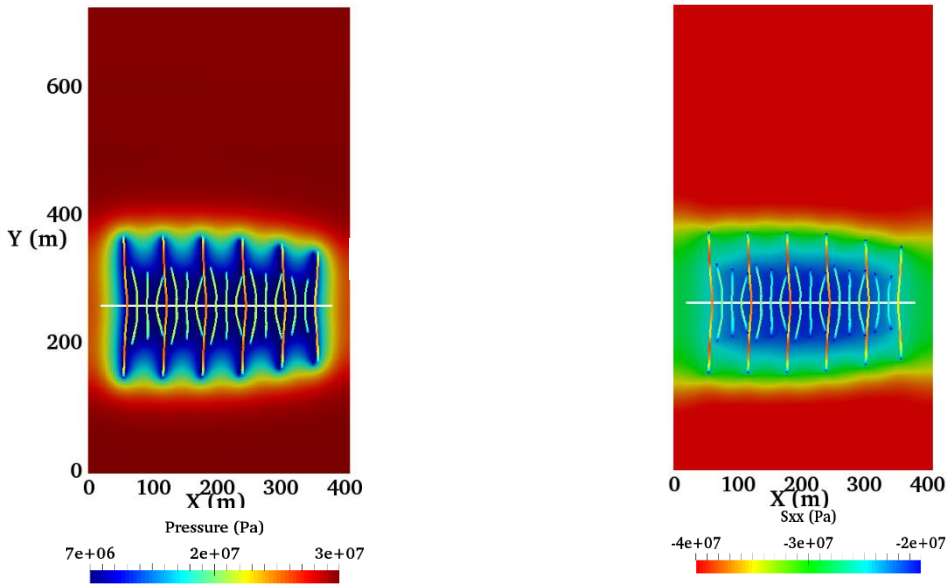

a) Pressure distribution b) S_{xx} distribution

Figure 5.4. Pressure (a) and S_{xx} (b) distribution after 5 years of production of case 1 (Sangnimnuan et al. 2019a).

Orientation of S_{yy} at 2-year and 5-year production are shown in Figures 5.5a and 5.5b respectively. Figure 5.5a shows orientation change or stress reversal (90^o change of orientation) at each fracture tip. This is due to the decrease in magnitudes of principle stresses, specifically S_{yy}, which eventually becomes smaller than S_{xx} at fracture tip area; however, as shown in Figure 5.5b for 5-year production, less orientation change can be observed at fracture tips, which is caused by a large reduction of S_{xx} causing S_{xx} to stay less than S_{yy} in magnitude. Figures 5.3b and 5.4b suggest that S_{xx} around SRV region becomes smaller as time progresses from 2 years to 5 years. As a result, S_{xx} becomes smaller than S_{yy} again causing stress to rotate back to its original direction.

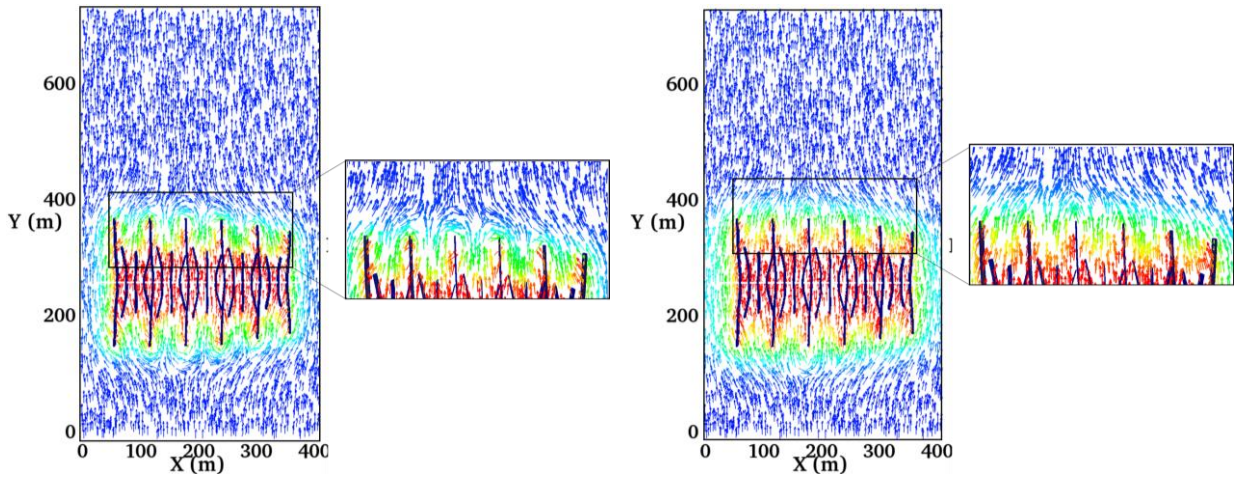

a) 2-year of production b) 5-year of production

Figure 5.5. Orientation change of S_{Hmax} after 2 years (a) and 5 years (b) of production (Sangnimnuan et al. 2019a).

Stress evolution directly affects completion sequence of infill well as fractures created from infill well may or may not hit fractures from parent well depending on the time at which infill well is completed as well spacing. Figures 5.6a and 5.6b show infill well fracture created after 2-year production of parent well in 3D at 150 and 210 m well spacing respectively. At 150 m well spacing, asymmetry fracture geometries can be observed with the longer fractures being on the depleted

side (closer to parent well). Some of the fractures tend to propagate towards existing fractures from parent well due to orientation change of principle stresses, which may eventually cause frac hits. On the other hand, at 210 m well spacing, symmetry fracture geometries can be observed, meaning that frac hit is less likely to occur as the fractures are less affected by depletion.

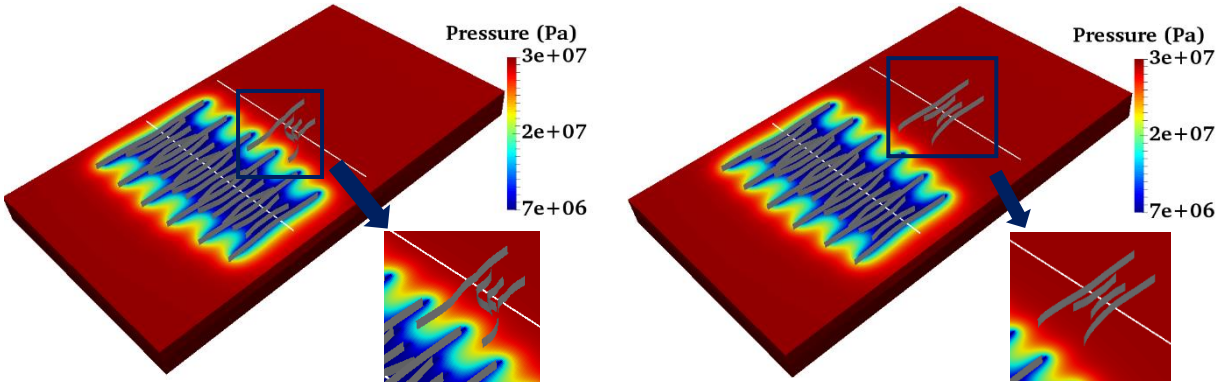

a) 150 m well spacing b) 210 m well spacing

Figure 5.6 Infill well fracture at 150 and 210 m well spacing after 2 years of production (Sangnimnuan et al. 2019a).

5.3.2.2 Case 2: Longer fracture length

Similar to case 1, orientation change of S_{Hmax} can mainly be observed around the fracture tip area after 2-year production, which suggests that frac hits can also occur if well spacing is short as shown in Figure 5.7. Figure 5.8 shows infill well fracture propagation at different well spacing (150 m, 210 m, and 270 m). Severe asymmetry fracture geometries can be observed for both outer fractures for the case of 150 and 210 m well spacing. This is due to large pressure depletion which significantly reduces S_{hmin} and induces fracture propagation. Frac-hits can clearly be observed for both outer fractures; however, the infill well fractures can still continue to propagate despite already hitting parent fractures as parent fractures are not included in the simulation of infill well fracture propagation. As the infill well moves further to 270 m, less asymmetry fracture geometry

can be observed due to less effect of reservoir depletion. It is however expected that frac-hits can still occur if injection time takes longer as fractures will continue to propagate towards depleted zone and become more asymmetry as they get closer.

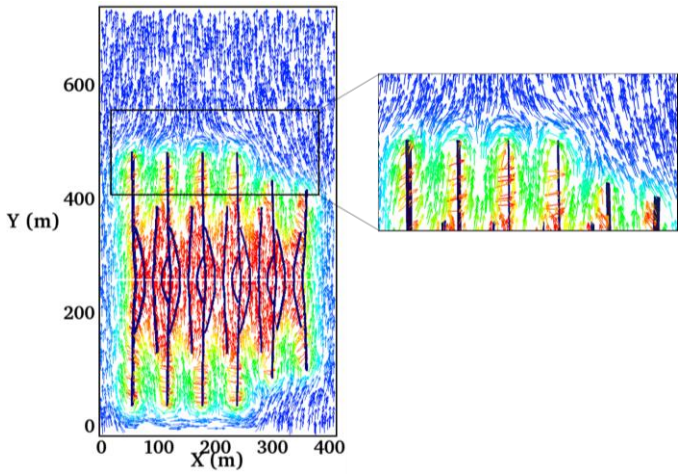

Figure 5.7. Orientation change of S_{Hmax} after 2-year production for case 2 (Sangnimnuan et al. 2019a).

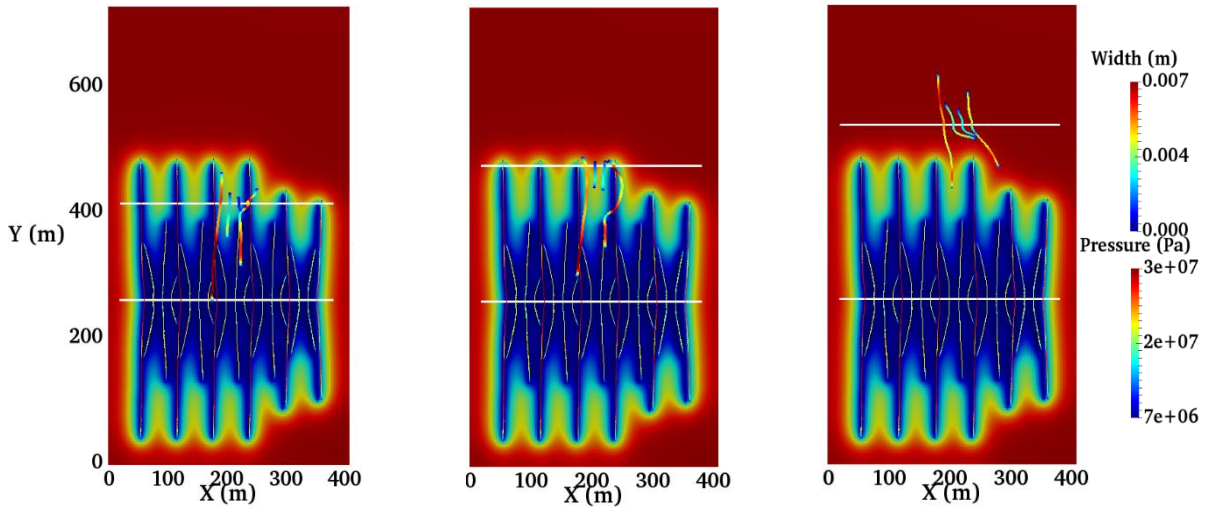

a) 150 m well spacing b) 210 m well spacing c) 270 m well spacing

Figure 5.8. Infill well geometry at different spacing for case 2 (Sangnimnuan et al. 2019a).

5.3.3 The case with natural fractures

As mentioned in section 5.3.1, natural fractures are included only when creating parent well fractures and during the production. This is to create more complex fracture system and geometries. More severe orientation change of S_{yy} can be observed after 2-year production as shown in Figure 5.9, which suggests that frac-hits are less likely to occur for this case as S_{yy} rotates almost 90^o. Therefore, infill well fractures are likely to turn 90^o rather than propagating directly towards parent fractures. In addition, it can be observed that infill well fractures do not interact with natural fractures as natural fractures are not included in the simulation of infill well fractures, thus, fractures will only follow the path of S_{yy}. Figure 5.10 shows infill well fracture propagation at different well spacing (150 m, 180 m, and 210 m), which is in good agreement with the orientation of S_{yy} as shown in Figure 5.9. Similar to case 2, unfavorable fracture geometries can mainly be observed at 150 and 180 m well spacing due to effect of depletion from parent well. However, the fractures tend to turn 90^o first before reaching the depleted zone due to presence of natural fractures, which creates more stress reorientations around tips of parent well fractures. According to Figure 5.10a, even fractures already turned almost 90^o, frac hits can still occur once infill well fractures reach depleted zone, which takes longer time compared to case without natural fractures. As the well moves further to 210 m, fractures become more symmetry due to less depletion effect. Similar to case 2, even at larger well spacing, fractures can still become more asymmetry as the injection time increases. Furthermore, less stress reorientation can be observed inside SRV region of parent well due to presence of natural fractures, which increases depletion rate, resulting in large reduction of S_{xx} compared to S_{yy}. Detailed explanations of stress reorientation mechanism can be found in Sangnimnuan et al. (2018b).

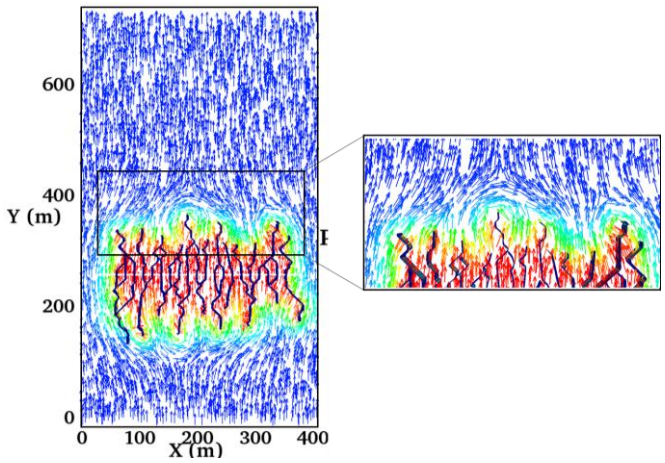

Figure 5.9. Orientation change of S_{Hmax} after 2-year production for case 3 (Sangnimnuan et al. 2019a).

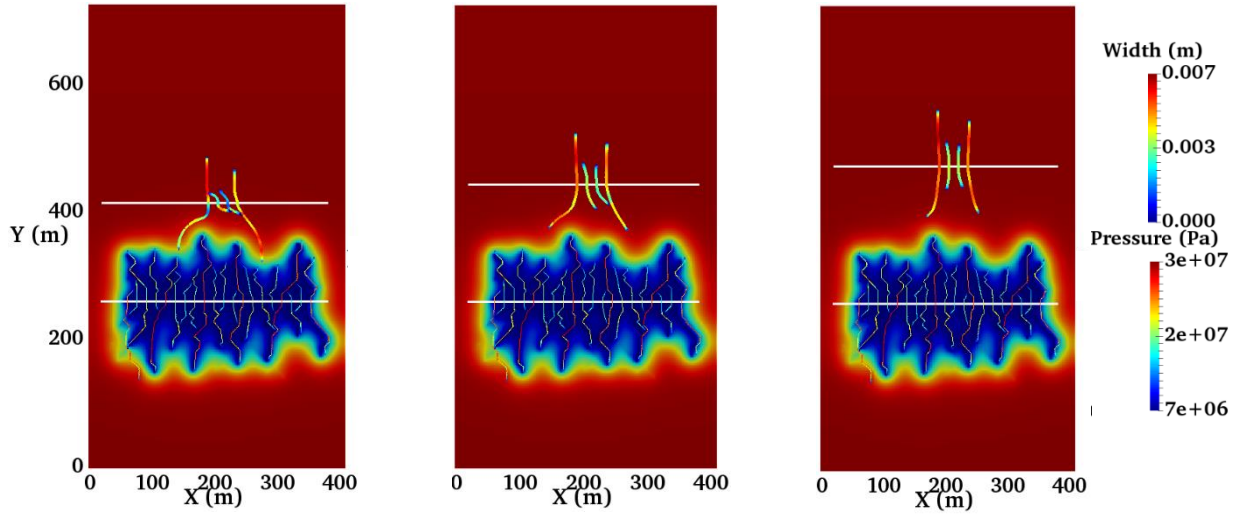

a) 150 m well spacing b) 180 m well spacing c) 210 m well spacing

Figure 5.10. Infill well geometry at different spacing for case 3 (Sangnimnuan et al. 2019a).

5.4 Conclusions

The coupled fluid flow and geomechanics was successfully applied to characterize stress change and evolution in reservoir with complex fracture geometries and natural fractures due to

depletion and fracture propagation model to investigate frac hits between parent and infill wells. Major findings can be summarized as follows:

1. Unsymmetrical fracture geometries with the longer fracture side being closer to the depleted zone can be observed in all cases as the main factor affecting fracture propagation is the distance between the depleted zone and infill well. The smaller the well spacing, the more likely fractures become unsymmetrical. This leads to detrimental production in infill well as the fracture length on the side with no depletion is very minimal compared to the side with depletion.
2. Frac hits can be seen in all cases whether the fracture geometry/system is very complicated or not. The main factor determining whether frac hits would occur is injection time or leak-off rate during infill well fracture propagation given the same well spacing. For case 2, it is very easy for infill well fractures to hit parent well fractures even at large well spacing due to length of parent well fractures. However, for the cases 1 and 3, it can take much longer time at the same well spacing for frac hits to occur due to stress reorientation. Loss of production in parent well is expected once frac hits occur as parent well fractures and infill well fractures are connected.
3. Completion time of infill well is also another main factor affecting frac hits as principal stresses evolve and change direction over time. Based on our case study, frac hits are more likely to be observed at 5-year production due to less orientation change; therefore, it is easier for infill well fractures to propagate towards parent well fractures. Operators should take into account not only well spacing but also completion time of infill well as well as fracture geometries if data is available to avoid frac hits.

CHAPTER 6: COUPLED GEOMECHANICS AND TWO-PHASE FLOW

6.1 Introduction

Understanding stress changes associated with reservoir depletion is very important for developments of unconventional reservoirs such as completion of infill well. Fluid flow in the reservoir often contains multiple phases mostly a mix of oil and water phase. Multiphase flow in porous media also involves in many applications including water injection. Coupling of geomechanics and multiphase flow is used to study stress change and reorientation due to reservoir depletion in petroleum engineering. Fluid contained in the reservoir can be a mix of multiple components. In addition, the capillary effect plays a significant role in pressure change in some cases, e.g. unsaturated soil in Opalinus clay. This directly affects material strength and subsurface deformation. Therefore, having considered multiphase flow in a coupling system of mechanical deformation and fluid flow is crucial for describing the aforementioned phenomena and performing accurate simulations.

For multiphase flow simulation, there are 2 well-known methods; (1) a sequential approach, Implicit Pressure Explicit Saturation (IMPES) and (2) a coupled approach, Fully Implicit Method (FIM). The IMPES method treats all terms that depend on saturation, except the transient terms, as explicit functions of saturation. This significantly reduces computational time as the system is completely decoupled. However, due to the presence of explicit terms, a numerical simulation can be unstable in some cases especially when the capillary effect is included. Reducing time step size can help maintain the stability of the simulation, but it also increases computational time which makes this method become inferior to FIM for certain types of problems. The FIM solves the same system of equations simultaneously (fully coupled), which makes the solutions

become unconditionally stable despite having a large system of equations (Cao, 2002, Gerritsen et al., 2005, and Chen et al., 2006).

In this chapter, the coupled fluid flow and geomechanics with Embedding Discrete Fracture Model (EDFM) was upgraded to be able to simulate two-phase flow using OpenFOAM, an open-source platform for CFD, in order to expand the model to wider range of applications including characterization of stress evolution associated with depletion of two-phase flow in unconventional reservoirs with complex fracture geometries. The two-phase model is based on Implicit Pressure Explicit Saturation (IMPES) method and is adopted from Horgue et al. (2014). Horgue applied an IMPES method to develop a dedicated toolbox in OpenFOAM for multiphase flow in porous media by modifying a generic porous medium model already available in OpenFOAM.. Validations of the single-phase model and EDFM were shown in chapter 2. Validation of two-phase model was done against analytical solution of Buckley-Leverett and Capillary-gravity equilibrium problems. In addition, validation of EDFM part was conducted against local grid refinement. The model was used to run a performance test on water injection-oil production problem with geomechanics and capillary effect. Non-planar fractures under production was also used to test for EDFM part. Finally, the model was applied in the simulation of 3D multiple fractures under production in a fully 3D reservoir.

6.2 Methodology

6.2.1 Two-phase flow model

The derivation of the two-phase flow model is based on Horgue et al. (2014). The model consists of mass and momentum conversation equations. Saturation S_i represents portion of

volume within the computational cell containing i-phase of fluid. The flow of a non-wetting phase o (oil) and wetting phase w (water) through the porous medium can be expressed as

$$S_w + S_o = 1. \quad \text{(6.1)}$$

Mass balance equation for each phase i can be written as

$$\phi \frac{\mathrm{d}(\rho_i S_i)}{\mathrm{dt}} + \nabla \cdot V_i = \rho_i q_i, \quad \text{(6.2)}$$

where ρ_i is density of phase i, q_i is the source or sink term of phase I, and V_i is fluid flow rate of phase i, which can be written in terms of pressure through Darcy's law as

$$V_i = -\frac{k_i}{\mu_i}(\nabla p_i - \rho_i g), \quad \text{(6.3)}$$

where μ_i is fluid viscosity and k_i is apparent permeability, which can be expressed as

$$k_i = K k_{ri}. \quad \text{(6.4)}$$

K is the matrix permeability (rank-2 tensor) and k_{ri} is the relative permeability of phase i, in which the value is in between 0 and 1 depending on local saturation of the phase i. Relationship between fluid saturation and relative permeability can usually be obtained from the field, but in some cases, the relationship can be obtained through relative permeability correlations (Brooks and Corey and Van Genuchten). The details of the two models can be found in Appendix B. Fluid density can be expressed in terms of pressure through compressibility terms as

$$c_i = \frac{1}{\rho_i}\frac{\partial \rho_i}{\partial p_i},$$

……...

(6.5)

With the presence of capillary effect inside the porous medium, pressure of each phase is not the same resulting in a macro-scale capillary pressure (p_c), which represents the difference between pressures of two phases as follows

$$p_c = p_o - p_w. \quad \text{(6.6)}$$

Substitute Eqs. (6.4), (6.5) and (6.6) in (6.3) and Eq. (6.3) in (6.2), mass balance equations can be rewritten as

$$\phi \frac{\partial S_w}{\partial t} + \phi S_w c_w \left(\frac{\partial p_o}{\partial t} - \frac{\partial p_c}{\partial t}\right) + \nabla \cdot \left(\frac{-Kk_{rw}}{\mu_w}(\nabla p_o - \nabla p_c - \rho_w g)\right) = q_w,$$

…….... (6.7)

$$-\phi \frac{\partial S_w}{\partial t} + \phi S_o c_o \left(\frac{\partial p_o}{\partial t}\right) + \nabla \cdot \left(\frac{-Kk_{ro}}{\mu_o}(\nabla p_o - \rho_o g)\right) = q_o.$$

....…….....…… (6.8)

Assuming capillary pressure only depends on saturation, the capillary terms can be rewritten as

$$\frac{\partial p_c}{\partial t} = \frac{\partial p_c}{\partial S_w}\frac{\partial S_w}{\partial t},$$

……..……..... (6.9)

$$\nabla p_c = \frac{\partial p_c}{\partial S_w}\nabla S_w.$$

……..…….... (6.10)

Momentum balance or pressure equation can be obtained by adding Eq. (6.8) to Eq. (6.7) and using relationship in Eqs. (6.9) and (6.10)

$$(\phi S_w c_w + \phi S_o c_o)\frac{\partial p_o}{\partial t} - \phi S_w c_w \frac{\partial p_c}{\partial S_w}\frac{\partial S_w}{\partial t} - \nabla \cdot \left(\frac{Kk_{ro}}{\mu_o} + \frac{Kk_{rw}}{\mu_w}\right)\nabla p_o + \nabla \cdot \frac{Kk_{rw}}{\mu_w}\frac{\partial p_c}{\partial S_w}\nabla S_w + \nabla \cdot \left(\frac{Kk_{ro}}{\mu_o}\rho_o + \frac{Kk_{rw}}{\mu_w}\rho_w\right) g = q_o + q_w.$$

…….. (6.11)

To simplify the formulation, phase mobility M_i and gravitational contribution L_i can be defined as follows

$$M_i = \frac{Kk_{ri}}{\mu_i},$$

……...…….. (6.12)

$$L_i = \frac{Kk_{ri}}{\mu_i}\rho_i,$$

……...……. (6.13)

Substitute Eqs. (6.12) and (6.13) in (6.11), we obtain

$$(\phi S_w c_w + \phi S_o c_o)\frac{\partial p_o}{\partial t} - \phi S_w c_w \frac{\partial p_c}{\partial S_w}\frac{\partial S_w}{\partial t} - \nabla \cdot (M_o + M_w)\nabla p_o + \nabla \cdot M_w \frac{\partial p_c}{\partial S_w}\nabla S_w + \nabla \cdot (L_o + L_w) g = q_o + q_w.$$

…….. (6.14)

And water saturation equation can be rewritten from Eq. (6.6) as

$$\phi \frac{\partial S_w}{\partial t} + \phi S_w c_w \left(\frac{\partial p_o}{\partial t} - \frac{\partial p_c}{\partial t}\right) + \nabla \cdot \left(-M_w \nabla p_o + M_w \frac{\partial p_c}{\partial S_w} \nabla S_w + L_w g\right) = q_w,$$

…….. (6.15)

Eqs. (6.14) and (6.15) have strong non-linearities due to relative permeabilities and capillary pressure correlations. Solving system of equations requires the use of non-linear solver and involves high computational time. In order to reduce computational time, IMPES algorithm is used in this work (Sheldon et al., 1959). IMPES allows the two equations to be solved sequentially rather than simultaneously, which results in less computational time but also less stable. In order to ensure the stability of the simulation, the time-step limitation is introduced.

6.2.2 Time-step limitations

As mentioned in Horgue et al. (2014), two conditions can be used to set the time-step. The first one is from classical OpenFOAM multiphase solvers (Jasak, 1996 and Rusche, 2002), which is related to the Courant number C_o. The second possible limitation commonly used for pressure equation in IMPES method is the CFL condition (Coats, 2003 and Preux, 2011). Definition of C_o and CFL condition can be found in Appendix A. The stability for both conditions, CFL or C_o is not ensured if source/sink term are present as they are not included in the formulations. In that case, a user-defined maximal variation of saturation $\Delta S_{w,max}$ is to be added along with either CFL or C_o condition. The variation of S_w between two-time steps should satisfy

$$\Delta S_{w,n\to n+1} \leq \Delta S_{w,max}, \quad \text{..... (6.16)}$$

which can be rewritten as

$$\Delta t_{S_w} = min\left\{\frac{V_c \Delta S_{w,max}}{\phi\left(-\sum_{f=0}^{m} V_w \cdot S_f + V_c q_w\right)}\right\},$$

……. (6.17)

where V_c is cell volume, S_f is face of computational grid. Then the global time step for the next iteration is given by

$$\Delta t_n = \min\left(\Delta t_{S_w}, \Delta t_p\right). \quad \text{……..……... (6.18)}$$

Δt_p can be obtained through either C_o or CFL condition. Algorithm to compute system of equation can be found as follows

1. Compute Δt_{n+1} from the two conditions (C_o or CFL and $\Delta S_{w,\,max}$).
2. Saturation S_w^{n+1} is explicitly computed using relative permeabilities and pressure field p^n from the previous time step
3. Relative permeabilties and capillary pressure are updated using S_w^{n+1} (either through Brooks and Corey/Van Genuchten or actual curve)
4. Pressure field p^{n+1} is implicitly computed using all updated properties
5. Repeat step 1 to 4 until residual of pressure equation is less than a specified tolerance then move onto next time step

6.2.3 Coupled two-phase flow and geomechanics

Coupled fluid-flow and geomechanics is based on biot's theory (Biot, 1941, 1955), which describes the poroelastic effect in isothermal linear isotropic poroelastic material. Mechanical deformation can be and relationship between stress and strain with poroelastic effect can be found in Eqs. (2.1) and (2.2). However, the pressure term shown in Eq. (2.2) is an averaged pressure between each phase (Yang, 2013), which can be rewritten as

$$\sigma - \sigma_0 = C_{dr} : \varepsilon - b(\bar{p} - \overline{p_0})I,\ \bar{p} = S_o p_o + S_w p_w.$$

…..…. (6.19)

Pressure equation with capillary and gravitational effect can be formulated as

$$\frac{1}{M}\frac{\partial p_o}{\partial t} - \left(\frac{b-\phi}{K_s}S_w\frac{\partial p_c}{\partial S_w} + \phi S_w c_w \frac{\partial p_c}{\partial S_w}\right)\frac{\partial S_w}{\partial t} + b\frac{\partial \varepsilon_v}{\partial t} - \nabla\cdot\left(M_o + M_w\right)\nabla p_o + \nabla \cdot M_w \frac{\partial p_c}{\partial S_w}\nabla S_w + \nabla\cdot\left(L_o + L_w\right)g = q_o + q_w.$$

……...…..……. (6.20)

Saturation equation can also be formulated in the same way as follows

$$\left(\phi - \phi S_w c_w \frac{\partial p_c}{\partial S_w} - S_w\frac{b-\phi}{K_s}S_w\frac{\partial p_c}{\partial S_w}\right)\frac{\partial S_w}{\partial t} + \left(\frac{b-\phi}{K_s} + \phi c_w\right)S_w\left(\frac{\partial p_o}{\partial t}\right) + S_w b\frac{\partial \varepsilon_v}{\partial t} - \nabla \cdot \left(-M_w\nabla p_o + M_w\frac{\partial p_c}{\partial S_w}\nabla S_w + L_w g\right) = q_w.$$

…….…...…….. (6.21)

where M is the Biot modulus and a scalar quanity. Relationship between Biot modulus and bio coefficient can be shown as

$$\frac{1}{M} = \phi S_w c_w + \phi S_o c_o + \frac{b-\phi}{K_s},$$

....…..…… (6.22)

$$b = 1 - \frac{K_{dr}}{K_s},$$

……..…...…… (6.23)

where K_s is bulk modulus of solid grain and K_{dr} is drained bulk modulus, which can be computed from drained rock properties, i.e. Young's modulus (E) and Poisson's ratio (ν) and according to

Kim et al. (2011), K_{dr} can be chosen to achieve an optimal convergence rate for the fixed-stress iterative coupling

$$K_{dr} = \frac{E(1-\nu)}{(1+\nu)(1-2\nu)}. \quad \text{..... (6.24)}$$

Volumetric mean total stress is trace of the stress tensor ($\sigma_v = \frac{1}{3}\, tr\sigma$). Eqs. (6.19), (6.20), and (2.8) are called fixed-strain split (Kim et al., 2011) for two-phase flow, in which the equations are solved in terms of strain. Fixed-strain represents the sequential method that geomechanics and fluid flow equations are solved separately starting by solving Eq. (6.20) first, following by Eq. (6.19), and finally Eq. (20) using relationship in Eq. (2.3). Iteration stops when convergent criteria are reached on pressure and mechanical equations. As demonstrated by Kim et al. (2011), this method is not stable for high coupling strength ($\tau = \frac{b^2 M}{K_{dr}} > 1$). Thus, Eqs. (6.20) and (6.21) are modified by writing volumetric strain in terms of volumetric strength (σ_v) as

$$\left(\frac{1}{M} + \frac{b^2}{K_{dr}}\right)\frac{\partial p_o}{\partial t} - \left(\frac{b-\phi}{K_s} S_w \frac{\partial p_c}{\partial S_w} + \phi S_w c_w \frac{\partial p_c}{\partial S_w}\right)\frac{\partial S_w}{\partial t} + b\frac{\partial \sigma_v}{\partial t} - \nabla \cdot \left(M_o + M_w\right)\nabla p_o + \nabla \cdot M_w \frac{\partial p_c}{\partial S_w}\nabla S_w + \nabla \cdot \left(L_o + L_w\right) g = q_o + q_w,$$

..... (6.25)

$$\left(\phi - \phi S_w c_w \frac{\partial p_c}{\partial S_w} - S_w \frac{b-\phi}{K_s} S_w \frac{\partial p_c}{\partial S_w}\right)\frac{\partial S_w}{\partial t} + \left(\phi S_w c_w + \frac{b^2}{K_{dr}} + S_w \frac{b-\phi}{K_s}\right)\frac{\partial p_o}{\partial t} + S_w b \frac{\partial \sigma_v}{\partial t} + \nabla \cdot \left(-M_w \nabla p_o + M_w \frac{\partial p_c}{\partial S_w}\nabla S_w + L_w g\right) = q_w.$$

..... (6.26)

Relationship between displacements and pressure under the momentum balance condition is similar to Eq. (2.14) but with an averaged pore pressure as follows

$$\nabla \cdot [\mu \nabla u + \mu \nabla u^T + \lambda I tr(\nabla u)] + \nabla \cdot \sigma_0 - b \nabla \bar{p} + b \nabla \overline{p_0} = 0. \quad \text{..... (6.27)}$$

Eqs. (6.25) and (6.26) can also be written in terms of displacement with fixed-stress split condition as

$$\left(\frac{1}{M} + \frac{b^2}{K_{dr}}\right)\frac{\partial {p_o}^n}{\partial t} - \frac{b^2}{K_{dr}}\frac{\partial {p_o}^{n-1}}{\partial t} - \left(\frac{b-\phi}{K_s} S_w \frac{\partial p_c}{\partial S_w} + \phi S_w c_w \frac{\partial p_c}{\partial S_w}\right)\frac{\partial S_w}{\partial t} + b\frac{\partial (\nabla \cdot u)}{\partial t} - \nabla \cdot (M_o + M_w)\nabla {p_o}^n + \nabla \cdot M_w \frac{\partial p_c}{\partial S_w}\nabla S_w + \nabla \cdot (L_o + L_w) g = q_o + q_w,$$

..... (6.28)

$$\left(\phi - \phi S_w c_w \frac{\partial p_c}{\partial S_w} - S_w \frac{b-\phi}{K_s} S_w \frac{\partial p_c}{\partial S_w}\right)\frac{\partial S_w}{\partial t} + \left(\phi S_w c_w + \frac{b^2}{K_{dr}} + S_w \frac{b-\phi}{K_s}\right)\frac{\partial {p_o}^n}{\partial t} - \frac{b^2}{K_{dr}}\frac{\partial {p_o}^{n-1}}{\partial t} + S_w b \frac{\partial (\nabla \cdot u)}{\partial t} + \nabla \cdot \left(-M_w \nabla p_o + M_w \frac{\partial p_c}{\partial S_w}\nabla S_w + L_w g\right) = q_w.$$

..... (6.29)

where n is the current time step and n-1 is previous time step. Eqs. (6.27), (6.28) and (2.14) are solved through an iteration loop to obtain saturation, pressure, and displacement as shown in Figure 6.1, detail of numerical discretization will be discussed in section 6.3.

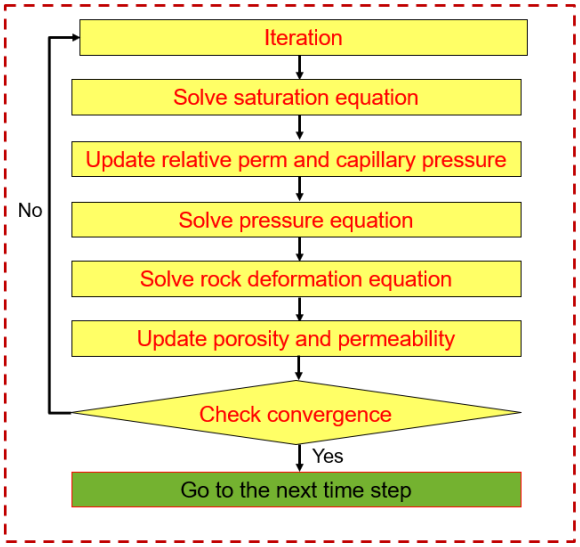

Figure 6.1. Diagram showing fixed-stress method for two-phase flow and geomechanics.

6.2.4 Coupled two-phase flow and geomechanics with EDFM

In this section, EDFM was implemented to the coupled model to efficiently simulate complex fracture geometry without using unstructured grids. As mentioned by Xu et al. (2015), EDFM has been developed with the concept to honor the accuracy of discrete fracture models (DFMs) while keeping the efficiency offered by structured grids. The implementation is similar to what is discussed in section 2.2.2 that is the reservoir is divided into two separated domains, fracture and matrix. Relative mobility is to be modified to represent two-phase flow as follows

$$\lambda_t = \left(\frac{k_{ro}}{\mu_o} + \frac{k_{rw}}{\mu_w}\right). \quad \text{..... (6.30)}$$

Following Eqs. (2.17) to (2.22), mass conservation inside matrix domain without capillary and gravitational effect can be expressed as

$$\left(\frac{1}{M}+\frac{b^2}{K_{dr}}\right)\frac{\partial {p_o}^n}{\partial t}-\frac{b^2}{K_{dr}}\frac{\partial {p_o}^{n-1}}{\partial t}+b\frac{\partial(\nabla\cdot u)}{\partial t}-\nabla\cdot(M_o+M_w)\nabla {p_o}^n+\lambda_t T_{f-m}({p_{of}}^n-{p_o}^n)=0.$$

(6.31)

Similarly, conservation in fracture can be written as

$$\frac{1}{M_f}\frac{\partial {p_{of}}^n}{\partial t}-\nabla\cdot\left(M_{of}+M_{wf}\right)\nabla {p_{of}}^n+\lambda_t T_{f-m}\left({p_o}^n-{p_{of}}^n\right)=q_o+q_w.$$

…….…. (6.32)

where subscript f represents fluid properties inside fracture. M_f is biot modulus inside the fracture domain calculated using modified porosity obtained from Eq. (2.18). M_{of} and M_{wf} can be computed using fluid viscosity and permeability of each phase inside the fracture domain. In addition to pressure equation, saturation equation needs to be modified as well for both matrix and fracture domain as follows

$$\phi\frac{\partial S_w}{\partial t}+\left(\phi S_w c_w+\frac{b^2}{K_{dr}}\right)\frac{\partial {p_o}^n}{\partial t}-\frac{b^2}{K_{dr}}\frac{\partial {p_o}^{n-1}}{\partial t}+S_w b\frac{\partial(\nabla\cdot u)}{\partial t}-\nabla\cdot(M_w\nabla {p_o}^n)+S_w\lambda_t T_{f-m}({p_{of}}^n-{p_o}^n)=0.$$

(6.33)

$$\phi_f\frac{\partial S_{wf}}{\partial t}+\phi_f S_{wf}c_{wf}\left(\frac{\partial {p_{of}}^n}{\partial t}\right)-\nabla\cdot\left(M_{wf}\nabla {p_{of}}^n\right)+S_{wf}\lambda_t T_{f-m}({p_o}^n-{p_{of}}^n)=q_w.$$

…..… (6.34)

S_{wf} is water saturation inside fracture domain. Eq. (6.33) is the saturation equation for the matrix domain and (6.34) is for fracture domain. Eqs. (6.32) and (6.34) are added to system of equations to solve for fracture pressure (p_f) and fracture water saturation (S_{wf}). With the presence of natural

fractures, additional transmissibility terms are added to pressure and saturation equation to incorporate communication between natural fractures and hydraulic fractures. Extra equations representing flow in each natural fracture set are also to be added to the system of equations Details of equation formulation can be found in Sangnimnuan et al. (2018b).

6.3 Numerical model

As stated in section 1, OpenFOAM has been used as a main solver for the model. Discretization is based on finite volume method (FVM), which is up to second-order accuracy and consists of time and space. Time discretization is implicit method and first-order accuracy, while spatial discretization consists of implicit and explicit methods, in which the majority is based on Gaussian linearization method. Discretization was discussed in Tian et al. (2015), which can be written in terms of integral form representing control volume (∂V) of each cell. Geomechanics Eq. (2.15) can be rewritten using Gauss's theorem to convert volume integral to surface integral as shown in Eq. (2.25). Fluid flow from Eq. (6.31) can be rewritten as

$$\int_V \left\{\left(\frac{1}{M}+\frac{b^2}{K_{dr}}\right)\frac{\partial {p_o}^n}{\partial t}\right\} d - \oint_{\partial V} ds \cdot \{(M_o + M_w)\nabla {p_o}^n\} - \int_V \left\{\lambda_t T_{f-m} {p_o}^n\right\} dV = \int_V \left\{\frac{b^2}{K_{dr}}\frac{\partial {p_o}^{n-1}}{\partial t}\right\} dV - b\oint_{\partial V} ds \cdot \frac{\partial u}{\partial t} - \int_V \left\{\lambda_t T_{f-m} {p_{of}}^n\right\} dV. \quad \text{..... (6.35)}$$

The first term in the left is an implicit time derivative of pressure. The second term is an implicit diffusion team and the last time is an implicit part of the flow transmissibility term. The first term in the right is an explicit term representing pressure from the previous time step, the second term

is an explicit displacement coupling term, and last term is an explicit part of flow transmissibility term. Fluid flow equation inside fractures (Eq. (6.32)) can be similarly discretized as Eq. (6.35).

$$\int_V \left\{\frac{1}{M_f}\frac{\partial {p_{of}}^n}{\partial t}\right\} dV - \oint_{\partial V} ds \cdot \left\{\left(M_{of} + M_{wf}\right)\nabla {p_{of}}^n\right\} - \int_V \left\{\lambda_t T_{f-m} {p_{of}}^n\right\} dV =$$

$$- \int_V \left\{\lambda_t T_{f-m} {p_o}^n\right\} dV + \int_V (q_o + q_w) dV.$$

…….....… (6.36)

Saturation equations for both matrix and fracture domain can also be discretized in a similar manner as follows

$$\int_V \left\{\phi \frac{\partial S_w}{\partial t}\right\} dV + \int_V \left\{\left(\phi S_w c_w + \frac{b^2}{K_{dr}}\right)\frac{\partial {p_o}^n}{\partial t}\right\} dV - \int_V \left\{\frac{b^2}{K_{dr}}\frac{\partial {p_o}^{n-1}}{\partial t}\right\} dV$$

$$+ \int_V \left\{S_w b \frac{\partial (\nabla \cdot u)}{\partial t}\right\} dV - \oint_{\partial V} ds \cdot \{M_w \nabla {p_o}^n\} =$$

$$- \int_V \left\{S_w \lambda_t T_{f-m}\left({p_{of}}^n - {p_o}^n\right)\right\} dV,$$

…… (6.37)

$$\int_V \left\{\phi \frac{\partial S_{wf}}{\partial t}\right\} dV + \int_V \left\{\phi S_{wf} c_{wf} \frac{\partial {p_{of}}^n}{\partial t}\right\} dV - \oint_{\partial V} ds \cdot \left\{M_{wf} \nabla {p_{of}}^n\right\} =$$

$$- \int_V \left\{S_{wf} \lambda_t T_{f-m}\left({p_{of}}^n - {p_o}^n\right)\right\} dV + \int_V q_w dV.$$

…… (6.38)

Eq. (6.37) is a discretization of the saturation equation for matrix domain and (6.38) is for fracture domain. With the discretization, system of equations consisting of three displacement equations, fluid-flow equations in matrix and fractures, and water saturation equations in matrix and fractures with 7 unknowns (i.e. u_x, u_y, u_z, p_o, p_{of}, S_w, S_{wf}) can then be solved sequentially using iterative method. Effective stress and total stress can be computed after obtaining displacement components and pressure using Eq. (2.2).

6.4 Validation

The validation part is divided into two sub-sections. The first part is the two-phase flow model, and the second part is implement of EDFM to the two-phase flow model. The validation of coupled geomechanics and fluid flow was carried out in Sangnimnuan et al., (2018a), in which our model shows a good agreement with analytical solution for both Terzaghi's and Mandel's problems.

6.4.1 Two-phase flow model

The first part of the model was validated against classical problems, in which analytical solutions exist. The validations consist of three cases, the first and second ones are Buckley-Leverett with and without gravitational effect and the last one is capillary-gravity equilibrium. The validation cases are similar to those provided by Horgue et al. (2014).

6.4.1.1 Buckley-Leverett

In this case, a simplified version of Buckley-Leverett is used, which is a two-phase flow in a 1D domain. The domain is initially fully saturated with non-wetting phase which is either air or oil, then wetting fluid (water) is being injected with a fixed constant velocity $V_w = 1 \times 10^{-5}$ m/s with fixed reference pressure = 0 Psi at the top. With this set-up, shock front saturation is expected

to be observed and as the time increases, shock front should propagate from one end (injection point) to another end of the domain (top). Problem geometry is shown in Figure 6.2a. Column height is 1 m with 400 computational cells to be able to capture shock-front. Parameters used in this problem are shown in Table 6.1.

Quantity	Value	Unit
Reservoir permeability (k)	$1x10^4$	d
Reservoir porosity (ϕ)	0.5	-
Water viscosity (μ_w)	1	cp
Oil viscosity (μ_o)	100	cp
Gas viscosity (μ_o)	0.0176	cp
Water density (ρ_w)	1000	kg/m^3
Oil density (ρ_o)	800	kg/m^3
Gas density (ρ_o)	1	kg/m^3

Table 6.1. Parameters used in the validation of two-phase flow model.

Two relative permeability models are used for numerical validation, the first one is the water-air system for Brooks and Corey model and the second one is a water-oil system for the Van Genuchten model. Figure 6.3 shows a comparison between analytical and numerical solutions for saturation profile along the domain at different times for both models (a and b). Both models show a good agreement between numerical results and analytical solution with some minor numerical diffusion mainly due to the upwind scheme used for the relative permeability computation.

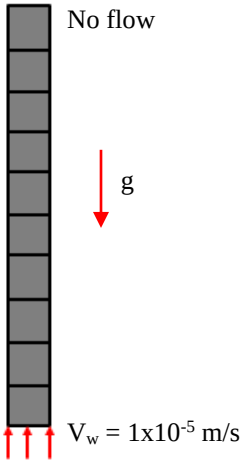

(a) Problem configuration for problem 6.4.1.1

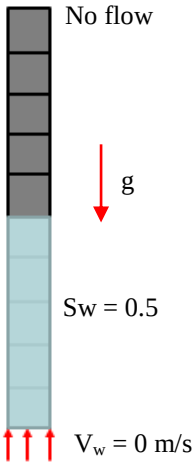

(b) Problem configuration for problem 6.4.1.2

Figure 6.2. Problem configuration for 1-dimension Buckley-Leverett with gravitational and capillary effect.

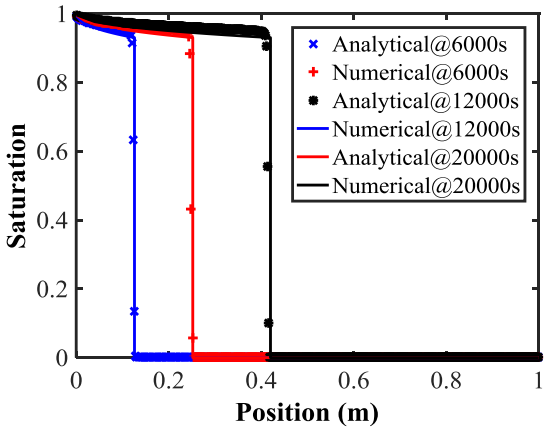

(a) Saturation profile for Brooks and Corey model

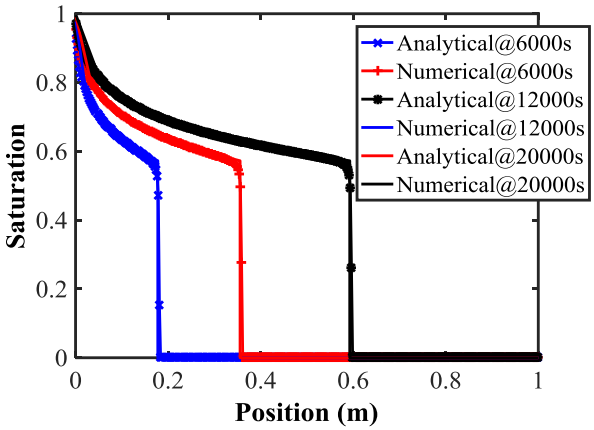

(b) Saturation profile for Van Genuchten model

Figure 6.3. Saturation profile for the Brooks and Corey (a) and the Van Genuchten model (b) for analytical and numerical solutions.

Gravitational effect is also studied in both models. The same set-up is used for Brooks and Corey's model; however, for Van Genuchten model, fluids change from oil-water to air-water. The difference is the gravitational term (Eq. 6.13) is taken into account when running the simulation.

Comparisons between numerical and analytical results can be found in Figure 6.4, which also shows a good agreement between the two for both models in terms of location of shock front at different times.

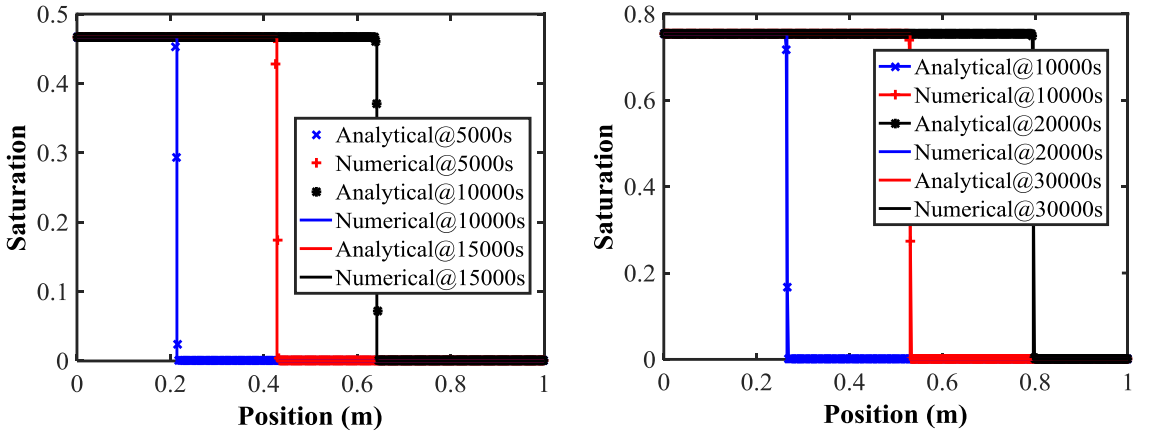

(a) Saturation profile for Brooks and Corey model

(b) Saturation profile for Van Genuchten model

Figure 6.4. Saturation profile with gravitational effect for the Brooks and Corey (a) and the Van Genuchten model (b) for analytical and numerical solutions.

6.4.1.2 Capillary-gravity equilibrium

Another validation case is a two-phase flow (air and water) with capillary effect in a vertical 1D domain. The set-up is similar to previous problem except that the bottom boundary is now a fixed wall or zero velocity both wetting and not-wetting phase with the top boundary being the same as previous problem. Lower half of the domain is set to have $S_w = 0.5$ then the simulation is run for a period of 2×10^6 s to allow the establishment of a saturation profile along the vertical axis. Problem configuration can be found in Figure 6.2b. Parameters used in this problem is similar to previous problem as shown in Table 1. A comparison between numerical and analytical solution can be found in Figure 6.5, which includes both saturation profile (a and c) and saturation gradient (b and d) for both Brooks and Corey and Van Genuchten model. For this problem, analytical

solutions only exist for gradient of saturation in which numerical solutions are seen to be in a good agreement with analytical solution for both models.

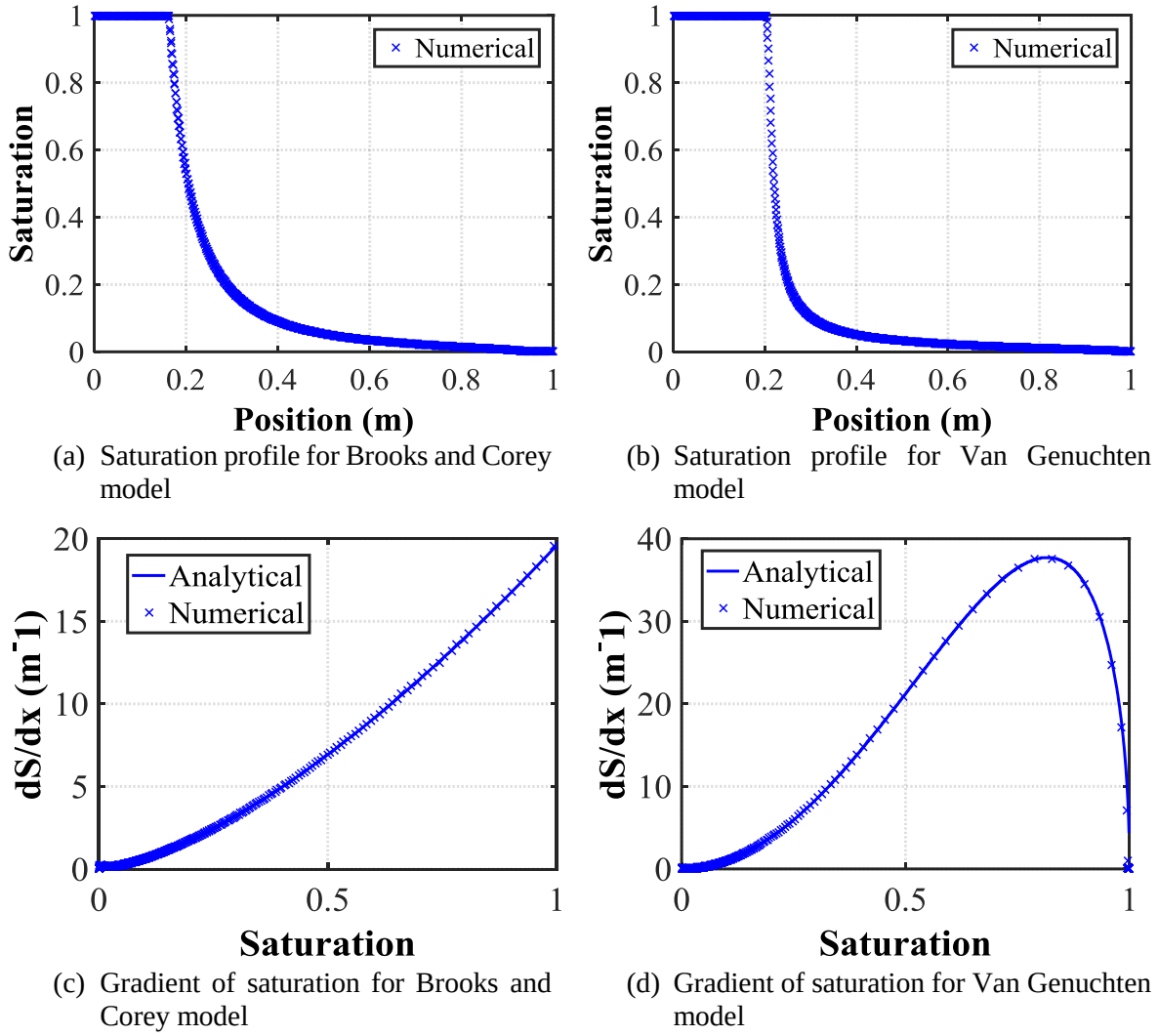

(a) Saturation profile for Brooks and Corey model

(b) Saturation profile for Van Genuchten model

(c) Gradient of saturation for Brooks and Corey model

(d) Gradient of saturation for Van Genuchten model

Figure 6.5. Saturation profile and gradient for the Brooks and Corey model (a and c) and the Van Genuchten model (b and d).

6.4.2 Coupled two-phase flow model with EDFM

As stated in section 6.1, EDFM is coupled to the two-phase flow model to allow simulation of complex fracture geometries using a structured grid. To ensure the accuracy of the model, validation was carried out using a reservoir consisting of 4 planar fractures with fracture spacing

of 80 ft as shown in Figure 6. Initially, the reservoir is filled with oil and water with water saturation being 0.42. Domain size is 1500x1600 ft with L_x = 75 and L_y = 80. Local grid refinement (LGR) was used as a reference when making comparison with our model. Reservoir pressure is 8125 psi and bottomhole pressure is 3500 psi. Brooks and Corey's model was used for relative permeability calculation. Other parameters used in the simulation can be found in Table 6.2.

Quantity	Value	Unit
Reservoir permeability (k)	464	μd
Reservoir porosity (ϕ)	0.12	-
Water compressibility (c_w)	$3.2x10^{-6}$	psi^{-1}
Oil compressibility (c_o)	$1x10^{-5}$	psi^{-1}
Water viscosity (μ_w)	1	cp
Oil viscosity (μ_o)	0.6	cp
Water density (ρ_w)	1000	kg/m^3
Oil density (ρ_o)	800	kg/m^3

Table 6.2. Parameters used in EDFM validation problem.

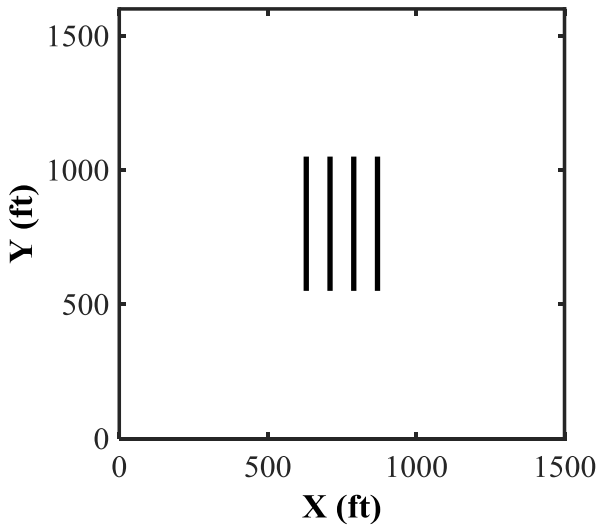

Figure 6.6. Problem configuration for 4 planar fractures under production.

Figures 6.7 and 6.8 show a comparison between LGR and EDFM on pressure distribution and water saturation at 1 year and 5 years production respectively. As shown in figures, the

difference between our model and local grid refinement is insignificant for pressure distribution plot. A very small difference can be observed along each fracture for water saturation at both 1 and 5 years with the LGR having a bit higher water concentration. However, this difference does not contribute to either water or oil production as shown in Figure 6.9. Water and oil productions obtained from our model are plotted against results from LGR for up to 10 years of production.

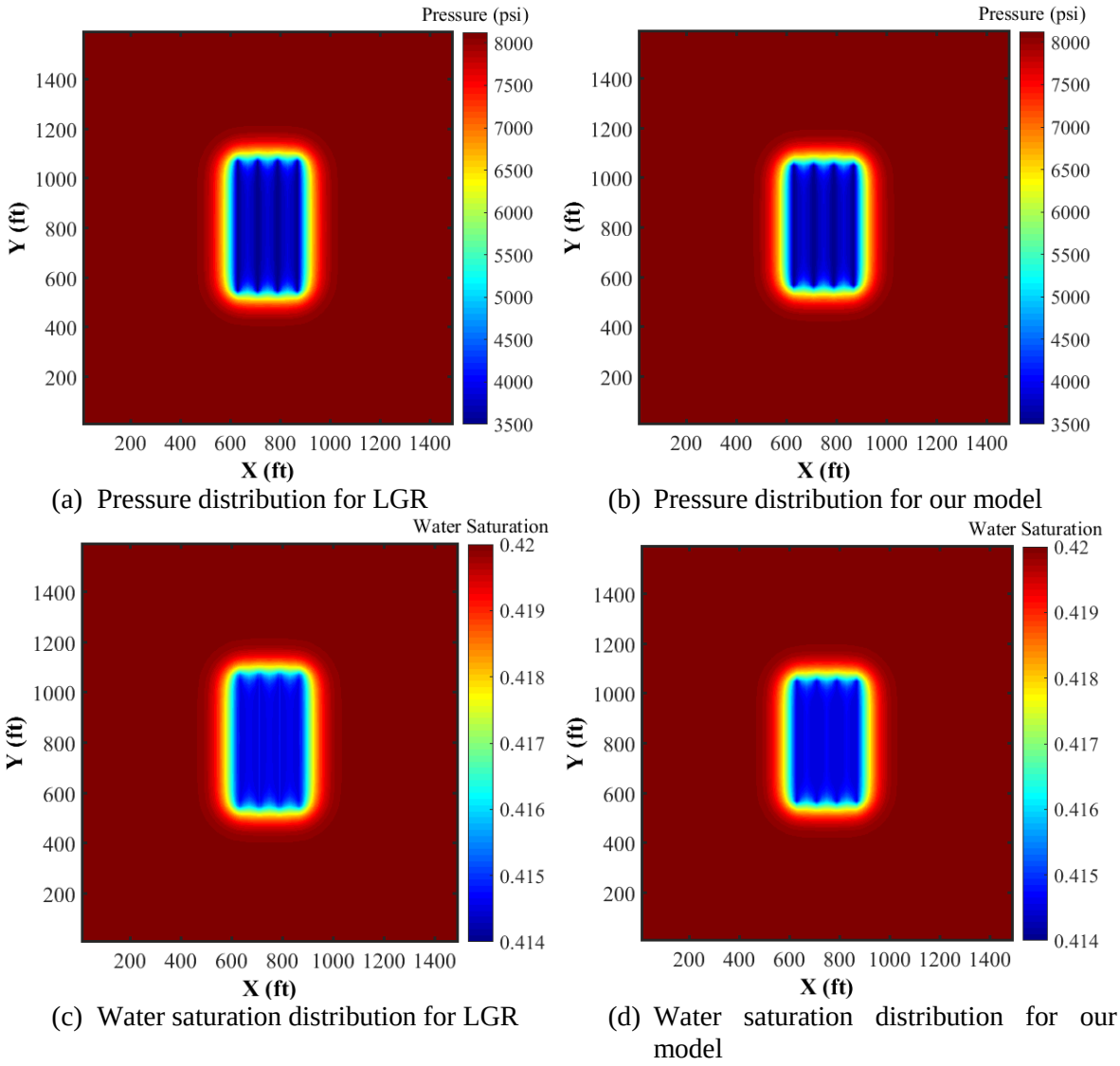

(a) Pressure distribution for LGR

(b) Pressure distribution for our model

(c) Water saturation distribution for LGR

(d) Water saturation distribution for our model

Figure 6.7. Pressure distribution for LGR (a) and our model (b) and water distribution for LGR (c) and our model (d) at 1 year of production.

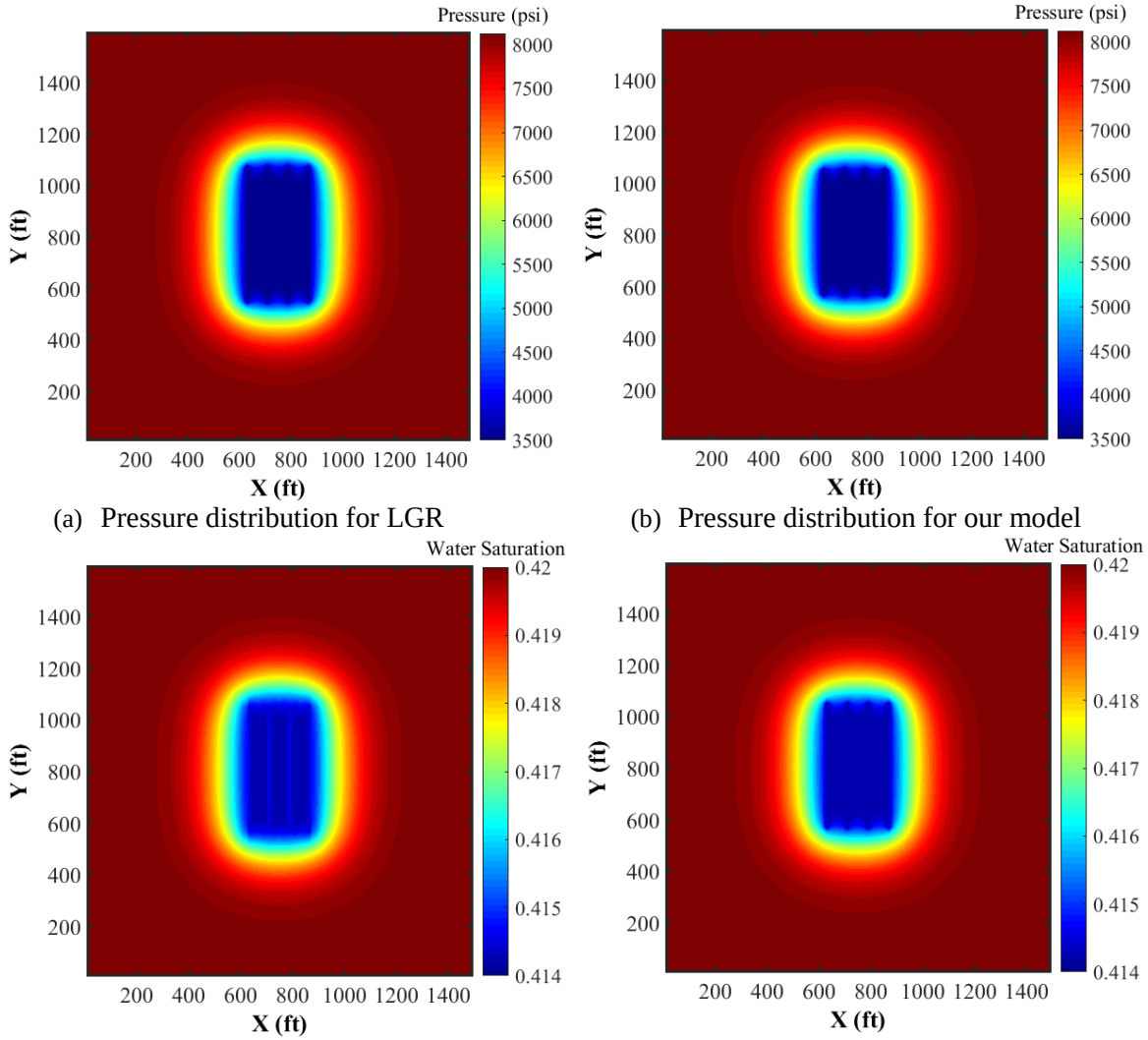

(a) Pressure distribution for LGR

(b) Pressure distribution for our model

(c) Water saturation distribution for LGR

(d) Water saturation distribution for our model

Figure 6.8. Pressure distribution for LGR (a) and our model (b) and water distribution for LGR (c) and our model (d) at 5 years of production.

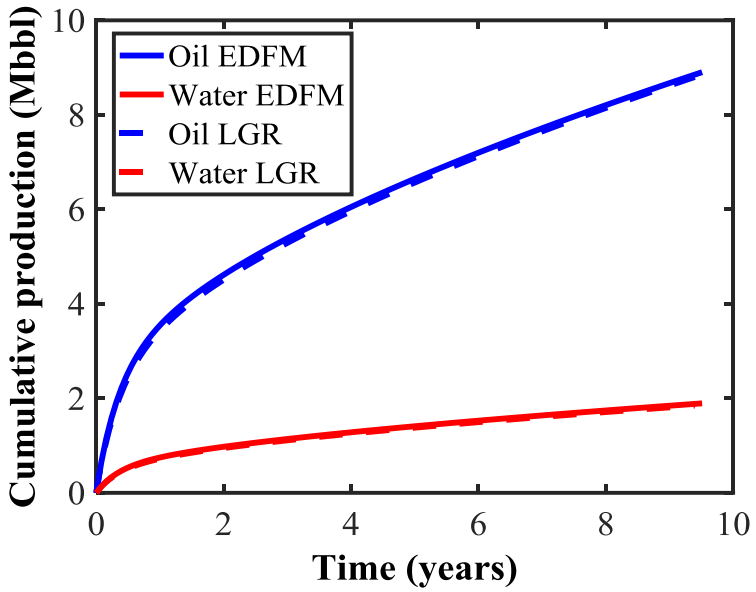

Figure 6.9. Comparison of cumulative production for oil and water phase for 9.5 years of production.

6.5 Performance tests

In this section, three different problems were selected to study the performance of our model. The first problem involves water injection-oil production in a 1D and 2D poroelastic medium. The second one is simulation of non-planar fracture geometry under production, and the last one is simulation of multiple fractures under production in a 3D reservoir with and without natural fractures. The data used in the second and last problem is based on Permian basin.

6.5.1 Water injection-oil production in a 1D and 2D poroelastic medium

This case study is used to test our coupled geomechanics-two phase flow model. The problem is adopted from Kim et al. (2013) and schematic diagram for both 1D and 2D problems can be found in Figure 6.10. Reservoir parameters used in the simulation of both 1D and 2D problems can be found in Table 6.3.

Quantity	Value	Unit
Initial reservoir pressure (psi)	1450	Psi
Initial water saturation	0.42	-
Reservoir permeability (k)	50	md
Reservoir porosity (ϕ)	0.1	-
Water compressibility (c_w)	2.76×10^{-6}	psi^{-1}
Oil compressibility (c_o)	2.76×10^{-5}	psi^{-1}
Water viscosity (μ_w)	1	cp
Oil viscosity (μ_o)	1	cp
Water density (ρ_w)	351	lbm/bbl
Oil density (ρ_o)	351	lbm/bbl
Young's Modulus (E)	3.48×10^{6}	Psi
Poisson's ratio	0.3	-
Drained bulk modulus (K_{dr})	4.69×10^{6}	Psi
Biot's coefficient (b)	1	-

Table 6.3. Parameters used in water injection-oil production problem.

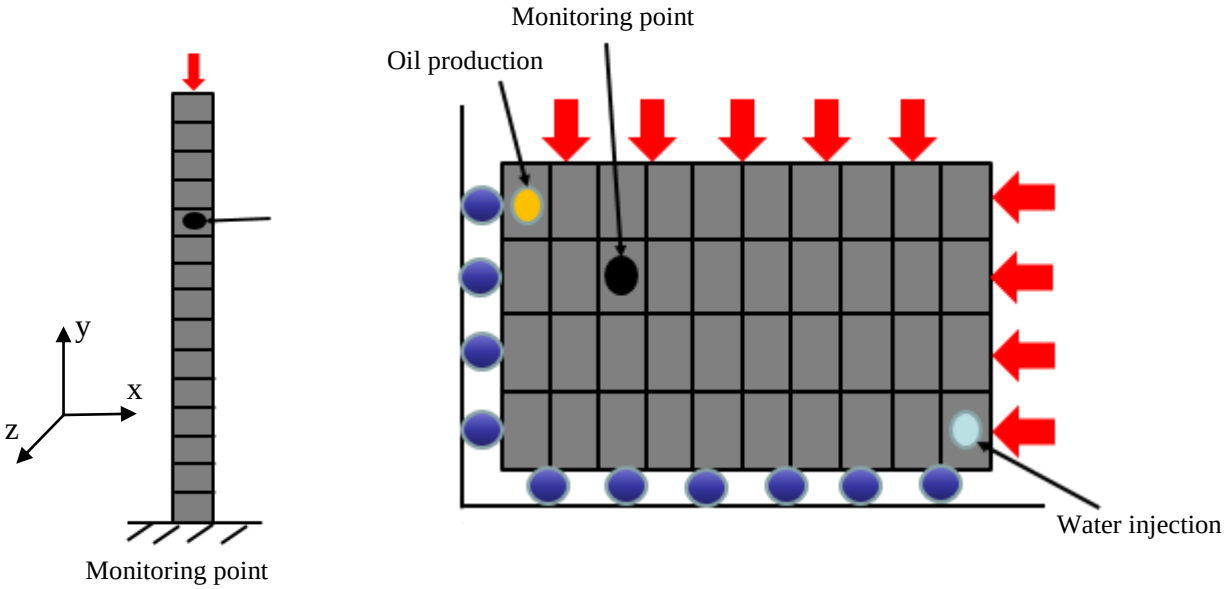

(a) Problem configuration for case 1D

(b) Problem configuration for case 2D

Figure 6.10. Problem configuration for 1D (a) and 2D (b) case.

For the 1D case, no-flow boundary conditions are applied at the top and bottom of the domain for pressure equation. While no displacement boundary condition is maintained at the bottom of the domain. The overburden stress (σ_b) of 1450 psi is applied at the top of the domain. The domain is initially filled with oil and water is being injected at the rate of 500 kg/d at the bottom cell, while oil is being produced at the same rate at the top cell. Domain length is 50 ft with 15 grid cells in total. The observation point is at cell 5^{th} from the top and gravitational is neglected in this case. Brooks and Corey's model was used for relative permeability calculation. The capillary effect is included in the study using linear model (see Appendix B) with pc_{max} being 2 MPa and 5 MPa for strong capillary case.

For the 2D case, no-flow boundary conditions are applied at all 4 boundaries. No displacement boundary conditions are applied at the left and bottom domain. The overburden stress (σ_b) and side burden stress (σ_s) of 1450 psi are applied at the top and right domains respectively. The domain is initially filled with oil and water is being injected at the rate of 500 kg/d at the bottom right corner, while oil is being produced at the same rate at the top left corner. Domain length is 333.33 ft and height is 66.67 ft with 10 grid cells in x-direction and 4 grid cells in y-direction. The observation point is as shown in Figure 10. Gravitational and capillary effects are also neglected in this case. Brooks and Corey's model was used for relative permeability calculation. The capillary effect is included in the study using linear model (see Appendix B) with pc_{max} being 2 MPa and 5 MPa for strong capillary case.

The plot of pressure evolution of oil phase at a monitoring point as a function of time is shown in Figure 6.11 for the 1D case (a) for 2D case (b). It can be observed from 1D case that a case without geomechanics effect yield larger pressure from early time to late time compared with a case with geomechanics effect. This is due to the change of porosity from rock deformation as a

result of change in reservoir pressure. The difference is less for a 2D case as shown in Figure 6.11b as the domain size for 2D case is much larger than 1D case resulting in less increase of pressure and less rock deformation compared with 1D case. The capillary effect also yields less pressure increase in both 1D and 2D cases compared with a case without capillary effect. Capillary pressure represents the difference between pressure of oil and water phase, therefore, presence of capillary pressure makes pressure of oil phase become less than water phase. Stronger (5 MPa) capillary pressure results in even smaller pressure increase. Similar behavior can be observed in 2D case showing a significant difference between case with and without capillary effect. This suggests that capillary effect should be considered in the reservoir simulation for the case of multi-phase flow as it directly affects pressure distribution, reservoir production as well as rock deformation. Although, in some cases, capillary effect might be neglected if if pressure difference between two fluid phase is not so significant.

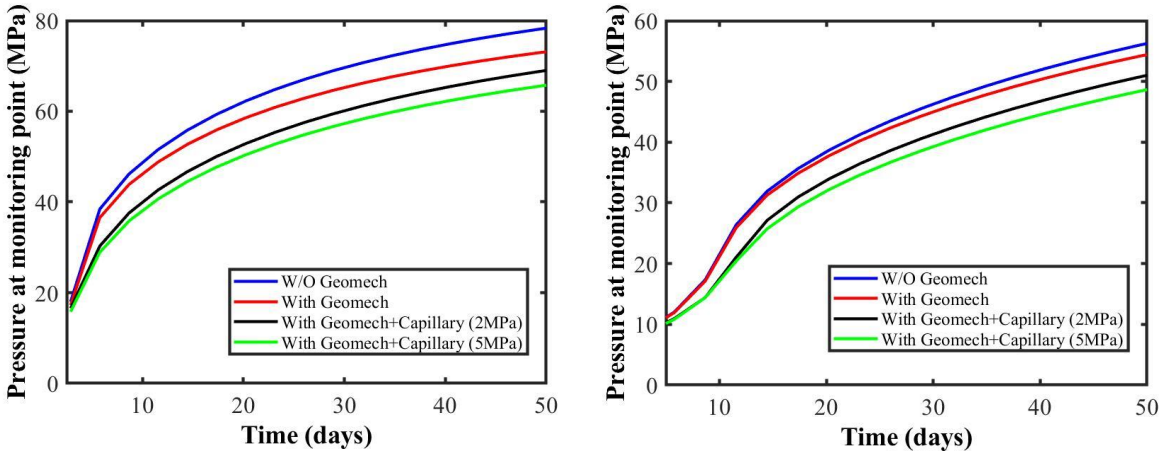

(a) Pressure evolution for 1D case (b) Pressure evolution for 2D case

Figure 6.11. Plot of pressure evolution for 1D case (a) and 2D case (b) for a case with and without geomechanics as well as with capillary effect.

Figure 6.12 shows pressure distribution with the direction of oil phase velocity (white arrow) and water saturation distribution with direction of water phase velocity (white arrow) at 5 days of injection-production. Longer arrows represent higher velocity magnitude. The pressure distribution plot shows pressure gradient along the domain with higher magnitude being on the injection side and lower on the production side. Higher oil phase velocity can be seen at the oil production side. Similarly, water saturation gradient decreases from injection to production side. Higher water phase velocity can be observed at the water injection side.

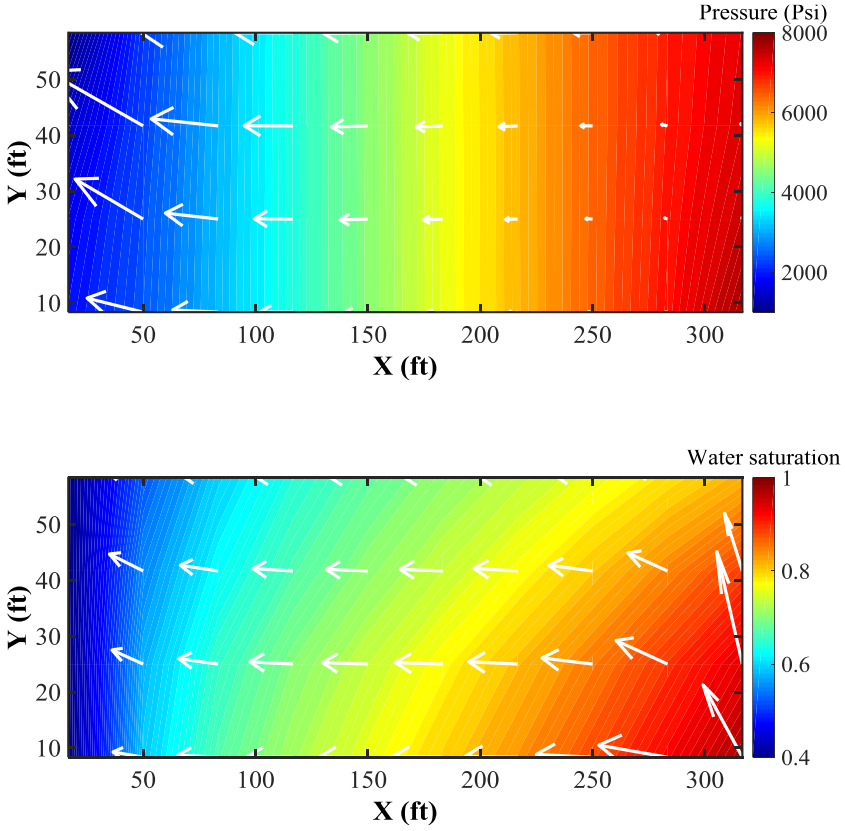

Figure 6.12. Pressure distribution with oil phase velocity direction (top) and water saturation distribution with water phase velocity direction (bottom).

6.5.2 Non-planar fracture geometry under production

This case study is similar to those from Figure 2.12e and f, section 2.4.2. The same non-planar fracture geometry is used to test the performance of our model. Fracture geometries can be found in Figure 6.13. Parameters used in this simulation can be shown in Table 6.4 with differential stress ($\sigma_{yy,0}$- $\sigma_{xx,0}$) being 500 psi. $N_x = N_y = 151$ and $L_x = L_y = 755$ft. Brooks and Corey's model was used for relative permeability calculation. No flow and no displacement boundary conditions are applied on all 4 boundaries. The simulation was carried out using coupled geomechanics-two phase flow with EDFM for 1 year of production. Figure 6.14 shows pressure and water saturation distribution with direction of maximum horizontal stress (σ_{Hmax}) shown in white dash lines after 1 year of production. Stress reversal (90^o change of direction of maximum horizontal stress) can be observed on top and bottom area of reservoir outside SRV region. This is due to large depletion inside the SRV region causing stress in y-direction outside SRV to rotate 90^o.

Quantity	Value	Unit
Initial reservoir pressure	8125	Psi
Bottomhole pressure	3500	Psi
Initial water saturation	0.42	-
Reservoir permeability (k)	464	μd
Reservoir porosity (ϕ)	0.12	-
Water compressibility (c_w)	$3.2x10^{-6}$	psi^{-1}
Oil compressibility (c_o)	$1x10^{-5}$	psi^{-1}
Water viscosity (μ_w)	0.8	cp
Oil viscosity (μ_o)	0.5	cp
Water density (ρ_w)	1000	kg/m^3
Oil density (ρ_o)	800	kg/m^3
Young's Modulus (E)	$2x10^6$	Psi
Poisson's ratio	0.2	-
Drained bulk modulus (K_{dr})	$2.22x10^6$	Psi
Initial stress in x direction ($\sigma_{xx,0}$)	10000	Psi

Table 6.4. Parameters used for non-planar fracture geometry under production.

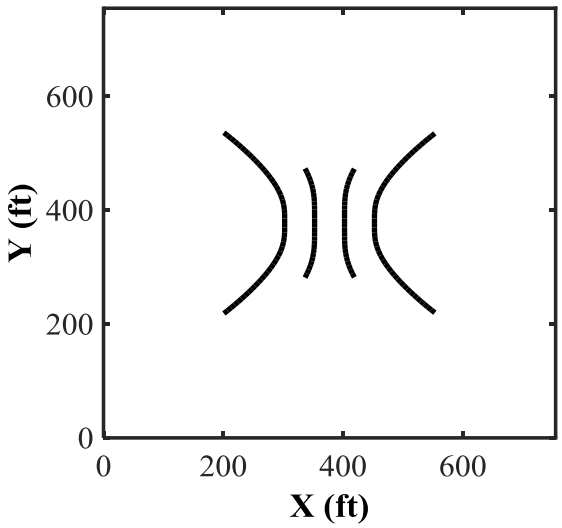

Figure 6.13. Fracture geometries for non-planar fractures under production.

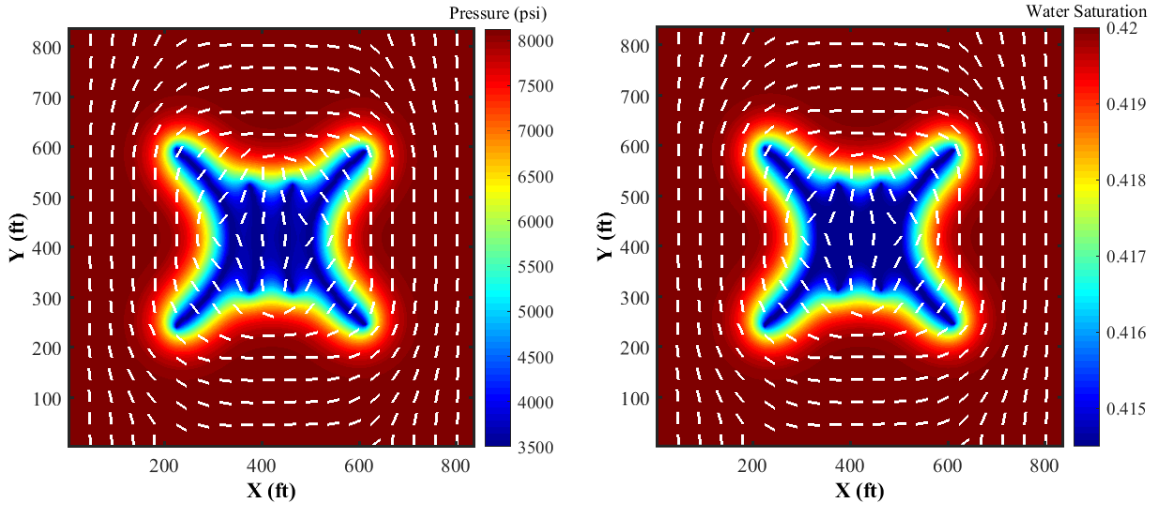

(a) Pressure distribution with direction of σ_{Hmax}

(b) Water saturation distribution with direction of σ_{Hmax}

Figure 6.14. Pressure and water saturation distribution with direction of σ_{Hmax} at 1 year of production.

6.5.3 Multiple fractures under production in a 3D reservoir

This case represents a well under production in a 3D reservoir. This well consists of 3 fracture stages with each stage having 4 fractures. Fracture spacing is 80 ft and fracture length of the two inner fractures are one-third of the two outer ones due to stress shadowing effect preventing inner fractures to grow as much as outer fractures. Longer fracture length is 600 ft and shorter ones are 200 ft. The reservoir comprises of 3 layers and the well is located in the middle layer as shown in Figure 6.15. All the fractures are also contained in the middle layer. Total reservoir height is 50 ft, length is 1315 ft, and width is 1500 ft. No displacement boundary conditions are applied on all 5 boundaries. Overburden of 8000 psi is applied on top boundary. Intial σ_{xx} is 6000 psi and differential stress is 500 psi. Similarly, no-flow boundary conditions are applied on all boundaries. Parameters used in the simulation are based on the Permian basin and can be shown in Table 5. Pressure and water saturation distribution at 4 months and 1 year of production with the direction of maximum horizontal stress at producing layer can be shown in Figure 6.16.

Quantity	Value	Unit
Initial reservoir pressure	4760	Psi
Bottomhole pressure	1000	Psi
Initial water saturation	0.42	-
Reservoir permeability (k)	464	µd
Reservoir porosity (ϕ)	0.12	-
Water compressibility (c_w)	3.2×10^{-6}	psi^{-1}
Oil compressibility (c_o)	1×10^{-5}	psi^{-1}
Water viscosity (μ_w)	0.8	cp
Oil viscosity (μ_o)	0.5	cp
Water density (ρ_w)	1000	kg/m^3
Oil density (ρ_o)	800	kg/m^3
Young's Modulus (E)	2×10^6	Psi
Poisson's ratio	0.2	-
Drained bulk modulus (K_{dr})	2.22×10^6	Psi
Biot's coefficient (b)	1	-

Table 6.5. Parameters used for multiple fractures under production.

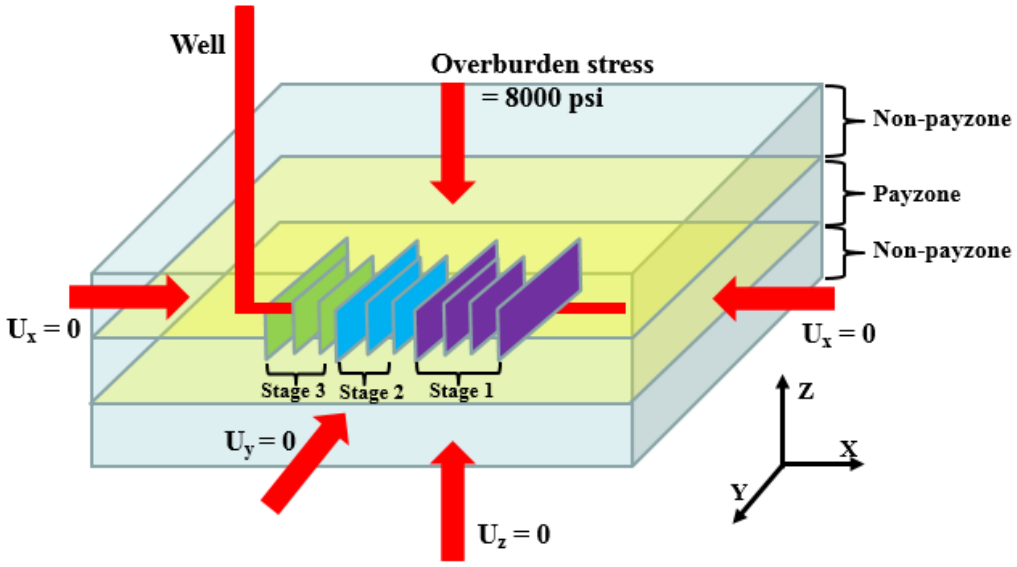

(a) 3D configuration of multiple fractures under production

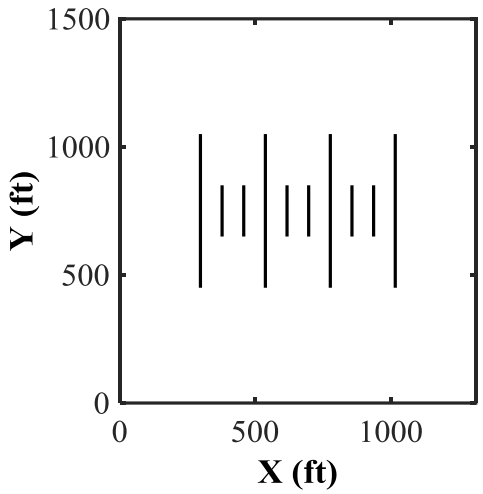

(b) 2D configuration on payzone layer of multiple fractures under production

Figure 6.15. 2D (a) and 3D (b) configuration for multiple fractures under production.

Figure 6.16 indicates that stress reversal (90° change of σ_{Hmax}) can only be observed outside the SRV region on top and bottom reservoir only at 1 year of production as pressure depletion inside SRV region at 4 months of production is not large enough to make σ_{yy} become smaller than σ_{xx}. This result is similar to what is observed in case study 6.5.2 and suggests that our model is

capable of simulating coupled geomechanics with two-phase flow in a 3D reservoir with multiple fractures.

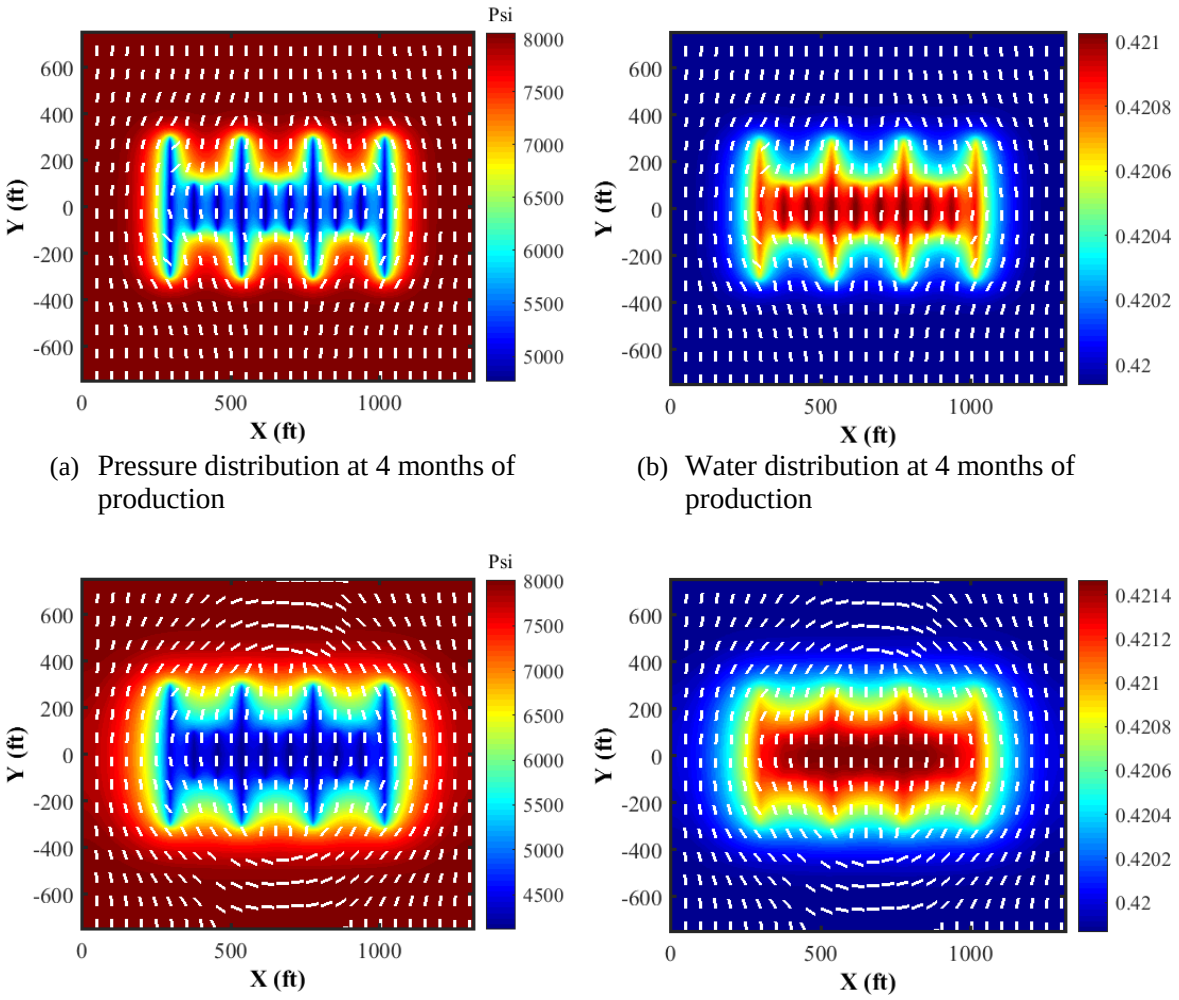

(a) Pressure distribution at 4 months of production

(b) Water distribution at 4 months of production

(c) Pressure distribution at 1 year of production

(d) Water distribution at 1 year of production

Figure 6.16. Pressure and water saturation distribution at 4 months (a and b) and 1 year (c and d) of production.

6.6 Conclusions

Geomechanics and two-phase finite volume-based model has been successfully developed using fixed stress method to ensure stability for high coupling strength problems. The two-phase

flow part is based on the IMPES method and sequentially coupled. Time step is controlled at every computational step using Courant number of CFL condition for stability of the simulation. The model is finally coupled with EDFM to simulate poroelastic effect of complex fracture geometry in unconventional reservoirs using structured gridding. This allows the study of multiple hydraulic and natural fractures in unconventional reservoirs for many applications including infill well drilling and optimization. The two-phase flow model was validated against classical Buckley-Leverett with gravitational and capillary effect. For EDFM part, local grid refinement was used as a reference for validating against our model.

Three case studies were included in this paper to test the performance of the developed model. Pressure evolution plot from the first case study suggests that geomechanics plays significant effect on pressure development in the 1D problem but very little to no effect on 2D problem. Similarly, the capillary effect is insignificant in the 2D problem compared to 1D problem, which suggests that capillary pressure might not need to be considered in the field case studies unless the reservoir is known to have strong capillary effect. Our model is capable of simulating stress evolution and redistribution due to production of two-phase flow in multiple fractures with both planar and non-planar geometries in a 3D reservoir using structured grids as shown in second and third case study. The model can further be used as a tool to characterize stress evolution due to reservoir depletion or water injection for unconventional reservoir developments.

CHAPTER 7: CONCLUSIONS AND FUTURE WORK

7.1 Conclusions

In this study, a coupled fluid flow and geomechanics has been developed based on the sequentially coupled method. The simulator is based on finite volume method using OpenFOAM and capable of simulating a field-scale reservoir in three dimensions. EDFM was coupled with the model to gain capability in simulating complex fracture geometries including the presence of natural fractures in highly fractured reservoirs with high computational efficiency as the simulator is only based on structured grids. Both coupled fluid flow and geomechanics model and EDFM part were validated against analytical solutions and local grid refinement respectively to ensure accuracy of the models. The main advantage of the developed model is the real-time predictions of stress evolution during the production of the reservoir with complex fracture geometries under the given field data. This provides critical guidelines for operators when performing field operations including parent well refracturing and infill well completion in tightly spaced horizontal wells. In addition, the model was upgraded to two-phase flow with capillary effect based on IMPES and sequentially coupled method in order to study cases involving two-phase flow such as water injection. The two-phase flow model was validated against classical Buckley-Leverett with gravitational and capillary effect. Followings are the conclusions drawn from this study:

(1) Stress redistribution is mainly controlled by fracture geometry as it directly affects the shape of the depleted area. Rectangular shape yields largest stress reorientation, while squared shape has much smaller likelihood to create stress reorientation. Large induced shear stress can be observed in inclined fracture geometries. In addition, differential stress (DS) also plays an important role in stress reorientation as the smaller the DS, the higher the chance of stress reorientation to occur.

(2) The presence of natural fractures is a key parameter that should be considered in unconventional study as it largely affects geometry of hydraulic fractures created during fracturing and change of stress state during the production. Natural fractures change the shape of the depleted area resulting in less stress reorientation and more complex stress distribution in SRV region. This leads to less stress reorientation inside SRV region and delay of stress redistribution outside SRV region. This produces totally different results from the simulations that only consider k_{SRV} without natural fractures as the change of depleted shape is not incorporated.

(3) There exists critical time during production, at which refracturing can be performed successfully. This critical time is subject to natural fracture distribution, fracture spacing, differential in-situ stress, and reservoir permeability. Beyond this time, a child fracture from refracturing may not be able to propagate to un-depleted areas in the reservoir and may hit parent fractures due to stress reversal. If refracturing time is predetermined, well candidates can then be selected based on well configuration, heterogeneity of the reservoir as well as reservoir properties. Optimum refracturing locations can subsequently be chosen in order to ensure the success of refracturing.

(4) Infill well completion in multi-payzone reservoirs is an important topic being considered by many operators. The challenges lie on the completion sequence, which determines location of both parent and infill wells. It was concluded from the study that placing two-parent wells in the same layer is likely to cause more stress change than placing them in different layers. Therefore, from this aspect, the vertical well layout is a better option to mitigate stress change induced by depletion in both parent well's and infill well's layer and fracture hits.

(5) Fracture penetration, fracture length, and natural fractures also play an important role in determining the completion sequence. Fracture penetration increases depletion rate in the penetrated layer, resulting in more stress reorientation. While longer fracture length can cause fracture overlapping in the layer between the two parent wells reducing stress orientation along

target infill zone. Natural fractures elevate depletion rate in parent wells and create more stress reorientation along target infill zone.

(6) Boundary effect is one of the parameters that should be considered when studying reservoir-geomechanics. The effect can be insignificant or significant depending on the problem being studied. If the study involves multiple-layer reservoir and mainly focuses on the the layers under production, it is not necessary to include non-payzone in the simulation as the difference in pressure depletion and stress change is very minimal. However, if the study involves the layers that are not under production but will be in the future, it is recommended including non-payzone region in the simulation to minimize boundary effect. Optimum size of non-payzone should be selected to ensure the correctness of solution as well as optimize computational cost.

(7) Well spacing is the key parameter affecting fracture geometry created in the infill well. Severe asymmetrical geometry with the longer side being closer to the depleted zone can be observed when the well spacing is too small. This leads to fracture interaction between parent and infill wells, which eventually causes a detrimental effect on production performance in both parent and infill wells. Fracture hits are more likely to be observed at 5-year production due to less orientation change; therefore, performing infill well completion at an early time is a better option to avoid fracture hits.

(8) For the two-phase flow model, the pressure evolution plot from the first case study suggests that geomechanics plays a significant effect on pressure development in 1D water injection-oil production problem but very little to no effect on the 2D problem. Similarly, capillary effect is insignificant in 2D problem compared to 1D problem, which suggests that capillary pressure might not need to be considered in field case studies unless the reservoir is known to have strong capillary effect.

7.2 Future work

The coupled model developed in this study is capable of simulating field scale reservoirs with complex fracture geometries with the given field data. Results obtained from the simulations can provide critical guidelines in refracturing or infill well completion. However, there are some more relevant aspects that can be investigated to widen and improve results obtained from this model. Followings are the suggestions:

(1) The developed model can be used to investigate more field case studies involving multiple parent/infill wells in a larger scale reservoir. Although, the simulator is currently able to handle up 3 fully 3D problem with up to millions of grid cells, the cases containing multiple hydraulic and natural fractures will require longer time for solutions to convert at each time step due to the coupling scheme. In this case, parallel solver should be considered and applied to the solver. OpenFOAM already provides parallel running using openMPI for users. The decompositions method consists of simple, hierarchical, scotch and manual.

(2) Effect of fluid injection in parent well is another interesting topic that should be examined since many studies have shown that parent well refracturing can reverse stress orientation to rotate back to its original direction after production. This may or may not help prevent fracture interference between parent and infill wells.

(3) Stress shadowing effect is another factor that should be considered. The model can easily couple with a fracture propagation model, e.g. 3D DDM (Tang et al. 2018). The updated stress field obtained from 3D DDM can be superimposed with a geomechanics-fluid model to obtain total stress change caused by both stress shadowing and poroelastic effect.

(4) Complex fracture propagation model as introduced in section 5.2 can be used to investigate fracture propagation in multiple stages since, in this work, only one stage consisting of 4 clusters was studied. The heterogeneous stress state created by production of parent well is likely to affect

fracture geometry as well as propagation direction. This can be used to study effect of cluster spacing/location to avoid fracture hits and improve production loss in both parent and infill wells.

(5) Thermal effects can be easily coupled to the model since OpenFOAM already provides thermal stress solver and heat transfer. The solver just needs to be coupled with the model. The two-phase flow part can also be upgraded to three-phase flow to examine more case studies.

Another main study that can be incorporated to the coupled model is the effect of fracture closing during reservoir production. In our coupled geomechanics and fluid flow model with EDFM, the geomechanical part is only considered in the matrix domain, which is mainly controlled by reservoir depletion. However, the fracture domain currently only takes into consideration the flow part meaning that the fracture rock deformation in not considered. The change of reservoir permeability and porosity can be computed through empirical formulas, which is widely acceptable but may not be accurate. Incorporating fracture closure model allows us to capture dynamic change of fracture aperture during the production, which consequently is used to compute the updated fracture permeability and porosity. The contribution of fracture rock deformation or fracture closure not only affect fracture permeability and porosity but can also affect stress magnitude and orientation around the fractures. In some cases, where the rock is less stiff, the fracture will be closed easily and may drastically change the reservoir production and stress evolution.

One way to incorporate this model is to apply Embedded fracture continuum approach (EFC) (Dang et al. 2019) to the model. This method is similar to Dual porosity model with the main difference being that the model can handle explicit fractures and does not assume that fractures are located everywhere, which suits our model that handles fracture explicitly using EDFM. The main idea is to separate total compliance tensor into matrix and fracture compliance

tensor. This allows the fracture to be modelled separately from matrix, while the total deformation is a summation between matrix and fracture deformation. Fracture stiffness in normal and shear direction is used to construct the fracture compliance tensor and the orientation of fracture present in each cell is also taken into consideration allowing the capture of fracture location and orientation. Rock deformation in the fracture cells can be used to calculate change of fracture aperature and subsequently update permeability and porosity at every time step.

APPENDIX A

Analytical solution of Terzaghi's and Mandel's problems

Analytical solution for pressure (p) and displacement (u_z) at different locations and time can be shown as

$$p(z,t) = -W\frac{a_{f-}a_i}{\alpha a_i}\sum_{j=0}^{\infty}\frac{4(-1)^j}{\pi(2j+1)}cos\left[\frac{(2j+1)\pi z}{2H}\right]exp\left[-\left(\frac{(2j+1)\pi}{2}\right)^2\frac{c_f t}{4H^2}\right],$$

…... (A-1)

$$u_z(z,t) = -W(a_f - a_i)H\sum_{j=0}^{\infty}\frac{8(-1)^j}{\pi^2(2j+1)^2}sin\left[\frac{(2j+1)\pi z}{2H}\right]exp\left[-\left[\frac{(2j+1)\pi}{2}\right]^2\frac{c_f t}{4H^2}\right] + W a_f z,$$

(A-2)

where:

$$a_f = \frac{(1+\nu)(1-2\nu)}{E(1-\nu)},$$

……..…...…… (A-3)

$$a_i = a_f\left[\frac{b^2 a_f}{\phi c_f}\right]^{-1},$$

…….……..……..…… (A-4)

W is external load on top of column, H is column height, z is location along z-direction.

Analytical solution for Mandels' problem for pressure (p), displacement (u_x), and (u_y) are written as:

$$u_x(x,t) = \left[\frac{W\nu}{2GL} - \frac{W\nu_u}{GL}\sum_{i=1}^{\infty}\frac{sin\alpha_i cos\alpha_i}{\alpha_i - sin\alpha_i cos\alpha_i} exp\left(\frac{-\alpha_i{}^2 ct}{L^2}\right)\right]x$$

$$+\frac{W}{G}\sum_{i=1}^{\alpha}\frac{cos\alpha_i}{\alpha_i - sin\alpha_i cos\alpha_i} sin\frac{\alpha_i x}{L} exp\left(\frac{-\alpha_i{}^2 ct}{L^2}\right),$$

…….…… (A-5)

$$u_y(y,t) = \left[-\frac{W(1-\nu)}{2GL} + \frac{w(1-\nu_u)}{GL}\sum_{i=1}^{\infty}\frac{sin\alpha_i cos\alpha_i}{\alpha_i - sin\alpha_i cos\alpha_i} \exp\left(\frac{-\alpha_i{}^2 ct}{L^2}\right)\right]y,$$

…… (A-6)

where ν_u is undrained Poisson's ratio, B is Skempton's pore pressure coefficient, x is location in x-direction, y is location in y-direction, L is domain length, G is shear modulus, and c is the general consolidation coefficient,

$$c = \frac{2kB^2G(1-\nu)(1+\nu_u)^2}{9(1-\nu_u)(\nu_u-\nu)},$$

…….……..…… (A-7)

t is time and α_i, i = 1, ∞, are the roots of the equation,

$$tan\alpha_i = \frac{1-\nu}{(\nu_u-\nu)}\alpha_i,$$

…….……..…..…… (A-8)

In our study, $\nu_u = 0.5$, B = $\frac{1}{(1+c_f \emptyset K_{dr})}$. Pressure, total stress σ_{xx}, σ_{yy}, and shear stress σ_{xy} can also be obtained using the following equations

$$p(x,t) = \frac{2WB(1+\nu_u)}{3L}\sum_{i=1}^{\infty}\frac{sin\alpha_i}{\alpha_i - sin\alpha_i cos\alpha_i}\left(cos\frac{\alpha_i x}{L} - cos\alpha_i\right)exp\left(\frac{-{\alpha_i}^2 ct}{L^2}\right),$$

…… (A-9)

$$\sigma_{xx} = 0, \text{ ……..…….....} \quad \text{(A-10)}$$

σ_{xx} is zero due to traction free boundary on the right of the domain.

$$\sigma_{yy} = \frac{-W}{L} - \frac{2W(\nu_u - \nu)}{L(1-\nu)}\sum_{i=1}^{\infty}\frac{sin\alpha_i}{\alpha_i - sin\alpha_i cos\alpha_i}cos\frac{\alpha_i x}{L}\exp\left(\frac{-{\alpha_i}^2 ct}{L^2}\right)$$

$$+\frac{2W}{L}\sum_{i=1}^{\infty}\frac{sin\alpha_i cos\alpha_i}{\alpha_i - sin\alpha_i cos\alpha_i}exp\left(\frac{-{\alpha_i}^2 ct}{L^2}\right),$$

…… (A-11)

$$\sigma_{xy} = 0, \text{ ……...…….……} \quad \text{(A-12)}$$

Since u_y is assumed to be uniform along x-direction. Thus, σ_{yy} is also uniform along x-direction. σ_{xy} is zero at all times and external force only acting in normal direction to surface. Finally, there is no force acting in direction parallel to the surface.

APPENDIX B

Time-step limitations

This section provides steps to compute Δt_p as introduced in Horgue et al. (2014) to be used in Eq. (18) to determine the time-step size for each computational step. Δt_p can be computed using the following equation

$$\Delta t_p = \min(\min(c_{\Delta t}, 1 + 0.1c_{\Delta t}), 1.2)\, \Delta t_{last}, \quad \text{(B-1)}$$

where Δ_{last} is previous time step size and $c_{\Delta t}$ is the coefficient for time-step change. Eq. (B-1) limits the increase of time step size to be not more than 20% of previous time step size. $c_{\Delta t}$ can be obtained through Courant number of CFL condition.

For Courant number, $c_{\Delta t}$ can be computed using the below equation

$$c_{\Delta t} = \frac{Co_{fixed}}{\max(Co_o, Co_w)}, \quad \text{(B-2)}$$

Co or Courant number of phase i can be computed using

$$Co_i = max_{Vcell}\left(0.5\frac{\sum_{f=0}^{m}|\varphi_i|}{V_{cell}}\right)\Delta t, \quad \text{(B-3)}$$

where φ_i is flux of phase i and V_{cell} is volume of each computational cell, m is the number of neighbor faces f to the considered cell. For CFL condition, $c_{\Delta t}$ can be computed using the below equation

$$c_{\Delta t} = \frac{C_{max}}{CFL},$$

……...……..… (B-4)

where C_{max} is less than or equal to 1. In this study, we set C_{max} as 0.75 to ensure the stability of the simulations. CFL can be calculated with following equation

$$CFL = max_{Vcell}\left[\frac{\Delta t}{\emptyset V_{cell}}\left(2\frac{\partial p_c}{\partial S_w}\frac{M_o M_w}{K(M_o + M_w)}\right)\sum_{f=0}^{m} T_f + \frac{\partial F_w}{\partial S_w}\sum_{f=0}^{m}\varphi\right],$$

……. (B-5)

where F_w is the fractional flow and can be computed using

$$F_w = \frac{\frac{k_{rw}}{\mu_w}}{\frac{k_{rw}}{\mu_w} + \frac{k_{ro}}{\mu_o}},$$

...…….. (B-6)

and T_f is the transmissivity of the face f calculated using

$$T_f = \frac{K_f \|S_f\|}{\Delta x_f},$$

……. (B-7)

where Δx_f is the distance between the centers of two neighboring cells.

Relative permeability models

Brooks and Corey Model (Brooks et al., 1964)

$$k_{rw}(S_w) = k_{rw,max}{S_w}^m, \quad \text{(B-8)}$$

$$k_{ro}(S_w) = k_{ro,max}(1 - S_w)^m. \quad \text{(B-9)}$$

Van Genuchten Model (Genuchten, 1980)

$$k_{rw}(S_w) = k_{rw,max}S_w^{\frac{1}{2}}\left(1 - \left(1 - S_w^{\frac{1}{m}}\right)^m\right)^2, \quad \text{(B-10)}$$

$$k_{ro}(S_w) = k_{ro,max}(1 - S_w)^{\frac{1}{2}}\left(1 - S_w^{\frac{1}{m}}\right)^{2m}, \quad \text{(B-11)}$$

where m is a power coefficient. The plot of relative permeability as a function of water saturation for both models with m = 2 can be shown in Figure B-1.

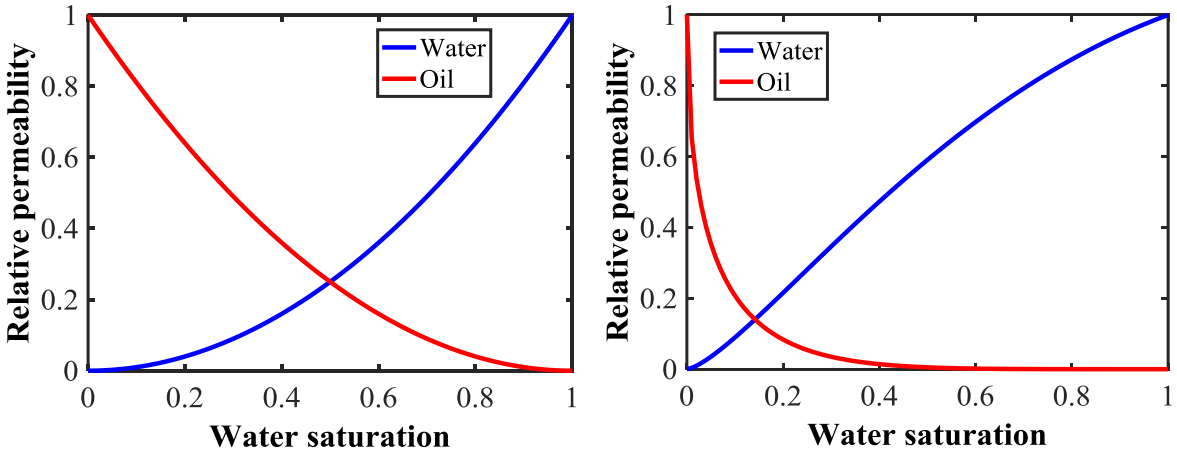

(a) Brooks and Corey model (b) Van Genuchten model

Figure B-1. Relationship between relative permeability and water saturation for Brooks and Corey model (a) and Van Genuchten model (b).

Capillary pressure models

Brooks and Corey Model (Brooks et al., 1964)

$$p_c(S_w) = p_{c,0} {S_w}^{-\alpha}, \quad \text{(B-12)}$$

where $p_{c,0}$ is the entry capillary pressure and $1/\alpha$ is pore size distribution index. The change of capillary pressure with respect to the change of water saturation can be computed by differentiating Eq. (61) with respect to S_w, which can be expressed as

$$\frac{\partial p_c}{\partial S_w}(S_w) = -\alpha p_{c,0} {S_w}^{-\alpha-1}. \quad \text{(B-13)}$$

Van Genuchten Model (Van Genuchten, 1980)

$$p_c(S_w) = p_{c,0} \left({S_w}^{-\frac{1}{m}} - 1 \right)^{1-m}, \quad \text{(B-14)}$$

Where m is the Van Genuchten coefficient. The change of capillary pressure with respect to the change of water saturation can be computed by differentiating Eq. (B-14) with respect to S_w as follows

$$\frac{\partial p_c}{\partial S_w}(S_w) = -\frac{1-m}{m} p_{c,0} \left({S_w}^{-\frac{1}{m}} - 1 \right)^{-m} {S_w}^{-\frac{1+m}{m}}. \quad \text{(B-15)}$$

Linear model

$$p_c(S_w) = p_{c,0} + (1 - S_w)\left(p_{c,max} - p_{c,0}\right), \quad \text{(B-16)}$$

where $p_{c,\,max}$ is maximal capillary pressure. The change of capillary pressure with respect to the change of water saturation can be computed by differentiating Eq. (B-16) with respect to S_w as follows

$$\frac{\partial p_c}{\partial S_w}(S_w) = -(p_{c,max} - p_{c,0}).$$

…….…….. (B-17)

Plot of capillary pressure as a function of water saturation with different models with $p_{c,0}$ = 1000 psi, m = α = 0.5, and $p_{c,max}$ = 10000 Psi can be shown in Figure B-2.

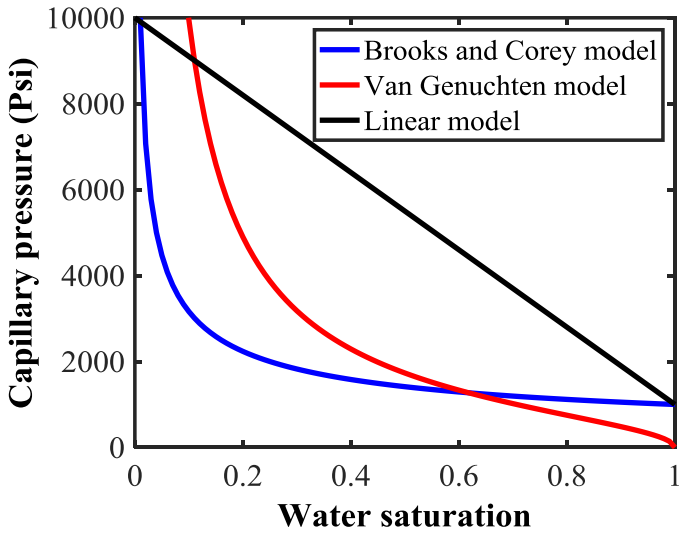

Figure B-2. Relationship between capillary pressure and water saturation for Brooks and Corey, Van Genuchten and Linear model.

REFERENCES

Ajani, A.A. and Kelkar, M.G. 2012. Interference study in shale plays. Presented at SPE Hydraulic Fracturing Technology Conference, The Woodlands, Texas, USA, 6-8 February. SPE-151045-MS.

Ajisafe, F.O., Solovyeva, I., Morales, A., Ejofodomi, E., and Porcu, M.M. 2017. Impact of Well Spacing and Interference on Production Performance in Unconventional Reservoirs, Permian Basin. Presented at Unconventional Resources Technology Conference, Austin, Texas, USA, 24-26 July. URTeC-2690466-MS.

Bai M., Ma Q., and Roegiers J. (1994). A nonlinear dual-porosity model. Applied Mathematical Modelling Volume 18, Issue 11, November 1994, Pages 602-610

Bai M. (1999). On equivalence of dual-porosity poroelastic parameters. *Journal of Geophysical Research: Solid Earth*; **104**(B5), 10461-10466.

Barenblatt, G.E., I.P. Zheltov and I.N. Kochina (1960): \Basic Concepts in the Theory of Seepage of Homogeneous Liquids in Fissured Rocks," J. Appl. Math. Mech. (USSR) vol. 24, No. 5.

Barton, Nick & C. Bandis, S & Bakhtar, K. (1985). Strength, deformation and conductivity coupling of rock Joints. International Journal of Rock Mechanics and Mining Sciences & Geomechanics Abstracts. 22. 121-140. 10.1016/0148-9062(85)93227-9.

Barree R.D., Barree & Associates, Miskimins J. L. (2017). Reservoir and Completion Considerations for the Refracturing of Horizontal Wells. Paper SPE-184837 presented at the

SPE Hydraulic Fracturing Technology Conference and Exhibition held in The Woodlands, Texas, USA, 24-26 January 2017.

Bandis C, Lumsdent S & C, Barton A, Nick. (1983). Fundamentals of Rock Joint Deformation. 20. 249-268.

Berryman JG, Wang HF. (1995) The elastic coefficients of double-porosity models for fluid transport in jointed rock. *J. Geophys. Res.*; **100**:24,611 – 24,627.

Berryman JG. (2002) Extension of poroelastic analysis to double-porosity materials: New technique in microgeomechanics. *J. Eng. Mech. ASCE*; **128**(8):840 – 847.

Biot M.A. (1941). General theory of three-dimensional consolidation. *Journal of Applied Physics*; **12**:155–164.

Biot M.A. (1955). Theory of Elasticity and Consolidation for a Porous Anisotropic Solid. *J. Appl. Phys.* **26**: 182–185.

Blanco-Martin, L., Rutqvist, J., Doughty, C. et al. (2016). Coupled Geomechanics and Flow Modeling of Thermally Induced Compaction in Heavy Oil Diato- mite Reservoirs Under Cyclic Steaming. Journal of Petroleum Science and Engineering 147: 474–484. https://doi.org/10.1016/j.petrol.2016.09.002.

Bowman, C. W. (2006, January 1). Increasing the Production from Marginal Gas Wells. Society of Petroleum Engineers. doi:10.2118/100514-MS.

Brooks R., Corey A. (1964), Hydraulic Properties of Porous Media, in: *Hydrology Paper* 3.

Bryant, E. C., Hwang, J., & Sharma, M. M. (2015). Arbitrary Fracture Propagation in Heterogeneous Poroelastic Formations Using a Finite Volume-Based Cohesive Zone Model. Society of Petroleum Engineers. doi:10.2118/173374-MS.

Cardiff P., Karac A. and Ivankovic AA. (2014). Large strain finite volume method for orthotropic bodies with general material orientations, Comput. *Methods Appl. Mech. Engrg.*; **268**:318–335.

Castelletto N., White J. A. and Tchelepi H. A. (2015). Accuracy and convergence properties of the fixed-stress iterative solution of two-way coupled poromechanics. *International Journal for Numerical and Analytical Methods in Geomechanics*; **39**(14): 1593-1618. DOI: 10.1002/nag.2400.

Cao H. (2002), Development of techniques for general-purpose simulators, PhD Dissertation. Stanford University.

Cao, R., Li, R., Girardi, A., Chowdhury, N., and Chen, C. 2017. Well Interference and Optimum Well Spacing for Wolfcamp Development at Permian Basin. Presented at Unconventional Resources Technology Conference, Austin, Texas, USA, 24-26 July. URTeC-2691962-MS.

Charry L., Malpani R., Clark B. (2016). A Step Change in the Learning Curve for Refracturing in the Eagle Ford. Paper URTeC 2461344 presented at the Unconventional Resources Technology Conference held in San Antonio, Texas, USA, 1-3 August 2016.

Chen, H.-Y., & Teufel, L. W. (1997). Coupling Fluid-Flow and Geomechanics in Dual-Porosity Modeling of Naturally Fractured Reservoirs. Society of Petroleum Engineers. doi:10.2118/38884-MS

Chen, Dong & Pan, Zhejun & Ye, Zhihui. (2015). Dependence of gas shale fracture permeability on effective stress and reservoir pressure: Model match and insights. Fuel. 139. 383-392. 10.1016/j.fuel.2014.09.018.

Chen Z., Huan G., Ma Y. (2006), Computational Methods for Multiphase Flows in Porous Media.

Cipolla, C.L., Lolon, E.P., Mayerhofer, M.J., and Warpinski, N.R. (2009). Fracture Design Considerations in Horizontal Wells Drilled in Unconventional Gas Reservoirs. Presented at the SPE Hydraulic Fracturing Technology Conference, The Woodlands, Texas, 19-21 January. SPE-119366-MS.

Cipolla C.L., Fitzpatrick T., and Williams M.J. et al. (2011). Seismic-to-Simulation for Unconventional Reservoir Development. Paper SPE 146876 presented at the SPE Reservoir Characterization and Simulation Conference and Exhibition, Abu Dhabi, 9–11 October.

Cipolla C.L., Motiee, M., & Kechemir, A. (2018). Integrating Microseismic, Geomechanics, Hydraulic Fracture Modeling, and Reservoir Simulation to Characterize Parent Well Depletion and Infill Well Performance in the Bakken. Unconventional Resources Technology Conference.

Coussy O. (1995), Mechanics of Porous Media, John Wiley & Sons, Chichester, England.

Chen Z., Huan G., Ma Y. (2006), Computational Methods for Multiphase Flows in Porous Media.

Cryer, C.W. (1963), A comparison of the three-dimensional consolidation theories of Biot and Terzaghi. Q. J. Mech. Appl. Math. 16: 401-412.

Daneshy A. (2012). Fracture Shadowing: A Direct Method for Determining of the Reach and Propagation Pattern of Hydraulic Fractures in Horizontal Wells. Paper SPE 151980 presented at the SPE Hydraulic Fracturing Technology Conference, The Woodlands, Texas, 6–8 February. doi: 10.2118/151980-MS.

Davies, J. P., & Davies, D. K. (1999). Stress-Dependent Permeability: Characterization and Modeling. Society of Petroleum Engineers. doi:10.2118/56813-MS.

Dean, R.H., Gai, X., Stone, C.M., and Minkoff, S.E. 2006. A comparison of techniques for coupling porous flow and geomechanics. *SPE Journal* **11**(01):132-140.

Demirdžić, I., and Martinović, D. 1993. Finite volume method for thermo-elasto-plastic stress analysis. Comput. Methods Appl. Mech. Eng. 109 (3-4): 331–349. http://dx.doi.org/10.1016/0045-7825(93)90085-C.

Ding, X. (2019, March 15). Using Unstructured Grids for Modeling Complex Discrete Fracture Network in Unconventional Reservoir Simulation. Society of Petroleum Engineers. doi:10.2118/195051-MS.

Doe, T., Shi, C., & Enachescu, C. (2014, August 25). Discrete Fracture Network Simulation of Production Data from Unconventional Wells. Unconventional Resources Technology Conference. doi:10.15530/URTEC-2014-1923802.

Du, S., Yoshida, N., Liang, B., & Chen, J. (2016). Application of multi-segment well approach: Dynamic modeling of hydraulic fractures. Journal of Natural Gas Science and Engineering, 34, 886-897.

Du, S., Liang, B., & Lin, Y. (2017) Field Study: Embedded Discrete Fracture Modeling with Artificial Intelligence in Permian Basin for Shale Formation, SPE-187202-MS, In SPE Annual Technical Conference and Exhibition held in San Antonio, Texas, 9-11, October 2017

Engelder T. and Fischer M.P. (1994). Influence of Poroelastic Behavior on the Magnitude of Minimum Horizontal Stress, Sh, in overpressured parts of sedimentary basins. *Geology* **22**: 949–952.

Fallah, N., Bailey, C., Cross, M., et al. 2000. Comparison of finite element and finite volume methods application in geometrically nonlinear stress analysis. *App. Math. Mod.* **24** (7): 439–455. http://dx.doi.org/10.1016/S0307-904X(99)00047-5.

Forand D., Heesakkers V., Schwartz K. (2017). Constraints on natural fracture and in-situ stress trends of unconventional reservoirs in the Permian Basin, USA. Paper URTeC 2669208 presented at the Unconventional Resources Technology Conference held in Austin, Texas, USA, 24-26 July 2017.

Fryer, Y.D., Bailey, C., Cross, M., et al. 1991. A control volume procedure for solving the elastic stress-strain equations on an unstructured mesh. *App. Math. Mod*. **15** (11-12): 639–645. http://dx.doi.org/10.1016/S0307-904X(09)81010-X.

Gai X. (2004). A Coupled Geomechanics and Reservoir Flow Model on Parallel Computers. PhD Dissertation. The University of Texas at Austin.

Gerritsen M., Durlofsky L. (2005), Modeling fluid flow in oil reservoirs, Annu. Rev. *Fluid Mech. 37 211-238*

Grieser B. and Calvin J. (2016). Lessons Learned: Refracs from 1980 to Present. Paper SPE 179152 presented at the SPE Hydraulic Fracturing Technology Conference held in The Woodlands, Texas, USA, 9-11 February 2016.

Gupta J., Zielonka M., Albert R. A., El-Rabaa A. M., Burnham H. A. and Choi N. H. (2012). Integrated Methodology for Optimizing Development of Unconventional Gas Resources. Paper SPE 152224 presented at the SPE Hydraulic Fracturing Technology Conference held in the Woodlands, Texas, USA, 6-8 February 2012. doi:10.2118/152224-MS.

Guo, X., Wu, K., An, C., Tang, J., Killough, J. 2018. Numerical Investigation of Effects of Subsequent Parent Well Injection on Interwell Fracturing Interference Using Reservoir-Geomechanics-Fracturing Modeling. *SPE Journal*, accepted.

Guo, X., Wu, K., Killough, J. 2018. Investigation of production-induced stress changes for infill-well stimulation in Eagle Ford Shale. SPE 189974. *SPE Journal*, 23(04): 1372-1388.

Holditch, S. A. (2003, November 1). The Increasing Role of Unconventional Reservoirs in the Future of the Oil and Gas Business. Society of Petroleum Engineers. doi:10.2118/1103-0034-JPT.

Horgue P., Soulaine C., Franc J., Guibert R., Debenest G. (2014), An open-source toolbox for multiphase flow in porous media. *Computer Physics Communications, Elsevier, 2014, vol. 187, pp. 217-226.*

Huang, J., Ma, X., Safari, R. et al. 2015. Hydraulic Fracture Design Optimization for Infill Wells: An Integrated Geomechanics Workflow. Presented at the 49th US Rock

Mechanics/Geomechanics Symposium, San Francisco, California, USA. 28 June-1 July. ARMA-2015-074

Hui, M.-H., Dufour, G., Vitel, S., Muron, P., Tavakoli, R., Rousset, M., Mallison, B. (2019, March 29). A Robust Embedded Discrete Fracture Modeling Workflow for Simulating Complex Processes in Field-Scale Fractured Reservoirs. Society of Petroleum Engineers. doi:10.2118/193827-MS.

Hwang, J., Bryant, E. C., and Sharma, M. M. 2015. Stress Reorientation in Waterflooded Reservoirs. Presented at the SPE Reservoir Simulation Symposium, Houston, 23-25 February. SPE-173220-MS. https://doi.org/10.2118//173220-MS.

Jasak H. and Weller H. (2000). Finite volume methodology for contact problems of linear elastic solids. *Proceedings of 3rd International Conference of Croatian Society of Mechanics*, Cavtat/Dubrovnik, Croatia; 253-260.

Jha B. and Juanes R. (2014). Coupled multiphase flow and poromechanics: A computational model of pore pressure effects on fault slip and earthquake triggering. *Water Resources Research*; 50(5):3776–3808.

Jiang J. and Younis R.M. (2015). Numerical study of complex fracture geometries for unconvential gas reservoirs using a discrete fracture-matrix model. *Journal of Natural Gas Science and Engineering*, **26**, 1174-1186.

Kazemi, H. and L.S. Merrill Jr., K.L. Porter_eld, and P.R. Zeman (1976): \Numerical Simulation of Water-Oil Flow in Naturally Fractured Reservoirs," SPE Journal.

K. Coats (2003), IMPES stability: selection of stable timesteps, *SPE Journal*. 8 (2) 181–187.

Kim J.M. (2000). Generalized poroelastic analytical solutions for pore water pressure change and land subsidence due to surface loading. *Geosciences Journal*; **4**(2):95-104.

Kim, J., Tchelepi, H.A., and Juanes, R. 2009. Stability, accuracy, and efficiency of sequential methods for coupled flow and geomechanics. Presented at SPE reservoir simulation symposium, The Woodlands, Texas, USA, 2-4 February. SPE-119084-MS.

Kim J., Tchelepi H.A. and Juanes R. (2011a), Stability and convergence of sequential methods for coupled flow and geomechanics: Drained and undrained splits, Comput. Methods Appl. Mech. Eng.; 200: 2094–2116.

Kim J., Tchelepi H.A. and Juanes R. (2011b), Stability and convergence of sequential methods for coupled flow and geomechanics: Fixed-stress and fixed-strain splits. *Comput. Methods Appl. Mech. Eng.*; 200: 1591–1606.

Kim J., Tchelepi H.A. and Juanes R. (2011c), Stability, accuracy and efficiency of sequential methods for coupled flow and geomechanics. *Soc. Pet. Eng. J*; **16**(2), 249–262.

Kim, Jihoon & Sonnenthal, Eric & Rutqvist, Jonny. (2012). Formulation and sequential numerical algorithms of coupled fluid/heat flow and geomechanics for multiple porosity materials. International Journal for Numerical Methods in Engineering. 92. 10.1002/nme.4340.

Kim J., Tchelepi H.A. and Juanes R. (2013), Rigorous coupling of geomechanics and multiphase flow with strong capillarity. *Soc. Pet. Eng. J.*; **18**(6), 1123–1139.

King, G.E., Rainbolt, M.F., and Swanson, C. 2017. Frac Hit Induced Production Losses: Evaluating Root Causes, Damage Location, Possible Prevention Methods and Success of Remedial Treatments. Presented at SPE Annual Technical Conference and Exhibition, San Antonio, Texas, USA. 9-11 October. SPE-187192-MS.

Kumar D. and Ghassemi A. (2017). 3D Geomechanical Analysis of Refracturing of Horizontal Wells. Paper URTeC 2697487 presented at the Unconventional Resources Technology held in Austin, Texas, USA, 24-26 July 2017.

Lee I.S. (2008). Computational Techniques for Efficient Solution of Discretized Biot's Theory for Fluid Flow in Deformable Porous Media. PhD Dissertation, Virginia Polytechnic Institute and State University.

Li L. and Lee S.H. (2008). Efficient Field-Scale Simulation of Black Oil in a Naturally Fractured Reservoir Through Discrete Fracture Networks and Homogenized Media. SPE Res Eval & Eng; **11**(4): 750–758. SPE-103901-PA.

Lim, K.T. & Aziz, Khalid. (1995). Matrix-fracture transfer shape factors for dual-porosity simulators. Journal of Petroleum Science and Engineering. 13. 169-178. 10.1016/0920-4105(95)00010-F.

Lindsay G., White D., Miller G., Baihly J., and Sinosic B. (2016). Understanding the Applicability and Economic Viability of Refracturing Horizontal Wells in Unconventional Plays. Paper SPE 179113 presented at the SPE Hydraulic Fracturing Technology Conference held in the Woodlands, Texas, USA, 9-11 February 2016.

Lindsay, G., Miller, G., Xu, T., Shan, D., and Baihly, J. 2018. Production Performance of Infill Horizontal Wells vs. Pre-Existing Wells in the Major US Unconventional Basins. Presented at SPE Hydraulic Fracturing Technology Conference and Exhibition, The Woodlands, Texas, USA, 23-25 January. SPE-189875-MS.

Lindner P., Bello, H. 2015. Eagle Ford well spacing: a methodology to integrate, analyze, and visualized multisource data in solving a complex value-focused problem. SPE-178712-MS/URTeC: 2174709. In Proceedings of *Unconventional Rescources Technology Conference*, San Antonio, Texas, USA, 20-22 July.

Liu, Y., Leung, J. Y., & Chalaturnyk, R. (2018). Geomechanical Simulation of Partially Propped Fracture Closure and Its Implication for Water Flowback and Gas Production. Society of Petroleum Engineers. doi:10.2118/189454-PA.

Lu, B. and Wheeler M.F. (2009), Iterative coupling reservoir simulation on high-performance computers. *Petroleum Science Journal 6: 43.*

Manchanda R. (2015). A General Poro-Elastic Model for Pad-Scale Fracturing of Horizontal Wells. PhD Dissertation. The University of Texas at Austin.

Manchanda R., Bryant E. C., Bhardwaj P. and Sharma, M. M. (2016). Strategies for Effective Stimulation of Multiple Perforation Clusters in Horizontal Wells. Paper SPE 179126 presented at the SPE Hydraulic Fracturing Technology Conference held in The Wooldlands, Texas, 9-11 February 2016. doi:10.2118/179126-MS.

Mandel, J. (1953), Consolidation des sols (étude mathématique), Geotechnique, 3(7), 287–299.

Malpani, R., Sinha, S., Charry, L., Sinosic, B., Clark, B., and Gakhar, K. 2015. Improving hydrocarbon recovery of horizontal shale wells through refracturing. Presented at SPE/CSUR Unconventional Resources Conference, Calgary, Alberta, Canada, 20-22 October. SPE-175920-MS.

McFall R., Mullen K., Baihly J., Lindsay G., Shin J. (2017). Refracturing in the Eagle Ford Shale: One Operator's Quest to Identify and Rank Candidates, Minimize Well Interference, and Understand Variability of Results. Paper URTeC 2691375 presented at the Unconventional Resources Technology Conference held in Austin, Texas, USA, 24-26 July 2017.

McDaniel, B. W., & Rispler, K. A. (2009, January 1). Horizontal Wells with Multi-Stage Fracs Prove to be Best Economic Completion for Many Low-Perm Reservoirs. Society of Petroleum Engineers. doi:10.2118/125903-MS.

McNamee J and Gibson RE (1960). Plane strain and axially symmetric problems of the consolidation of a semi-infinite clay stratum. *Quarterly Journal of Mechanics and Applied Mathematics*; **13**(2):210–227.

Miller G., Lindsay G., Baihly J., and Xu T. (2016). Parent Well Refracturing: Economic Safety Nets in an Uneconomic Market. Paper SPE 180200 presented at the SPE Low Perm Symposium held in Denver, Colorado, USA, 5-6 May 2016.

Moinfar, A., Sepehrnoori, K., Johns, R. T., & Varavei, A. (2013). Coupled geomechanics and flow simulation for an embedded discrete fracture model. In *Society of Petroleum Engineers - SPE Reservoir Simulation Symposium 2013* (Vol. 2, pp. 1238-1250).

Mi, L., Jiang, H., Tang, L., Liu, C., Li, J., Wang, Y., Killough, J. (2016, June 1). A Utility Discrete Fracture Network Model for Field-Scale Simulation of Naturally Fractured Shale Reservoirs. Society of Petroleum Engineers. doi:10.2118/180968-MS.

Offenberger, R., Ball, N., Kanneganti, K., & Oussoltsev, D. (2013, August 12). Integration of Natural and Hydraulic Fracture Network Modeling with Reservoir Simulation for an Eagle Ford Well. Unconventional Resources Technology Conference. doi:10.15530/URTEC-1563066-MS.

Pankaj P., Gakhar K., and Lindsay G. (2016). When to Refrac? Combination of Reservoir Geomechanics with Fracture Modeling and Reservoir Simulation Holds the Answer. Paper SPE 182161 presented at the SPE Asia Pacific Oil & Gas Conference and Exhibition held in Perth, Australia, 25-27 October 2016.

Preux C., McKee F. (2011), Study and approximation of IMPES stability: the CFL criteria, *Finite* Volumes for *Complex Applications VI Problems* & *Perspectives* pp 713-721.

Rahim, Z., Al-anazi Hamoud Ali, Kanaan, A., Habbtar, A. H., Omair, A. M., Senturk, N. H., & Kalinin, D. A. (2012, January 1). Productivity Increase Through Hydraulic Fracturing in Conventional and Tight Gas Reservoirs - Expectation versus Reality. Society of Petroleum Engineers. doi:10.2118/153221-MS.

Rimedio, M., Shannon, C., Monti, L., Lerza, A., Roberts, M., Quiroga, J. 2015. Interference behavior analysis in Vaca Muerta shale oil development, Loma Campana field, Argentina. URTeC 2154850. In Proceedings of *the unconventional Resources Technology Conference.* San Antonio, Texas, USA, 20-22 July.

Ren G., Jiang J., and Younis R. M. (2017). Fully-Coupled XFEM-EDFM Hybrid Model for Geomechanics and Flow in Fractured Reservoirs. Paper SPE 182726 presented at the SPE Reservoir Simulation Conference held in Montgomery, Texas, 20-22 February 2017. doi:10.2118/182726-MS.

Rezaei A., Rafiee M., Bornia G., Soliman M., Morse S. (2017). Protection Refrac: Analysis of Pore Pressure and Stress Change Due to Refracturing of Legacy Wells. Paper URTeC 2667433 presented at the Unconventional Resources Technology Conference held in Austin, Texas, USA, 24-26 July 2017.

Roussel N.P. and Sharma M.M. (2010a). Quantifying Transient Effects in Altered-Stress Refracturing of Vertical Wells. *SPE Journa*; **15**(3): 770-782. SPE-119522-PA. doi: 10.2118/119522-PA.

Roussel N.P. and Sharma M.M. (2010b). Role of Stress Reorientation in the Success of Refracture Treatments in Tight Gas Sands. Paper SPE 134491 presented at the 2010 SPE Annual Technical Conference and Exhibition, Florence, Italy, 19–22 September. doi:10.2118/134491-MS.

Roussel N.P. (2011). Stress Reorientation in Low-Permeability Reservoirs. PhD Dissertation. The University of Texas Austin.

Roussel N. P., Florez H. and Rodriguez A. A. (2013). Hydraulic Fracture Propagation from Infill Horizontal Wells. Paper SPE 166503 presented at the SPE Annual Technical Conference and Exhibition held in New Orleans, Louisiana, USA, 30 September–2 October 2013. doi:10.2118/166503-MS.

Rusche H. (2002), Computational fluid dynamics of dispersed two-phase flows at high phase Fractions. PhD Dissertation. Imperial College of Science, Technology & Medicine.

Rutqvist, Jonny, Yu-Shu Wu, Chin-Fu Tsang and Gudmundur S. Bodvarsson (2002). "A modeling approach for analysis of coupled multiphase fluid flow, heat transfer, and deformation in fractured porous rock."

Safari R., Lewis R., Ma X., Mutlu U. and Ghassemi A. (2015). Fracture Curving Between Tightly Spaced Horizontal Wells. Paper SPE 178513 presented at the Unconventional Resources Technology Conference, San Antonio, Texas, 20-22 July 2015. doi:10.15530/URTEC-2015-2149893.

Sangnimnuan, A., Li, J., Wu, K. (2018a). Development of efficiently coupled fluid flow and geomechanics models to predict stress evolution in unconventional reservoirs with complex fracture geometry. SPE-189452. *SPE Journal, 23(03): 640-660.*

Sangnimnuan, A., Li, J., Wu, K., Holditch S. A. (2018b). Development of Efficiently Coupled Fluid Flow and Geomechanics Model for Refracturing Optimization in Highly Fractured Reservoirs. SPE-189870. *SPE Hydraulic Fracturing Technology Conference.* Woodlands, Texas, USA, 23-25 January.

Sangnimnuan, A., Li, J., Wu, K. (2019a). Fracture Hits Analysis for Infill-Parent well Development. ARMA 19-1542. American Rock Mechanics Association

Sangnimnuan, A., Li, J., Wu, K., & Holditch, S. (2019b). Impact of Parent Well Depletion on Stress Changes and Infill Well Completion in Multiple Layers in Permian Basin.

Unconventional Resources Technology Conference, Denver, Colorado, 24-26 July 2019. doi:10.105530/urtec-2019-972

Seth, P., Kumar, A., Manchanda, R., Shrivastava, K., & Sharma, M. M. (2018). Hydraulic Fracture Closure in a Poroelastic Medium and Its Implications on Productivity. American Rock Mechanics Association.

Sheldon J.W., Zondek B., Cardwell W.T. (1959), One-dimensional, incompressible, non-capillary, two-phase fluid flow in a porous medium, *T. SPE. AIME* 216 290–296.

Sierra, L. (2016, June 1). Is Induced Fracture Complexity Always Required in Unconventional Reservoir Stimulation? Society of Petroleum Engineers. doi:10.2118/180979-MS.

Singh V., Roussel N.P. and Sharma M.M. (2008). Stress Reorientation around Horizontal Wells. Paper SPE 116092 presented at the 2008 SPE Annual Technical Conference and Exhibition, Denver, Colorado, 21-24 September. doi: 10.2118/116092-MS.

Skempton, A.W. (1954). The pore pressure coefficients A and B. Geotechnique. 4: 143-147.

Sun, S.Z., Zhou, X., Yang, H. et al. Pet. Sci. (2011) 8: 433. Fractured reservoir modeling by discrete fracture network and seismic modeling in the Tarim Basin, China https://doi.org/10.1007/s12182-011-0161-x

Tang T., Hededal O. and Cardiff P. (2015). On finite volume method implementation of poro-elasto-plasticity soil model. *International Journal for Numerical and Analytical Methods in Geomechanics*. DOI: 10.1002/nag.2361.

Tang, J., Wu, K., Zeng, B., Huang, H., Hu, X., Guo, X. and Zuo, L. 2017. Investigate effects of weak bedding interfaces on fracture geometry in unconventional reservoirs. *Journal of Petroleum Science and Engineering*. doi: 10.1016/j.petrol.2017.11.037.

Tang, J., Wu, K., Zuo, L., Ehlig-Economides, C. 2018. A Coupled Three-Dimensional Hydraulic Fracture Propagation Model Considering Multiple Bedding Layers. Presented at Unconventional Resources Technology Conference (URTeC) in Houston, Texas, USA, 23 July – 25 July.

Tang, J., Wu, K., Zuo, L., Xiao, L., Sun, S., Ehlig-Economides, C. 2019. Investigation of Rupture and Slip Mechanisms of Hydraulic Fracture in Multiple-layered Formations. *SPE Journal*. Preprint. SPE-197054-PA. doi:10.2118/197054-PA.

Tang, J., Ehlig-Economides, C., Fan, B., Cai, B., Mao, W. 2019. A Microseismic-based Fracture Properties Characterization and Visualization Model for the Selection of Infill Wells in Shale Reservoirs. *Journal of Natural Gas Science and Engineering*. 67: 147-159. doi:10.1016/j.jngse.2019.04.014.

Terzaghi K. *Erdbaumechanik auf Bodenphysikalischer Grundlage*. F. Deuticke: Wien, 1925.

Thomas, L.K., T.N. Dixon, and R.G. Pierson (1983): \Fractured Reservoir Simulation," SPE Journal, 42-54.

Tukovic Z., Ivankovic A. and Karac A. (2013). Finite-volume stress analysis in multi-material linear elastic body. *International Journal for Numerical Methods in Engineering*; **93**(4):400–419.

Van Genuchten M.T. (1980), A closed-form equation for predicting the hydraulic conductivity of unsaturated soils, *Soil Sci. Soc. Am. J.* 44 (5) 892.

Vidal-Gilbert S. and Tisseau E. (2006). Sensitivity analysis of geomechanical behavior on time-lapse seismic velocity modeling. Paper SPE 100142 presented at the SPE EUropec/EAGE Annual Conference and Exhibition, Vienna, Austria, 12-15 June 2006. doi:10.2118/100142-MS.

Wang HF. (2000). Theory of Linear Poroelasticity. Princeton University Press: Princeton, NJ.

Wang B. (2014). Parallel Simulation of Coupled Flow and Geomechanics in Porous Media. PhD Dissertation. The University of Texas at Austin.

Wang, C., Wu, Y.-S., Xiong, Y., Winterfeld, P. H., & Huang, Z. (2015). Geomechanics Coupling Simulation of Fracture Closure and Its Influence on Gas Production in Shale Gas Reservoirs. Society of Petroleum Engineers. doi:10.2118/173222-MS.

Wang, K., Peng, X., Du, Z., Haghighi, M., & Yu, L. (2016, October 25). An Improved Grid Generation Approach for Discrete Fracture Network Modelling Using Line Fracture Concept for Two-Phase Flow Simulation. Society of Petroleum Engineers. doi:10.2118/182260-MS.

Wang K., Liu H., Luo J., Wu K., and Chen Z. (2017). A Comprehensive Model Coupling Embedded Discrete Fractures, Multiple Interacting Continua, and Geomechanics in Shale Gas Reservoirs with Multiscale Fractures. *Energy Fuels*20173187758-7776.

Warren, J.E. and P.J. Root. (1963): \The Behavior of Naturally Fractured Reservoirs," SPE Journal, 245-255.

Webster, P., Cox, B., and Molenaar, M. 2013. Developments in diagnostic tools for hydraulic fracture geometry analysis. Presented at Unconventional Resources Technology Conference, Denver, Colorado, USA, 12-14 August. URTEC-1619968-MS.

Weng, X., Kresse, O., Cohen, C.E., Wu, R., and Gu, H. 2011. Modeling of hydraulic fracture network propagation in a naturally fractured formation. Presented at SPE Hydraulic Fracturing Technology Conference, The Woodlands, Texas, USA, 24-26 January. SPE-140253-MS.

Whitield, T., Watkins, M., Dickinson, L.J. 2018. Pre-loads: Successful mitigation of damaging frac hits in the Eagle Ford. SPE 191712. In Proceedings of *SPE Annual Technical Conference and Exhibition*, Dallas, Texas, 24-26 September.

Wu K., Olson J. E. (2014). Numerical Investigation of Complex Hydraulic Fracture Development in Naturally Fractured Reservoirs. Paper SPE 173326 presented at the SPE Hydraulic Fracturing Technology Conference held in The Woodlands, Texas, USA, 3-5 February 2015.

Wu, K. and Olson, J.E. 2015a. A simplified three-dimensional displacement discontinuity method for multiple fracture simulations. *International Journal of Fracture*. Vol.193 (02): 191-204.

Wu, K. and Olson, J.E. 2015b. Simultaneous multi-frac treatments: fully coupled fluid flow and fracture mechanics for horizontal wells. SPE 167626-PA. *SPE Journal*. Vol.20 (02).

Wu R., Kresse, O., Weng, X., Cohen, C., and Gu, H. 2012. Modeling of interaction of hydraulic fractures in complex fracture networks. Presented at SPE Hydraulic Fracture Technology Conference, Texas, USA, 6-8 February. SPE-152052-MS.

Xu Y. (2015). Implementation and Application of the Embedded Discrete Fracture Model (EDFM) for Reservoir Simulation in Fractured Reservoirs. PhD Dissertation. The University of Texas at Austin.

Yaich, E., Diaz de Souza O.C., Foster R.A., Abou-sayed, I. 2014. A methodology to quantify the impact of well interference and optimize well spacing in the Marcellus shale. SPE 171578. In Proceedings of *SPE/CSUR Unconventional Resources Conference – Canada.* Calgary, Alberta, Canada, 30 September – 2 October.

Yang D. (2013), A simulator with numerical upscaling for the analysis of coupled multiphase flow and geomechanics in heterogeneous and deformable porous and fractured media. PhD Dissertation. Texas A&M University.

Yang, D., Xue, X., & Chen, J. (2018). High Resolution Hydraulic Fracture Network Modeling Using Flexible Dual Porosity Dual Permeability Framework. Society of Petroleum Engineers. doi:10.2118/190096-MS.

Yu, X., Winterfeld, P., Wang, S., Wang, C., Wang, L., & Wu, Y. (2019). A Geomechanics-Coupled Embedded Discrete Fracture Model and its Application in Geothermal Reservoir Simulation. Society of Petroleum Engineers. doi:10.2118/193931-MS.

Zhang, C., Rothfuchs, T., Su K., et al. (2007), Experimental Study of the Thermo-Hydro-Mechanical Behaviour of Indurated Clays. *Phys. Chem. Earth* 32 (8–14): 957–965.

Zhang, Deliang & Dai, Yu & Ma, Xinhua & Zhang, Liehui & Zhong, Bing & Wu, Jianfa & Tao, Zhengwu. (2018). An Analysis for the Influences of Fracture Network System on Multi-Stage

Fractured Horizontal Well Productivity in Shale Gas Reservoirs. Energies. 11. 414. 10.3390/en11020414.

Zhenzhen D., Weirong Li,, Gang L., Huijie W. and Cai W. (2019). Embedded Discrete Fracture Modeling as a Method to Upscale Permeability for Fractured Reservoirs. Energies 2019, 12, 812; doi:10.3390/en12050812.

Zoback, M.D. 2010. Reservoir geomechanics. Cambridge University Press.